

# **Volcano-tectonic controls of hydrothermalism on a hot spot-influenced mid-ocean ridge: Insights from Iceland and Reykjanes Ridge**

**Dissertation**

zur Erlangung des Doktorgrades  
der Mathematisch-Naturwissenschaftlichen Fakultät  
der Christian-Albrechts-Universität zu Kiel

vorgelegt von  
*Dominik Palgan*

Kiel, 2017



Referent:.....Prof. Dr. Colin W. Devey

Koreferent:..... PD Dr. Thor H. Hansteen

Tag der mündlichen Prüfung:.....04.07.2017

Zum Druck genehmigt:.....04.07.2017

Prof. Dr. Natascha Oppelt, Dekanin

## **Erklärung**

Hiermit erkläre ich, dass ich die vorliegende Doktorarbeit selbständig und ohne Zuhilfenahme unerlaubter Hilfsmittel erstellt habe. Sie stellt, abgesehen von der Beratung durch meinen Betreuer, nach Inhalt und Form meine eigene Arbeit dar.

Weder diese, noch eine ähnliche Arbeit wurde an einer anderen Abteilung oder Hochschule im Rahmen eines Prüfungsverfahrens vorgelegt, veröffentlicht oder zur Veröffentlichung vorgelegt.

Ferner versichere ich, dass die Arbeit unter Einhaltung der Regeln guter wissenschaftlicher Praxis der Deutschen Forschungsgemeinschaft entstanden ist.

Kiel, den

Dominik Pałgan

**Abstract**

Hydrothermal systems along mid-ocean ridges play an important role in the evolution of our planet by contributing to planetary cooling, geochemical mass balance, the formation of ore deposits and influencing the biogeography of the deep-sea ecosystems. Empirical studies suggest that high-temperature hydrothermal systems, which should mostly be confined to ridge axes, can be expected every ~100 km along-axis. The ~950 km long, shallow and hot spot-influenced Reykjanes Ridge, south of Iceland, does not conform to this scenario, with only one high-temperature vent field (Steinahóll) found to date. This suggests that another type of venting, perhaps at low-temperature (<100°C), may be dominant along this ridge. Little is known about the global distribution of low-temperature systems as they are difficult to detect and might be widespread in under-surveyed off-axis regions. Currently no techniques for prospecting for low-temperature venting other than visual surveys (for shimmering water, bacterial mats etc.) are available.

The primary aim of this thesis was to investigate the abundance and volcano-tectonic controls of low-temperature, off-axis hydrothermal activity along the flanks of an active divergent plate boundary, initially using the subaerial Westfjords region of Iceland as a proxy. A secondary aim was to put constraints on the age of features controlling hydrothermal circulation in off-axis setting. A third aim was to postulate where hydrothermal venting along the Reykjanes Ridge may occur and determine if and where more high-temperature systems could be present.

Icelandic hot springs were used as direct analogues for seafloor hydrothermal systems and results of on-land observations extrapolated to the adjacent Reykjanes Ridge. Field observations were collected in two field seasons in 2013 and 2014, mainly from the off-axis Westfjords (NW Iceland) but also from the on-axis Reykjanes Peninsula (SW Iceland). Dating of vents-hosting features was done using the  $^{40}\text{Ar}/^{39}\text{Ar}$  method. The bathymetry of the northern Reykjanes Ridge was interpreted for volcano-tectonic status and hydrothermal prospecting, based on on-land observations.

The results presented in this thesis show that even the Tertiary Icelandic crust of the Westfjords (>10 Ma) is hydrothermally active, with the location of abundant low-temperature systems exclusively controlled by dike intrusions cutting the lava pile. This is in contrast to fault-controlled vent sites usually observed in on-axis regions. This dissimilarity between the controls of off- and on-axis venting is most likely linked to the drastic drop of permeability of faults once they become inactive upon leaving the axial region. This permeability drop is probably linked to sealing of the fault gouge by secondary mineralization. It appears that, in



contrast, the lower fluid temperatures, low water/rock ratios and overall low dissolved species load allows dike margins to remain permeable over millions of years in the off-axis regions. These results can be used to predict the locations of off-axis low-temperature vent sites along the Reykjanes Ridge and suggests that one such site may be expected for every 13 km<sup>2</sup> of the >2 Ma crust along this ridge. <sup>40</sup>Ar/<sup>39</sup>Ar ages of the dikes from Westfjords show that they overlap with the ages of the host lava pile (within 2σ errors), suggesting they were intruded on-axis at the Snæfellsnes–Skagi Rift Zone (SSRZ), which was active from 15 to 7 Ma.

Observations from the subaerial on-axis setting (Reykjanes Peninsula, SW Iceland) show that hydrothermalism is confined to four distinctive volcanic systems intersected by fissure swarms. These observations were then extrapolated to the Reykjanes Ridge (between 62°30'N and 63°30'N). Interpretation of the bathymetry shows that the plate boundary is organized in seven en echelon, right-stepping Axial Volcanic Ridges (AVRs) which are the submarine equivalents of the on-land volcanic systems and fissure swarms on the Reykjanes Peninsula. These AVRs have a complex formation history, apparently much more complicated than had been implied by previously published evolution models. Based on the geomorphological similarities between the on-land Reykjanes Peninsula and the submarine Reykjanes Ridge, these seven AVRs may also be hydrothermally active, with vent sites probably occupying the youngest volcanic features, some of which appear to be local topographic highs.

## Zusammenfassung

Hydrothermalsysteme an Mittelozeanischen Rücken spielen bei der Entwicklung unseres Planeten eine wichtige Rolle, in dem sie zum Abkühlen des Planeten, der geochemischen Massenbilanz der Ozeane und der Bildung von Erzen beitragen, sowie die Bio-geographie von Tiefsee-Ökosystemen beeinflussen. Empirische Studien deuten darauf hin, dass alle ~100 km Hochtemperatur Hydrothermalsysteme zu erwarten sind, welche sich vor allem an der Rückenachse befinden. Der ~950 km lange, seichte, Hotspot-beeinflusste Reykjanesrücken südlich von Island entspricht nicht diesem Bild, da bisher nur ein einziges Hochtemperatur-Hydrothermalfeld (Steinahóll) gefunden wurde. Dies deutet darauf hin, dass hydrothermale Aktivität entlang dieses Rückens vermutlich durch niedrigen Temperaturen dominiert wird. Bisher ist wenig zur globalen Verteilung von Niedertemperaturfeldern bekannt, da sie schwer aufzuspüren sind und vor allem in wenig untersuchten achsenfernen Regionen vorkommen können. Zur Zeit gibt es außer visuellen Untersuchungen (für flirrendes Wasser, Bakterienmatten etc.) keine Technik, um Niedertemperaturfelder zu erkunden.

Der Hauptziel diese Arbeit war, Häufigkeit und vulkan-tektonischen Einfluss auf niedertemperatur, achsenferne hydrothermale Aktivität entlang der Flanken einer aktiven divergenten Plattengrenze zu untersuchen. Dazu wurde zunächst die subaerische Region der Westfjorde als Näherung genutzt. Ein weiteres Ziel war es, das Alter der geologischen Elemente einzuschränken, welche die hydrothermale Zirkulation in einem achsenfernen Umfeld beeinflussen. Ein drittes Ziel war es, die Lokation hydrothermalen Aktivität am Reykjanesrücken vorherzusagen, und zu bestimmen ob und wo weitere Hochtemperatursysteme liegen könnten.

Heiße Quellen auf Island wurden daher als direktes Gegenstück zu Hydrothermalsystemen am Meeresboden genutzt, und die Ergebnisse der Beobachtungen an Land auf den angrenzenden Reykjanesrücken extrapoliert. Geländebeobachtungen an den achsenfernen Westfjords (NW Island) sowie auf der axialen Reykjanes-Halbinsel (SW Island) wurden im Rahmen von zwei Geländearbeiten in 2013 und 2014 erhoben. Datiert wurden die Vulkanschlote mit der  $^{40}\text{Ar}/^{39}\text{Ar}$  Methode. Die vulkanisch-tektonische Entwicklung des nördlichen Reykjanesrückens wurde auf Grundlage der bathymetrischen Daten und unter Nutzung der Landbeobachtungen interpretiert.

Die Ergebnisse der vorliegenden Arbeit zeigen, dass sogar die Tertiäre Kruste Islands an den Westfjorden (>10 Ma) hydrothermal aktiv ist, wobei die räumliche Verteilung von zahlreichen Niedertemperatursystemen durch Gangintrusionen, welche die Lava durchschlagen, kontrolliert wird. Dies steht im Gegensatz zur normalerweise

störungsgebundenen Kontrolle hydrothormaler Aktivität in axialen Regionen. Diese fehlende Ähnlichkeit zwischen axialen- und nicht-axialen Ventlokationen wird wahrscheinlich durch drastische Permeabilitätsänderungen von Störungen hervorgerufen, wenn diese die axiale Region verlassen und inaktiv werden. Die verminderte Permeabilität könnte an das Versiegeln der Störungen durch sekundäre Mineralneubildung gebunden sein. Im Gegensatz dazu scheint es, dass in den außeraxialen Bereichen die niedrigeren Fluidtemperaturen, die niedrigen Fluid/Gesteinsverhältnisse und die insgesamt geringe die insgesamt geringen Gehalte gelöster Species dazu beitragen, dass die Randbereiche von den Gangintrusionen über Millionen von Jahren durchlässig bleiben. Die Beobachtungen dieser Studie können genutzt werden, um die Lage von niedrig temperierten Austrittsstellen außerhalb der Reykjanes Rückenachse vorherzusagen. Eine solche Austrittsstelle wird dabei für jede 13 km<sup>2</sup> der >2 Ma alten Kruste entlang des Rückens erwartet. Das <sup>40</sup>Ar/<sup>39</sup>Ar Alter der Gänge in den Westfjorden zeigen, dass diese sich mit den Altern des Lava-Nebengesteins überlappen (innerhalb des 2σ Fehlers), was darauf schließen lässt, dass sie an des Snæfellsnes-Skagi Rifts (SSRZ) axial intrudierten, welches vor 15–7 Ma aktiv war.

Beobachtungen des subaerischen axialen Umfelds (Reykjanes-Halbinsel, SW Island) zeigen, dass sich der Hydrothermalismus auf vier markante vulkanische Systeme beschränkt, welche von Gangscharen gekreuzt werden. Diese Beobachtungen wurden anschließend auf den Reykjanesrücken extrapoliert (zwischen 62°30'N und 63°30'N). Die Interpretation der Bathymetrie zeigt dass die Plattengrenze in sieben en echelon, rechtstretende Axiale Vulkanische Rücken (AVR), welche das submarine Äquivalent zu den vulkanischen System an Land und den Gangscharen der Reykjanes-Halbinsel sind. Diese AVRs haben eine komplexe Entstehungsgeschichte, welche anscheinend komplizierter ist als durch bereits publizierte Entstehungsmodelle angedeutet. Aufgrund der geomorphologischen Ähnlichkeiten zwischen der subaerischen Reykjaneshalbinsel und dem submarinen Reykjanesrücken scheinen diese sieben AVRs auch hydrothermal aktiv zu sein, wobei die Austrittsstellen auf den jüngsten und meist auch topographisch flachsten Vulkanstrukturen sitzen.

## Contents

Abstract .....	4
Zusammenfassung .....	6
Contents .....	8
Acknowledgements .....	11
1 Introduction .....	14
1.1 Introduction and aims .....	14
1.2 Background information .....	16
1.2.1 Volcanism along mid-ocean ridges .....	16
1.2.2 Volcanic landforms .....	20
1.2.3 Hydrothermal activity along mid-ocean ridges .....	29
1.3 Geological setting .....	34
1.3.1 Iceland .....	34
1.3.2 Reykjanes Ridge .....	44
1.4 References .....	50
2. Field seasons .....	68
2.1. Introduction .....	68
2.1.1. Why observations on land? .....	68
2.2 Field season 2013 .....	69
2.2.1 Methods .....	70
2.2.2 Preliminary results .....	75
2.3 Field season 2014 .....	84
2.3.1 Methods and preliminary results .....	84
2.4 References .....	87
3 Dike control of hydrothermal circulation in the Tertiary Icelandic crust and implications for cooling of the seafloor .....	90
3.1 Introduction .....	90
3.2 Geological setting of Westfjords low-temperature hydrothermal systems .....	92
3.3 Methods .....	93
3.4 Results .....	94
3.4.1 Reykjanes Peninsula, Westfjords .....	94
3.4.2 Heydalur .....	96
3.4.3. Submerged mound (N65°49.248' W22°29.762') .....	97

3.4.4 Hamarsháls Peninsula .....	99
3.5 Discussion.....	101
3.5.1 Present low-temperature activity – dike-controlled hydrothermal circulation .....	101
3.5.2 Former hydrothermal activity associated with dikes in Westfjords?.....	105
3.5.3 Can we predict the locations of hydrothermal activity along slow-spreading ridges – case for the Reykjanes Ridge? .....	106
3.6 Conclusions .....	109
3.7 References .....	110
4 <sup>40</sup> Ar/ <sup>39</sup> Ar dating of dikes from the Westfjords, Iceland: insights into timing of hydrothermal activity in the off-axis oceanic crust.....	120
4.1 Introduction to <sup>40</sup> Ar/ <sup>39</sup> Ar dating .....	120
4.2 Previous dating work in Westfjords .....	124
4.3 Methods .....	127
4.3.1 <sup>40</sup> Ar/ <sup>39</sup> Ar dating.....	127
4.3.2 Chemistry of plagioclase phenocrysts and overall alteration of dikes.....	129
4.5 Results .....	130
4.5.1 Petrography of the dikes, chemical composition of plagioclases and hydrothermal alteration .....	130
4.5.2 <sup>40</sup> Ar/ <sup>39</sup> Ar dating.....	133
4.6 Discussion.....	147
4.6.1 Alteration of the dikes and its impact on the plagioclase phenocrysts .....	147
4.6.2 Ages of the dikes and implications for off-axis hydrothermal activity.....	148
4.6.3 Quality and reliability of <sup>40</sup> Ar/ <sup>39</sup> Ar dating method for dating Icelandic dikes .....	152
4.7 Conclusions .....	156
4.8 References .....	156
5 Volcanism and hydrothermalism on a hot spot–influenced ridge: Comparing Reykjanes Peninsula and Reykjanes Ridge, Iceland.....	164
5.1 Introduction .....	164
5.2 Datasets and methods .....	165
5.3 Geological setting .....	167
5.3.1 Reykjanes Peninsula .....	167
5.3.2. Reykjanes Ridge .....	171
5.4 Results and interpretations.....	174
5.4.1 General morphology of the spreading axis .....	174
5.4.2 Morphology of the AVRs .....	174

5.4.3 Seismic activity .....	175
5.4.4 Interpretations .....	176
5.5 Discussion.....	189
5.5.1 Volcanism on Axial Volcanic Ridges.....	189
5.5.2 Status of volcanic activity on the Reykjanes Peninsula.....	192
5.5.3 Volcanic control of venting at Steinahóll Vent Field and elsewhere.....	194
5.5.4 Signs of off-axis volcanism on the Reykjanes Ridge?.....	196
5.6 Conclusions .....	198
5.7 References .....	199
6 Conclusions .....	210
Appendix A .....	215
Appendix B .....	227
Curriculum Vitae.....	239

## Acknowledgements

During my PhD studies, I have been fortunate to be surrounded by many people that supported me and provided a lot of help, and it is my great pleasure to thank them all.

First and foremost I would like to thank my supervisor Colin Devey for giving me the opportunity to do my PhD and introducing me to a fascinating world of mid-ocean ridges, volcanology and hydrothermalism. Thank you for the guidance, support, discussions and patience (especially with constant shortening of my texts, endless reminding me to leave the speculations out and convincing me to remove “Moreover” from my vocabulary!). I also want to thank you for giving me the chance to learn methods for studying ocean floor from first hand by participating in two cruises in the Atlantic Ocean.

I want to give my special thanks to Isobel Yeo. Izzy, thank you for the support, encouragement, discussions and faith in me! Even though you would disagree with me, you became my mentor. I learned so much about the ocean research (and research overall) from you and I will never be able to thank you enough! Your friendship and patience helped me keep some of my sanity, there is no doubt about that ... but let's face it, I am not a completely normal human ☺. Thank you for all the best fun we managed to have all over the world, on cruises, holidays, road trips ... and yes, even in Kiel.

I would like to acknowledge the Helmholtz Research School for Ocean System Science and Technology (HOSST) for providing my PhD fellowship and enabling me to perform this dissertation. My great thanks to HOSST and Future Ocean cluster of excellence for allowing me to participate in conferences in Vienna, New York and San Francisco. Christel van den Bogaard: thank you for all the support, especially at the beginning of my stay in Kiel but also with all the administrative issues I would not be able to solve myself. Many thanks also to Frauke Rathjen for administrative help and always welcoming me in the office with a big smile.

I would like to thank Thor Hansteen for all the discussions and will to answer even the most basic and stupid questions I had. Thank you also for the review of this dissertation, invaluable input and suggestions.

I would like to thank Jo-Anne Wartho for leading the  $^{40}\text{Ar}/^{30}\text{Ar}$  dating of my Icelandic samples, despite how difficult they were to work with. Your help was instrumental for this significant part of my thesis. Thank you for the great introduction to geochronology and for all the discussions, and countless reviewing of my texts. I also want to thank Paul van den Bogaard for early suggestions on how to pick the best sample for  $^{40}\text{Ar}/^{30}\text{Ar}$  dating, and for answering to my emails even sent for the filed.

I would like to thank Þráinn Friðriksson and Bryndís Brandsdóttir for the discussions and support before, during and after field seasons in Iceland. Without your input and directions I would not be able to organize them and prepare myself for, what I consider now the absolute highlights of my PhD. I want to thank Ólafur S. Ástþórsson, the Director of Marine Research Institute in Reykjavik, for providing and allowing me to work with the

bathymetric data of the northern Reykjanes Ridge used in this thesis. I also thank Þórey Dagmar Möller for sending me all the papers from the Jökull journal.

I would like to thank Mario Thöner for help with the Electron Microprobe measurements I know so little about and for staying late to re-focus most of my points ... I swear I always tested the focus before moving on to another point ☺

I would like to thank all the Magmatic and Hydrothermal Systems working group for all the discussions and conversations (including gossip) especially during the lunch and cake breaks. Izzy, John, Hannah, Thor, Nico, Sven, Khalhela, Tom, Melissa, Froukje, Tea, Florent, Sebastian F., Sebastian G., Philipp, Lisa, Tatum, Stefan, Sabine, Meike, Anne and everyone who was there even for shorter time, thank you for creating such an amazing atmosphere! Froukje, Lisa and Tatum thanks for being such great office mates. Lisa and Tatum: coffee machine was a great idea and one of the best investments. Also, many thanks to Jon, Ollie, Jenn, Matt and those I forgot to mention (I am sorry!) for being there for great fun and conversations not necessarily related to work. Hannah and Melissa: thank you for the suggestions on writing and proof reading. Lisa, Sven and Stefan: thank you for help with the German Abstract of this dissertation.

I would like to thank my fellow HOSSTies (Annika, Arne, Corinna, Eyram, Ibrahim, Judith, Maryam, Nadine, Sasha, Sebastian, Stéphanie and Swaantje) and TOSSTies from Halifax for great times and lots of fun during all the softskill courses and summer schools!

I would like to thank my friends, Agnieszka, Aleksandra, Emilia, Joanna, Karolina, Mateusz, Natalia and others for support, great fun (and making fun of me), and finding time to hang out with me whenever I visited, and for your visits in Kiel ... what happens in Kiel stays in Kiel!

Finally, I would like to thank my family for support and for believing in me. I obviously cannot forget about the food parcels (especially towards the end of my PhD) which brought me so much and so needed joy in the final phase of my PhD ... the writing.  
Dziękuję wam bardzo!

Thank you all!!!



# Chapter 1

Introduction

# 1 Introduction

## 1.1 Introduction and aims

Seafloor hydrothermal systems play an important role in the evolution of our planet by facilitating the continuous and dynamic interaction between the lithosphere, hydrosphere and biosphere (Pirajno, 2009). Hydrothermal systems occur in many seafloor environments and over a wide spectrum of ocean depths (see section 1.2.2); in particular, seafloor hydrothermal circulation along the mid-ocean ridges has been an important ore-forming process throughout geological history, producing some of the largest and most valuable ore deposits mined to date (Hannington et al., 2005). On the modern seafloor, the potential for seafloor mineral resources is large as oceans cover ~70% of Earth's surface, with seafloor deposits forming predominantly along 60 000 km of mid-ocean ridges. Seafloor massive sulfide (SMS) deposits may be an important future resource, especially as the demand for minerals and metals will grow with the constantly growing population. This is particularly relevant for countries and communities living in the areas where hydrothermal activity occurs and which plan future exploration (with potential for future exploitation) of their territorial seas or seek to extend their Exclusive Economic Zones, such as Iceland. Therefore, it becomes clear that in the near future more effort will be given to explore for large deposits on the ocean floor.

Presently, locating hydrothermal fields on the seafloor remains challenging as it requires expensive ship time and a combination of sophisticated geophysical, chemical, optical and visual methods. These techniques are useful for finding deposits with active hydrothermal venting; however, locating inactive deposits is much more difficult. Inactive deposits are potentially larger in size than their active counterparts, and it may be possible to mine these deposits without the impacts on important vent communities that grow on active deposits (Hannington et al., 2010; Van Dover, 2014). In general, there is still very little known about the global abundance of both active and inactive hydrothermal systems and ore deposits (e.g., Hannington et al., 2010). Exploration for these deposits, in particular 'hidden' (e.g., buried under sediments) inactive deposits, requires an understanding how and where hydrothermal systems form. Therefore, we need to develop predictive models which can help us to improve future exploration strategies. Iceland is a unique setting where a section of the mid-ocean ridge is elevated above the seafloor. This gives a natural laboratory for direct observations of hydrothermalism along and around the mid-ocean ridge, providing a proxy for the development of predictive models for the occurrence of new hydrothermal sites on the mid-ocean ridges.

The main aims of this study are to answer the following questions:

- What are the dominating hydrothermal systems in Iceland, and what is their volcano-tectonic framework?
- Are volcano-tectonic controls of hydrothermal venting on Iceland the same in both on- and off-axis regions?
- Can Icelandic hydrothermal systems be used as a proxy for seafloor hydrothermal systems?
- What are the ages of the features hosting hydrothermal systems in far off-axis regions of Iceland, and what is their potential influence on the life-span of such systems?
- What is the volcano-tectonic history of the Reykjanes Ridge between 62°30'N and 63°30'N?
- What is the volcano-tectonic setting of the single known hydrothermal vent field, Steinahóll, on Reykjanes Ridge, south Iceland?
- Is it possible that the Axial Volcanic Ridges observed on the Reykjanes Ridge between 62°30'N and 63°30'N are hydrothermally active?

Results presented in this thesis could be used for the future exploration activities not only on the mid-ocean ridges adjacent to Iceland, like the Reykjanes Ridge, but also on other hot spot influenced ridges and possibly ridges of different spreading rates.

This thesis comprises six chapters covering the introduction (including the main aims and background of the work), and original results reported, published or submitted for publication in a peer-reviewed journals and main conclusions of the study.

The rest of Chapter 1 (sections 1.2 and 1.3) gives an overview of (1) the current state of knowledge about the volcanism along the global mid-ocean ridge system with emphasis on the slow-spreading Mid-Atlantic Ridge; (2) an overview of hydrothermal activity along the global mid-ocean ridge system with closer look at some of the best studied fields on the Mid-Atlantic ridge; and (3) the geological setting of the regions studied in this thesis (Iceland and Reykjanes Ridge).

## 1.2 Background information

### 1.2.1 Volcanism along mid-ocean ridges

The mid-ocean ridge system is the longest mountain chain on Earth (e.g., Rubin et al., 2012), where thousands of volcanoes create new oceanic crust as plates continuously diverge from each other (e.g., Perfit and Davidson, 1999). The characteristics of volcanic style and morphology of the spreading centers strongly vary depending on the spreading rate and magma supply to the system (Macdonald, 2001). At fast-spreading ridges ( $>90 \text{ mm y}^{-1}$ ), such as the East Pacific Rise (EPR), the ridge axis is characterized by an elongated elevation of the seafloor called the axial high whose summit has a small (10s of meters deep, 100s of meters wide) summit graben. At slower spreading rates ( $10\text{--}40 \text{ mm y}^{-1}$ ), such as the Mid-Atlantic Ridge (MAR), the axis is marked by a relatively deep (1-3 km) and wide (5-15km) rift valley (Macdonald, 2001). Axial highs may also form along the segments of slow-spreading ridges, which have higher magma supply, for example due to proximity of hot spots, like on the Reykjanes Ridge (e.g., Searle et al., 1994). The area within which the majority of the volcanic activity occurs is called the “neovolcanic zone.” It generally consist of elongated, low-lying volcanoes constructed by the mutual effects of eruptive construction and tectonic destruction due to the constant separation of the plates (Rubin et al., 2012). At fast-spreading ridges, the bathymetric relief of the neovolcanic zone is low due to higher magma supply, associated with more frequent eruptions that cover the seafloor (Macdonald, 1998), and former eruption products that build up the volcanoes merging into semicontinuous ridges along the ridge axis (Bergmanis et al., 2007). Eruptions along these fast-spreading ridges originate from nearly-continuous along-ridge, melt-rich axial magma chambers (Singh et al., 1998). These subaxial melt bodies can be connected even for tens of kilometers (Burnett et al., 1989; Perfit and Chadwick, 1998; Singh et al., 1998) and melt can be distributed away from the injection regions (mantle upwelling zone) by so-called ‘downhill’ flow in sub-seafloor dikes (Macdonald, 2001). Moreover, this kind of melt redistribution may be unique for the high magma supply ridges like EPR or Reykjanes Ridge, where the along-axis regions are sufficiently hot at shallow depths to enable such subaxial flow (e.g., Macdonald, 2001; Martinez and Hey, 2017). The bathymetric relief along slow-spreading ridges is higher because crustal accretion is dominated by tectonic extension during the amagmatic periods (Escartin et al., 2008), and eruptions there are not sufficient to completely overprint tectonic features, such as normal faulting. In addition, because of the overall lower magma supply to slow-spreading ridges, volcanic activity in slow-spreading ridges is commonly localized along smaller, mid-segment ridges (e.g., Axial Volcanic Ridges, or AVRs; Searle et al., 2010; Yeo,

2012). A short summary of the differences in axial morphology and magma supply mechanisms along fast- and slow-spreading mid-ocean ridges is shown in Figure 1.

Both effusive and explosive volcanic styles have been observed along mid-ocean ridges at all spreading rates; however, the effusive volcanoes are by far the most common and effusive lava flows are the dominant volcanic products of the mid-ocean ridges (e.g., Embley and Chadwick, 1994; Fornari et al., 2004; Rubin et al., 2012; Escartin et al., 2014). Volcanic style and eruptive products depend on the chemical and physical properties of the magma, including: the formation process, temperature, composition, crystal and volatile content, viscosity, depth and size of the magma chamber, replenishment rate, and convective heat loss (e.g., due to hydrothermal activity) (Perfit and Chadwick, 1998; Rubin et al., 2012). Petrological and geophysical data suggest that the majority of the eruptions along mid-ocean ridges are fed from melt reservoirs whose presence and size are controlled by the level of magma supply to the ridge (Sinton and Detrick, 1992; Perfit and Chadwick, 1998; Singh et al., 1998). Where axial magma chambers (AMCs) can be detected by seismic imaging, their size, continuity and depth can be directly correlated with the spreading rate, for example, along faster spreading segments AMCs are more continuous and shallower at 1.5–2 km below the seafloor (Fig. 1; Macdonald, 2001). Furthermore, Phipps Morgan and Chen (1993) modeled that the depth of an AMC is directly controlled by the level of magma supply from below of the ridge and the level of hydrothermal cooling from above the seafloor. The depth of a shallow magma chamber and the average regional calculated temperature of an eruption are strongly correlated (Rubin et al., 2012). Hence, at fast-spreading ridges, a shallower magma chamber promotes the eruption of cooler, more degassed and more differentiated lavas, while at slow-spreading ridges, deeper magma chambers favor eruptions of hotter, more gas-rich and less differentiated magmas (Rubin and Sinton, 2007).

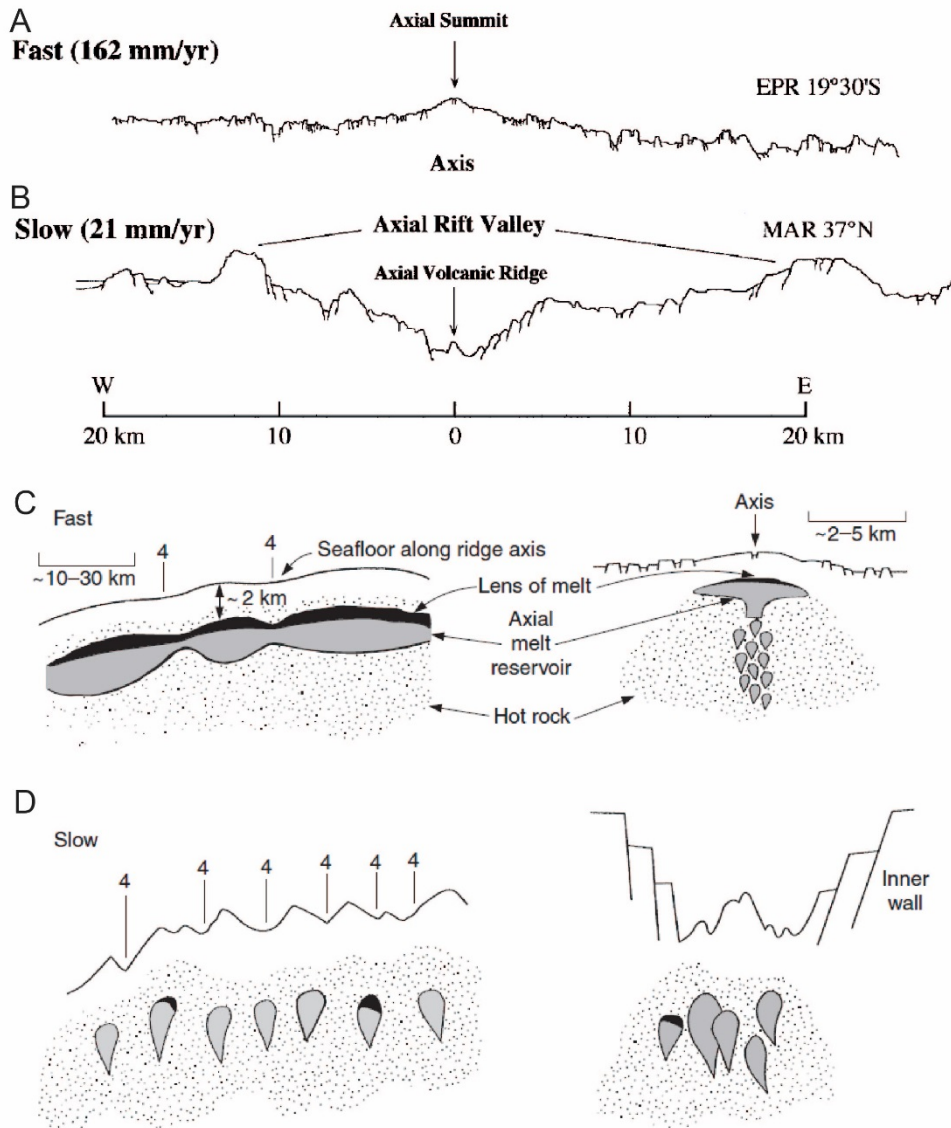


**Fig. 1** Comparison between the fast- and slow-spreading mid-ocean ridge; Cross-axis bathymetric profiles across (A) fast-spreading ridge (southern EPR) and (B) slow-spreading (MAR) ridge, showing main differences in the axial morphology. Fast-spreading ridges display axial high while slow-spreading ridges have prominent rift valley. Note that axial high may also form along high magma supply slow-spreading ridges, like the Reykjanes Ridge. Panels (C) and (D) show along-axis cross-sections along fast- and slow-spreading ridges, respectively, and represent schematic models of magma supply to such ridges. On fast-spreading or hot spot influenced ridges with axial high and robust magmatism, magma chambers form elongated, probably connected chains. On slow-spreading ridge with prominent rift valley bounded by inward-facing normal faults magma is probably stored in ephemeral and laterally restricted pockets. Cross-axis profiles are from Perfit and Davidson (1999). Magma supply model based on Macdonald (1998) and modified from Macdonald (2001).

Calculations of the thickness, volume, size and spatial extent of the volcanic products provides substantial information on the conditions of the eruption that produced them. In addition, the thickness, extent, and surface morphology of the lava flows directly reflects the effusion rate of the eruption, the local slope of the seafloor, topographic obstacles (e.g., faults and/or fissures) and the sequence of emplacement events during individual eruptions or eruptive episodes (e.g., Rubin et al., 2012; Yeo, 2012; Yeo and Searle, 2013). Additionally,

other factors may also control the lava morphology and lava dispersal across the seafloor, including: lava rheology (which is a function of composition, volatile content, temperature, vesicularity and crystallinity), pre-eruption seafloor roughness, slope angle and its variations, e.g., obstructions like fissures, faults or edges of the former flows (Griffiths and Fink, 1992a; Griffiths and Fink, 1992b; Gregg and Fink, 1995; Gregg et al., 1996; Caress et al., 2012; Chadwick et al., 2013; Clague et al., 2013). The diversity of submarine lava flow morphologies is comparable to those observed on land. They are typically classified by the length scale of the quenched-crust units that jointly make up the lava flow. Each of such units forms as a function of flow and cooling rate (Rubin, 2014). The most common types of lava morphologies observed on the mid-ocean ridges are pillow lavas, lobate flows, and sheet flows (Fig. 2).

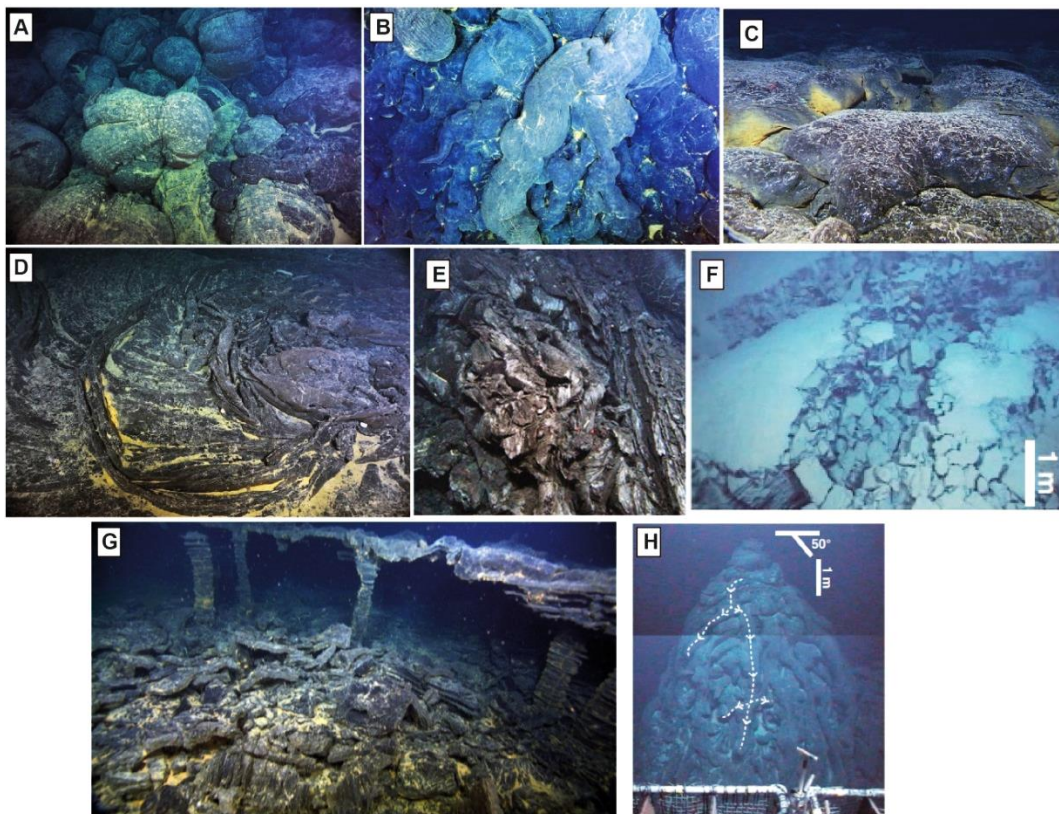


**Fig. 2** Typical lava morphologies observed on mid-ocean ridges of all spreading rates. (A) Pillow lava with well-developed bread-crust textures (left side of the image) and some lobate lava flowing around pillows (right side of the image) on the floor of Axial Seamount, Juan de Fuca Ridge. Field of view is ~3m; (B) Elongated pillow lava overlying older lobate lavas (floor of Axial Seamount, Juan de Fuca Ridge). Field of view is ~3m; (C) Lobate lava flow with low relief erupted on the East Pacific Rise near 9°50'N. Field of view is ~2m; (D) A sheet flow with ropy and folded edges erupted east of the ASHES hydrothermal field on the Axial Seamount, Juan de Fuca Ridge. Field of view is ~2m; (E) A sheet flow of the Puipui eruption, Northeast Lau Spreading Center; (F) Broken and sedimented sheet flow imaged on the Mid-Atlantic Ridge, near 45°N; (G) A 2-3 m high lava pillars in the interior of a partly collapsed lava pond with some solidified roof composed of lobate lava; (H) A haystack feature made of pillows with dashed arrows showing length of one pillow. Images credits: (A) and (B) Kelley D. S., UW, CSSF-ROV ROPOS, (C) Lange W., ©WHOI, WHOI-NDSF-Alvin, (D) Kelley D. S., UW, CSSF-ROV ROPOS, (E) Rubin et al. (2012), Jason dive J2-415, 2009, (F) Yeo and Searle (2013), Isis dive 81, 2008, (G) Kelley D. S., UW, CSSF-ROV ROPOS, (H) Yeo and Searle (2013), Isis dive 92, 2008.

### 1.2.2 Volcanic landforms

Several morphological features and edifices can be observed on the slow-spreading Mid-Atlantic ridge, including the Reykjanes Ridge, including volcanic hummocks, hummocky ridges, eruptive fissures, flat-topped seamounts and Axial Volcanic Ridges.

#### *Volcanic Hummocks*

Volcanic hummocks (Fig. 3A) are the smallest volcanic cones that can be observed everywhere along slow-spreading ridges within the median valley (e.g., Smith and Cann, 1990; Smith and Cann, 1992; Yeo et al., 2012). They can be conical-, subcircular- or dome-shaped and between 50–500 m in diameter (Briais et al., 2000). They are usually <300 m high and have steep flank slopes, usually  $>25^\circ$  (Smith and Cann, 1990). Qin and Buck (2008) concluded that volcanic hummocks are rather monogenic landforms which probably form in one volcanic episode as it is unlikely that dikes that feed such hummock-forming eruptions are active for more than one eruption. This is because ~1 m wide dike (typical for mid-ocean ridges) will solidify before the next eruption starts (Qin and Buck, 2008). Due to the high abundance of hummocks on the seafloor, they are believed to be the most common volcanic landform along slow-spreading ridges and most likely account for the majority of volcanic activity there, including the construction of Axial Volcanic Ridges (Yeo et al., 2012). They are erupted from one central vent with lavas extruding to the sides; hence, their flanks are predominantly constructed of pillow lavas while the summits sometimes exhibit pillow lavas, elongated pillows and lobate flows (Yeo et al., 2012). One eruption can construct more than one hummock, which may lead to coalescence of a few hummocks and formation of hummocky ridges, mounds (see below) or hummocky seamounts. To date, very few high-resolution surveys comprehensively investigating the construction of the upper oceanic crust along the neovolcanic zone of slow-spreading ridges have been performed. Smith and Cann (1990) measured an average density of hummocky seamounts in the northern Mid-Atlantic Ridge between  $24^\circ\text{N}$  and  $30^\circ\text{N}$ , assuming ‘seamount’ to be an edifice with relief  $>50$  m above the surrounding seafloor. They found an abundance of 80 such seamounts per 1 000  $\text{km}^2$ , which is an order of magnitude higher than in the Pacific (Fornari et al., 1987) or the southern Mid-Atlantic Ridge (Batiza et al., 1989); however, their density estimates probably represent only a minimum, because, for example, AVRs often observed on slow-spreading ridges are constructed almost entirely of piled-up hummocky seamounts (e.g., Yeo et al., 2012; Yeo and Searle, 2013). Similar studies of seamount density have been performed along the Reykjanes Ridge. Assuming the same parameters for seamounts (relief  $>50$  m), Magde and Smith (1995)



estimated an abundance of  $310 \pm 20$  seamounts per 1 000 km<sup>2</sup>, but admitted that there is a possibility that there are many more seamounts lower than 50 m, and therefore the estimation only represents a minimum. Due to the lack of large magma chambers underneath the Mid-Atlantic Ridge (e.g., Calvert, 1995; Calvert, 1997), hummocks along the slow-spreading ridges are probably fed from individual small pockets of melt episodically present in the crust (Smith and Cann, 1990). It is also possible that some hummocks can form by fissure eruptions when dikes intrude into pre-existing conduits like fractures or faults, even on the flanks of the neovolcanic zone (see Chapter 5).

### ***Hummocky ridges***

Sometimes volcanic hummocks cluster into distinctive and much larger features called hummocky ridges (Fig. 3B), hummocky mounds, or alternatively hummocky seamounts (Smith and Cann, 1993; Head et al., 1996; Lawson et al., 1996; Smith and Cann, 1998; Briaies et al., 2000). Hummocky ridges have a strong linear arrangement, where narrow rows of volcanic hummocks or elongated composite piles of hummocks connect forming ridges often relatively easy to distinguish in the bathymetry. These hummocky ridges can be up to several kilometers long, and between 100 m to 2 km wide (Lawson et al., 1996), and may rise ~50 m above the surrounding seafloor (e.g., Head et al., 1996). These features usually align parallel to the direction of spreading, which suggests that their formation is strongly controlled by the stress regime within the oceanic crust (Lawson et al., 1996). Hummocky ridges are probably formed during fissure eruptions (Lawson et al., 1996) and, therefore, resemble subaerial fissure eruptions which can also be observed on Iceland (e.g., Thorarinsson, 1969) or Hawaii (e.g., Macdonald et al., 1970). When the hummocky eruption is arranged in several discrete point-source vents rather than along a prominent linear trend, hummocky seamounts develop. They form by bulbous overgrowths of lavas when eruption rates are slow and steady, and the cooling is rapid (e.g., Head et al., 1996). Hummocky ridges and seamounts concentrate within the inner median valley and by overlapping and piling up they form hummocky terrain in the neovolcanic zone (e.g., Smith and Cann, 1998). Such terrain, for example, can be distinguished along the ~15 km wide volcanic zone along the northern Reykjanes Ridge (see Chapter 5).

### ***Eruptive fissures***

The eruptive fissures are suggested to be the most common sites of effusive eruptions along the mid-ocean ridges (e.g., Rubin et al., 2012 and Chapter 5). The development of an open fissure which can later host an eruption in the neovolcanic zone of the mid-ocean ridge

is a result of (a) lithospheric stretching (amagmatic, tensile cracking as the ridge accelerates from zero velocity to its full spreading rate, resulting in tectonic fissures); (b) magmatic intrusion (extensional cracking in the crust overlying dikes, resulting in eruptive fissures); or (c) thermal contraction of aging crust where tension cracks result from the shrinkage of cooling rock (Wright, 1998). The eruptive fissures mentioned in (b) occur when the magma migrates upwards and along the segment of mid-ocean ridge through a dike or vertical (or nearly vertical) crack in the crust until it intersects the surface of the seafloor and flows onto the seafloor through a fissure (Smith and Cann, 1998). Eruptive fissures are scattered along the floor of the neovolcanic zones of the slow-spreading ridges (e.g., Searle et al., 2010; Yeo, 2012), and have also been observed on land (e.g., Laki, Iceland; Thorarinnsson, 1969). The characteristics of eruptive fissure eruptions on land are well known. For example, the latest Bardarbunga-Holuhraun eruption in Iceland (2014–15) was observed from the early eruption precursors to its conclusion (Gudmundsson et al., 2014; Gudmundsson, 2015). At the beginning of such eruptions, the lava flows are vigorous and can spread out very quickly (e.g., Pedersen et al., 2017). As the eruption continues, the effusion rate drops and eruption focuses down to a few discrete vents (Smith and Cann, 1998). Towards the end of the eruption, flow may only occur from a single vent until the eruption completely wains (Smith and Cann, 1998). Yeo and Searle (2013) mapped many eruptive fissures along the neovolcanic zone of the Mid-Atlantic Ridge near 45°N, where they occupy a prominent AVR. They strike roughly parallel to the overall ridge orientation, dissect the hummocky terrain on and around the AVR, and erupt pillow and/or lobate lavas (Yeo and Searle, 2013). Several eruptive fissures can be active at once during an eruption, for example, Chadwick et al. (2013) observed 11 en echelon arranged eruptive fissures within the Axial Seamount caldera (Juan de Fuca Ridge), extruding lava during one eruption in 1998. They described that this eruption produced two distinctive lava morphologies: inflated lobate and inflated pillow lavas, with the inflated lobate lavas located close to the vents and inflated pillow lavas occupying areas further away from the vents.

#### ***Flat-topped seamounts (flat-topped volcanoes)***

Flat-topped seamounts are distinctive volcanic features which can be easily recognized in the side-scan sonar or bathymetry data (Fig. 3C). They are characterized by a combination of very smooth-textured surfaces and quite broad summits with steep sides. They are one of the most circular features on the seafloor, but their geometry can be strongly affected by tectonic deformation. Flat-topped volcanoes are 1–2 km in diameter and 50–200 m high (e.g.,

Clague et al., 2000), with a typical height to diameter ratio of around 1:10 (Smith et al., 1995a). Sometimes a prominent cone or a crater can be observed at their summits (white arrow in Fig. 3C), indicating that they can be fed by point-source vents (Smith et al., 1995a). Lawson et al. (1996) suggested that they are usually located at the ends of segments especially near non-transform offsets; however, Devey et al. (2014) observed that they can be randomly distributed within the axial valleys on particular segments of slow-spreading MAR. The most common morphology of these seamounts are pillow and lobate lavas located at the sloped and summits edges, but some flat (probably sheet flows), have also been mapped (Yeo et al., 2016) (Fig. 3D) and recovered from their summits (Lawson et al., 1996).

There are few models that define the mechanism of the formation of flat-topped volcanoes, proving how complex this process is and, yet, how much about it still remains unclear. The most recent model proposed by Clague et al. (2000) suggests that flat-topped seamounts are steady-state features of monogenetic origin that form by steady effusive eruptions on a gentle slope, which can last years to even decades. In this model, these volcanoes form as a consequence of continuous overflowing of the lava in submarine lava ponds. The lava pond is surrounded by a levee, when the level of lava in the pond reaches the lowest point on the levee it spills over as pillow lavas, enlarging the levee and raising the height of the volcano slightly (Clague et al., 2000). As the process continues, a circular edifice is built up and a flat-topped volcano evolves. This model requires the existence of lava ponds (or lava lakes) on the seafloor which have been observed both on the fast-spreading (e.g., EPR; Fornari et al., 1998; Haymon et al., 1991) and slow-spreading ridges (e.g., Lucky Strike segment, MAR; Fouquet et al., 1995). Another model suggests that flat-topped volcanoes may form from the fissure-fed, radially spreading lava flows piling up one on top of the other (e.g., Head et al., 1996; Magde and Smith, 1995). In this case, the circularity of the volcanoes would be determined by the length of the lava flows that are erupted during the construction stage of the edifice. It would also require some periodicity of volcanic activity along any given fissure in order to maintain the round shape of the seamount.

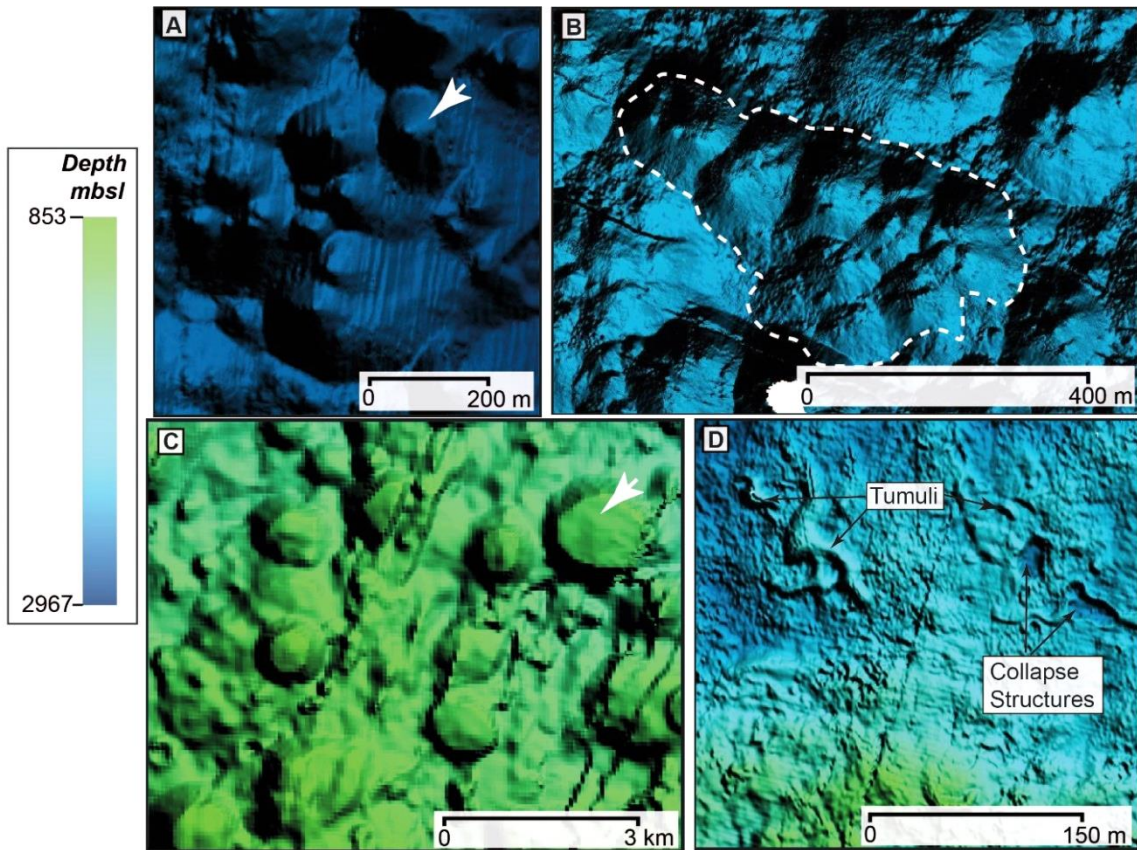


**Fig. 3** Examples of volcanic features observed along mid-spreading ridges and derived from the interpretation of the multibeam bathymetry: (A) Volcanic hummocks with diameters between 50 and 200 m and heights <300 m (image from Searle et al., 2010). Bathymetry gridded at 50 m. White arrow shows an example of a single hummock; (B) Hummocky ridges are clusters of aligned hummocky volcanoes. These ridges can be several kilometers long, from 100 m to 2 km wide and rise ~50 m above the surrounding seafloor (from Yeo et al., 2013). AUV bathymetry of 1 m resolution; (C) Flat-topped volcanoes with typical dimensions of 1–2 km in diameter, 50–200 m in height and height to diameter ratio of 1:10 (from Yeo et al., 2016). Bathymetry gridded at 35 m; (D) Flat lava flows (lobate or sheet flows) with very smooth surfaces easily distinguishable from hummocks and conical volcanoes. In the AUV bathymetry (1 m resolution), very detailed structures can be observed on the surface of the flows, e.g., tumuli or collapse pits (from Yeo et al., 2016). The depth scale is applicable to all four panels.

#### *Axial Volcanic Ridges: general information and evolution models*

Axial Volcanic Ridges on slow-spreading and some ultraslow-spreading segments of the mid-ocean ridges are built of a superposition of the volcanic landforms, features and edifices described above (Yeo, 2014). These distinctive composite volcanoes are the main locus of volcanic activity and the main constructors of the neovolcanic zone of the Reykjanes Ridge. Axial Volcanic Ridges are the most common volcanic features that can be found along almost all segments of slow-spreading mid-ocean ridge segments, especially along the Mid-Atlantic Ridge (Ballard and Van Adel, 1977; Sempéré et al., 1990; Smith and Cann, 1990; Parson et al., 1993; Bryan et al., 1994; Grácia et al., 1998; Searle et al., 1994; Bideau et al., 1998; Briais et al., 2000; Yeo and Searle, 2013). These features have also been observed on ultraslow-spreading segments of the Southwest Indian Ridge (Mendel et al., 2003).

Axial Volcanic Ridges form by repeated eruptions of relatively small volumes, which build up on top of each other as the volcanic activity continues over time (e.g., Ballard and Van Adel, 1977; Sempéré et al., 1990; Smith et al., 1995b; Yeo et al., 2012). Axial Volcanic Ridges are typically elongated structures that strike roughly parallel to the ridge axis (Fig. 4). They vary in size but are usually a few kilometers wide and some tens of kilometers long. They may rise up to several hundreds of meters above the surrounding seafloor which very often is much flatter than the AVR itself. Axial Volcanic Ridges usually develop in the middle of the segments of the mid-ocean ridges and very often have a clear relation to the hourglass-shaped axial valleys (Fig. 4). However, sometimes AVRs can extend all the way from the middle of the segment to the faults scarps that bound the axial valley (Keeton and Searle, 1996; Searle et al., 2010; Yeo, 2012; Yeo and Searle, 2013).

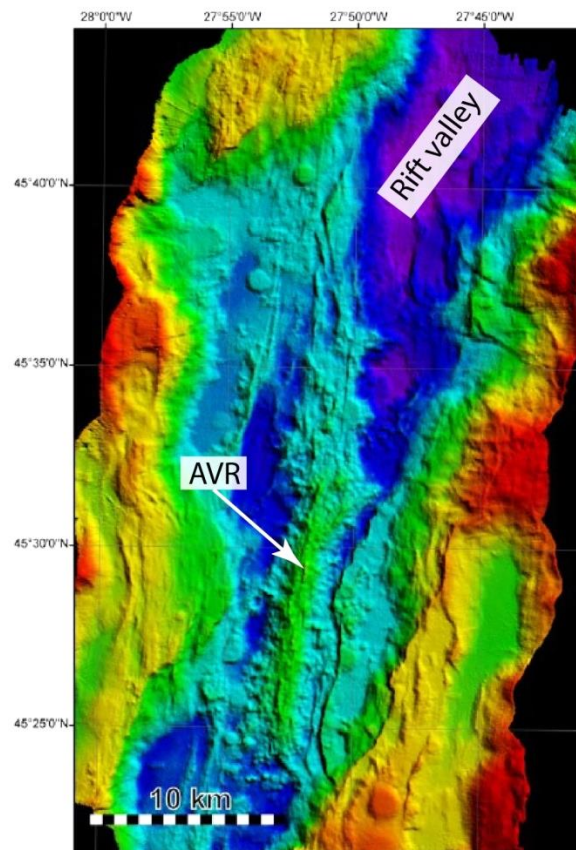


**Fig. 4** Example of an Axial Volcanic Ridge mapped using ship-based multibeam system (EM120) located in the rift valley (blue colors) near 45°30'N on the Mid-Atlantic Ridge. Image by the courtesy of Dr. Isobel Yeo.

The process which leads to the construction of AVRs, usually forming in the middle of the segment and axial valley, can be explained by the models of mantle upwelling. Kelemen et al. (1995) suggest that magma supply is the strongest in the middle of the ridge segment because at the same time the majority of magma is extracted there. They showed that melt

flow in a spreading environment is focused in the dunite channels which form continuously in the regions of vertical upwelling of the mantle (such as spreading centers at the mid-ocean ridges).

Early interpretations of bathymetry (at ~50 m resolution) found abundant AVRs along the Reykjanes Ridge (Keeton et al., 1997; Searle and Laughton, 1981), and later high-resolution mapping showed the apparently different levels of magmatic construction vs. tectonic degradation of the AVRs (Parson et al., 1993; Murton and Parson, 1993; Briais et al., 2000; Peirce et al., 2005; Peirce and Sinha, 2008). These observations led to the theory of life cycles of AVRs, which can be divided into two phases: magmatic (constructive) and amagmatic (destructive due to tectonic deformation) (Murton and Parson, 1993; Parson et al., 1993; Mendel et al., 2003; Peirce et al., 2005). Such life cycles are linked to the presence of a magma chamber underneath the AVR and its solidification during the cycle. At the same time, Detrick et al. (1990) and Sinha et al. (1998) suggested that magma chambers either do not exist underneath the slow-spreading ridges, are very small (thus difficult to detect) or are only periodically present in the crust. Sinha et al. (1998) showed that a small magma chamber underneath an AVR on the Reykjanes Ridge (near 57°N) contained an amount of magma equivalent of 20 000 years of crustal accretion at that region but that, due to its the small size, it would solidify after only ~2 000 years. Therefore, they suggested that the magmatic phase of the AVR life cycle is only a small proportion of the cycle and occurs only when the magma chamber is present underneath the given AVR. There have been a few life cycle models suggested for the AVRs observed on the Reykjanes Ridge (Crane and Ballard, 1981; Murton and Parson, 1993; Parson et al., 1993).

In the latest model by Murton and Parson (1993) and Parson et al. (1993) (Fig. 5), the formation of an AVR begins with eruptions from relatively short-lived, linear eruptive fissures. These eruptions produce hummocky ridges and hummocky terrain comprised mostly of pillow and lobate lavas (Head et al., 1996). As the process continues (simultaneously with plate separation), the AVR becomes a broad feature and linear fissure eruptions change into eruptions from multiple discrete point-source cones and flat-topped volcanoes (Murton and Parson, 1993; Parson et al., 1993). Flat-topped volcanoes have flatter summits most likely made of higher effusion rate products like lobate and sheet flows (e.g., Murton and Parson, 1993; Yeo et al., 2016), which may indicate an increase in effusion rates with time, higher temperatures of magma and deeper sources (Karson et al., 2015). According to the Murton and Parson (1993) and Parson et al. (1993) model, after the initial construction stage, AVRs go through a much longer period of tectonic deformation. The amagmatic extension leads to



the formation of faults which break up the AVR. As the spreading continues, scarps of old and broken up AVRs migrate away from the ridge axis and apparently become bounding faults of the axial valley (e.g., Briais et al., 2000; Mendel et al., 2003). Based on the model by Murton and Parson (1993) and Parson et al. (1993), the shape of an AVR (aspect ratio of width/length) may directly reflect its stage of construction. This means that AVRs become wider and more lens-shaped as they get more mature. Parson et al. (1993) also suggested that the life cycles are connected to the tectonic focusing of magma extraction in which cyclic tectonic extension along the mid-ocean ridge initiates decompression melting underneath the ridge, which then directly leads to eruptions. A similar idea was proposed by Briais et al. (2000), who suggested that the cycles in magmatic phase are controlled by deviations in melt supply to the systems from the mantle.

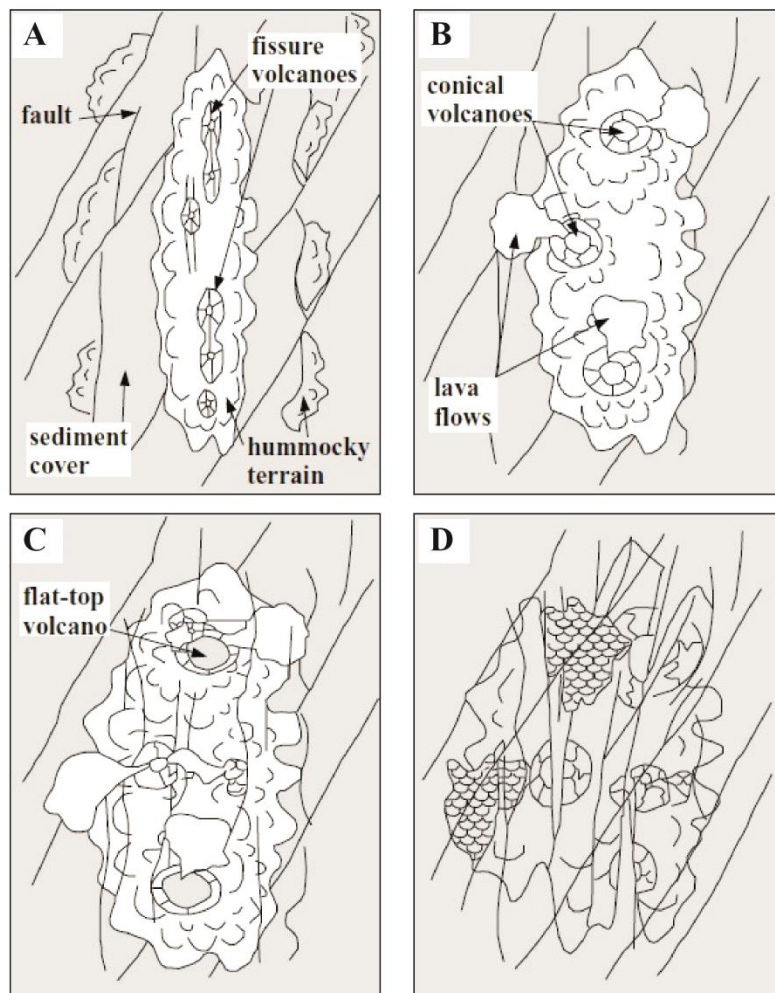


**Fig. 5** Magmato-tectonic evolution model of Axial Volcanic Ridge showing four stages of its suggested life cycle, from Murton and Parson (1993) and Parson et al. (1993). The magmatic build up comprises of young (A) and adolescent (B) stages, while the tectonic degradation comprises of mature (C) and old stages (D). As the evolution continues, the linear fissure eruptions progress into multiple point-source eruptions from conical and later from flat-topped volcanoes. Note the change in the main direction of faults which form with the time. They change from spreading orthogonal (early stages) to ridge-parallel (later stages) until the AVR is completely dismembered.

An earlier model by Crane and Ballard (1981) also suggested four stages of AVR construction, similar to the one presented later by Murton and Parson (1993) and Parson et al. (1993). In contrast, they proposed that the tectonic deformation, and hence tectonic extension, occurs only on the sides of AVRs and not in their central part. This would mean that the AVR is never split in half in its middle part, but rather it will entirely be faulted off to one side.

An alternative model of the AVR evolution has been suggested by Murton et al. (2012), who proposed that AVRs are steady-state features constructed by relatively frequent and small-volume eruptions (producing volcanic hummocks) from the shallowest, axial part of the AVR (AVR's crest). As spreading continues, hummocky terrain is transported to the flanks of the AVR, leading to its subsidence and eventual faulting due to release of stress accumulated in the crust. Once outside the region of the AVR, the hummocky terrain gets buried by episodic, yet less frequent, and larger volume lava flows from numerous flat-topped seamounts. These massive lava flows may apparently cover the majority of the seafloor within the median valley as the amount of the erupted material is sufficient to cover up topographically low hummocks (Murton et al., 2012).

A recent study by Yeo (2012) shows that neither the life cycle model suggested by Murton and Parson (1993) and Parson et al. (1993) nor the steady-state model proposed by Murton et al. (2012) entirely fits the observations from an AVR at 45°N on the MAR. Yeo (2012) suggested that AVRs are surface expressions of a robust magmatic crustal extension and the volumes of magma bodies (i.e., magma chambers or lenses), along with the time that passes between magma bodies accumulating beneath the ridge, will control growth of an AVR. Therefore, magmatic extension will produce magmatically-robust AVRs, while amagmatic extension will produce normal faulting that will cause degradation of an AVR. Hence, it seems that the period of tectonic deformation will control both the presence or absence and the size of an AVR. However, the degradation may not destroy the AVR entirely before the next episode of magmatic extension begins. Yeo (2012) also showed that the melt transport along the AVR at 45°N is restricted to its southern end (characterized by young and unfaulted features), while older and tectonized features can be observed in its northern part. This suggests that melt supplied to the AVRs may not be evenly distributed along their length, which may also have implications for the development, location and life span of potential hydrothermal systems.



### 1.2.3 Hydrothermal activity along mid-ocean ridges

More than 40 years ago, a remotely operated still-camera surveyed the mid-ocean ridge northeast of the Galápagos Islands and discovered the first hydrothermal vent field (Lonsdale, 1977; Spiess et al., 1980). Since then, mid-ocean ridges, back-arc spreading centers and arc volcanoes have been surveyed for the presence of hydrothermal activity (Fig. 6). This exploration of ~60 000 km of the global mid-ocean ridge system (ridges of all spreading rates) has led to the discovery of nearly 300 high-temperature (black smoker) hydrothermal fields, of which 113 have been visually observed and confirmed, and a further 159 have been inferred from water column plume hunting surveys (Beaulieu et al., 2015).

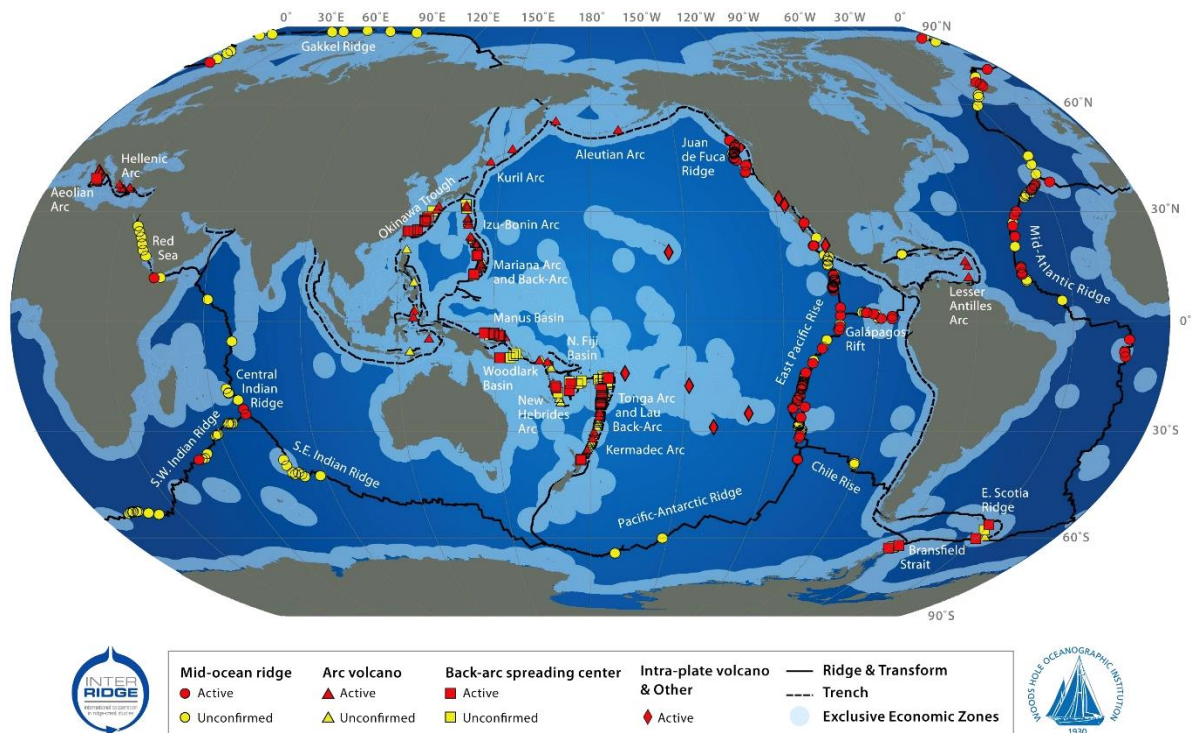


**Fig. 6** Global distribution of hydrothermal vents along the mid-ocean ridge system, back-arc spreading centers and arc volcanoes, summarized in the InterRidge Vents Database Version 2.1. Some vents have been visually confirmed and some have been inferred from water column plume surveys. Credits: Beaulieu, S., Joyce, K., Cook, J. and Soule, S.A., Woods Hole Oceanographic Institution (2015).

Baker et al. (1996) proposed that there is a linear correlation between the incidence of hydrothermal vents and spreading rate (higher spreading rate = more vents), which German et al. (2016) extended according to new discoveries in the intervening time (Fig. 7). Based on both models and advancements in the hydrothermal vent exploration of the Mid-Atlantic Ridge, they proposed that at least one active hydrothermal vent should be expected every 100 km of the ridge but the number of inactive sites may be even larger (Fig. 7 and Baker et al., 1996; German et al., 2016). Conversely, an extensive investigation of 200 km of the ridge axis

south of the Azores showed the incidence of at least one hydrothermal vent per 25–30 km (German et al., 1996). Based on the most recent calculation presented by German et al. (2016), more than 800 new hydrothermal vents remain to be discovered, predominantly along the slow-spreading ridges. This figure does not include the hydrothermal vents which can also be found along back-arc spreading centers, arc volcanoes and in intraplate settings, so more than 800 new vents should be expected globally (e.g., Beaulieu et al., 2015; German et al., 2016).

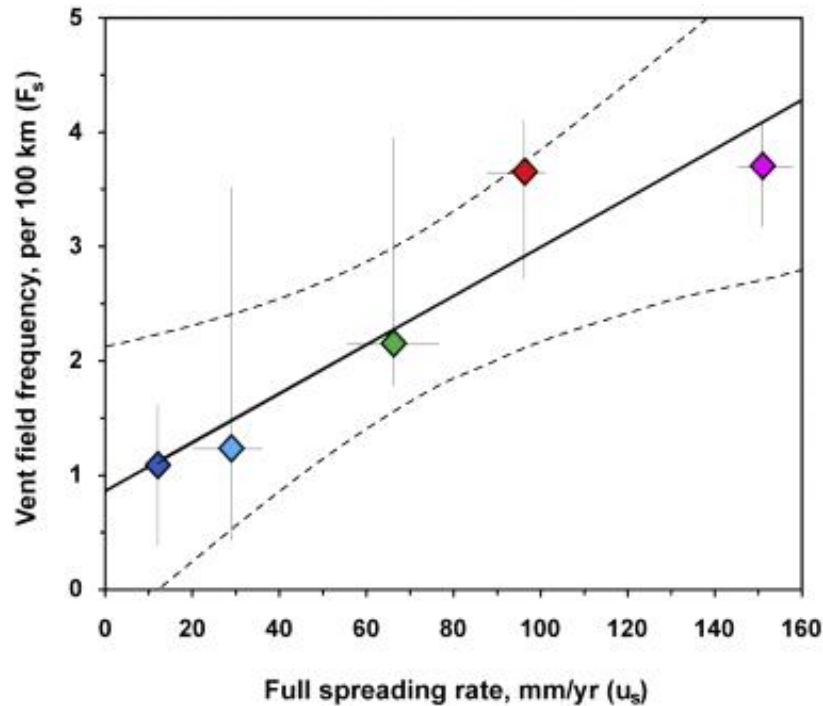


**Fig. 7** Scattered plot showing correlation between hydrothermal vent fields frequencies (per 100 km strike length,  $F_s$ ) and full spreading rate (weighted average mm/yr,  $u_s$ ) from German et al. (2016). Colored diamonds represent five ridge categories based on spreading rate: ultraslow (dark blue), slow (light blue), intermediate (green), fast (red) and superfast (purple). Horizontal and vertical bars indicate ranges for values from separate field-surveys considered within each spreading-rate data set. Solid line represents modern, global, linear fit of vent field frequency to spreading rate; dashed lines show 95% confidence.

Many hydrothermal vents have been discovered or inferred along the Mid-Atlantic Ridge (see Fig. 6), with 19 high-temperature hydrothermal sites along the MAR between 8°S and 45°N having been visited and visually observed in order to determine their detailed geological setting and describe the unique deep-sea ecosystems they might be supporting (revised by German et al., 2016). The majority these known systems are high-temperature vents located within the neovolcanic zone along mid-ocean ridges, close to the ridge axis, e.g., TAG (Rona et al., 1986), Lucky Strike (Langmuir et al., 1997), Grimsey (Hannington et al., 2001), Snake Pit (Kong et al., 1985) or Steinahóll (German et al., 1994), but some low-temperature venting have also been documented in such settings, such as the Saldanha field (German et al., 1996). High-temperature fields have also been reported in off-axis regions,

e.g., Nibelungen, located on an outward-facing fault scarp outside the axial valley (Devey et al., 2005; Melchert et al., 2008), Logatchev, located on a forming oceanic core complex (Escartin and Cannat, 1999; Petersen et al., 2009), or Moytirra which developed up on a step inward-facing, axial valley bounding fault scarp (Wheeler et al., 2013). The furthest off-axis and low-temperature vent field – Lost City (Kelley et al., 2001) – have been discovered ~15 km west of the ridge axis on MAR where it is hosted by ultramafic rocks exposed on an oceanic core complex.

Hydrothermal circulation of heated seawater is driven by a magmatic heat source (Fig. 8) (e.g., Lowell, 1991). Cold, dense seawater seeps through permeable oceanic crust along faults and fissures, getting progressively warmer with depth and reacting with the rock to produce a hydrothermal fluid of modified seawater (Lowell, 1991). When the fluid reaches temperatures of 350-400°C, it becomes buoyant and rises towards the surface (Jupp and Schultz, 2000). Hydrothermal fluids leach economically valuable elements from the crust, which precipitate at the seafloor forming massive sulfide deposits (SMS) (e.g., Herzig, 1999; Hannington et al., 2010). Even though hydrothermal vents can be found along all mid-ocean ridges, the largest SMS deposits have been found along the slow-spreading ridges (e.g., the MAR; Fouquet, 1995), making such ridges important targets for current and future exploration (e.g., Hannington et al., 2010; German et al., 2016). Modelling of hydrothermal fluid flux results indicates that 3 to 6 x 10<sup>-13</sup> kg/year of seawater must be circulated through the neovolcanic zone of the mid-ocean ridge system and be heated to ~350°C to account for the removal of the heat from newly formed oceanic crust (Alt, 2003; Mottl, 2003).

Seafloor hydrothermal systems discharge fluids of diverse temperatures, from as low as 5°C to as high as >400°C (e.g., Beaulieu et al., 2013). Based on the temperature of fluids, they can be divided into two types: high-temperature (>200°C) and low-temperature (<200°C) systems (e.g., Fornari and Embley, 1995). Although proven optical, chemical and physical techniques exist for detecting active high-temperature hydrothermal venting on the seafloor (e.g., Baker et al., 2001; Baker et al., 2004; German et al., 1991; German et al., 1994; German et al., 1998; German et al., 2008), no self-sufficient techniques for prospecting for low-temperature venting other than visual survey (for shimmering water, bacterial mats etc.) are available.

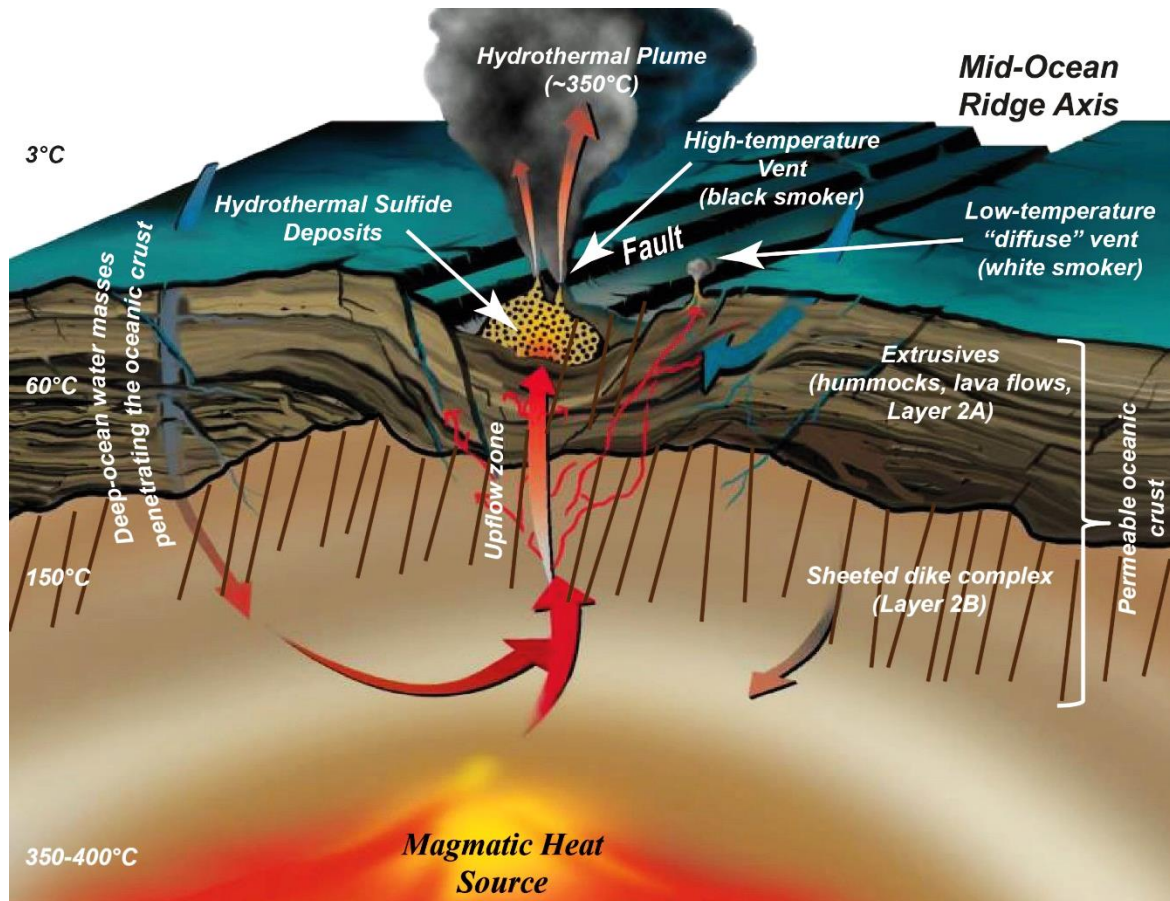


Fig. 8 Schematic model of the hydrothermal circulation cell along the spreading axis modified from Humphris and McCollom (1998). Cold seawater constantly seeps through permeable oceanic crust along faults and fractures. The fluids gain heat as penetrate deeper into the crust. The heat necessary to drive the hydrothermal circulation comes from the magmatic source. When fluids approach the heat source they are heated up, become less dense and ascend back to the surface by the buoyancy driven flow. The gradual heating of water increases their reactivity with the surrounding crust. This leads to leaching of many metals, e.g., gold or zinc. When fluids reach the seafloor, rapid cooling leads to the precipitation of metals around the manifestations, which accumulate and create seafloor massive sulfide (SMS) deposits. The type of the deposit is strongly controlled by the temperature of fluids. Hydrothermal fluids with temperatures  $\sim 300^{\circ}\text{C}$  usually discharge fluids with dark particulate in the fluid causing black smokers. These vents build up distinctive chimneys. Lower-temperature vents usually have lighter particulate in the fluid causing white or no smoke and rarely form chimneys.

Hydrothermal fluid discharge in high-temperature systems is often accompanied by ‘black smoke’ (Fig. 9A) which comes from the enrichment of the hydrothermal fluids in minerals and metals leached from the oceanic crust during the circulation at depth. The substantial metal leaching from the crust can lead to the formation of large SMS deposits, the largest of which have been found along the slow-spreading mid-ocean ridges (Hannington et al., 2011). This is because more frequent eruptive events at fast-spreading ridges reorganize flow channels of hydrothermal cells and bury older hydrothermal deposits under younger lava flows (Karson et al., 2015). On the other hand, the dating studies of black smoker chimneys and associated collapse debris of systems at intermediate- and slow-spreading ridges indicate that a hydrothermal system may switch on and off, and therefore, large associated SMS



deposits can form even for thousands of years (e.g., Alt et al., 1987; Lalou et al., 1998; Cave et al., 2002; Kuznetsov et al., 2011; Jamieson et al., 2013).

Low-temperature hydrothermal systems (also called ‘diffuse’ vents) discharge fluids cooler than 200°C and usually occur on the flanks of high-temperature systems or away from the ridge axis (e.g., Kelley et al., 2001a; Kelley et al., 2001b). They usually form when hotter hydrothermal fluids mix with cooler seawater at shallower depths. Above 50°C, fluids become sufficiently reactive to leach some of the minerals and metals from the oceanic crust. Sometimes these are the sites of abundant bacterial mats (Fig. 9B) which thrive on oxidation of sulfur, iron, CH<sub>4</sub> and H<sub>2</sub> (Jannasch, 1995). Between 100°C and 200°C, the color of the particulate matter in the venting fluid usually becomes white (Fig. 9B) due to enrichment in ions of silica, anhydrite and barite (Hannington et al., 1995; Kelley et al., 2001b).

The heat flux in one single black smoker chimney can range from 2 to 5 MW (Bemis et al., 1993; Ginster et al., 1994), while the heat output of an entire hydrothermal vent fields have been measured to range from 200 to 500 MW (Becker and Herzen, 1996; Kelley et al., 2001a; Kelley et al., 2002). Up to present, the highest temperature ever documented in a hydrothermal system was measured in the Sisters Peak Vent Field (southern MAR) with fluids discharging at 464°C (Koschinsky et al., 2008).

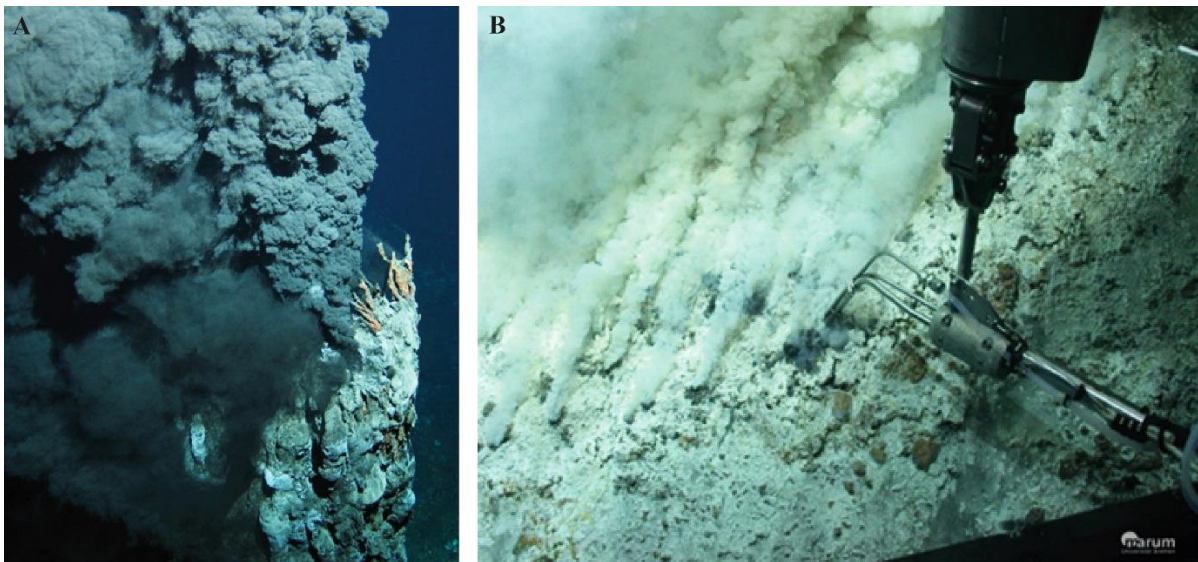


**Fig. 9** Two main types of seafloor hydrothermal activity: (A) The ‘One Boat’ black smoker chimney in the Turtle Pits hydrothermal vent field (near 5°S, Mid-Atlantic Ridge) visited during the expedition M78-2 with the ROV KIEL 6000. Image by the courtesy of Dr. Sven Petersen (GEOMAR). (B) Active white smokers, discharging low-temperature hydrothermal fluids with bacterial mats around them, located in the Lau Basin, SE Pacific. Image by the courtesy of MARUM, University of Bremen.

## 1.3 Geological setting

### 1.3.1 Iceland

Iceland is the largest part of the ~60 000 km long mid-ocean ridge system and the only section of the Mid-Atlantic Ridge (MAR) that is elevated above the sea level forming the Iceland Basalt Plateau (Fig. 10). Iceland is part of a large entity situated at the junction of two large submarine physiographic structures: the MAR and Greenland-Iceland-Faeroe Ridge (Fig. 10). In total, 350 000 km<sup>2</sup> of the ocean floor is elevated 3 000 m above the surrounding seafloor, and ~103 000 km<sup>2</sup> of this area is above the sea level. Here, the North American and Eurasian plates separate at slow rate with the full spreading rate of ~20 mm y<sup>-1</sup> (e.g., Ward, 1971; Palmason and Sæmundsson, 1974; Sæmundsson, 1979; Einarsson, 1991; Kaban et al., 2002). Iceland is underlain by a hot spot (Fig. 10) and shows increased volcanic activity along the neovolcanic zone that formed abnormally thick crust. Therefore, Iceland is a unique laboratory for the direct study of the dynamic processes associated with seafloor spreading and hot spots dynamics, and their interactions. Based on the hypothesis of Morgan (1971), the Icelandic hot spot was centered beneath Greenland some 60–40 Ma ago (Lawver and Müller, 1994). Due to the westward drift of Greenland, the hotspot center is currently located underneath the northern part of the Vatnajökull glacier (Figs. 10 and 11) (e.g., Wolfe et al., 1997). Early K-Ar dating of the lava pile in northwest Iceland—the Westfjords Peninsula—yielded ages of 16 Ma, making these rocks the oldest exposed in Iceland. A more detailed description of the geology of the Westfjords Peninsula is presented in Chapters 3 and 4.

The Icelandic lava pile is characterized by the presence of inter-lava sediments (including pelagic sediments, ashes and paleosoils) and volcanic breccia. They captured the climate conditions in Iceland at the time of deposition and, together with the correlations of paleomagnetic reversal patterns and absolute ages of the lavas, these characteristics have been used to divide the Icelandic lava pile into four major stratigraphic groups (Fig. 11) (Sæmundsson, 1979):

Postglacial:	last 9 000 to 13 000 years
Upper Pleistocene:	younger than 0.7 Ma
Plio-Pleistocene:	0.7 – 3.1 Ma
Tertiary:	older than 3.1 Ma

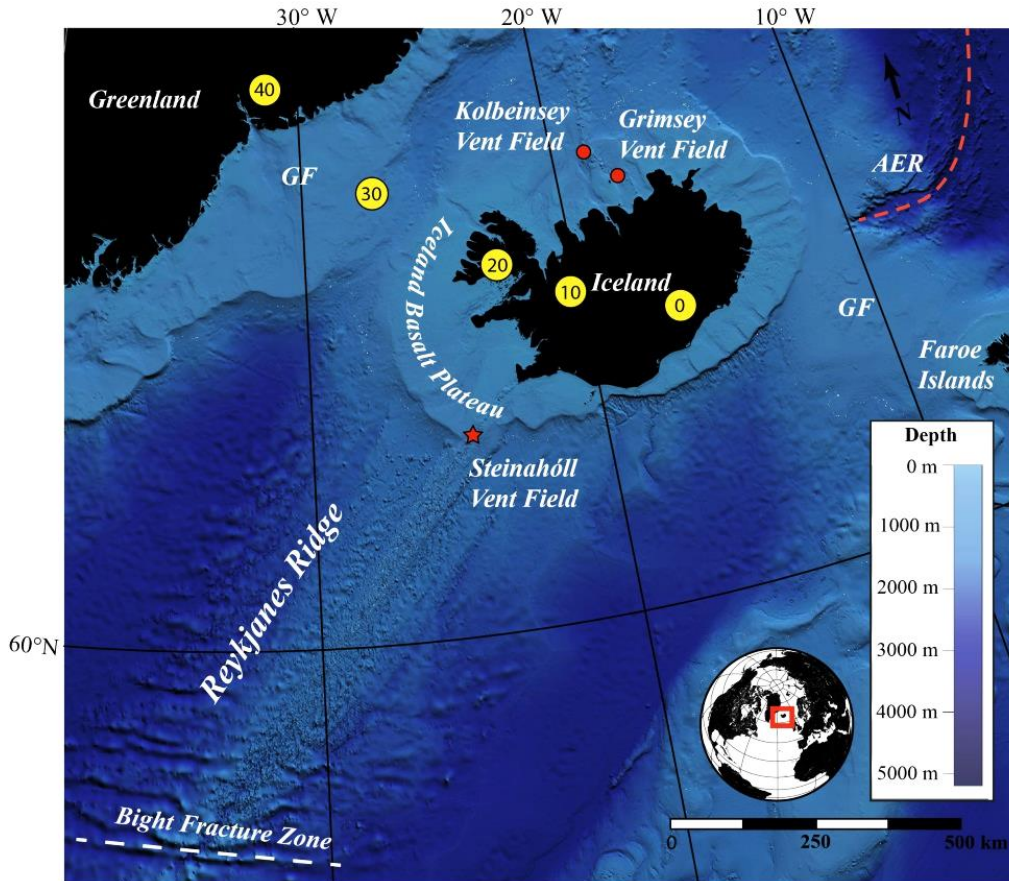


**Fig. 10** General bathymetry and geography of the North-East Atlantic Ocean and location of the Reykjanes Ridge from Lawver and Müller (1994) and Brandsdóttir et al. (2015).. Yellow circles indicate position of the Iceland plume relative to Greenland and Iceland at different ages (given in Ma in the circles). Abbreviations: AAER = extinct Aegir Ridge; GF = Greenland-Faroes Ridge. Globe shows location of the zoomed area.

Tertiary rocks cover almost half of Iceland's surface. They are confined to the eastern- and western-most parts of the country, where strong erosion exposed few central volcanoes with acidic rocks, visible hydrothermal alteration, and irregular dip of lava flows. In total, only 15 central volcanoes have been recognized in Tertiary formations, but 40 unidentified volcanoes are expected to be present due to the presence of acidic rocks. More detailed mapping needs to be done to confirm their exact locations (e.g., Kristjánsson, 1968; Sæmundsson, 1979). Plio-Pleistocene rocks cover nearly 25% of the total area of Iceland. They occupy a fairly wide zone between old Tertiary and the freshest lava flows of the present neovolcanic zone. Volcanic activity followed the Tertiary patterns, and six central volcanoes have been recognized, but additional unidentified volcanoes are also expected here. Although Tertiary rocks are characterized by primary subaerial flows, the Plio-Pleistocene sequence consists mainly of subglacial material with pillow lavas, different types of breccia, and hyaloclastite (Sæmundsson, 1979). Upper Pleistocene rocks also cover nearly 25% of the total area of Iceland. Two types of volcanics have been recognized in the Upper Pleistocene pile: subaerial

lavas flows erupted during interglacial periods, and subglacial pillow lavas and hyaloclastites (Sæmundsson, 1979). Postglacial rocks cover nearly 10% of the total area of Iceland. The pile consists mainly of lava flows and pyroclastics (Sæmundsson, 1979). The most recent lavas erupted within the neovolcanic zone in 2014–2015 just north of the Vatnajökull glacier (Gudmundsson et al., 2014; Gudmundsson, 2015). Iceland is mostly made of basalts, which make up nearly 92% of the surface lavas of the Postglacial pile; 4% are basaltic andesite, 3% are dacite–rhyolite, and the remaining 1% are andesite (Jakobsson, 1979a; Jakobsson, 1979b; Sæmundsson, 1979; Sigmundsson, 2006).

### ***Volcanic systems and tectonics***

Over the past 20 Ma, rift systems in Iceland have repeatedly jumped eastwards, probably to remain fixed over the Icelandic hot spot (e.g., Sæmundsson, 1979; Foulger and Anderson, 2005). This has led to the development of a very complex volcano–tectonic setting of the Icelandic rifting system (Fig. 11) (Sæmundsson, 1979; Einarsson, 1991; Johannesson, 2014).

The currently active volcanic systems in Iceland consist of three rift zones, each about 40–50km wide: Northern Rift Zone (NRZ), Eastern Rift Zone (ERZ), Western and Reykjanes Rift Zones (WRZ+RRZ) (Sæmundsson, 1979). Together, the WRZ, RRZ, northern part of ERZ and NRZ form the ‘Axial Rifting Zone’ (ARZ, also referred to as neovolcanic zone), which is typical for mid-ocean ridge environments where recent volcanism occurs. The remaining parts of the ERZ together with the Eastern and Snæfellsnes Volcanic Flank Zones (Eastern and Snæfellsnes VFZ, respectively) represent active intraplate volcanic zone, which, due to different setting, erupt lavas of different composition to those observed in the Axial Rifting Zone (Sæmundsson, 1979). Intensive magma production from the abnormally hot sub-Icelandic mantle led to the formation of the Icelandic Basalt Plateau (see Fig. 10 and McKenzie, 1984). The Postglacial-aged eruptions (including pre-historic and historic eruptions) can be found in both ARZ and intraplate volcanic zone (Johannesson, 2014).

Fracturing within the ARZ is focused in fissure swarms typically 20 km wide and up to 100 km long (Fig. 11). They form an echelon arrays with offsets that can be either dextral or sinistral, depending on the trend of the individual swarm in relation to the general direction of the spreading (which is east-westerly) (Sæmundsson, 1979). Fissure swarms include hundreds of tensional fractures (~100 m long), normal faults (~1000 m long) and volcanic or tectonic fissures of similar length (Gudmundsson, 1995). The mean throw on the Holocene normal faults is only a few meters (Gudmundsson, 1995). Normal faults in the fissure swarms



are often intruded by dikes, especially observed in the older parts of the lava pile. This is probably due to longer exposure to erosion of older formations. Most tensional fractures are confined to the uppermost few hundred meters of the crust, and below this, down to ~1 km, steeply dipping normal faults are the dominant extensional structures (Gudmundsson, 1995). At depths greater than 1 km, dikes become the dominant extensional structures that most probably continue to the base of the crust (Gudmundsson, 1995). Most of the fissure swarms are focused on the central volcanoes, which are features with distinguishable characteristics (e.g., circular shape, craters on the summits, shallow magma reservoirs and basaltic to acidic eruption products) (Sæmundsson, 1979). Brandsdóttir and Menke (1992) suggested that the majority of the central volcanoes (e.g., Krafla, Katla or Askja) are fed by vertical dike emplacements from a shallow crustal magma chamber located at 1–3 km depth. Such magma chambers have been detected by geophysical studies, e.g., on the Hengill central volcano (Foulger and Toomey, 1989).

Basaltic volcanoes are the most common volcanoes among the volcanic systems in Iceland. They often form crater rows, lava shields (many of which have been active in early postglacial times), and table mountains formed beneath the Pleistocene ice sheets (Gudmundsson, 1995). Large central volcanoes generally erupt every several hundred years, although in some cases eruptions may occur even more frequently (e.g., during the past 1100 years, Hekla erupted once every 55 years (Gudmundsson et al., 1992). Each eruptive period is usually 5–20 years long and only one volcanic system is active at any one time (Björnsson et al., 1977). The ARZ is connected to the submerged mid-ocean ridges by transverse structures that have been classified in the literature as fracture zones based on earthquakes patterns (Sæmundsson, 1979). In southwest Iceland, the Reykjanes Peninsula is a direct extension of the submerged Reykjanes Ridge. It is connected to the ERZ by the South Iceland Fracture Zone (SIFZ) (Fig. 11). Tectonic features in this east–west-trending zone show a left-lateral transform sense. The ARZ in northern Iceland connects with the Kolbeinsey Ridge along the Tjörnes Fracture Zone (TFZ) (Fig. 11), which is a broad deformation zone, roughly 150 km E-W and 75 km N-S, characterized by right-lateral transform motion (Brandsdóttir et al., 2003).

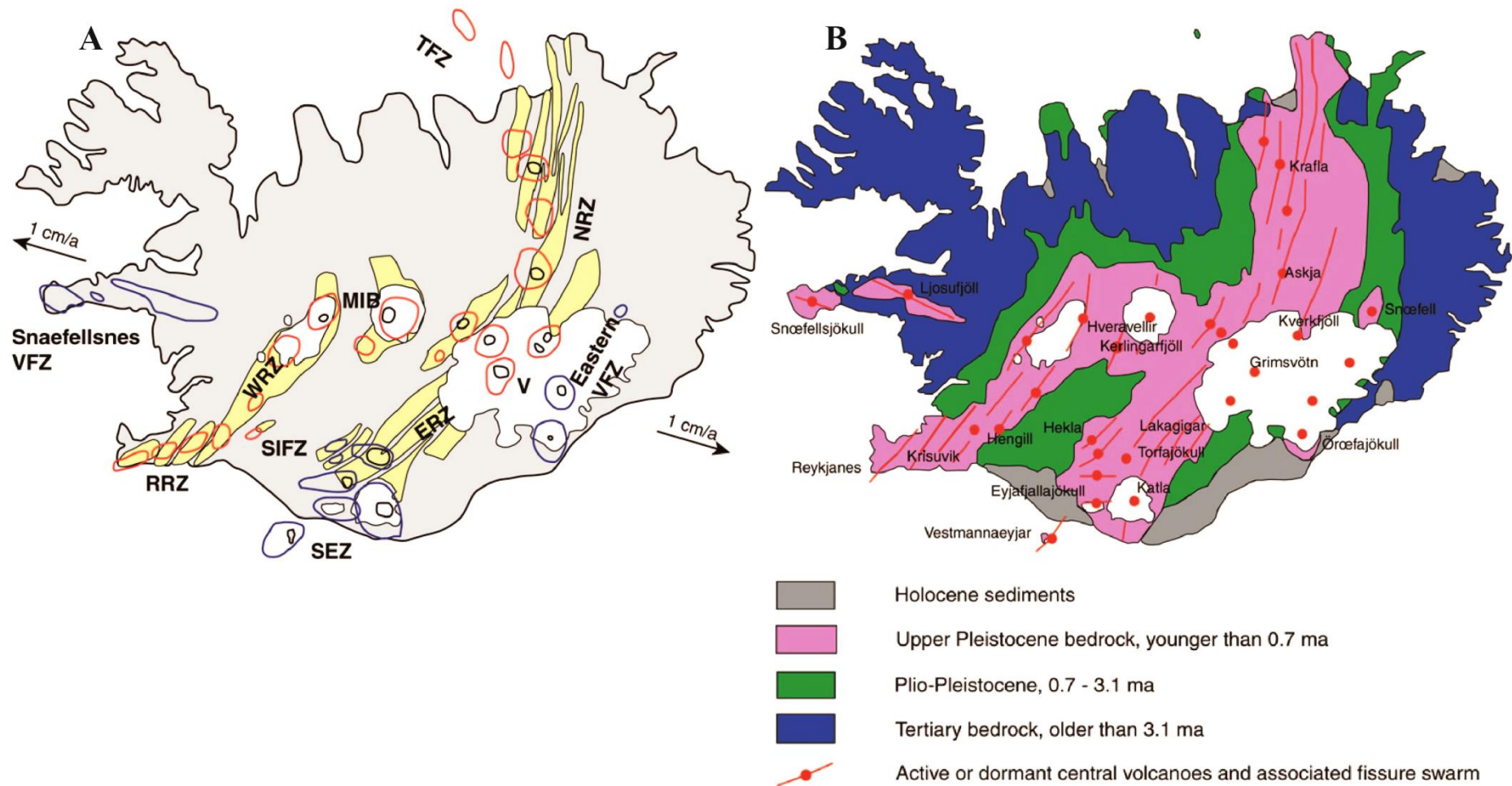


**Fig. 11** Simplified maps of volcano-tectonic setting and bedrock ages of Iceland: (A) Main volcano-tectonic features. Active volcanic systems are outlined in red, some of which have developed calderas (black circles). Fissure swarms are shown by yellow polygons. Volcanic systems located in the volcanic flank rift zones are outlined in blue. (B) The bedrock age and main volcanoes (Figure by the courtesy of Dr Tobias Weisenberger, based on Johannesson and Sæmundsson, 2009). Abbreviations: VFZ = Volcanic Flank Zone; RRZ = Reykjanes Rift Zone; WRZ = Western Rift Zone; ERZ = Eastern Rift Zone; NRZ = Northern Rift Zone; MIB = Mid-Icelandic Belt; SIFZ = South Iceland Fracture Zone; TFZ = Tjörnes Fracture Zone; SEZ = South Eastern Zone; V = Vatnajökull (made by Dr Tobias Weisenberger based on Sæmundsson, 1979).

Basaltic volcanoes are the most common volcanoes among the volcanic systems in Iceland. They often form crater rows, lava shields (many of which have been active in early postglacial times), and table mountains formed beneath the Pleistocene ice sheets (Gudmundsson, 1995). Large central volcanoes generally erupt every several hundred years, although in some cases eruptions may occur even more frequently (e.g., during the past 1100 years, Hekla erupted once every 55 years (Gudmundsson et al., 1992). Each eruptive period is usually 5–20 years long and only one volcanic system is active at any one time (Björnsson et al., 1977). The ARZ is connected to the submerged mid-ocean ridges by transverse structures that have been classified in the literature as fracture zones based on earthquake patterns (Sæmundsson, 1979). In southwest Iceland, the Reykjanes Peninsula is a direct extension of the submerged Reykjanes Ridge. It is connected to the ERZ by the South Iceland Fracture Zone (SIFZ) (Fig. 11). Tectonic features in this east–west-trending zone show a left-lateral transform sense. The ARZ in northern Iceland connects with the Kolbeinsey Ridge along the Tjörnes Fracture Zone (TFZ) (Fig. 11), which is a broad deformation zone, roughly 150 km E-W and 75 km N-S, characterized by right-lateral transform motion (Brandsdóttir et al., 2003).

### *Seismic activity*

The majority of seismic activity in Iceland (Fig. 12) is associated with the plate boundary, although some activity has also been observed in intraplate settings (e.g., Tryggvason, 1973; Einarsson, 1991; Jakobsdóttir, 2008). Since the initiation of the new digital seismic system South Iceland Lowland (SIL) in 1993, the detection capacity of seismic activity in Iceland has significantly increased (Stefánsson et al., 1993; Jakobsdóttir, 2008). This, for example, helps directly monitor tectonic deformation along an active plate boundary or investigate magma behavior prior to eruptions. The largest earthquakes in Iceland occur within the two transform zones: SIFZ and TFZ (Fig. 12). In the SIFZ, earthquakes predominantly occur along strike-slip faults. The largest recorded earthquake in the history of Iceland (1784) occurred along one of the SIFZ faults with a magnitude of 7.5–8 (Tryggvason, 1973). The TFZ is more complex and the earthquakes occur along three WNW-ESE trending segments (e.g., Einarsson, 1991; Rögnvaldsson et al., 1998; Jakobsdóttir, 2008). Seismic activity associated with the volcanic systems is characterized by spatial clustering of epicenters usually confined to the central volcanoes (Einarsson, 1991). Fissure swarms and normal faults on the flanks of fissure swarms — typical structures associated with a rifting environment — are mostly aseismic except during the episodes of rifting and volcanic

eruptions, such as during the Krafla eruption in 1975–84 (e.g., Brandsdóttir and Einarsson, 1979) or the most recent Bardarbunga-Holuhraun eruption 2014–15 (e.g., Gudmundsson et al., 2014; Gudmundsson, 2015).

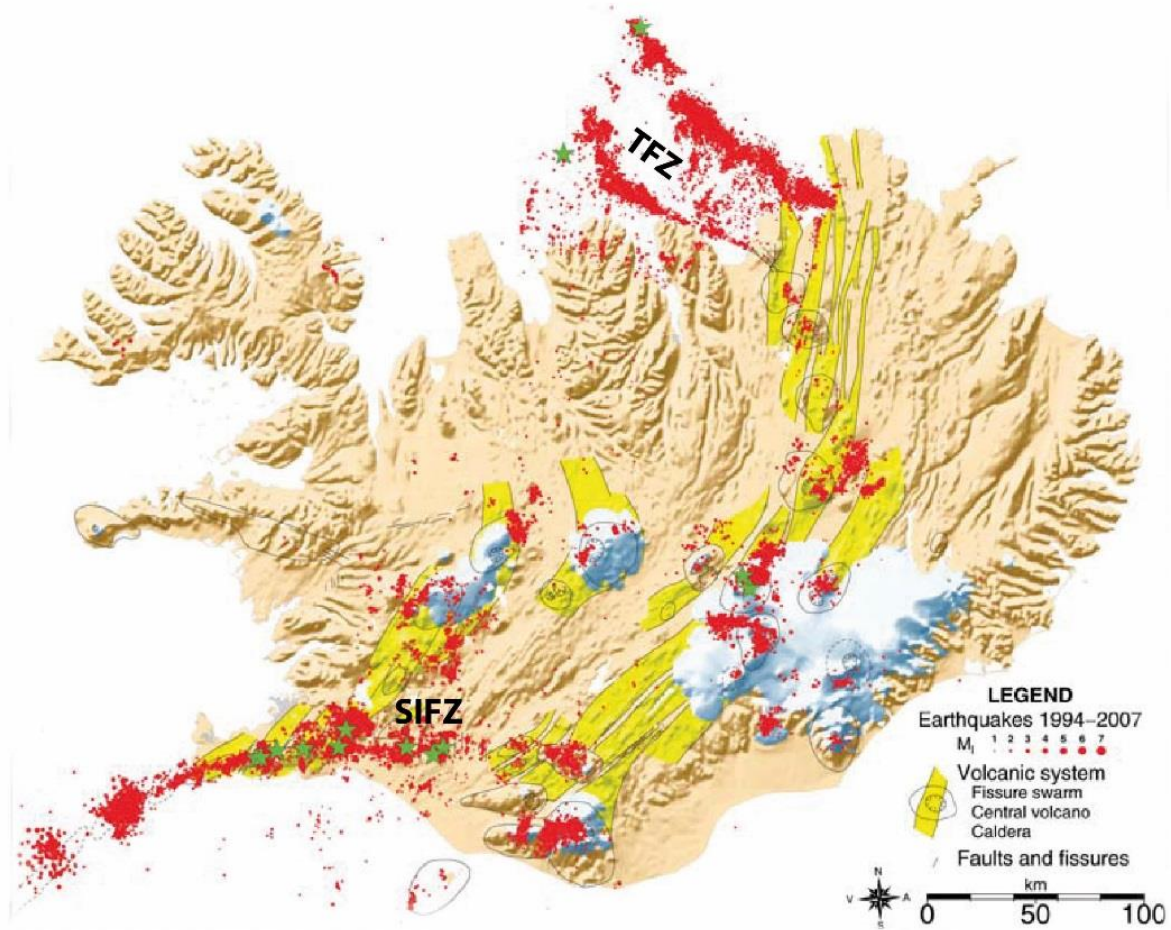


**Fig. 12** Map of Iceland showing the locations of earthquakes in years 1994–2007. Green stars represent events with  $M_l > 5$ , while red dots events with  $M_l > 1$ . Earthquakes are recorded by the SIL (South Iceland Lowland) seismic network. Figure modified from Jakobsdóttir (2008).

### *Geothermal Activity*

Geothermal activity plays an important role in Iceland's economy and future plans for sustainable development (Björnsson and co-editors, 2010). Energy produced by this renewable resource provides about 89% of the space heating in the whole country, increased significantly since 1979 when it was only 47% (Axelsson et al., 2010). Iceland one of the leading countries in utilization of geothermal resources, although only about 0.3% of global energy consumption comes from geothermal sources (Arnórsson et al., 2008).

Bödvarsson (1961) classified all Icelandic geothermal systems into two types: high- and low-temperature. This classification was established based on the potential of particular geothermal systems for utilization and, therefore, on temperatures of the reservoirs. Thus, Fridleifsson (1979) suggested that temperatures are below  $\sim 150^\circ\text{C}$  in the uppermost 1 km of



the low-temperature systems, but  $>200^{\circ}\text{C}$  above 1 km depth in the high-temperature systems. This classification is currently used for all the Icelandic systems (e.g., Arnórsson et al., 2008). Based on distribution of geothermal systems in Iceland, it is clear that this classification is strongly related to the geology of this island (Fig. 13).

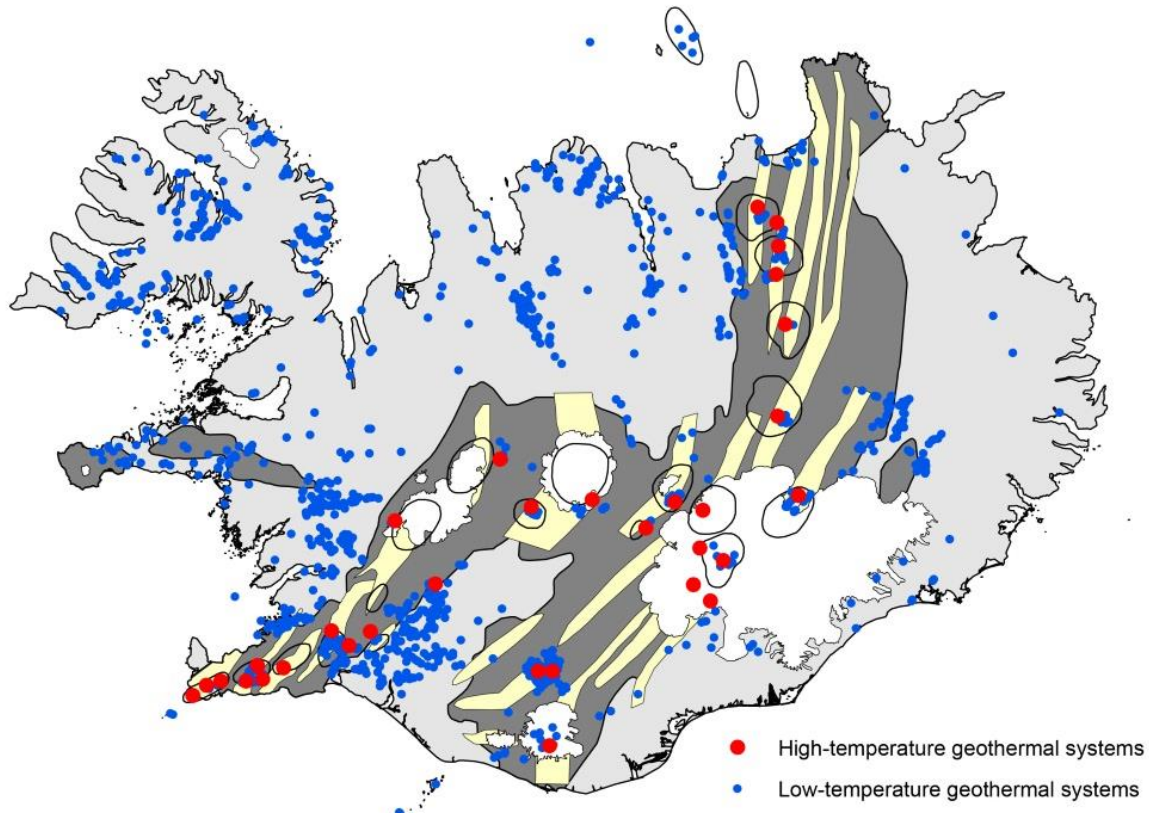


**Fig. 13** Map of Iceland showing the distribution of high- and low-temperature geothermal activity. All of the 32 mapped high-temperature systems are confined to the neovolcanic zone (dark grey) where they are often associated with active volcanic belts (black outlines) and intersecting them fissure swarms (yellow polygons). The ~1 000 confirmed and mapped low-temperature systems are mainly widespread in older formations (light grey). Figure modified from Torfason (2003a).

### *High-temperature activity*

There are at least 32 high-temperature geothermal areas in Iceland (Fig. 13) containing steam fields with underground temperatures reaching  $200^{\circ}\text{C}$  at 1 km depth (Palmason et al., 1985; Arnórsson, 1995a; Arnórsson et al., 2008). Most of the high-temperature systems are located within the belts of active volcanism and rifting, and lie astride active fissure swarms where these swarms intersect the plate boundary and often central volcanoes. This complex correlation is more evident in the ERZ and NRZ, because in the WRZ only the Hengill has developed central volcano and is intersected by fissure swarm. Due to the constant spreading, some high-temperature systems may have migrated away from the ARZ and are now located near margins of volcanic belts and fissure swarms (e.g., Arnórsson, 1995a;

Arnórsson et al., 2008). It seems reasonable to assume that the heat source for high-temperature systems is shallow level magma chambers located under the central volcano complexes. In contrast, on the Reykjanes Peninsula, there are no central volcanoes, and dike swarms probably provide the heat for hydrothermal circulation (Johannesson and Sæmundsson, 2009). The highest documented temperature drilled in the high-temperature systems was  $>380^{\circ}\text{C}$  at 2 km depth, recorded in the Nesjavellir area near Hengill, SW Iceland (Sæmundsson, 1963).

The bedrock geology of the high-temperature systems in Iceland has been extensively studied, with deep drilling showing that the rocks underlying geothermal systems are fine to medium grained intrusives, present at depths as shallow as 1 km. Deeper than 1.5 km, gabbro and sometimes granophyre dominates the succession (e.g., Arnórsson, 1995; Franzson, 1998; Franzson, 2004). Such intrusions (dikes, sills, stocks, cone sheets and irregularly shaped bodies) represent multiple intrusive events that have contributed heat to the geothermal systems over some period of time. The identification of such features from single cores is impossible in presently active systems; these features are assumed to be the same as in fossil high-temperature systems exposed in old volcanic complexes. Some of the high-temperature systems are associated with silicic volcanism, such as near Torfajökull and Kerlingarfjöll (see Fig. 11). It has been suggested that mafic intrusives, revealed by local high gravity anomalies, below these two volcanoes provide long-lived heat sources for the local geothermal activity (Walker, 1974), and that silicic magma chambers may act as density traps for rising mafic magma (Walker, 1974).

The flow paths for convective fluid recognized in high-temperature systems are tectonic fractures, contraction fractures, permeable sedimentary layers between lava flows, scoriaceous tops of lava flows and brecciated rocks around faults and dikes (Arnórsson et al., 2008). Permeability within the geothermal systems is very variable and is generally the highest where vertical and sub-vertical fractures occur together with faults, which occurs within the active fissure swarms (Sæmundsson, 1978).

The water in the majority of high-temperature systems is of meteoric origin. The potential recharge zones for many Icelandic geothermal systems have been determined by deuterium (D) analyses (Árnason, 1977; Darling and Ármannsson, 1989), showing that the geothermal waters come from the precipitation that has fallen in highlands (inland) and migrated to lowlands in a shallow ground water flow.

*Low-temperature activity*

More than 950 low-temperature geothermal systems are scattered across Iceland (Torfason, 2003b). These systems are widespread in Quaternary and Tertiary lavas (Fig. 13) (Arnórsson, 1995b). The vast majority of them are located on the North-American Plate and Hreppar micro-plate (SIFZ), while their occurrence on the European Plate is relatively sparse. This asymmetry in distribution probably arises because both the North-American Plate and Hreppar micro-plate have complicated stress fields that are caused by: (1) the shape of the volcanic belts and rifting sites; (2) the direction of the tensional forces across the plate boundary; and (3) the displacement of the boundary by transform faults (Arnórsson et al., 2008). To a large extent, the activity can be correlated with seismic activity and is mostly associated with young faults and fractures in older crust and can, therefore, be classified as tectonically-controlled (Arnórsson, 1995b; Arnórsson et al., 2008; Khodayar et al., 2006; Khodayar et al., 2010; Khodayar and Björnsson, 2014). In some Quaternary and Tertiary formations (outside known low-temperature systems), up to 1 km deep drill holes reached hot and productive aquifers where no surface hot springs were observed before the drilling, suggesting that at shallow levels these aquifers are overlaid by lavas with low permeability (i.e., impenetrable for low-temperature fluids) (Arnórsson, 1995b; Axelsson et al., 2005). Some low-temperature systems are located far away from active tectonism, e.g., Westfjords, where they are controlled by old volcanic edifices (e.g., this study - Pałgan et al. 2016, Chapter 3).

The theoretical calculations based on Bodvarsson's (1983), modeled by Axelsson (1985) and Björnsson et al. (1990) demonstrate that the existence and heat source of low-temperature systems in Iceland are related to the temperature and stress conditions in the abnormally hot Icelandic crust, in particular the local stress field, which controls whether open fractures are available for the heat-mining process and how fast these fractures can migrate downward.

Arnórsson and Gislason (1990) and later Arnórsson (1995b) proposed that low-temperature systems in Iceland developed as a consequence of one or more of the following processes: (1) deep flow of groundwater from the highlands to the lowlands through permeable structures (faults, dikes, contraction fractures) driven by the hydraulic head; (2) convection in young faults and fractures formed by the deformation of older and relatively impermeable bedrock; (3) drift of high-temperature systems away from the active volcanic belts and displacement from the magmatic heat source which results in cooling of the system;

and (4) intrusions of magma into the formations located near the margins of the volcanic belts or even outside them.

Most of the water in low-temperature circulation in Iceland comes from atmospheric precipitation (Arnórsson, 1995b; Arnórsson et al., 2008). Conversely, in the coastal systems up to 10% of the water may be seawater. The typically low- $\Delta D$  values of Icelandic low-temperature systems indicate that their water recharges in the highlands, up to 150 km inland, similarly to the high-temperature systems. Low values of deuterium also indicate a minimal content of 'ice-age waters' (i.e., older than 10 000 years) in the low-temperature systems, as such waters are generally depleted in deuterium relative to the present-day atmospheric precipitation (Arnórsson, 1995b; Arnórsson et al., 2008).

### **1.3.2 Reykjanes Ridge**

The Reykjanes Ridge is the largest hot spot-influenced and obliquely spreading mid-ocean ridge in the world (e.g., Talwani et al., 1971; Murton and Parson, 1993; Searle et al., 1998; Sandwell et al., 2014). This ~950 km long segment of the northern Mid-Atlantic Ridge is located between the Bight Fracture Zone (near 57°N) and Iceland (see Fig. 10), and lacks any first-order (transform faults) discontinuities (Macdonald et al., 1991; Macdonald, 2001). White (1997) attributed this phenomenon to the increase in mantle temperature, and calculated that a temperature rise of 50°C increases crustal thickness by 30% and allows mantle to remain too hot and ductile to react to axial extension by forming large, first-order discontinuities. The Reykjanes Ridge trends 036° (e.g., Murton and Parson, 1993) with a spreading direction of 096° (DeMets et al., 1990), resulting in 30° of obliquity. Vogt (1971) attributed this obliquity to the along-axis asthenospheric flow from the Iceland hot spot but the actual origin of this obliquity is still under debate.

The Reykjanes Ridge progressively shoals from the south towards Iceland (see Fig. 10). The depth of the ridge axis almost linearly decreases from ~2 500 mbsl near the Bight Fracture Zone to ~1 000 mbsl near 60°N, while more gradual decrease can be observed closer to Iceland with depths reaching ~500 mbsl near 63°N. Between the Bight Fracture Zone and ~59°N, the axis is characterized by a prominent ~1 500 m deep median valley with an axial high in its center. North of 59°N, the median valley changes into an axial high, typical for ridges of higher spreading rates like, for example, the intermediate-spreading Juan de Fuca Ridge or the fast-spreading East Pacific Rise (Searle and Loughton, 1981; Lin and Phipps Morgan, 1992; Keeton et al., 1997).



Murton and Parson (1993) identified three higher-order segmentation patterns based on the analysis of the bathymetry: (1) long-wavelength depth variations related to the shoaling of the ridge towards Iceland; (2) intermediate-wavelength depth variation of order of 40–120 km; and (3) short-wavelength segmentation between AVRs of the order of 5–30 km as they are overall relatively small scale morphologies. Searle et al. (1998) surveyed the detailed bathymetry of the Reykjanes Ridge, distinguishing 40 AVRs between 57°09'N and 62°01'N. Höskuldsson et al. (2007) revealed 10 more AVRs located between 63°10'N and Iceland. The AVRs appear as right-stepping, en echelon, elongated volcanic constructs, separated from each other by 3–11 km-wide areas of flatter seafloor (e.g., Searle et al., 1998; Höskuldsson et al., 2007). Individual AVRs are 20–30 km long, 3–6 km wide and 200–500 m high (Parson et al., 1993; Keeton et al., 1997; Searle et al., 1998). The smallest-scale features within the neovolcanic zone of the Reykjanes Ridge are small seamounts (conical-, fissure- and shield-like volcanoes up to several kilometers in diameter) confined to the ridge axis, where they often overlay the axial volcanic ridges (e.g., Höskuldsson et al., 2007). They also occur outside the AVRs on an overall rough volcanic terrain.

One indication of the influence of the Iceland hot spot on the Reykjanes Ridge is the presence of asymmetrical V-shaped ridges (VSRs), troughs, and scarps stretching along the flanks of the current ridge axis (Fig. 14). VSRs are prominent features elevated 300–600 m above the surrounding seafloor and were first recognized by Vogt (1971). Their origin is still under debate. The tip of the youngest VSR intersects the Reykjanes Ridge axis between 60°N and 61°N, where the density of seamounts is higher and there are fewer faults (e.g., Magde and Smith, 1995; Parnell-Turner et al., 2013). Parnell-Turner et al. (2013) related these observations with a 25°C thermal anomaly, which they attributed to the passage of a pulse of hot material from the Iceland hot spot, resulting in an increase in melt generation and a decrease in hydrothermal circulation in this region. Based on the assumption of variable fluxes from the Icelandic plume, Vogt (1971) suggested that these fluxes are either channeled along the Reykjanes Ridge axis, or spread radially away from the plume center, progressively reaching farther along the Reykjanes Ridge axis to form the diachronous VSRs. Ito (2001) argued that channeled flow would need very low mantle viscosities, which, if present, would produce much thicker crust under Iceland than actually observed. Poore et al. (2009) proposed that the plume flux has been decreasing over the past 3 Ma, and calculated present day flux of around  $0.6 \times 10^{14}$  kg yr<sup>-1</sup>, or a buoyancy flux of 8.8 Mg s<sup>-1</sup>. Hey et al. (2010) concluded that the formation of asymmetric VSRs may be due to plume pulses but that an additional mechanism, i.e., rift propagation south of Iceland, can help produce these distinctive features. Recently,

Martinez and Hey (2017) also showed that during such plume pulses, cells of sub-axial buoyant mantle upwelling propagate away from the Iceland hot spot, contributing to the local increase in crustal thickness, which may explain the VSRs flanking the linear Reykjanes Ridge. Based on the geometry of VRSs, the estimated along-axis flow rates range widely from  $168 \text{ mm yr}^{-1}$  (Ito, 2001) to over  $1\,000 \text{ mm yr}^{-1}$  (Wright and Miller, 1996).

The crest of the Reykjanes Ridge is dominated by normal faulting mainly striking parallel to the ridge axis (Searle et al., 1998). Parnell-Turner et al. (2013) re-interpreted the bathymetry from Searle et al. (1998) to investigate the general geometry of the faults along the Reykjanes Ridge between  $\sim 57^\circ\text{N}$  and  $63^\circ\text{N}$ . They showed that a great majority of faults occurs south of  $59^\circ\text{N}$ , where mean fault length is 12 km (ranging from 2 to 30 km), fault throws are  $>200 \text{ m}$  and fault density (i.e., cumulative fault length) is  $120 \text{ m km}^{-2}$ . Between  $59^\circ50'\text{N}$  and  $61^\circ50'\text{N}$ , the mean fault length drops to  $\sim 6 \text{ km}$ , fault throws are  $<200 \text{ m}$ , and the density of faults is only  $40 \text{ m km}^{-2}$ . North of  $61^\circ50'\text{N}$ , the mean fault length increases again to 7 km and fault density is  $80 \text{ m km}^{-2}$ .

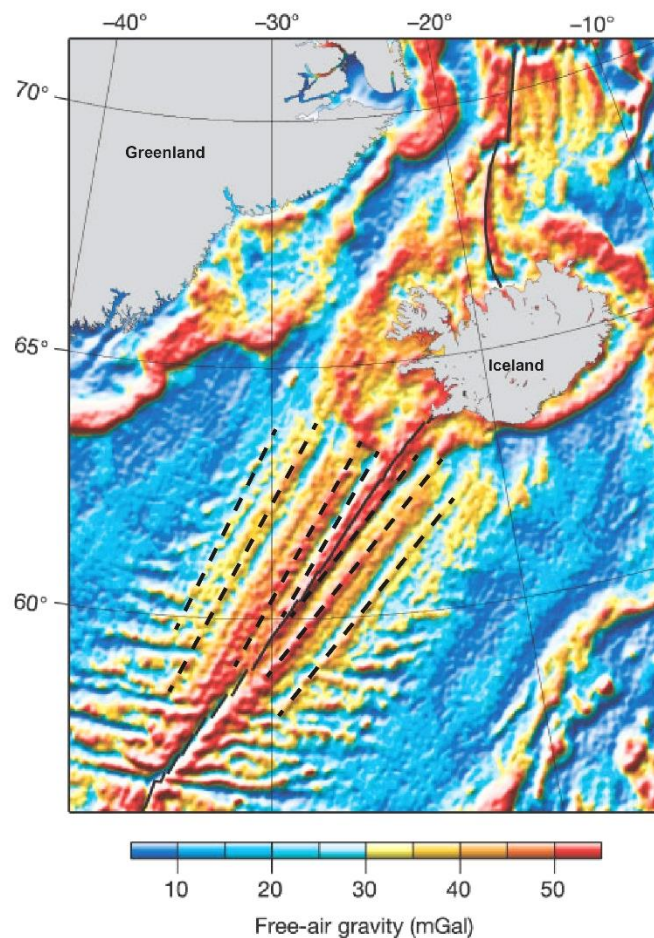


**Fig. 14** Satellite-derived free-air gravity anomaly (FAA) along the Reykjanes Ridge from Ito (2001) and based on Sandwell and Smith (1997). The solid black lines indicate the ridge axis. The black dashed lines show V-shaped ridges extending southwards from Iceland Basalt Plateau and the Icelandic hot spot.

In 1996, the Reykjanes-Iceland Seismic Experiment (RISE) was set up to investigate the crustal structure of the transition between Iceland and the Reykjanes Ridge (Weir et al., 2001). The results show that the thickness of zero-age crust decreases with increasing distance from the Iceland hot spot. Along the Reykjanes Peninsula, the thickness of crust is ~21 km (under Hengill) and continuously decreases to ~11 km at 62°40'N on the Reykjanes Ridge (Fig. 15). Thinning of the crust away from Iceland along the 250-km long section of the spreading axis was likely associated with decrease in mantle potential temperature of ~130°C (Weir et al., 2001). The thinning of the crust can also be observed off-axis. Near 63°N, the thickness varies from ~12.7 km at zero-age, to 9.8 km at 5 Ma. This has been attributed to a probable ~40°C change in the asthenospheric mantle temperature between 0 and 5 Ma, which has again been linked to pulses of hotter asthenospheric mantle material traveling beneath the Reykjanes Ridge (Weir et al., 2001). Additionally, a zone of high seismic velocities ( $\geq 7.5 \text{ km s}^{-1}$ ) at 9–11 km depth implies the presence of high-magnesium rocks in the lower crust, and the P to S wave velocity ratio implies that the crustal temperatures there are below solidus (Weir et al., 2001). Bell and Buck (1992) suggested that the thick crust of the Reykjanes Ridge is hot enough to allow ductile flow of hot material in the lower crust. The distribution of earthquakes in the northern Reykjanes Ridge (reaching a maximum of 8–10 km depth, i.e., within the seismically imaged crust (e.g., Weir et al., 2001)) provides supporting evidence for this.

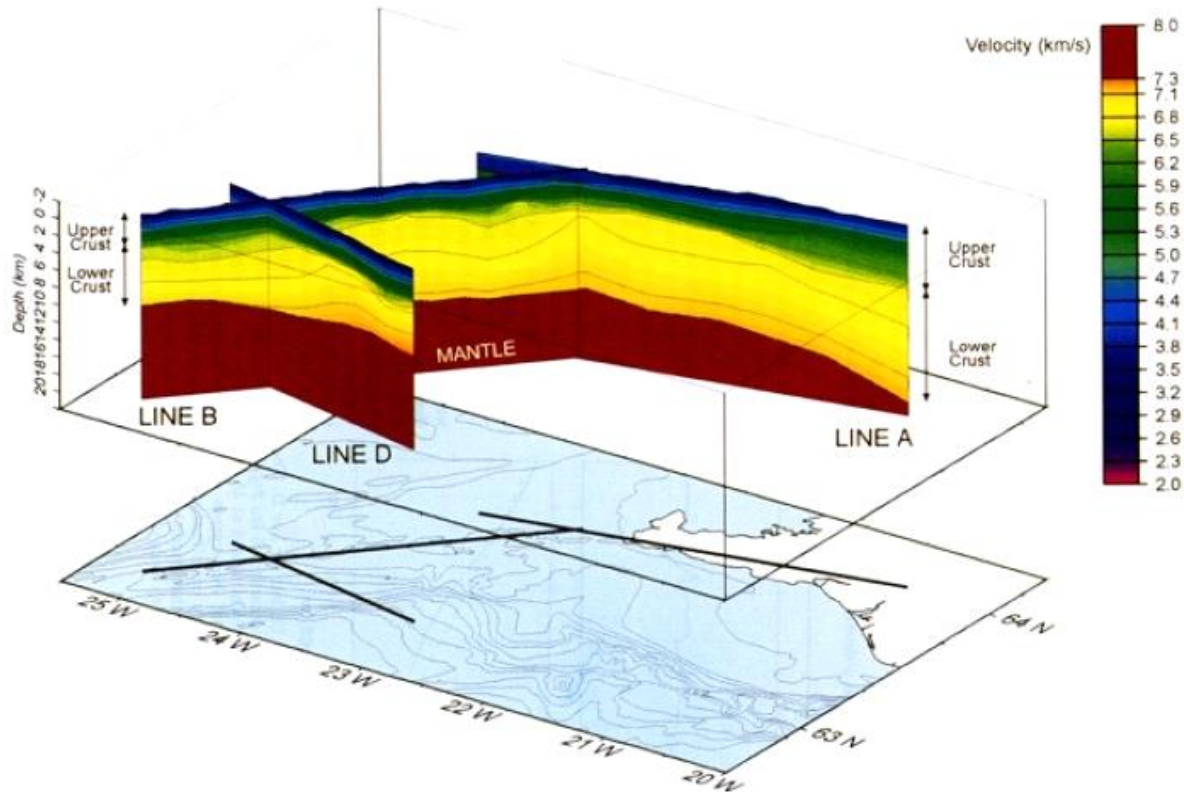


**Fig. 15 (Previous page)** Three-dimensional representation of the RISE experiment results. One along- and two across-spreading axis surveys showing smooth thinning of the oceanic crust both away from Iceland and Icelandic hot spot, and away from the spreading axis. This is attributed to the pulses of asthenospheric material traveling down the spreading axis at 5-10 Ma intervals (Weir et al., 2001).

Crustal accretion along slow-spreading ridges is dominated by tectonic extension during amagmatic periods as a result of lower magma supply to such ridges (Escartin et al., 2008). This has a significant impact on the crustal structure and thickness, as well as the size and duration of magma chambers (e.g., Detrick et al., 1990; Sinha et al., 1998). It is unlikely that slow-spreading segments are underlain by steady-state magma chambers, and eruptions there are probably linked to periods of injection of new magma from the mantle to the crust (Sinton and Detrick, 1992). Therefore, it is likely that magma chambers on slow-spreading segments are transient and small (hard to detect). Conversely, this may be different on a hot spot-influenced, slow-spreading ridge where melt supply is increased relative to normal slow-spreading ridges. A comprehensive multidisciplinary study of the Reykjanes Ridge near the Bight Fracture Zone (near 57°N) provided the first evidence for the existence of a magma chamber under this slow-spreading ridge (Sinha et al., 1998; Navin et al., 1998; MacGregor et al., 1998). The RAMESSES (Reykjanes Axial Melt Experiment: Structural Synthesis from Electromagnetics and Seismics) experiment aimed to combine interpretation of wide-angle seismic, normal incidence seismic, gravity, controlled source electromagnetic (CSEM) and magnetotelluric (MT) data to examine the subsurface of the AVR near 57°45'N. This study

showed that small and short-lived magma chambers (or melt lenses) may develop underneath slow-spreading ridge (Fig. 16); however, the volume of erupted material may not be sufficient to account for all the extension and, therefore, ridge-parallel faults must accommodate the rest (e.g., Escartin et al., 2008). Further investigations are necessary to find out if more magma chambers exist anywhere else along the Reykjanes Ridge.

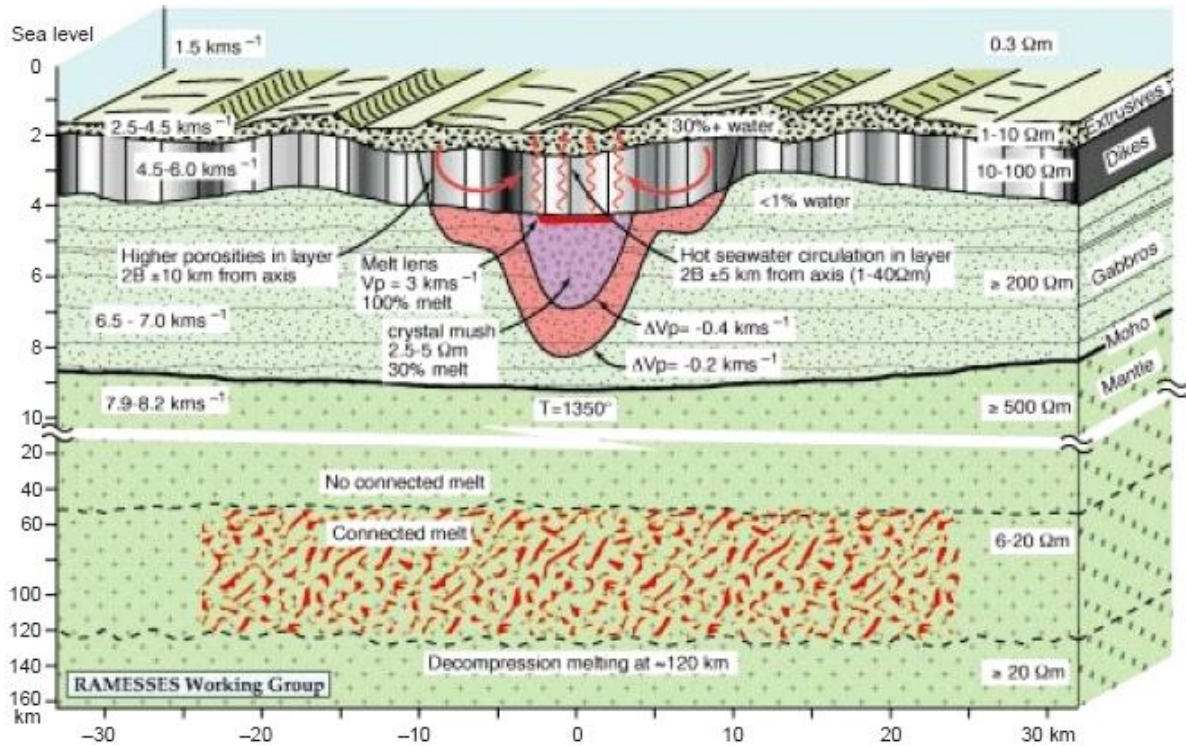


**Fig. 16** The cross-section through the Axial Volcanic Ridge near  $57^{\circ}45'N$  on the Reykjanes Ridge summarizing the interpretation of wide-angle seismic, normal incidence seismic, gravity, controlled source electromagnetic (CSEM) and magnetotelluric (MT) datasets collected during the RAMESSES experiment. Results indicate the existence of a magma chamber underneath the AVR and that the partial melt zone extends from 50 to 100 km depth in the upper mantle. The locations of seismic layer boundaries and velocity estimates, electrical resistivity, porosity, melt content and temperature are based on the collected datasets and modelling. Note the break in scale occurring around depth of 10 km bsl. Figure from Sinha et al. (1998).



## 1.4 References

- Alt, J.C., 2003, Hydrothermal fluxes at mid-ocean ridges and on ridge flanks: *Comptes Rendus Geoscience*, v. 335, p. 853–864, doi: 10.1016/j.crte.2003.02.001.
- Alt, J.C., Lonsdale, P., Haymon, R., and Muehlenbachs, K., 1987, Hydrothermal sulfide and oxide deposits on seamounts near 21 ° N , East Pacific Rise: *Geological Society of America Bulletin*, v. 98, p. 157–168, doi: 10.1130/0016-7606(1987)98<157:HSAODO>2.0.CO;2.
- Árnason, B., 1977, Hydrothermal systems in Iceland traced by deuterium: *Geothermics*, v. 5, p. 125–151, doi: 10.1016/0375-6505(77)90015-3.
- Arnórsson, S., 1995a, Geothermal systems in Iceland: Structure and conceptual models—I. High-temperature areas: *Geothermics*, v. 24, p. 561–602, doi: 10.1016/0375-6505(95)00025-9.
- Arnórsson, S., 1995b, Geothermal systems in Iceland: Structure and conceptual models—II. Low-temperature areas: *Geothermics*, v. 24, no. 5-6, p. 603–629, doi: 10.1016/0375-6505(95)00026-7.
- Arnórsson, S., Axelsson, G., and Sæmundsson, K., 2008, Geothermal systems in Iceland: *Jökull*, v. 58, p. 269–302.
- Arnórsson, S., and Gíslason, S.R., 1990, On the origin of low-temperature geothermal activity in Iceland: *Náttúrufræðingurinn*, v. 60, p. 39–56.
- Axelsson, G., 1985, Hydrology and thermomechanics of liquid-dominated hydrothermal systems in Iceland [PhD Thesis]: Oregon State University, USA, pp. 305.
- Axelsson, G., Björnsson, G., Egilson, T., Flóvenz, Ó.G., and Gautason, B., 2005, Nature and Properties of Recently Discovered Hidden Low-Temperature Geothermal Reservoirs in Iceland: *World Geothermal Congress, Antalya, Turkey*, pp. 10.
- Axelsson, G., Gunnlaugsson, E., Jónasson, T., and Ólafsson, M., 2010, Low-temperature geothermal utilization in Iceland – Decades of experience: *Geothermics*, v. 39, p. 329–338, doi: 10.1016/j.geothermics.2010.09.002.
- Baker, E.T., Chen, J.Y., and Morgan, J.P., 1996, The relationship between near-axis hydrothermal cooling and the spreading rate of mid-ocean ridges: *Earth and Planetary Science Letters*, v. 142, p. 137–145, doi: 10.1016/0012-821X(96)00097-0.
- Baker, E.T., Cormier, M.-H., Langmuir, Charles, H., and Zavala, K., 2001, Hydrothermal plumes along segments of contrasting magmatic influence, 15°20'–18°30'N, East Pacific Rise: Influence of axial faulting: *Geochemistry, Geophysics, Geosystems*, v. 2, doi: 10.1029/2000GC000165.
- Baker, E.T., Edmonds, H.N., Michael, P.J., Bach, W., Dick, H.J.B., Snow, J.E., Walker, S.L., Banerjee, N.R., and Langmuir, C.H., 2004, Hydrothermal venting in magma deserts: The

- ultraslow-spreading Gakkel and Southwest Indian Ridges: *Geochemistry, Geophysics, Geosystems*, v. 5, no. 8, doi: 10.1029/2004GC000712.
- Ballard, R.D., and Van Adel, T.H., 1977, Morphology and tectonics of the inner rift valley at lat 36°50'N on the Mid-Atlantic Ridge: *Geological Society of America Bulletin*, v. 88, p. 507–530, doi: 10.1130/0016-7606(1977)88<507:MATOTI>2.0.CO;2.
- Batiza, R., Fox, P.J., Vogt, P.R., Cande, S.C., Grindlay, N.R., Melson, W.G., and O'Hearn, T., 1989, Morphology, Abundance, and Chemistry of Near-Ridge Seamounts in the Vicinity of the Mid-Atlantic Ridge ~26°S: *Journal of Geology*, v. 97, p. 209–220.
- Beaulieu, S.E., Baker, E.T., and German, C.R., 2015, Where are the undiscovered hydrothermal vents on oceanic spreading ridges?: *Deep-Sea Research Part II*, v. 121, p. 202–212, doi: 10.1016/j.dsr2.2015.05.001.
- Beaulieu, S.E., Baker, E.T., German, C.R., and Maffei, A., 2013, An authoritative global database for active submarine hydrothermal vent fields: *Geochemistry, Geophysics, Geosystems*, v. 14, p. 4892–4905, doi: 10.1002/2013GC004998.
- Becker, K., and Von Herzen, R.P., 1996, Pre-drilling observations of conductive heat flow at the TAG active mound using Alvin: *Proceedings of the Ocean Drilling Program, Initial Reports*, v. 158, p. 23–29.
- Bell, R.E., and Buck, W.R., 1992, Crustal control of ridge segmentation inferred from observations of the Reykjanes Ridge: *Nature*, v. 357, p. 583–586, doi: 10.1038/357583a0.
- Bemis, K.G., Herzen, R.P. Von, and Mottl, M.J., 1993, Geothermal heat flux from hydrothermal plumes on the Juan de Fuca Ridge: *Journal of Geophysical Research Solid Earth*, v. 98, p. 6351–6365, doi: 10.1029/92JB02273.
- Bergmanis, E.C., Sinton, J., and Rubin, K.H., 2007, Recent eruptive history and magma reservoir dynamics on the southern East Pacific Rise at 17°30S: *Geochemistry, Geophysics, Geosystems*, v. 8, p. Q12O06, doi: 10.1029/2007GC001742.
- Bideau, D., Roger, H., Sichler, B., Bollinger, C., and Guivel, C., 1998, Contrasting volcanic-tectonic processes during the past 2 Ma on the Mid-Atlantic Ridge: submersible mapping, petrological and magnetic results at lat. 34°52'N and 33°55'N: *Marine Geophysical Research*, v. 20, p. 425–458, doi: 10.1023/A:1004760111160.
- Björnsson, A., Axelsson, G., and Flóvenz, Ó.G., 1990, On the origin of hot and warm springs in Iceland: *Náttúrufræðingurinn*, v. 60, p. 15–38.
- Björnsson, S., Gudmundsdóttir, I.D., and Ketilsson, J., 2010, Geothermal development and research in Iceland, *Orkustofnun, Reykjavík*, pp. 40.
- Björnsson, A., Sæmundsson, K., Einarsson, P., Tryggvason, E., and Grönvold, K., 1977, Current rifting episode in North Iceland: *Nature*, v. 266, p. 318–323, doi: 10.1038/266318a0.

- Bodvarsson, G., 1961, Physical characteristics of natural heat resources in Iceland: *Jökull*, v. 11, p. 29–38.
- Bodvarsson, G., 1983, Temperature/flow statistics and thermomechanics of low-temperature geothermal systems in Iceland: *Journal of Volcanology and Geothermal Research*, v. 19, p. 255–280, doi: 10.1016/0377-0273(83)90114-2.
- Brandsdóttir, B., and Einarsson, P., 1979, Seismic activity associated with the September 1977 deflation of the Krafla central volcano in North-Eastern Iceland: *Journal of Volcanology and Geothermal Research*, v. 6, p. 197–212, doi: 10.1016/0377-0273(79)90001-5.
- Brandsdóttir, B., Einarsson, P., Detrick, R.S., Mayer, L., Calder, B., Driscoll, N., and Richter, B., 2003, Lost in Iceland? Fracture Zone Complications Along the Mid-Atlantic Plate Boundary [Abstract], AGU Fall Meeting, San Francisco, USA.
- Brandsdóttir, B., Hooft, E.E.E., Mjelde, R., and Murai, Y., 2015, Origin and evolution of the Kolbeinsey Ridge and Iceland Plateau, N-Atlantic: *Geochemistry, Geophysics, Geosystems*, v. 16, p. 612–634, doi: 10.1002/2014GC005540.
- Brandsdóttir, B., and Menke, W.H., 1992, Thin low-velocity zone within the krafla caldera, ne-Iceland attributed to a small magma chamber: *Geophysical Research Letters*, v. 19, p. 2381–2384, doi: 10.1029/92GL02541.
- Briaies, A., Sloan, H., Parson, L.M., and Murton, B.J., 2000, Accretionary processes in the axial valley of the Mid-Atlantic Ridge 27°N–30°N from TOBI side-scan sonar images: *Marine Geophysical Research*, v. 21, p. 87–119, doi: 10.1023/A:1004722213652.
- Bryan, W.B., Humphris, S.E., Thompson, G., and Casey, J.F., 1994, Comparative volcanology of small axial eruptive centres in the MARK area: *Journal of Geophysical Research Solid Earth*, v. 99, p. 2973–2984, doi: 10.1029/93JB02157.
- Burnett, M.S., Caress, D.W., and Orcutt, J.A., 1989, Tomographic image of the magma chamber at 12°50'N on the East Pacific Rise: *Nature*, v. 339, p. 206–208, doi: 10.1038/339206a0.
- Calvert, A.J., 1995, Seismic evidence for a magma chamber beneath the slow-spreading Mid-Atlantic Ridge: *Nature*, v. 377, p. 410–414, doi: 10.1038/377410a0.
- Calvert, A.J., 1997, Backscattered coherent noise and seismic reflection imaging of the oceanic crust: An example from the rift valley of the Mid-Atlantic Ridge at 23°N: *Journal of Geophysical Research Solid Earth*, v. 102, p. 5119–5133, doi: 10.1029/96JB03798.
- Caress, D.W., Clague, D.A., Paduan, J.B., Martin, J.F., Dreyer, B.M., Jr, W.W.C., Denny, A., and Kelley, D.S., 2012, Repeat bathymetric surveys at 1-metre resolution of lava flows erupted at Axial Seamount in April 2011: *Nature Geoscience*, v. 5, p. 483–488, doi: 10.1038/ngeo1496.
- Cave, R.R., German, C.R., Thomson, J., and Nesbitt, R.W., 2002, Fluxes to sediments underlying the Rainbow hydrothermal plume at 36°14'N on the Mid-Atlantic Ridge:



- Geochimica et Cosmochimica Acta*, v. 66, no. 11, p. 1905–1923, doi: 10.1016/S0016-7037(02)00823-2.
- Chadwick, Jr., W.W., Clague, D.A., Embley, R.W., Perfit, M.R., Butterfield, D.A., Caress, D.W., Paduan, J.B., Martin, J.F., Sasnett, P., Merle, S.G., and Bobbitt, A.M., 2013, The 1998 eruption of Axial Seamount: New insights on submarine lava flow emplacement from high-resolution mapping: *Geochemistry, Geophysics, Geosystems*, v. 14, p. 3939–3968, doi: 10.1002/ggge.20202.
- Clague, D.A., Dreyer, B.M., Paduan, J.B., Martin, J.F., Chadwick, Jr., W.W., and Guilderson, T.P., 2013, Geologic history of the summit of Axial Seamount, Juan de Fuca Ridge: *Geochemistry, Geophysics, Geosystems*, v. 14, p. 4403–4443, doi: 10.1002/ggge.20240.
- Clague, D.A., Moore, J.G., and Reynolds, J.R., 2000, Formation of submarine flat-topped volcanic cones in Hawai'i: *Bulletin of Volcanology*, v. 62, p. 214–233, doi: 10.1007/s004450000088.
- Crane, K., and Ballard, R.D., 1981, Volcanics and structure of the FAMOUS Narrowgate Rift: evidence for cyclic evolution: *AMAR 1: Journal of Geophysical Research Solid Earth*, v. 86, p. 5112–5124, doi: 10.1029/JB086iB06p05112.
- Darling, W.G., and Ármannsson, H., 1989, Stable isotopic aspects of fluid flow in the Krafla, Námafjall and Theistareykir geothermal systems of northeast Iceland: *Chemical Geology*, v. 76, p. 197–213, doi: 10.1016/0009-2541(89)90090-9.
- DeMets, C., Gordon, R.G., Argus, D.F., and Stein, S., 1990, Current plate motions: v. 101, p. 425–478, doi: 10.1111/j.1365-246X.1990.tb06579.x.
- Detrick, R.S., Mutter, J.C., Buhl, P., and Kim, I.I., 1990, No evidence from multichannel reflection data for a crustal magma chamber in the MARK area on the Mid-Atlantic Ridge: *Nature*, v. 347, p. 61–64, doi: 10.1038/347061a0.
- Devey, C.W., Lackschewitz, K.S., and Baker, E., 2005, Hydrothermal and Volcanic Activity Found on the Southern Mid-Atlantic Ridge: *Eos Transactions AGU*, v. 86, p. 209–212, doi: 10.1029/2005EO220001.
- Devey, C.W., and The Scientific Party of MSM25, 2014, MSM25 Cruise Report, SoMARTerm: The Mid-Atlantic Ridge 13-33°S, pp. 93, doi: 10.2312/cr\_msm25.
- Van Dover, C.L., 2014, Impacts of anthropogenic disturbances at deep-sea hydrothermal vent ecosystems: A review: *Marine Environmental Research*, v. 102, p. 59–72, doi: 10.1016/j.marenvres.2014.03.008.
- Einarsson, P., 1991, Earthquakes and present-day tectonism in Iceland: *Tectonophysics*, v. 189, p. 261–279, doi: 10.1016/0040-1951(91)90501-I.
- Embley, R.W., and Chadwick, Jr., W.W., 1994, Volcanic and hydrothermal processes associated with a recent phase of seafloor spreading at the northern Cleft segment: Juan de Fuca Ridge: *Journal of Geophysical Research Solid Earth*, v. 99, p. 4741–4760, doi: 10.1029/93JB02038.

- Escartin, J., and Cannat, M., 1999, Ultramafic exposures and the gravity signature of the lithosphere near the Fifteen-Twenty Fracture Zone (Mid-Atlantic Ridge, 14°-16.5°N): *Earth and Planetary Science Letters*, v. 171, p. 411–424, doi: 10.1016/S0012-821X(99)00169-7.
- Escartín, J., Smith, D.K., Cann, J., Schouten, H., Langmuir, C.H., and Escrig, S., 2008, Central role of detachment faults in accretion of slow-spreading oceanic lithosphere.: *Nature*, v. 455, p. 790–794, doi: 10.1038/nature07333.
- Escartín, J., Soule, S.A., Cannat, M., Fornari, D.J., Düşünür, D., and Garcia, R., 2014, Lucky Strike seamount: Implications for the emplacement and rifting of segment-centered volcanoes at slow spreading mid-ocean ridges: *Geochemistry, Geophysics, Geosystems*, v. 15, p. 4157–4179, doi: 10.1002/2014GC005477.Received.
- Fornari, D.J., Batiza, R., and Luckman, M.A., 1987, Seamount abundances and distribution near the East Pacific Rise 0°-24°N based on Seabeam data, In: Keating, B.H., Fryer, P., Batiza, R., and Boehlert, G. [Eds.], *Seamounts, Islands, and Atolls*, AGU Geophysical Monograph, v. 43, p. 13–21, doi: 10.1029/GM043p0013.
- Fornari, D.J., and Embley, R.W., 1995, Tectonic and Volcanic Controls on Hydrothermal Processes at the Mid-Ocean Ridge: an Overview Based on Near-Bottom and Submersible Studies, In: Humphris, S.E., Zierenberg, R.A., Mullineaux, L.S., and Thomson, R.E. [Eds.], *Seafloor Hydrothermal Systems: Physical, Chemical, Biological, and Geological Interactions*, American Geophysical Union, Washington D.C., p. 1-46, doi: 10.1029/GM091p0001.
- Fornari, D.J., Haymon, R.M., Perfit, M.R., Gregg, T.K.P., and Edwards, M.H., 1998, Axial summit trough of the East Pacific Rise 9°-10°N: Geological characteristics and evolution of the axial zone on fast spreading mid-ocean ridge: *Journal of Geophysical Research Solid Earth*, v. 103, p. 9827–9855, doi: 10.1029/98JB00028.
- Fornari, D., Tivey, M., Schouten, H., Perfit, M., Yoerger, D., Bradley, A., Edwards, M., Haymon, R., Scheirer, D., Damm, K. Von, Shank, T., and Soule, A., 2004, Submarine lava flow emplacement at the East Pacific Rise 9°50'N: implications for uppermost ocean crust stratigraphy and hydrothermal fluid circulation, In: German, C.R., Lin, J., and Parson, L.M. [Eds.], *Mid-Ocean Ridges: Hydrothermal Interactions Between the Lithosphere and Oceans*, Am, Washington D.C., p. 187–218, doi: 10.1029/148GM08.
- Foulger, G.R., and Anderson, D.L., 2005, A cool model for the Iceland hotspot: *Journal of Volcanology and Geothermal Research*, v. 141, p. 1–22, doi: 10.1016/j.jvolgeores.2004.10.007.
- Foulger, G.R., and Toomey, D.R., 1989, Structure and evolution of the Hengill-Grensdalur Volcanic Complex, Iceland: Geology, geophysics, and seismic tomography: *Journal of Geophysical Research*, v. 94, p. 17511–17522, doi: 10.1029/JB094iB12p17511.
- Fouquet, Y., 1995, Where are the large hydrothermal sulphide deposits in the oceans?: *Philosophical Transactions of the Royal Society: A Mathematical, Physical and Engineering Sciences*, v. 355, p. 427–441, doi: 10.1098/rsta.1997.0015.

- Fouquet, Y., Ondreas, H., Charlou, J.-L., Donval, J.-L., Radford-Knoery, J., Costa, I., Lourenço, N., Tivey, M.K., and Tivey, M.K., 1995, Atlantic lava lakes and hot vents: *Nature*, v. 377, p. 201, doi: 10.1038/377201a0.
- Franzson, H., 1998, Reservoir geology of the Nesjavellir high-temperature field, SW-Iceland, in *Proceeding of the 19th Annual PNOC-EDC Geothermal Conference*, Manila, Philippines, p. 13–20.
- Franzson, H., 2004, Reykjanes high-temperature geothermal system. Geological and geothermal model (in Icelandic): Iceland GeoSurvey Report ISOR-2004/012, pp. 68, Reykjavik.
- Fridleifsson, I.B., 1979, Geothermal activity in Iceland: *Jökull*, v. 29, p. 47–56.
- German, C.R., Baker, E.T., Mevel, C., Tamaki, K., and the FUJI Science Team, 1998, Hydrothermal activity along the southwest Indian ridge: *Nature*, v. 395, p. 490–493, doi: 10.1038/26730.
- German, C.R., Bennett, S. a., Connelly, D.P., Evans, A.J., Murton, B.J., Parson, L.M., Prien, R.D., Ramirez-Llodra, E., Jakuba, M., Shank, T.M., Yoerger, D.R., Baker, E.T., Walker, S.L., and Nakamura, K., 2008, Hydrothermal activity on the southern Mid-Atlantic Ridge: Tectonically- and volcanically-controlled venting at 4–5°S: *Earth and Planetary Science Letters*, v. 273, p. 332–344, doi: 10.1016/j.epsl.2008.06.048.
- German, C.R., Briem, J., Chin, C., Danielsen, M., Holland, S., James, R., Jónsdóttir, A., Ludford, E., Moser, C., Ólafsson, J., Palmer, M.R., and Rudnicki, M.D., 1994, Hydrothermal activity on the Reykjanes Ridge: the Steinahóll vent-field at 63°06'N: *Earth and Planetary Science Letters*, v. 121, no. 3-4, p. 647–654, doi: 10.1016/0012-821X(94)90098-1.
- German, C., Campbell, A.C., and Edmond, J.M., 1991, Hydrothermal scavenging at the Mid-Atlantic Ridge: Modification of trace element dissolved fluxes: *Earth and Planetary Science Letters*, v. 107, p. 101–114, doi: 10.1016/0012-821X(91)90047-L.
- German, C.R., Parson, L.M., and Team, H.S., 1996, Hydrothermal exploration near the Azores Triple Junction: tectonic control of venting at slow-spreading ridges?: *Earth and Planetary Science Letters*, v. 138, p. 93–104, doi: 10.1016/0012-821X(95)00224-Z.
- German, C.R., Petersen, S., and Hannington, M.D., 2016, Hydrothermal exploration of mid-ocean ridges: Where might the largest sulfide deposits be forming?: *Chemical Geology*, v. 420, p. 114–126, doi: 10.1016/j.chemgeo.2015.11.006.
- Ginster, U., Mottl, M.J., and Herzen, R.P. Von, 1994, Heat flux from black smokers on the Endeavour and Cleft segments, Juan de Fuca Ridge: *Journal of Geophysical Research Solid Earth*, v. 99, p. 4937–4950, doi: 10.1029/93JB02800.
- Grácia, E., Parson, L.M., Bideau, D., and Hekinian, R., 1998, Volcano-tectonic variability along segments of the Mid-Atlantic Ridge between Azores platform and Hayes fracture zone: evidence from submersible and high resolution sides-can sonar data: *Geological Society Special Publications London*, v. 148, p. 1–15, doi: 10.1144/GSL.SP.1998.148.01.01.

- Gregg, T.K.P., and Fink, J.H., 1995, Quantification of submarine lava-flow morphology through analog experiments: *Geology*, v. 23, p. 73–76, doi: 10.1130/0091-7613(1995)023<0073:QOSLFM>2.3.CO;2.
- Gregg, T.K.P., Fornari, D.J., Perfit, M.R., Haymon, R.M., and Fink, J.H., 1996, Rapid emplacement of a mid-ocean ridge lava flow on the East Pacific Rise at 9°46′-51′N: *Earth and Planetary Science Letters*, v. 144, p. E1–E7, doi: 10.1016/S0012-821X(96)00179-3.
- Griffiths, R.W., and Fink, J.H., 1992a, Solidification and morphology of submarine lavas: A dependence on extrusion rate: *Journal of Geophysical Research Solid Earth*, v. 97, p. 19729–19737, doi: 10.1029/92JB01594.
- Griffiths, R.W., and Fink, J.H., 1992b, The morphology of lava flows in planetary environments: Predictions from analog experiments: *Journal of Geophysical Research Solid Earth*, v. 97, p. 19739–19748, doi: 10.1029/92JB01953.
- Gudmundsson, A., 2015, Dyke-path formation in relation to the eruptions of Eyjafjallajökull 2010 and Bardarbunga-Holuhraun 2014 [Abstract], EGU, Vienna, Austria.
- Gudmundsson, A., 1995, Infrastructure and mechanics of volcanic systems in Iceland: *Journal of Volcanology and Geothermal Research*, v. 64, p. 1–22, doi: 10.1016/0377-0273(95)92782-Q.
- Gudmundsson, A., Lecoœur, N., Mohajeri, N., and Thordarson, T., 2014, Dike emplacement at Bardarbunga, Iceland, induces unusual stress changes, caldera deformation, and earthquakes: *Bulletin of Volcanology*, v. 76 (869), pp. 7, doi: 10.1007/s00445-014-0869-8.
- Gudmundsson, A., Oskarsson, N., Gronvold, K., Sæmundsson, K., Sigurdsson, O., Stefansson, R., Gislason, S.R., Einarsson, P., Brandsdóttir, B., Larsen, G., Johannesson, H., and Thordarson, T., 1992, The 1991 eruption of Hekla, Iceland: *Bulletin of Volcanology*, v. 54, p. 238–246, doi: 10.1007/BF00278391.
- Hannington, M., Herzig, P., Stoffers, P., Scholten, J., Botz, R., Jonasson, I.R., Roest, W., and Scienti, S., 2001, First observations of high-temperature submarine hydrothermal vents and massive anhydrite deposits off the north coast of Iceland: *Marine Geology*, v. 177, p. 199–220, doi: 10.1016/S0025-3227(01)00172-4.
- Hannington, M.D., Jamieson, J.W., Monecke, T., and Petersen, S., 2010, Modern seafloor massive sulfides and base metal resources: toward an estimate of global seafloor massive sulfide potential: *Society of Economic Geologists Special Publication*, v. 15, p. 317–338.
- Hannington, M., Jamieson, J., Monecke, T., Petersen, S., and Beaulieu, S., 2011, The abundance of seafloor massive sulfide deposits: *Geology*, v. 39, p. 1155–1158, doi: 10.1130/G32468.1.
- Hannington, M.D., Jonasson, I.R., Herzig, P.M., and Petersen, S., 1995, Physical and chemical processes of seafloor mineralization at mid-ocean ridges, In: Humphirs, S.E., Zierenberg, R.A., Mullineaux, L.S., and Thomson, R.E. [Eds.], *Seafloor Hydrothermal*

Systems: Physical, Chemical, Biological, and Geological Interactions, AGU Geophysical Monograph, v. 91, p. 115–157, doi: 10.1029/GM091p0115.

- Hannington, M.D., de Ronde, C.D.J., and Petersen, S., 2005, Sea-Floor Tectonics and Submarine Hydrothermal Systems, In: Hedenquist, J.W., Thompson, J.F.H., Goldfarb, R.J., and Richards, J.P. [Eds.], *Economic Geology: 100th Anniversary Volume*, Littleton, Colorado, p. 111–141.
- Haymon, R.M., Fornari, D.J., Edwards, M.H., Carbotte, S., Wright, D., and Macdonald, K.C., 1991, Hydrothermal vent distribution along the East Pacific Rise crest (9°09'–54'N) and its relationship to magmatic and tectonic processes on fast-spreading mid-ocean ridges: *Earth and Planetary Science Letters*, v. 104, p. 513–534, doi: 10.1016/0012-821X(91)90226-8.
- Head, W., Wilson, L., and Smith, D.K., 1996, Mid-ocean ridge eruptive vent morphology and substructure: Evidence for dike widths, eruption rates, and evolution of eruptions and axial volcanic ridges: *Journal of Geophysical Research Solid Earth*, v. 101, p. 28265–28280, doi: 10.1029/96JB02275.
- Herzig, P.M., 1999, Economic potential of sea-floor massive sulphide deposits: ancient and modern: *Philosophical Transactions of the Royal Society: A Mathematical, Physical and Engineering Sciences*, v. 357, p. 861–873, doi: DOI: 10.1098/rsta.1999.0355.
- Hey, R., Martinez, F., Höskuldsson, Á., and Benediksdóttir, Á., 2010, Propagating rift model for the V-shaped ridges south of Iceland: *Geochemistry, Geophysics, Geosystems*, v. 11, Q03011, doi: 10.1029/2009GC002865.
- Höskuldsson, Á., Hey, R., Kjartansson, E., and Guðmundsson, G.B., 2007, The Reykjanes Ridge between 63°10'N and Iceland: *Journal of Geodynamics*, v. 43, p. 73–86, doi: 10.1016/j.jog.2006.09.003.
- Humphris, S.E., and McCollom, T., 1998, The Cauldron Beneath the Seafloor: Percolating Through Volcanic Subsurface Rocks, Seawater is Chemically Transformed into Hydrothermal Fluid: *Oceanologica Acta*, v. 41, p. 18–21.
- Ito, G., 2001, Reykjanes “V”-shaped ridges originating from a pulsing and dehydrating mantle plume: *Nature*, v. 411, p. 681–684, doi: 10.1038/35079561.
- Jakobsdóttir, S.S., 2008, Seismicity in Iceland: 1994 – 2007: *Jökull*, , no. 58, p. 75–100.
- Jakobsson, S.P., 1979a, Outline of the petrology of Iceland: *Jökull*, v. 29, p. 57–73.
- Jakobsson, S.P., 1979b, Petrology of recent basalts of the Eastern Volcanic Zone: *Acta Naturalia Islandica*, v. 26, p. 1–103.
- Jamieson, J.W., Hannington, M.D., Clague, D.A., Kelley, D.S., Delaney, J.R., Holden, J.F., Tivey, M.K., and Kimpe, L.E., 2013, Sulfide geochronology along the Endeavour Segment of the Juan de Fuca Ridge: *Geochemistry, Geophysics, Geosystems*, v. 14, p. 2084–2099, doi: 10.1002/ggge.20133.

- Jannasch, H.W., 1995, Microbial interactions with hydrothermal fluids, In: Humphris, S.E., Zierenberg, R.A., Mullineaux, L.S., and Thomson, R.E. [Eds.], *Seafloor Hydrothermal Systems: Physical, Chemical, Biological, and Geological Interactions*, American Geophysical Union, Washington D.C., v. 91, p. 273–296.
- Johannesson, H., 2014, *Geological Map of Iceland: Bedrock Geology*: [Map], 1: 600 000, Náttúruminjasafn Íslands, Reykjavík.
- Johannesson, H., and Sæmundsson, K., 2009, *Geological Map of Iceland: Tectonics* [Map], 1: 600 000, Náttúruminjasafn Íslands, Reykjavík.
- Jupp, T., and Schultz, A., 2000, A thermodynamic explanation for black smoker temperatures: *Nature*, v. 403, p. 880–883, doi: 10.1038/35002552.
- Kaban, M.K., Flóvenz, Ó.G., and Palmason, G., 2002, Nature of the crust-mantle transition zone and the thermal state of the upper mantle beneath Iceland from gravity modelling: *Geophysical Journal International*, v. 149, p. 281–299, doi: 10.1046/j.1365-246X.2002.01622.x.
- Karson, J.A., Kelley, D.S., Fornari, D.J., Perfit, M.R., and Shank, T.M., 2015, *Discovering the deep: A photographic atlas of the seafloor and ocean crust*: Cambridge University Press, Cambridge, pp. 414.
- Keeton, J.A., and Searle, R.C., 1996, Analysis of Simrad EM12 multibeam bathymetry and acoustic backscatter data for seafloor mapping, exemplified at the Mid-Atlantic Ridge at 45°N: *Marine Geophysical Researches*, v. 18, p. 663–688, doi: 10.1007/BF00313880.
- Keeton, J.A., Searle, R.C., Parsons, B., White, R.S., Murton, B.J., Parson, L.M., Peirce, C., and Sinha, M.C., 1997, Bathymetry of the Reykjanes Ridge: *Marine Geophysical Research*, v. 19, p. 55–64, doi: 10.1023/A:1004266721393.
- Kelemen, P.B., Shimizu, N., and Salters, V.J.M., 1995, Extraction of mid-ocean ridge basalt from the upwelling mantle by focused flow of melt in dunite channels: *Nature*, v. 375, p. 747–753, doi: 10.1038/375747a0.
- Kelley, D.S., Baross, J. a., and Delaney, J.R., 2002, *Volcanoes, Fluids, and Life At Mid-Ocean Ridges Spreading Centers*: *Annual Review of Earth and Planetary Sciences*, v. 30, p. 385–491, doi: 10.1146/annurev.earth.30.091201.141331.
- Kelley, D.S., Box, P.O., and Delaney, J.R., 2001a, Geology and venting characteristics of the Mothra hydrothermal field, Endeavour segment, Juan de Fuca Ridge: *Geology*, v. 29, p. 959–962, doi: 10.1130/0091-7613(2001)029<0959:GAVCOT>2.0.CO;2.
- Kelley, D.S., Karson, J.A., Blackman, D.K., Früh-Green, G.L., Butterfield, D.A., Lilley, M.D., Olson, E.J., Schrenk, M.O., Roe, K.K., Lebon, G.T., and Rivizzigno, P., 2001b, An off-axis hydrothermal vent field near the Mid-Atlantic Ridge at 30° N: *Nature*, v. 412, p. 145–149, doi: 10.1038/35084000.
- Khodayar, M., and Björnsson, S., 2014, Fault ruptures and geothermal effects of the second earthquake, 29 May 2008, South Iceland Seismic Zone: *Geothermics*, v. 50, p. 44–65, doi: 10.1016/j.geothermics.2013.07.002.

- Khodayar, M., Björnsson, S., Einarsson, P., and Franzson, H., 2010, Effect of tectonics and earthquakes on geothermal activity near plate boundaries: A case study from South Iceland: *Geothermics*, v. 39, no. 3, p. 207–219, doi: 10.1016/j.geothermics.2010.06.003.
- Khodayar, M., Markusson, S.H., and Einarsson, P., 2006, GPS-mapping of geothermal areas in West Iceland and tectonic interpretation, Phase 2. Klettur-Runnar - an overview: Orkustofnun Report ISOR-06038, Reykjavik, pp. 13.
- Kjartansson, G., 1969, Geological map of Iceland: Sheet 1 North-West Iceland [Map], 1: 250 000, Náttúruminjasafn Íslands, Reykjavik.
- Kong, L., Ryan, W.B.F., Mayer, L.A., Detrick, R.S., and Manchester, K., 1985, Bare-rock drill sites, ODP Legs 106 and 109: Evidence for Hydrothermal Activity at 23°N in the Mid-Atlantic Ridge: *Eos Transactions AGU*, v. 66, p. 936.
- Koschinsky, A., Garbe-Schönberg, D., Sander, S., Schmidt, K., Gennerich, H.-H., and Strauss, H., 2008, Hydrothermal venting at pressure-temperature conditions above the critical point of seawater, 5°S on the Mid-Atlantic Ridge: *Geology*, v. 36, p. 615, doi: 10.1130/G24726A.1.
- Kristjánsson, L., 1968, The Paleomagnetism and Geology of North-Western Iceland: *Earth and Planetary Science Letters*, v. 4, p. 448–450, doi: 10.1016/0012-821X(68)90022-8.
- Kuznetsov, V., Maksimov, F., A., Z., Cherkashov, G., Bel'Tenev, V., and Lazareva, L., 2011, <sup>230</sup>Th/U chronology of ore formation within the Semyenov hydrothermal district (13°31'N) at the Mid-Atlantic Ridge: *Geochronometria*, v. 38, p. 72–76, doi: 10.2478/s13386-011-0001-1.
- Lalou, C., Münch, U., Halbach, P., and Reyss, J.-L., 1998, Radiochronological investigation of hydrothermal deposits from the MESO zone, Central Indian Ridge: *Marine Geology*, v. 149, p. 243–254, doi: 10.1016/S0025-3227(98)00042-5.
- Langmuir, C., Humphris, S., Fornari, D., Van Dover, C., Von Damm, K., Tivey, M.K., Colodner, D., Charlou, J.-L., Desonie, D., Wilson, C., Fouquet, Y., Klinkhammer, G., and Bougault, H., 1997, Hydrothermal vents near a mantle hot spot: the Lucky Strike vent field at 37°N on the Mid-Atlantic Ridge: *Earth and Planetary Science Letters*, v. 148, p. 69–91, doi: 10.1016/S0012-821X(97)00027-7.
- Lawson, K., Searle, R.C., Pearce, J. a., Browning, P., and Kempton, P., 1996, Detailed volcanic geology of the MARNOK area, Mid-Atlantic Ridge north of Kane transform Mid-Atlantic Ridge North Of Kane transform: Geological Society, London, Special Publications, v. 118, p. 61–102, doi: 10.1144/GSL.SP.1996.118.01.05.
- Lawver, L.A., and Müller, D.R., 1994, Iceland hotspot track: *Geology*, v. 22, p. 311–314, doi: 10.1130/0091-7613(1994)022<0311:IHT>2.3.CO;2.
- Lin, J., and Phipps Morgan, J., 1992, The spreading rate dependence of three-dimensional mid-ocean ridge gravity structure: *Geophysical Research Letters*, v. 19, p. 13–16, doi: 10.1029/91GL03041.



- Lonsdale, P., 1977, Clustering of suspension-feeding macrobenthos near abyssal hydrothermal vents at oceanic spreading centers: *Deep-Sea Research*, v. 24, p. 857–863, doi: 10.1016/0146-6291(77)90478-7.
- Lowell, R.P., 1991, Modeling continental and submarine hydrothermal systems: *Reviews of Geophysics*, v. 29, p. 457–476, doi: 10.1029/91RG01080.
- Macdonald, K.C., 1998, Linkages between faulting, volcanism, hydrothermal activity and segmentation on fast spreading centers, In: Buck, W.R., Delaney, P.T., Karson, J.A., and Lagabriele, Y. [Eds.], *Faulting and Magmatism at Mid-Ocean Ridges*, AGU Geophysical Monograph v. 106, Washington D.C.
- Macdonald, K.C., 2001, Mid-Ocean Ridge Tectonics, Volcanism, and Geomorphology, In: Steele, J.H., Turekian, K.K., and Thorpe, S.A. [Eds.], *Encyclopedia of Ocean Sciences*, Academic Press, p. 852–866.
- Macdonald, G.A., Abbott, A.T., and Peterson, F.L., 1970, *Volcanoes in the sea: the geology of Hawaii*: University of Hawaii, Honolulu, pp. 517.
- Macdonald, C., Scheirer, D.S., and Carbotre, S.M., 1991, Mid- Ocean Ridges: Discontinuities, Segments and Giant Cracks of: *Science*, v. 253, p. 986–994, doi: 10.1126/science.253.5023.986.
- MacGregor, L.M., Constable, S., and Sinha, M.C., 1998, The RAMESSES experiment - III. Controlled-source electromagnetic sounding of the Reykjanes Ridge at 57°45'N: *Geophysical Journal International*, v. 135, p. 773–789, doi: 10.1046/j.1365-246X.1998.00705.x.
- Magde, L.S., and Smith, D.K., 1995, Seamount volcanism at the Reykjanes Ridge: Relationship to the Iceland hot spot: *Journal of Geophysical Research*, v. 100, p. 8449–8468, doi: 10.1029/95JB00048.
- Martinez, F., and Hey, R., 2017, Propagating buoyant mantle upwelling on the Reykjanes Ridge: *Earth and Planetary Science Letters*, v. 457, p. 10–22, doi: 10.1016/j.epsl.2016.09.057.
- McKenzie, D.P., 1984, The generation and compaction of partially molten rocks: *Journal of Petrology*, v. 25, p. 713–765, doi: 10.1093/petrology/25.3.713.
- Melchert, B., Devey, C.W., German, C.R., Lackschewitz, K.S., Seifert, R., Walter, M., Mertens, C., Yoerger, D.R., Baker, E.T., Paulick, H., and Nakamura, K., 2008, First evidence for high-temperature off-axis venting of deep crustal/mantle heat: The Nibelungen hydrothermal field, southern Mid-Atlantic Ridge: *Earth and Planetary Science Letters*, v. 275, p. 61–69, doi: 10.1016/j.epsl.2008.08.010.
- Mendel, V., Sauter, D., Rommevaux-Jestin, C., Patriat, P., Lefebvre, F., and Parson, L.M., 2003, Magmato-tectonic cyclicality at the ultra-slow spreading Southwest Indian Ridge: Evidence from variations of axial volcanic ridge morphology and abyssal hills pattern: *Geochemistry, Geophysics, Geosystems*, v. 4, doi: 10.1029/2002GC000417.

- Morgan, W.J., 1971, Convection plumes in the lower mantle: *Nature*, v. 230, p. 42–43, doi: 10.1038/230042a0
- Mottl, M.J., 2003, Partitioning of energy and mass fluxes between mid-ocean ridge axes and flanks at high and low temperature, In: Halbach, P.E., Tunnicliffe, V., and Hein, J.R. [Eds.], *Energy and Mass Transfer in Marine Hydrothermal Systems*, Dahlem University Press, Berlin, p. 271–286.
- Murton, B.J., and Parson, L.M., 1993, Segmentation, volcanism and deformation of oblique spreading centres: a quantitative study of the Reykjanes Ridge: *Tectonophysics*, v. 222, p. 237–257, doi: 10.1016/0040-1951(93)90051-K.
- Murton, B.J., Schroth, N., LeBas, T., Van Calsteren, P.W., Yeo, I.A., Achenbach, K.L., and Searle, R.C., 2012, Slow-Spreading Oceanic Crust Formed By Steady-State Axial Volcanic Ridges [Abstract]: AGU Fall Meeting, San Francisco, #OS13B-1723.
- Navin, D.A., Peirce, C., and Sinha, M.C., 1998, The RAMESSES experiment - II. Evidence for accumulated melt beneath a slow spreading ridge from wide-angle refraction and multichannel reflection seismic profiles: *Geophysical Journal International*, v. 135, p. 746–772, doi: 10.1046/j.1365-246X.1998.00709.x.
- Pałgan, D., Devey, C.W., and Yeo, I.A., 2016, Dike control of hydrothermal circulation in the Tertiary Icelandic crust and implications for cooling of the seafloor: *Journal of Volcanology and Geothermal Research*, v. 316, p. 22–33, doi: 10.1016/j.jvolgeores.2016.02.021.
- Palmason, G., Johnsen, G. V., Torfason, H., Sæmundsson, K., Ragnars, K., and Haraldsson, G. I. Halldorsson, G.K., 1985, Geothermal resource assessment for Iceland (in Icelandic), Orkustofnun Report OS-85076/JHD-10, Reykjavík, pp. 134.
- Palmason, G., and Sæmundsson, K., 1974, Iceland in relation to the mid-atlantic ridge: *Annual Review of Earth and Planetary Sciences*, v. 2, p. 25–50, doi: 10.1146/annurev.earth.02.050174.000325.
- Parnell-Turner, R.E., White, N.J., Maclennan, J., Henstock, T.J., Murton, B.J., and Jones, S.M., 2013, Crustal manifestations of a hot transient pulse at 60°N beneath the Mid-Atlantic Ridge: *Earth and Planetary Science Letters*, v. 363, p. 109–120, doi: 10.1016/j.epsl.2012.12.030.
- Parson, L.M., Murton, B.J., Searle, R.C., Booth, D., Evans, J., Field, P., Keeton, J., Laughton, A., McAllister, E., Millard, N., Redbourne, L., Rouse, I., Shor, A., Smith, D., et al., 1993, En echelon axial volcanic ridges at the Reykjanes Ridge: a life cycle of volcanism and tectonics: *Earth and Planetary Science Letters*, v. 117, p. 73–87, doi: 10.1016/0012-821X(93)90118-S.
- Pedersen, G.B.M., Höskuldsson, A., Dürig, T., Thordarson, T., Jónsdóttir, I., Riishuus, M.S., Óskarsson, B.V., Dumont, S., Magnusson, E., Gudmundsson, M.T., Sigmundsson, F., Drouin, V.J.P.B., Gallagher, C., Askew, R., Guðnason, J., Moreland, W.M., P. Nikkola, P., Reynolds, H.I., Schmith, J. and the IES eruption team, 2017, Lava field evolution and emplacement dynamics of the 2014–2015 basaltic fissure eruption at Holuhraun, Iceland:

- Journal of Volcanology and Geothermal Research, In Press, doi: 10.1016/j.jvolgeores.2017.02.027.
- Peirce, C., Gardiner, A., and Sinha, M., 2005, Temporal and spatial cyclicity of accretion at slow-spreading ridges-evidence from the Reykjanes Ridge: *Geophysical Journal International*, v. 163, p. 56–78, doi: 10.1111/j.1365-246X.2005.02738.x.
- Peirce, C., and Sinha, M.C., 2008, Life and death of axial volcanic ridges: Segmentation and crustal accretion at the Reykjanes Ridge: *Earth and Planetary Science Letters*, v. 274, p. 112–120, doi: 10.1016/j.epsl.2008.07.011.
- Perfit, M.R., and Chadwick, Jr., W.W., 1998, Magmatism at mid-ocean-ridges: constraints from volcanological and geochemical investigations, In: Buck, W.R., Delaney, P.T., Karson, J.A., and Lagabriele, Y. [Eds.], *Faulting and Magmatism at Mid-Ocean Ridges*, American Geophysical Union, Washington D.C., p. 59–116, doi: 10.1029/GM106p0059.
- Perfit, M.R., and Davidson, J.P., 1999, Plate Tectonics and Volcanism, In: Sigurdsson, H. [Ed.], *Encyclopedia of volcanoes*, Academic Press, p. 89–113.
- Petersen, S., Kuhn, K., Kuhn, T., Augustin, N., Hékinian, R., Franz, L., and Borowski, C., 2009, The geological setting of the ultramafic-hosted Logatchev hydrothermal field (14°45'N, Mid-Atlantic Ridge) and its influence on massive sulfide formation: *Lithos*, v. 112, p. 40–56, doi: 10.1016/j.lithos.2009.02.008.
- Phipps Morgan, J., and Chen, J.Y., 1993, The genesis of oceanic crust: Magma injection, hydrothermal circulation, and crustal flow: *Journal of Geophysical Research: Solid Earth*, v. 98, p. 6283–6297, doi: 10.1029/92JB02650.
- Pirajno, F., 2009, Hydrothermal Processes and Wall Rock Alteration, In: Pirajno, F. [Ed.], *Hydrothermal Processes and Mineral Systems*: Springer Netherlands, Amsterdam, p. 73–163, doi: 10.1007/978-1-4020-8613-7\_2.
- Poore, H.R., White, N., and Jones, S., 2009, A Neogene chronology of Iceland plume activity from V-shaped ridges: *Earth and Planetary Science Letters*, v. 283, p. 1–13, doi: 10.1016/j.epsl.2009.02.028.
- Qin, R., and Buck, W.R., 2008, Why meter-wide dikes at oceanic spreading centers?: *Earth and Planetary Science Letters*, v. 265, p. 466–474, doi: 10.1016/j.epsl.2007.10.044.
- Rögnvaldsson, S.T., Gudmundsson, A., and Slunga, R., 1998, Seismotectonic analysis of the Tjornes Fracture Zone, an active transform fault in north Iceland: *Journal of Geophysical Research: Solid Earth*, v. 103, p. 30117–30129, doi: 10.1029/98JB02789.
- Rona, P., Klinkhammer, G., Nelsen, T.A., Trefry, J.H., and Elderfield, H., 1986, Black smokers, massive sulphides and vent biota at the Mid-Atlantic Ridge: *Nature*, v. 321, p. 33–37, doi: 10.1038/321033a0.
- Rubin, K.H., 2014, Mid-Ocean Ridge Magmatism and Volcanism, In: Harff, J., Meschede, M., Petersen, S., and Thiede, J. [Eds.], *Encyclopedia of Marine Geosciences*, p.1-21, Springer-Verlag Berlin Heidelberg. DOI: 10.1007/978-94-007-6644-0\_28-3.

- Rubin, K.H., and Sinton, J.M., 2007, Inferences on mid-ocean ridge thermal and magmatic structure from MORB compositions: *Earth and Planetary Science Letters*, v. 260, p. 257–276, doi: 10.1016/j.epsl.2007.05.035.
- Rubin, K.H., Soule, S.A., Chadwick, Jr., W.W., Fornari, D.J., Clague, D.A., Embley, R.W., Baker, E.T., Perfit, M.R., Caress, D.W., and Dziak, R.P., 2012, Volcanic Eruptions in the Deep Sea: *Oceanography*, v. 25, p. 142–157, doi: 10.5670/oceanog.2012.12.
- Sæmundsson, K., 1963, Das Alter des Ausbruches von Nesjahraun, SW-Island: *Naturufraedingurinn*, v. 33, p. 41.
- Sæmundsson, K., 1978, Fissure swarms and central volcanoes of the neovolcanic zones in Iceland, In: Bowes D.R., Leake, B.E. [Eds.], *Crustal evolution in NW Britain and adjacent regions: Geological Journal Special Issue*, v. 10, p. 415–432.
- Sæmundsson, K., 1979, Outline of the geology of Iceland: *Jökull*, v. 29, p. 7–28.
- Sandwell, D.T., Müller, R.D., Smith, W.H.F., Garcia, E., and Francis, R., 2014, New global marine gravity model from CryoSat-2 and Jason-1 reveals buried tectonic structure: *Science*, v. 346, p. 65–67, doi: 10.1126/science.1258213.
- Sandwell, D., and Smith, W.H.F., 1997, Marine gravity from Geosat and ERS-1 altimetry: *Journal of Geophysical Research*, v. 102, p. 10039–10054, doi: 10.1029/96JB03223.
- Searle, R.C., Field, P.R., and Owens, R.B., 1994, Segmentation and nontransform ridge offset on the Reykjanes Ridge near 58°N: *Journal of Geophysical Research*, v. 99, p. 159–172, doi: 10.1029/94JB01549.
- Searle, R.C., Keeton, J.A., Owens, R.B., White, R.S., Mecklenburgh, R., and Parsons, B., 1998, The Reykjanes Ridge: structure and tectonics of a hot-spot-influenced, slow-spreading ridge, from multibeam bathymetry, gravity and magnetic investigations: *Earth and Planetary Science Letters*, v. 160, p. 463–478.
- Searle, R.C., and Laughton, A.S., 1981, Fine-scale sonar study of tectonics and volcanism on the Reykjanes Ridge: *Oceanologica Acta, Special Issue (0399-1784)*, p. 5–13.
- Searle, R.C., Murton, B.J., Achenbach, K., LeBas, T., Tivey, M., Yeo, I., Cormier, M.H., Carlut, J., Ferreira, P., Mallows, C., Morris, K., Schroth, N., van Calsteren, P., and Waters, C., 2010, Structure and development of an axial volcanic ridge: Mid-Atlantic Ridge, 45°N: *Earth and Planetary Science Letters*, v. 299, p. 228–241, doi: 10.1016/j.epsl.2010.09.003.
- Sempéré, J.-C., Purdy, G.M., and Schouten, H., 1990, Segmentation of the Mid-Atlantic Ridge between 24°N and 30°40'N: *Nature*, v. 344, p. 427–431, doi: 10.1038/344427a0.
- Sigmundsson, F., 2006, *Iceland Geodynamics: Crustal Deformation and Divergent Plate Tectonics*: Praxis Publishing Ltd, Chichester, United Kingdom, pp. 247.
- Singh, S.C., Kent, G.M., Collier, J.S., Harding, A.J., and Orcutt, J.A., 1998, Melt to mush variations in crustal magma properties along the ridge crest at the Southern East Pacific Rise: *Nature*, v. 394, p. 874–878, doi: 10.1038/29740.

- Sinha, M.C., Constable, S.C., Peirce, C., White, A., Heinson, G., Macgregor, L.M., and Navin, D.A., 1998, Magmatic processes at slow spreading ridges: implications of the RAMESSES experiment at 57°45'N on the Mid-Atlantic Ridge: *Geophysical Journal International*, v. 135, p. 731–745, doi: 10.1046/j.1365-246X.1998.00704.x.
- Sinton, J.M., and Detrick, R.S., 1992, Mid-Ocean Ridge Magma Chambers: *Journal of Geophysical Research Solid Earth*, v. 97, p. 197–216, doi: 10.1029/91JB02508.
- Smith, D.K., and Cann, J., 1990, Hundreds of small volcanoes on the median valley floor of the Mid-Atlantic Ridge at 24–30° N: *Nature*, v. 348, p. 152–155, doi: 10.1038/348152a0.
- Smith, D.K., and Cann, J., 1992, The role of seamount volcanism in crustal construction and the Mid-Atlantic Ridge (24°–30°N): *Journal of Geophysical Research Solid Earth*, v. 97, p. 1645–1658, doi: 10.1029/91JB02507.
- Smith, D.K., and Cann, J., 1993, Building the crust at the Mid-Atlantic Ridge: *Nature*, v. 365, p. 707–715, doi: 10.1038/365707a0.
- Smith, D.K., and Cann, J., 1998, Mid-Atlantic Ridge Volcanic Processes: how erupting lava forms Earth's anatomy: *Oceanus*, v. 41, p. 11–14.
- Smith, D.K., Cann, J.R., Dougherty, M.E., Lin, J., Spencer, S., Macleod, C., Keeton, J., Mcallister, E., Brooks, B., Pascoe, R., and Robertson, W., 1995a, Mid-Atlantic Ridge volcanism from deep-towed side-scan sonar images, 25°N–29°N: *Journal of Volcanology and Geothermal Research*, v. 67, p. 233–262, doi: 10.1016/0377-0273(94)00086-V.
- Smith, D.K., Humphris, S.E., and Bryan, W.B., 1995b, A comparison of volcanic edifices at the Reykjanes Ridge and the Mid-Atlantic Ridge at 24°–30°N: *Journal of Geophysical Research Solid Earth*, v. 100, p. 22485–22498, doi: 10.1029/95JB02392.
- Spiess, F.N., Macdonald, K.C., Atwater, T., Ballard, R., Carranza, A., Cordoba, D., Cox, C., Garcia, V.M.D., Francheteau, J., Guerrero, J., Hawkins, J., Haymon, R., Hessler, R., Juteau, T., Kastner M, Larson R, Luyendyk B, Macdougall JD, Miller S, Normark W, Orcutt J, Rangin C., 1980, East Pacific Rise: hot springs and geophysical experiments: *Science*, v. 207, p. 1421–1433, doi: 0.1126/science.207.4438.1421.
- Stefánsson, R., Böðvarsson, R., Slunga, R., Einarsson, P., Jakobsdóttir, S., Bungum, H., Gregersen, S., Havskov, J., Hjelme, J., and Korhonen, H., 1993, Earthquake prediction research in the South Iceland Seismic Zone and the SIL project: *Seismol. Soc. Am. Bull.*, v. 83, no. 3, p. 696–716.
- Talwani, M., Windisch, C.C., and Langseth, M.G., 1971, Reykjanes Ridge crest: A detailed geophysical study: *Journal of Geophysical Research*, v. 76, p. 473–577, doi: 10.1029/JB076i002p00473.
- Thorarinsson, S., 1969, The Lakagigar Eruption of 1783: *Bulletin of Volcanology*, v. 33, p. 910–929, doi: 10.1007/BF02596756.
- Torfason, H., 2003a, Geothermal Map of Iceland [Map], 1: 500 000, Náttúruminjasafn Íslands og Orkustofnun, Reykjavík.

- Torfason, H., 2003b, *Jardhitakort af islandi og gagnasafn urn jardhita*, Orkustofnun Report OS-2003/062, Reykjavik, pp. 168.
- Tryggvason, B.Y.E., 1973, Seismicity, earthquake swarms, and plate boundaries in the Iceland region: *Bulletin of the Seismological Society of America*, v. 63, no. 4, p. 1327–1348.
- Vogt, P.R., 1971, Asthenosphere motion recorded by the ocean floor south of Iceland: *Earth and Planetary Science Letters*, v. 13, p. 153–160, doi: 10.1016/0012-821X(71)90118-X.
- Walker, G.P.L., 1974, Eruptive Mechanisms in Iceland, In Kristjánsson, L., [Ed.] *Geodynamics of Iceland and the North Atlantic Area*, NATO, p. 189–201.
- Ward, P.L., 1971, New Interpretation of the Geology of Iceland: *Geological Society of America Bulletin*, v. 82, p. 2991–3012, doi: 10.1130/0016-7606(1971)82[2991:NIOTGO]2.0.CO;2.
- Weir, N.R., White, R.S., Brandsdottir, B., Einarsson, P., Shimamura, H., Shiobara, H., and Team, R.F., 2001, Crustal structure of the northern Reykjanes Ridge and Reykjanes Peninsula, southwest Iceland: *Journal of Geophysical Research*, v. 106, p. 6347–6368, doi: 10.1029/2000JB900358.
- Wheeler, A.J., Murton, B., Copley, J., Lim, A., Carlsson, J., Collins, P., Dorschel, B., Green, D., Judge, M., Nye, V., Benzie, J., Antoniacomi, A., Coughlan, M., and Morris, K., 2013, Moytirra: Discovery of the first known deep-sea hydrothermal vent field on the slow-spreading Mid-Atlantic Ridge north of the Azores: *Geochemistry, Geophysics, Geosystems*, v. 14, p. 4170–4184, doi: 10.1002/ggge.20243.
- White, R.S., 1997, Rift-Plume Interaction in the North Atlantic: *Philosophical Transactions of the Royal Society: A Mathematical, Physical and Engineering Sciences*, v. 355, p. 319–339, doi: 10.1098/rsta.1997.0011.
- Wolfe, C.J., Bjarnason, I.T., VanDecar, J.C., and Solomon, S.C., 1997, Seismic structure of the Iceland mantle plume: *Nature*, v. 385, p. 245–247, doi: 10.1038/385245a0.
- Wright, D.J., 1998, Formation and Development of Fissures at the East Pacific Rise: Implications for Faulting and Magmatism at Mid-Ocean Ridges, *in* Buck, W.R., Delaney, P.T., Karson, J.A., and Lagabriele, Y. eds., *Faulting and Magmatism at Mid-Ocean Ridges*, American Geophysical Union, Washington D.C., p. 137–152.
- Wright, D., and Miller, G., 1996, Control of North Atlantic Deep Water Circulation by the Greenland-Scotland Ridge: *Paleoceanography*, v. 11, p. 157–170, doi: 10.1029/95PA03696.
- Yeo, I.A., 2014, Axial Volcanic Ridges, In: Harff, J., Mesched, M., Petersen, S., and Thiede, J. [Eds.], *Encyclopedia of Marine Geosciences*, Springer Netherlands, p. 36–39, doi: 10.1007/978-94-007-6238-1\_2.
- Yeo, I.A., 2012, Detailed studies of mid-ocean ridge volcanism at the Mid-Atlantic Ridge (45°N) and elsewhere, [PhD Thesis], Durham University, United Kingdom, pp. 299.

- Yeo, I. A., Clague, D. A., Martin, J.F., Paduan, J.B., and Caress, D.W., 2013, Preeruptive flow focussing in dikes feeding historical pillow ridges on the Juan de Fuca and Gorda Ridges: *Geochemistry, Geophysics, Geosystems*, v. 14, p. 3586–3599, doi: 10.1002/ggge.20210.
- Yeo, I.A., Devey, C.W., LeBas, T.P., Augustin, N., and Steinführer, A., 2016, Segment-scale volcanic episodicity: Evidence from the North Kolbeinsey Ridge, Atlantic: *Earth and Planetary Science Letters*, v. 439, p. 81–87, doi: 10.1016/j.epsl.2016.01.029.
- Yeo, I.A., and Searle, R.C., 2013, High-resolution Remotely Operated Vehicle (ROV) mapping of a slow-spreading ridge: Mid-Atlantic Ridge 45°N: *Geochemistry, Geophysics, Geosystems*, v. 14, p. 1693–1702, doi: 10.1002/ggge.20082.
- Yeo, I.A., Searle, R.C., Achenbach, K.L., Le Bas, T.P., and Murton, B.J., 2012, Eruptive hummocks: Building blocks of the upper ocean crust: *Geology*, v. 40, p. 91–94, doi: 10.1130/G31892.1.



# Chapter 2

Field seasons

## **2. Field seasons**

### **2.1. Introduction**

Iceland is one of the few locations on Earth where a section of mid-ocean ridge is exposed above sea level, apparently as the result of excess magmatism resulting from the presence of a hot spot in the mantle (see Chapter 1). Similar phenomena can be observed in other parts of the world, for example the East African Rift system, a section of the Main Ethiopian Rift (Bonini et al., 2005). This surface exposure gives a unique opportunity to study geological processes occurring at a divergent plate boundary.

To determine the exact movement of tectonic plates in Iceland, the Icelandic Meteorological Office (IMO) created a network of Global Positioning System (GPS) stations for constant monitoring of crustal motion and deformation in Iceland (e.g., Geirsson et al., 2000). However, since 1968 and before this network was established, direct and short-term GPS measurements were carried out by numerous researchers (e.g., Foulger et al., 1987; Hackman et al., 1990; Jahn, 1990; Sigmundsson et al., 1992; Camitz et al., 1995; Heki et al., 1993; Sturkell et al., 1994; Sigmundsson et al., 1995; Hreinsdóttir et al., 2001). Results of their studies show that spreading rates in numerous locations along the plate boundary in Iceland agree to a large extent with velocities predicted by plate motion models such as NUVEL-1A, introduced by DeMets et al. (1990). This and many other facts and observations (e.g., rock types, geomorphology, tectonics, seismicity or geothermal activity) justify the general assumption that geological processes associated with active spreading both in Iceland and at the adjacent seafloor are similar to each other. Therefore, widespread direct observations across Iceland permit a closer look into the geological controls of hydrothermal activity at an active plate boundary of the northern Mid-Atlantic Ridge.

#### **2.1.1. Why observations on land?**

The primary aim of this study is to better understand the geological control of seafloor hydrothermal activity and to determine its tectonic and volcanological framework within the North Atlantic Ocean. Field work in Iceland provides direct observations of Icelandic hot springs as onshore analogues for seafloor hydrothermal vents. Onshore observations of hot springs provide reliable information about the relationship between hydrothermal manifestations and their geological background. With the ability to carry out research on land, it is possible to obtain high-resolution information about the local scale geological features that control the occurrence of the hot springs locations. Despite the harsh Icelandic

environment (with rough terrain, unpredictable weather and remoteness of many sites), its reduced vegetation and lack of wild life make it preferable to areas such as the Main Ethiopian Rift, where the tropical environmental factors significantly impeded field observations (e.g., Russel-Smith, 1984).

## **2.2 Field season 2013**

During this field season, direct observations of geothermal systems on Iceland allowed classification of them as either high- or low-temperature systems, according to Arnórsson et al. (2008). However, because the research area chosen for this fieldwork (Westfjords) is located so far from the neovolcanic zone (~150 km NW), mostly low-temperature springs were expected to be encountered (see also Chapter 1). Fieldwork allowed collection and description of physical characteristics of observed manifestations, such as sizes of particular hot springs and extend of ground area affected by their presence (e.g., extent of surface alteration). Most importantly, fieldwork allowed recognition of the local and small scale geological structures in the direct vicinities of particular hot springs, which appear to control their locations and support circulation of the fluid, i.e., volcanic cones, lava flows and lava flows boundaries, faults, fissures, dikes, plus cross-cutting between two or more of such features. Overall, on land observations in Westfjords significantly helped to acquire in situ 3D information and the direct visualization of relationships between geological features (including topography and cross-correlations between the geological features) that control the locations of hot springs. The results obtained from this fieldwork could be used to identify similar structures on adjacent seafloor off the coast of Iceland (and possibly other mid-ocean ridges) by using appropriate off-shore survey methods.

This fieldwork had three main goals:

- To catalogue as many off-axis, naturally occurring hot springs in Iceland as possible and to relate them to their volcano-tectonic framework.
- To acquire first-hand skills in 3D visualization of relationships between geological structures in a slow-spreading ridge environment and the influence on the off-axis hydrothermal circulation.
- To determine the volcano-tectonic controls of the mapped hot springs in order to develop a predictive model of the occurrence of new potential hydrothermal vents mainly along off-axis regions of the Reykjanes Ridge (south of Iceland).

## 2.2.1 Methods

### 2.2.1.1 *Pre-fieldwork preparation*

Overall, the pre-fieldwork involved:

- Acquisition of existing topographic, geomorphological and geological maps of Iceland.
  - Due to different scales (from general, large-scale overview maps, e.g., 1:250 000, to small-scale, detailed local maps, e.g., 1:10 000) the maps collected had a large range of detail. Later, they had to be ground-truthed in the field.
- Acquisition of all existing and catalogued locations of natural hot springs in Iceland.
  - Precise locations (GPS positions) of hot springs in Iceland were critical for planning and picking the main research areas. The locations were obtained from the existing literature thanks to collaboration with Icelandic scientists at the University of Iceland and ÍSOR (Iceland GeoSurvey) (Torfason, 2003a; Torfason, 2003b), and personal communication with the local land owners.
  - Comparison of the aerial images with ground-truthed observations.
- Digitization of all obtained maps of Iceland, logging the precise locations of hot springs from Torfason (2003b), and incorporation of all the data into one digital Global Information Systems (GIS) project (see section 2.2.1.4).
  - Digitalization of the geological maps and locations of the hot springs using ArcGIS 10.1 software (see section 2.2.1.4).
  - Targeting areas of interest for the first field season.
- Acquisition of freely available satellite images (mostly Google Earth<sup>TM</sup>) of the areas selected for further investigations in the field.

### 2.2.1.2 *Acquisition of existing maps of Iceland*

The first step in the fieldwork preparation was to gather existing large- and small-scale topographic and geological maps of Iceland. To investigate the potential volcano-tectonic controls of hydrothermal activity along the axial rift zone in Iceland (ARZ, see Chapter 1), two maps at a scale of 1:100 000 published by ÍSOR and Landsvirkjun were used (Sæmundsson et al., 2010; Sæmundsson et al., 2012). Both maps show the bedrock and main tectonic features and focus on detailed mapping of the youngest, postglacial features. The

geological map of Southwest Iceland (Sæmundsson et al., 2010) is based on numerous local maps ranging in scales from 1:20 000 to 1:50 000. The oldest units presented there are 4 Ma old (Pliocene) while the youngest are lava flows from the youngest historic eruption on the Reykjanes Peninsula (AD 1210–1249). The geological map of the Northern Volcanic Zone (Sæmundsson et al., 2012) is based on several smaller-scale maps of this region and regional observations from the field. The oldest features are of Miocene age and the youngest are from the most recent Krafla fires in 1975–1984.

Unfortunately, there are no detailed, small-scale maps of Westfjords where the main research area is located. Therefore, only a large-scale map (1:250 000) was used for the overview of the geology of that area (Kjartansson, 1969). Hence, the majority of information about the geology of Westfjords available in the literature were small-scale, local investigations (summarized in Geological setting section in Chapter 3), and the investigations carried out in this thesis.

### ***2.2.1.3 Acquisition of catalogued known locations of natural hot springs in Iceland***

For the purposes of this study, the precise location of Icelandic hot springs were taken from the published Geothermal Map of Iceland which is summarized in the Geothermal Database of Iceland report (in Icelandic: Jarðhitakort af Íslandi og gagnasafn um jarðhita) by Torfason (2003b). This report, published by the Museum of Natural History Iceland, is a summary of years of work dedicated to geothermal utilization in Iceland. It presents a database of natural geothermal sites and their relationship with the environment of the island but also points out the geothermal systems that have been drilled, mostly by the Iceland GeoSurvey. The report is divided into two main parts: The first consists of tables containing detailed information about all the catalogued hot springs (including drilled holes), e.g., temperature of the fluids, flows rates and additional information which could help localize them in the field (Fig. 17A), and the second part consists of precise GPS locations of hot springs and drill holes (Fig. 17B) in decimal degrees (DD). This database was used to choose the hot springs which were then visited during the 2013 field season (see section 2.2.2. and Chapter 3).

## VIÐAUKAR

## 1. viðauki. Númer reita og hnit

Reitur	X_COORD	Y_COORD	Arc-Nr				
2001	-21,88330	64,13840	731	2063	-22,69050	63,82030	808
2002	-21,91370	64,14480	405	2064	-22,68670	63,81510	809
2003	-21,93430	64,12620	149	3001	-21,27860	64,38250	157
2004	-21,84300	64,10230	514	3002	-21,29040	64,38850	158
2005	-21,83840	64,11450	404	3003	-21,49660	64,48760	159
2006	-21,76230	64,18730	1001	3004	-21,43170	64,39350	3004
2007	-21,78570	64,12850	151	3005	-21,86220	64,42440	617
2008	-21,79440	64,12200	150	3006	-21,55350	64,63110	741
2009	-21,54330	64,17130	487	3007	-21,54820	64,62280	740
2011	-21,76190	64,13050	1008	3008	-21,54290	64,61600	777
2012	-21,73620	64,13300	1	3009	-21,69930	64,53730	616
2013	-21,80730	64,15200	343	3010	-21,40920	64,51680	516
2014	-21,74070	64,16200	2014	3011	-21,31700	64,48960	161
2015	-22,03860	64,09520	1002	3012	-21,26560	64,46900	160
2016	-21,67710	64,15360	707	3013	-21,29920	64,45960	5
2017	-21,66640	64,15010	732	3014	-21,32500	64,48030	162
2018	-21,66180	64,15760	733	3015	-21,34280	64,48420	163
2019	-21,67310	64,16040	734	3016	-21,39950	64,50390	1023
2020	-21,65820	64,16540	662	3021	-21,36800	64,54370	664
2021	-21,55670	64,17610	2021	3022	-21,34820	64,54770	14
2023	-21,62470	64,17540	708	3023	-21,32420	64,53160	766
2024	-21,61080	64,17390	735	3024	-21,20530	64,50870	519
2025	-21,69930	64,20710	595	3025	-21,18960	64,50310	663
2026	-21,77250	64,21560	2	3026	-21,17690	64,49450	736
2028	-21,42780	64,22590	3	3027	-21,16920	64,49810	709
2029	-22,00580	64,15910	2029	3028	-21,15020	64,49040	515
2030	-21,38970	64,25030	4	3029	-21,14620	64,48490	1021
2031	-21,38100	64,35860	153	3030	-21,12370	64,47630	9
2032	-21,28730	64,36450	486	3031	-21,11990	64,48680	11
2033	-21,30830	64,36550	155	3032	-21,12670	64,47110	8
2034	-21,28620	64,35570	154	3033	-21,13000	64,46400	7
2035	-21,47900	64,29340	152	3035	-21,09800	64,45060	3035
2037	-21,25450	64,37410	485	3036	-21,08570	64,45200	164
2039	-21,56910	64,37400	2039	3037	-21,16080	64,53530	408
2040	-22,19690	63,88820	814	3038	-21,17500	64,53060	167
2041	-22,10510	63,92940	815	3039	-21,12820	64,53360	615
2042	-22,12490	63,93580	816	3040	-21,14270	64,52600	13
2043	-22,09080	63,94640	817	3041	-21,15980	64,52000	518
2044	-22,04290	63,93740	818	3042	-21,09960	64,51100	407
2045	-22,08480	63,88950	819	3043	-21,08110	64,52090	12
2046	-22,09410	63,90200	820	3044	-21,49140	64,64990	666
2047	-22,07410	63,89510	821	3045	-21,48570	64,64380	710
2048	-22,06310	63,89170	822	3046	-21,48310	64,63480	778
2049	-22,04180	63,90150	823	3047	-21,46910	64,64070	738
2050	-22,01890	63,90550	824	3048	-21,47040	64,63200	18
2051	-21,99560	63,91050	825	3049	-21,41280	64,66410	776
2052	-21,98500	63,92380	826	3050	-21,39890	64,65850	775
2053	-22,09460	63,95380	1004	3051	-21,43450	64,66310	19
2054	-22,13960	63,91820	1005	3052	-21,42990	64,65800	711
2055	-22,03600	63,89040	1006	3053	-21,37730	64,66910	773
2056	-21,50490	64,16870	2056	3054	-21,36120	64,66620	772
2057	-21,55720	64,16020	2057	3055	-21,36960	64,66010	774
2058	-22,67340	63,82160	810	3056	-21,32290	64,65740	771
2059	-22,69950	63,81360	1003	3057	-21,28210	64,66620	769
2060	-22,52680	63,86000	811	3058	-21,28310	64,65790	770
2061	-22,44640	63,87500	812	3059	-21,24420	64,66970	525
2062	-22,42880	63,87970	813	3060	-21,24780	64,66300	409
				3061	-21,22270	64,65770	174



B

Hr.nr	AræNR	Hinnab	Reitar	Þypping	Þypping- eðrar	Bær (eyðibýti)	Náfn reits	Ormeini-stak	Staðarlýsing	Háðiti	mxHiti	l/s	Athugasemdir	Heimildir
0						GULLRINGU- og KJOSARSÝSLA								
0	731	1	2001	2001-00		Laugarnes	Laugarnes				89	10.55		
0			2001	2001-01	G-00	Laugarnes	Laugarnes				88	10.55	Rennsli mælt; (Hítav; Rvk.) hvarf 1966	Ben Grönd. 1926
0			2001	2001-01	G-00	Laugarnes					88	10.55		Ben Grönd. 1927
0			2001	2001-01	G-00	Laugarnes					86		ekki getið hita, not til baða, bornað nóður á 13.7 fet	C. Ostentfeld (1899)
0			2001	2001-01	G-00	Laugarnes		Hverinn					nokkrar laugar, notað til baða og fatapvottar, kort	Eggert og Bjarni (1943)
0			2001	2001-01	G-00	Laugarnes					87		efnasýni	Holland 1960
0			2001	2001-01	G-00	Laugarnes					86		efnasýni	Jarðboranir rik.
0			2001	2001-01	G-00	Laugarnes					83		skv. staðarmæfni	Jarðboranir rik. 1951
0			2001	2001-01	G-00	Laugarnes					83		nytt til þvotta, suðu fiðks-þjós, baða	Landnáma (um 1200)
0			2001	2001-01	G-00	Laugarnes					87		ekki getið hitasta laugin, nokkrar laugar	Landnáma (1836)
0			2001	2001-01	G-00	Laugarnes					88		3 stöðir, 86.7, 88.3 og 89.4°C, lík af-b	Muckenzie 1811
0			2001	2001-01	G-00	Laugarnes					89		n. þvotur, 4 laugar, sú vestasta bernst og vatnsmest	Stanley (1979)
0			2001	2001-01	G-00	Laugarnes					89		ekki getið hita	Steenstrup (1840)
0			2001	2001-01	G-00	Laugarnes					89		líklega ekki heitasta laugin, nokkrar laugar	Steenstrup 1846
0			2001	2001-01	G-00	Laugarnes					57		líklega ekki heitasta laugin, nokkrar laugar	Sveinn Fálsson (1945)
0			2001	2001-01	G-00	Laugarnes					89		líklega ekki heitasta laugin, nokkrar laugar	Uno v. Troil (1961)
0			2001	2001-01	G-00	Laugarnes					89		líklega ekki heitasta laugin, nokkrar laugar	Þ.Th 1910a; b
0			2001	2001-01	G-00	Laugarnes					89		líklega ekki heitasta laugin, nokkrar laugar	Þork. A. Vidalin
0			2001	2001-01	G-00	Laugarnes					89		líklega ekki heitasta laugin, nokkrar laugar	Þork.P. 1928
0			2001	2001-01	G-00	Laugarnes					0		líklega ekki heitasta laugin, nokkrar laugar	Þorsteinn Thorsteinn OS (víðk. 1993).
0			2001	2001-01	G-00	Laugarnes					88.8		líklega ekki heitasta laugin, nokkrar laugar	Þ.P. 1928
0			2001	2001-01	G-00	Laugarnes					75	1.20	líklega ekki heitasta laugin, nokkrar laugar	Ben Grönd. 1927
0			2001	2001-02	G-067	Laugarnes					75	0.60	líklega ekki heitasta laugin, nokkrar laugar	Ben Grönd. 1926
0			2001	2001-02	G-067	Laugarnes					65		líklega ekki heitasta laugin, nokkrar laugar	Sveinn Fálsson (1945)
0			2001	2001-02	G-067	Laugarnes					75		líklega ekki heitasta laugin, nokkrar laugar	Þork.P. 1928
0			2001	2001-02	G-067	Laugarnes					60		líklega ekki heitasta laugin, nokkrar laugar	Þ.P. 1928
0	405	1	2002	2002-00		Rauðará	(Rauðará)		enn súð-austur af aðalhver fjarn sjó		30		líklega ekki heitasta laugin, nokkrar laugar	
0			2002	2002-01	G-02	Rauðará					30		líklega ekki heitasta laugin, nokkrar laugar	Þ.P. 1928
0	149	1	2003	2003-00		Rauðará	Oskjahlíð		V hlúð; 20 m SV af rett fjarn sjó		11.5		líklega ekki heitasta laugin, nokkrar laugar	Þ.P. 1928
0			2003	2003-00	G-04	Rauðará	Oskjahlíð		V hlúð; 20 m SV af rett fjarn sjó		11.5		líklega ekki heitasta laugin, nokkrar laugar	Þ.P. 1928
0			2003	2003-00	G-04	Rauðará	Oskjahlíð		V hlúð; 20 m SV af rett fjarn sjó		10.7		líklega ekki heitasta laugin, nokkrar laugar	Þ.P. 1928
0	514	1	2004	2004-00		Breiholt	Breiholt		NV bejar		40		líklega ekki heitasta laugin, nokkrar laugar	
0			2004	2004-01	G-05	Breiholt			NV bejar		30.0		líklega ekki heitasta laugin, nokkrar laugar	Atv.Hil 1966
0			2004	2004-01	G-05	Breiholt			NV bejar		31		líklega ekki heitasta laugin, nokkrar laugar	Helgi Sigurðsson 1931
0			2004	2004-01	G-05	Breiholt			Næst bæ		40		líklega ekki heitasta laugin, nokkrar laugar	OS 85

Fig. 17 Examples of the Iceland GeoSurvey database containing precise locations of all known natural and drilled hot springs in Iceland. (A) GPS coordinates given in decimal degrees (DD); (B) Main information about the hot springs, such as the name of the region where it is located (Bær), maximum measured temperature (mxHiti) or flow rates (l/s). From Torfason (2003b).

### 2.2.1.4 Digitization of geological maps and satellite images of Iceland

The digitization of all geological maps of the Reykjanes Peninsula, North Neovolcanic Zone, and the satellite images of Westfjords from Google Earth™ was undertaken early in the project and later combined with the exact locations of known hot springs across Iceland. All acquired data have been combined into a large GIS project, for which the ArcGIS 10.1 software from ESRI was used (Fig. 18). All the maps (Fig. 18) and satellite images (Fig. 19) were rectified in the ArcMap project and then digitized, therefore, creating a database which could be used in the future.

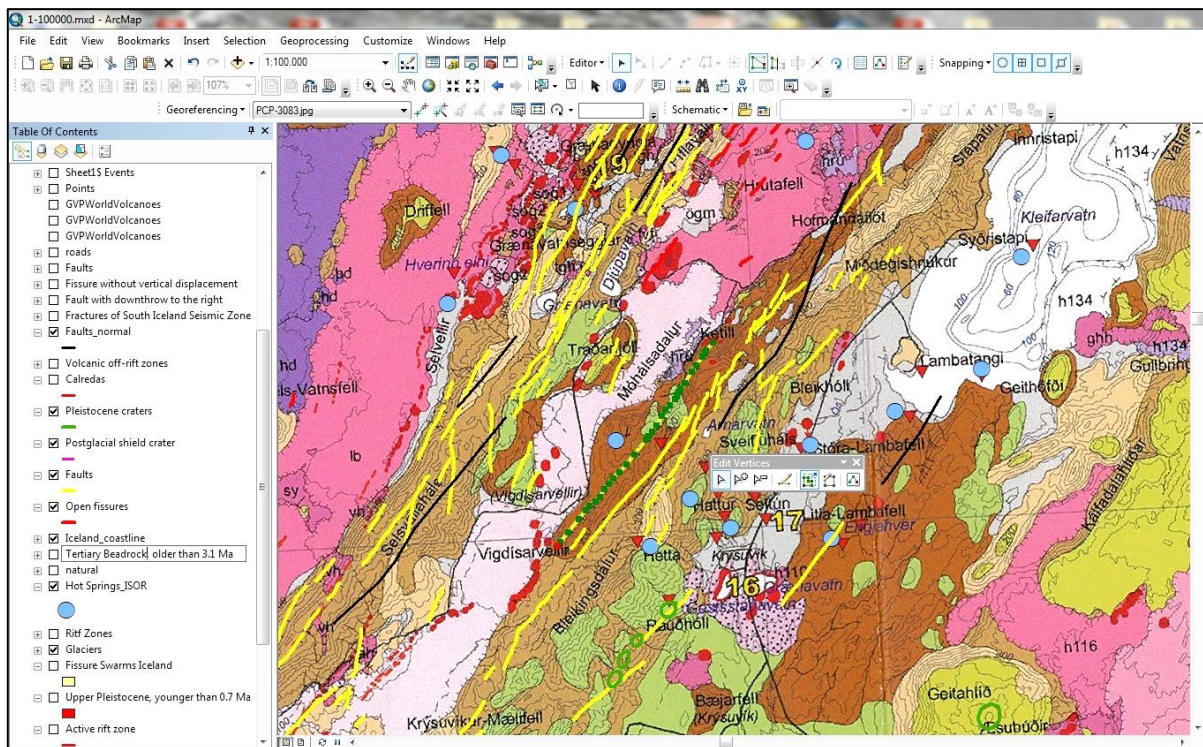


**Fig. 18** Example of digitizing exercise of the geological maps using ArcMap® software. Green boxes in the central part indicate where the digitizing is in process. Black and yellow lines are faults taken from large- and small-scale maps, respectively. Blue dots represent the locations of hot springs taken from Torfason (2003b) and field observations (from this project?). The exact legend of this map can be found on the map published by ISOR (Sæmundsson et al., 2010).



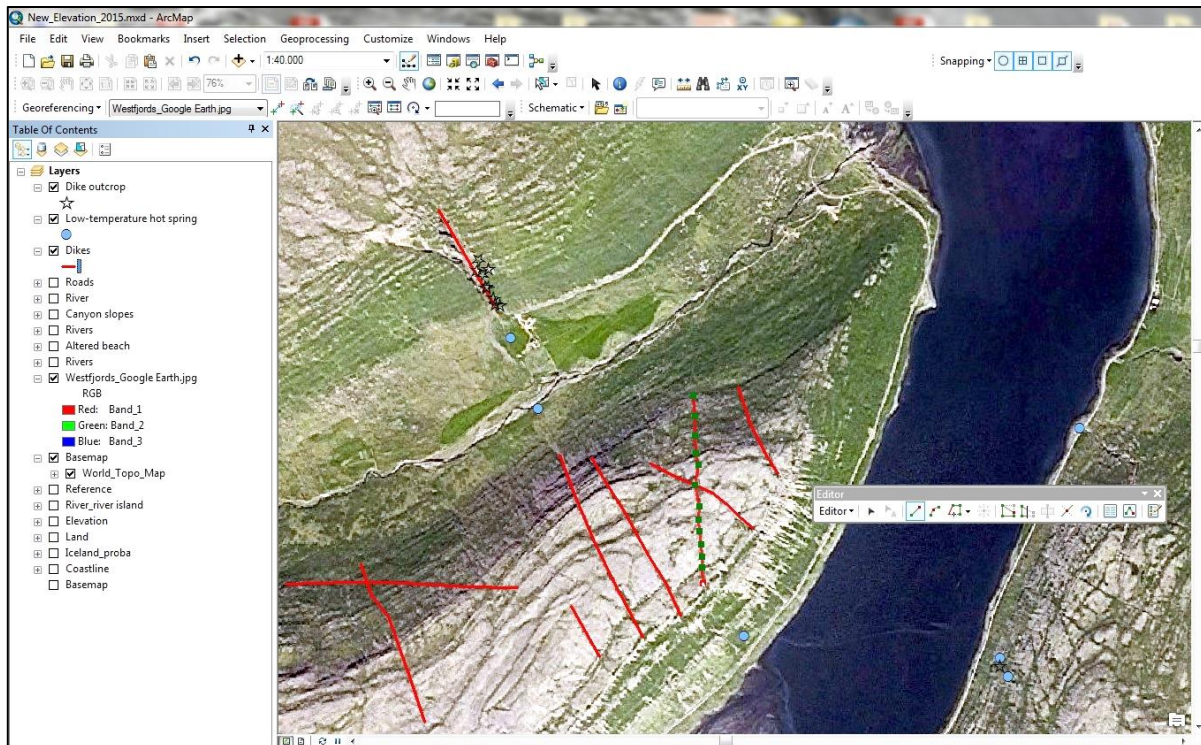


**Fig. 19** Mapping of the lineaments located in the Westfjords (Heydalur valley) using ArcMap® software. Lineaments mapped from the satellite images were recognized in the field as dikes (outcrops marked with open stars). Red lines represent mapped lineaments while blue dots are low-temperature hot springs taken from Torfason (2003b) and field observations from this study.

## 2.2.2 Preliminary results

### 2.2.2.1 Introduction

The Westfjords region is not extensively geologically mapped (e.g., Sæmundsson, 1979) and the reasons for such widespread low-temperature geothermal activity there is still unclear (see Chapter 1). In particular, outstanding geological questions include: 1) what controls the geothermal activity and which geological features host hot springs?; 2) where is the heat supporting the circulation coming from?; and 3) what is the role of these low-temperature sites in the total heat output in Westfjords and potentially Iceland?

More detailed information about the fieldwork and the results (locations of the visited hot springs, mapped dike outcrops, implication for the cooling of the seafloor and role of low-temperature hot springs in the heat budget of Westfjords and Iceland) are presented in Chapter 3 which contains a published manuscript in the *Journal of Volcanology and Geothermal Research*. In the sub-chapters below, some of the preliminary results are presented.

#### 2.2.2.2 Hot springs without visible correlation with geological features

Many of the Westfjords hot springs mapped and observed in the northern region, along the Isafjardardjup fjord, and in southern region, along the Breidafjörður fjord, could not be

correlated with any geological features. This means that no prominent features (e.g., eroded volcanoes, faults or dikes) in their direct vicinity (radius of  $\geq 500$  m) have been observed in both satellite images and field observations. Moreover, some of the hot springs are man-made wells, many of which have been drilled for commercial use (e.g., space heating, electricity production, hot water or leisure) by the local landowners. Other springs percolate down the steep slopes of fjords but appear to be natural in origin (i.e., where not drilled). They are usually overgrown by low vegetation and/or algae, and show silicate precipitation on the surrounding rock fragments. Fjord slopes were climbed as far up as possible to find the source, but no evident outcrops were found in the vicinity. Many manifestations are located along the coastline (beaches) or within the valleys of the fjords. Their origin is unknown, but it appears that many could have been drilled and are now manifested as small ponds and pools. It is very likely that the geological features which could provide information on the controls of such hot springs locations have probably been eroded by, e.g., glaciers and/or fluvio-glacial processes, waves or tides. Finally, in some cases hot springs mentioned in the database did not appear to exist anymore, so have presumably ceased venting. These have not been reported, and therefore, no update in the general database has been made. Therefore, the lack of convincing evidence of geological setting and unknown origin of some of the hot springs (natural versus drilled) resulted in the need for discrimination of them in further investigations. However, it should be stressed that regardless of whether the hot springs whose specific geological settings could not be observed are of natural or man-made origin, they still have an impact on the general heat budget of the Westfjords. It has been shown for these low-temperature hot springs that their heat output may range from 0.002 to 5.83 MW<sub>t</sub>, and all of the hot springs of Westfjords have temperatures <100°C (Torfason, 2003a, Palgan et al., 2016). Moreover, if the on land Icelandic hot springs are analogues for off-shore vents, they should not be neglected in these calculations because low-temperature vent sites could play an important role in the biogeography of the deep-sea ecosystems, acting as distribution stepping stones for larvae dispersal (e.g., Breusing et al., 2015). The locations of these low-temperature hot springs (numbered from 1 to 10) are shown in Fig. 20 and briefly described below.

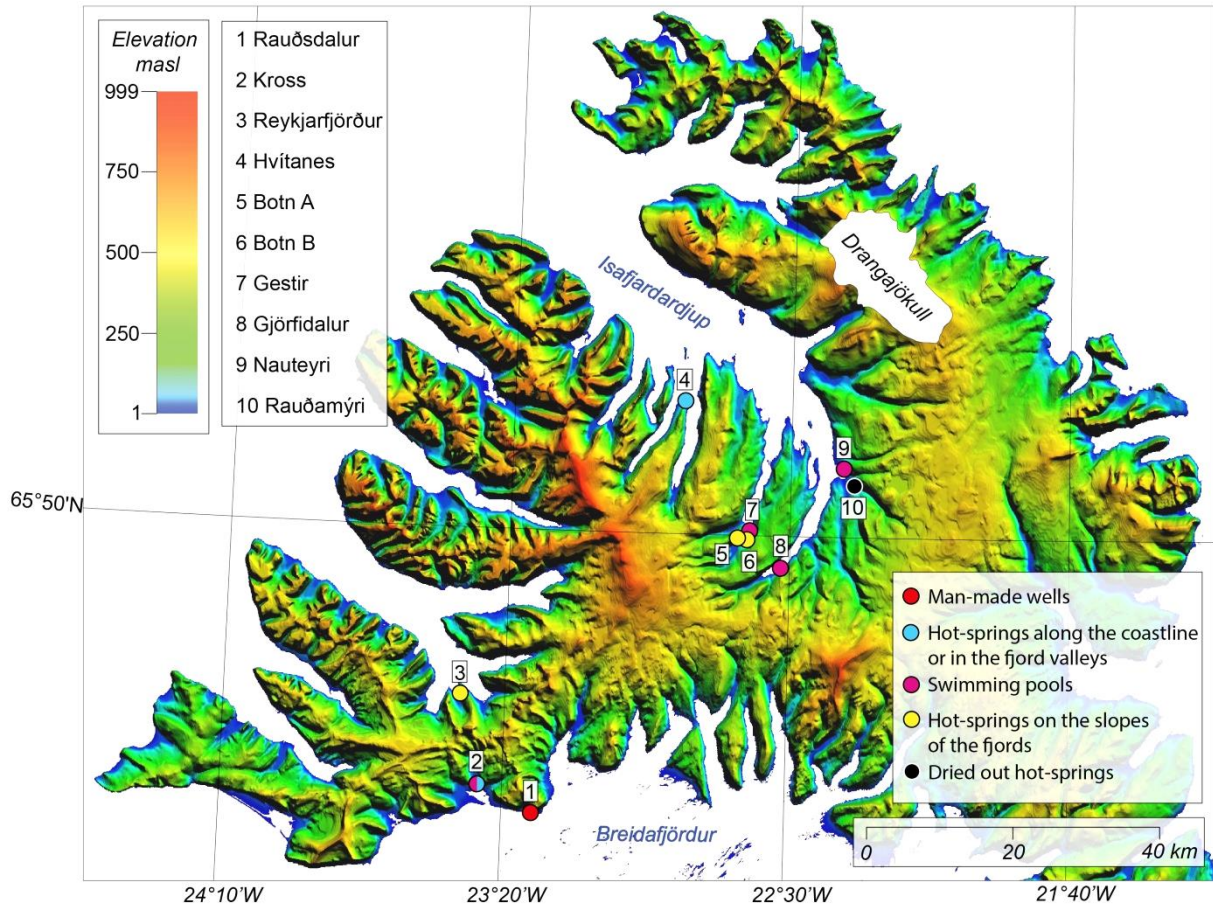
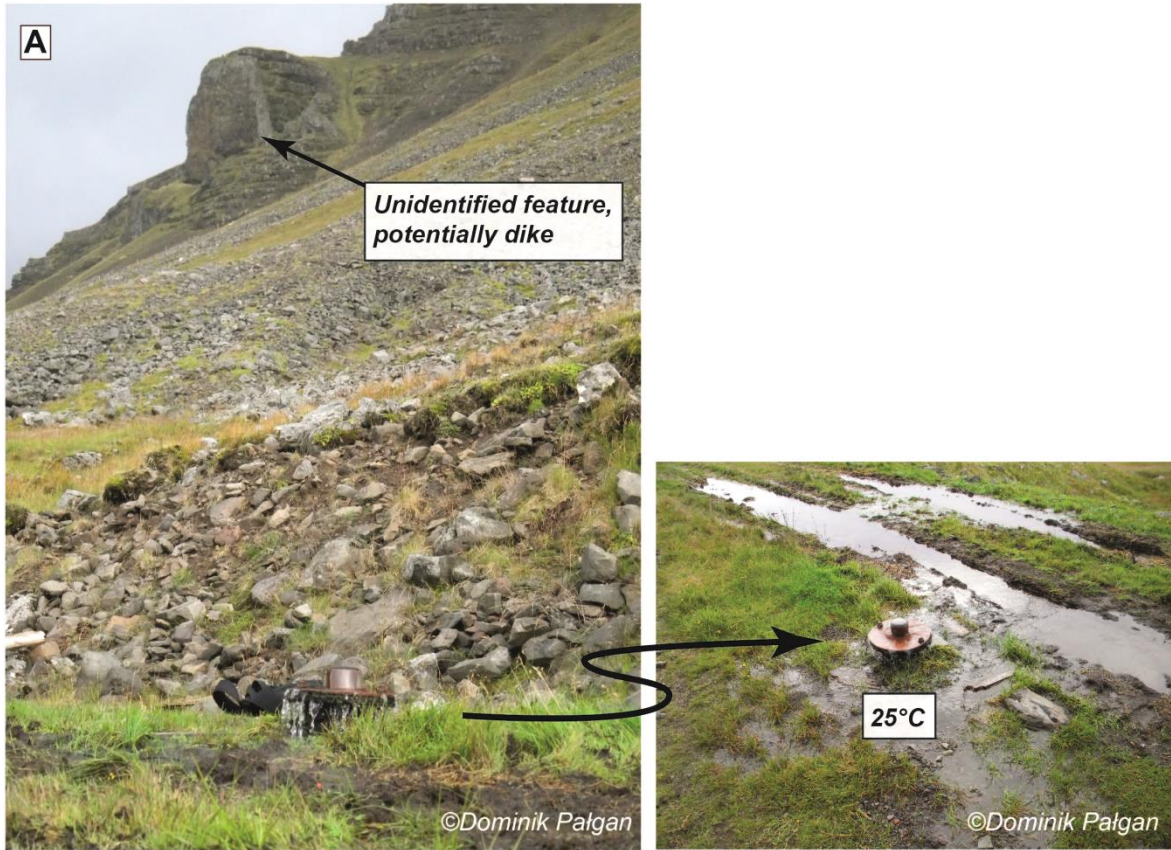


**Fig. 20** Location of some of the hot springs visited during the 2013 field season in Westfjords. They are scattered along the coasts of Breidafjörður and Isafjardardjúp. They represent cases where the correlation with geological features was impossible due to location in highly eroded and/or dynamic environmental settings. Some of the hot springs are man-made wells, of which some have been adopted by the local communities for commercial or leisure use. Some hot springs percolate through the rocks beneath the roads or from the steep slopes of the fjords. One hot spring (#10) was found to be dried up.

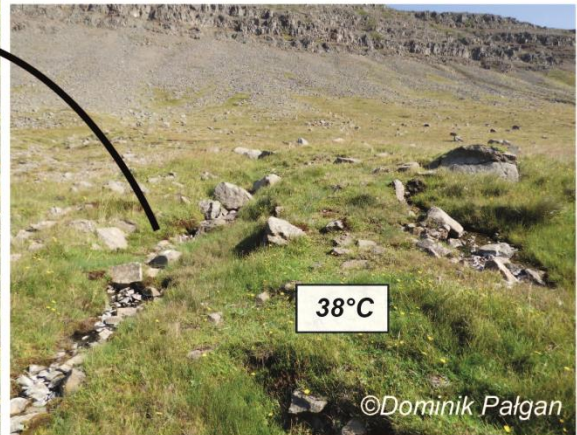
The Rauðsdalur hot spring (1) is a man-made well drilled by the local landowner (Fig. 21A). It is located at the bottom of the steep fjord wall and its maximum measured temperature is 25°C. The hot spring near the village of Kross (2) is located directly by the beach by the Breidafjörður fjord. The history of the spring is unclear; however, currently an old, nearby hot spring is now a ~3 m diameter pond (Fig. 21B). Subsequently, in the same area a small swimming pool has been built using heated water from the same source. The maximum measured temperature in the pond is 38°C. The manifestation in Reykjarfjörður (3) is located on the slope of the fjord (Fig. 21C). The area downslope from the manifestation is overgrown with algae and the surrounding rocks are covered by white silicate precipitation. The maximum measured temperature in this hot spring is 38°C. The hot spring in Hvítanes (4) is located directly on the coast of Isafjardardjúp. This ~30°C hot manifestation percolates through the rock fragments piled up underneath the local road (Fig. 21D). The area is highly overgrown by algae and some of the nearby rock fragments show silicate precipitation when

the tide is low. The Botn hot springs (5) and (6) are both located on the steep slopes of the fjord. Similarly to the Reykjarfjörður hot spring (3), they are overgrown by algae and have silicate precipitation around them. Silicate precipitation and algae can be traced for ~50 m and ~100 m away from the manifestation, down the slope in Botn A (5) and ~ Botn B (6), respectively. The maximum measured temperature in Botn A (Fig. 21E) is 50°C while in Botn B it is 30°C (Fig. 21F). This temperature difference is probably due to the fact that Botn B is located at higher elevation. Heated water has a greater distance to ascend, and more heat is probably being lost during this process along with the conduction of heat with the host basalts. The Gestir hot spring (7) is a manifestation that has been turned into a small swimming pool. It is located on the beach (Fig. 21G) and its maximum measured temperature is 47°C. The Gjörfdalur manifestation (8) is a small ~2 m in diameter pond located at the foot of a fjord's slope (Fig. 21H). Similarly to other springs, it is overgrown by algae and shows silicate precipitation. Its measured temperature is ~43°C. Small canyons observed on fjord slopes in the vicinity of manifestations, often expose faults or dikes (e.g., Heydalur, Chapter 3 or Fig. 5H). However, no outcrops have been observed in this canyon and there are no signs of fault deformation (fault gouge, breccia or a displacement of lava pile). The Nauteyri hot spring (9) is ~3.5 m diameter pond with maximum measured temperatures of 45°C (Fig. 21I). This manifestation flows into a small stream nearby where algae growth typical for these hot springs is also observed. The Rauðamýri hot spring (10) used to be the warmest among all the hot springs listed above (Fig. 21J). Its maximum measured temperature was reported to reach ~64°C. However, currently this hot spring has dried out. The most prominent sign of former activity are the red/orange precipitations of Fe-OOH around the area (Fig. 21J).

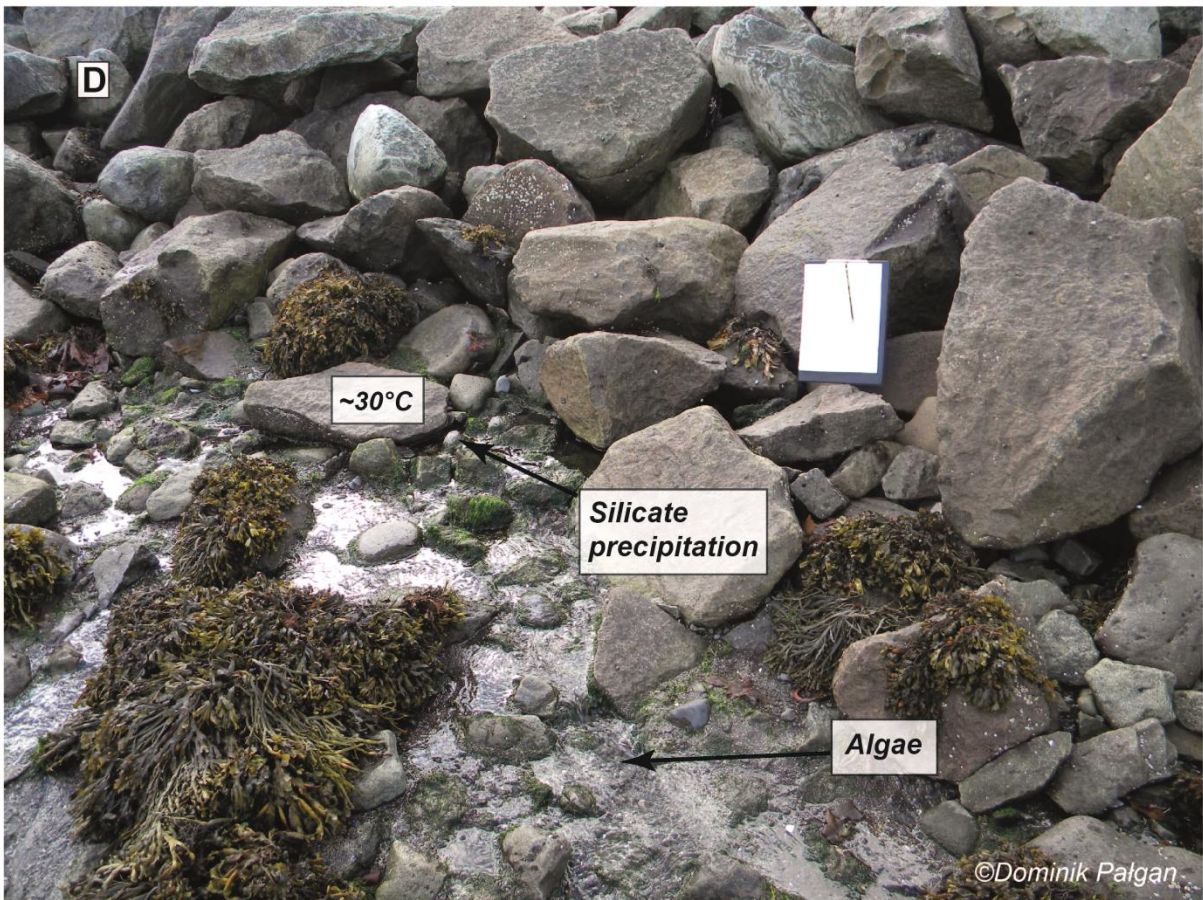




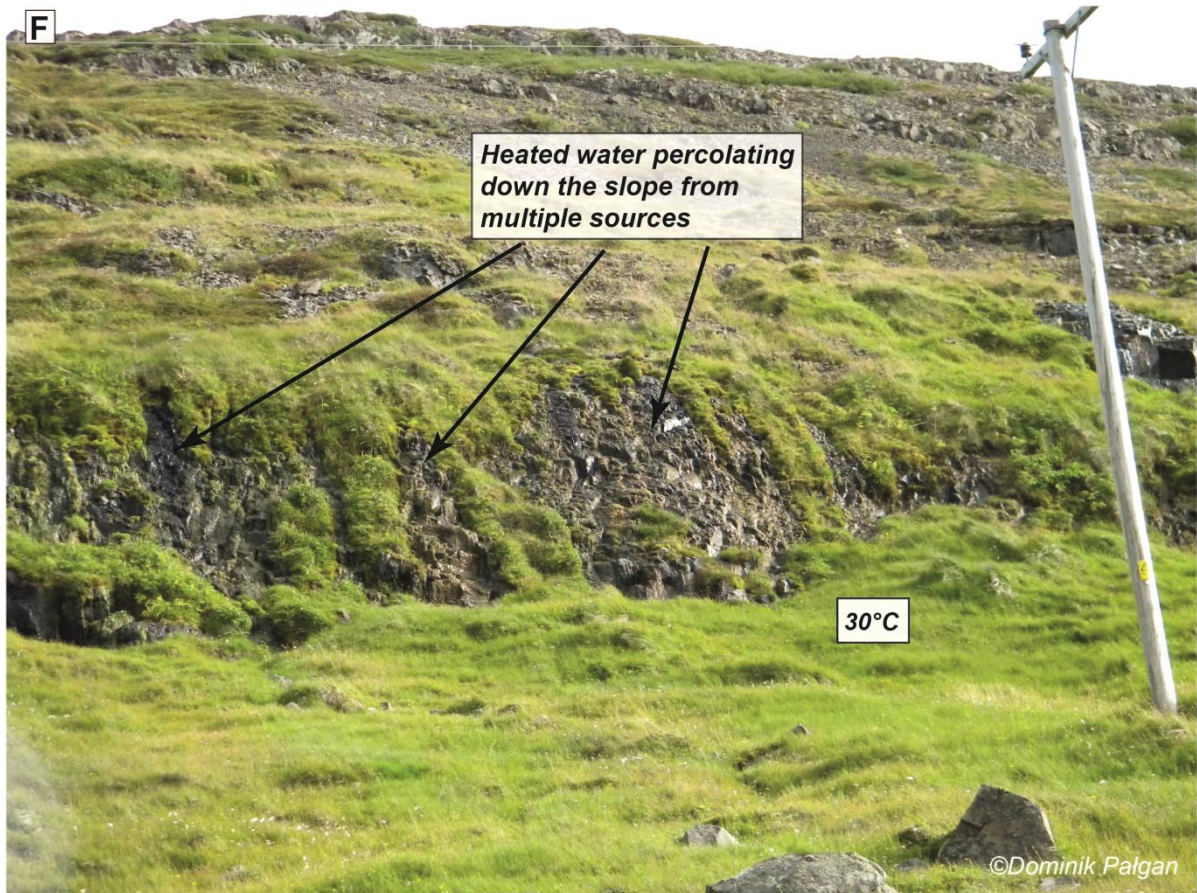
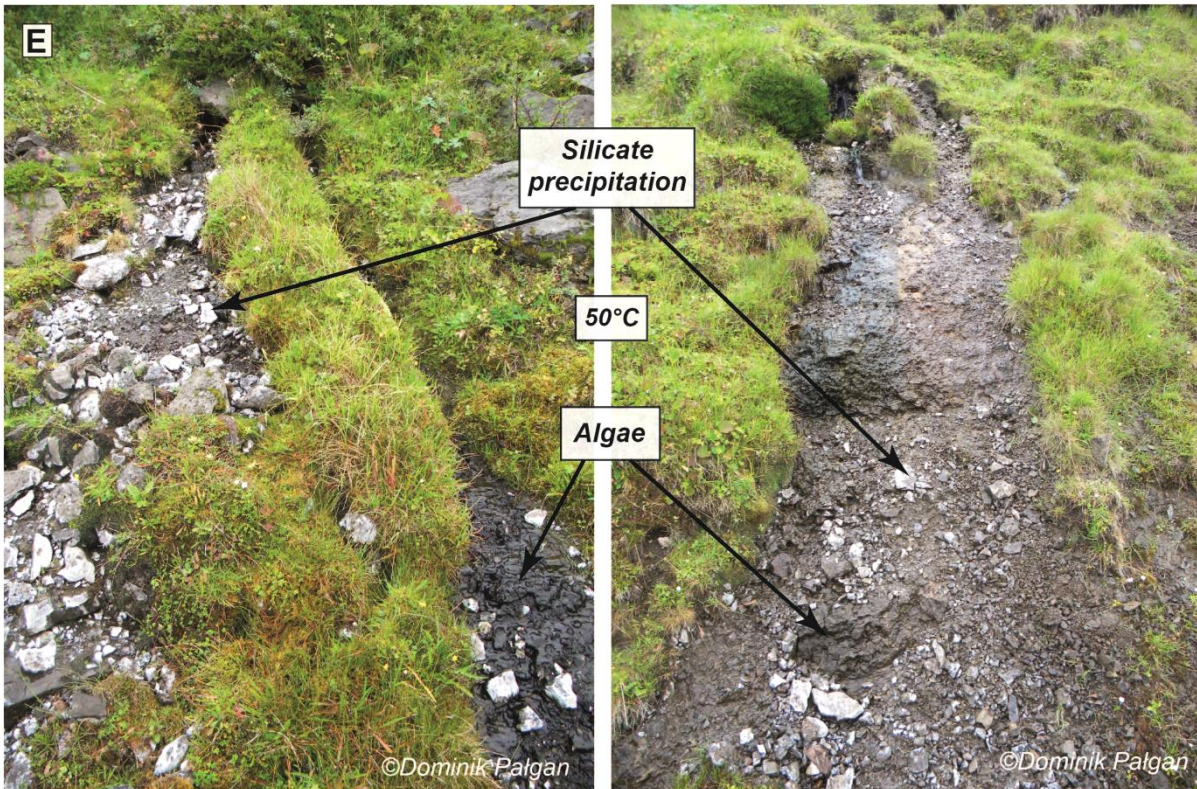




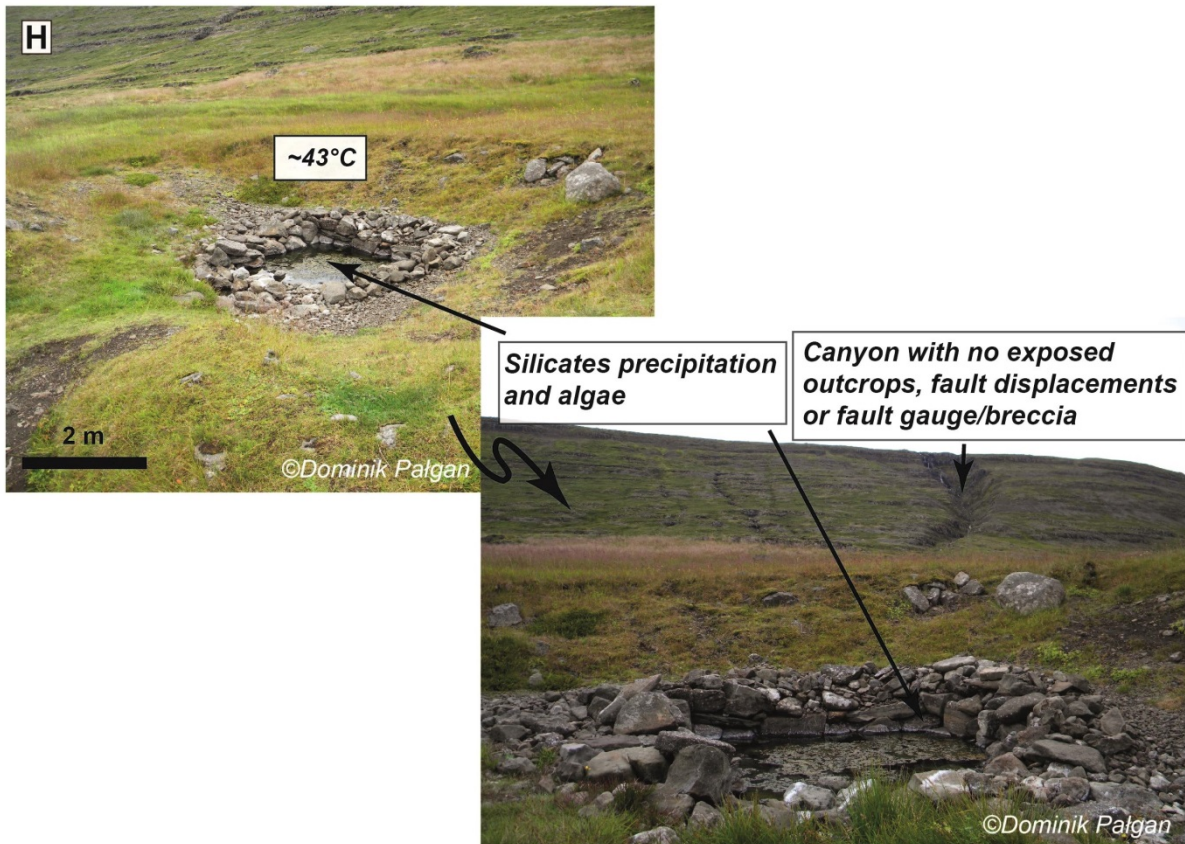
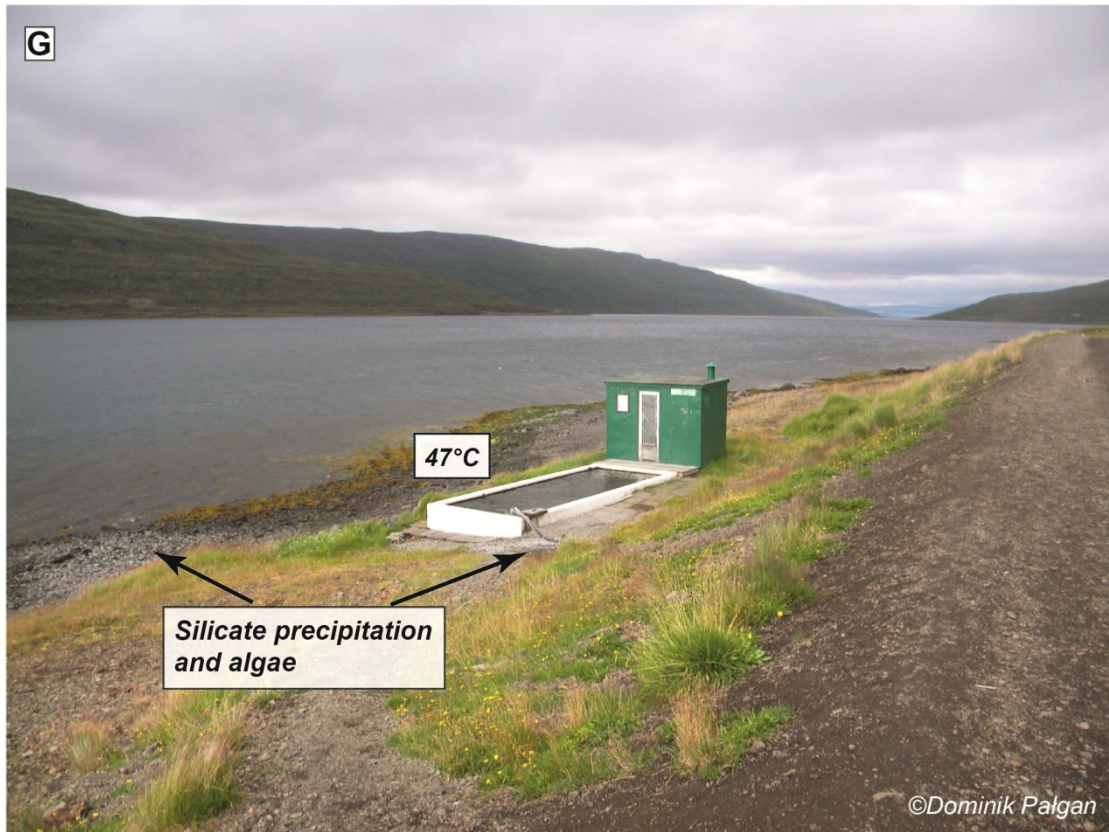
*Silicate precipitation and algae*



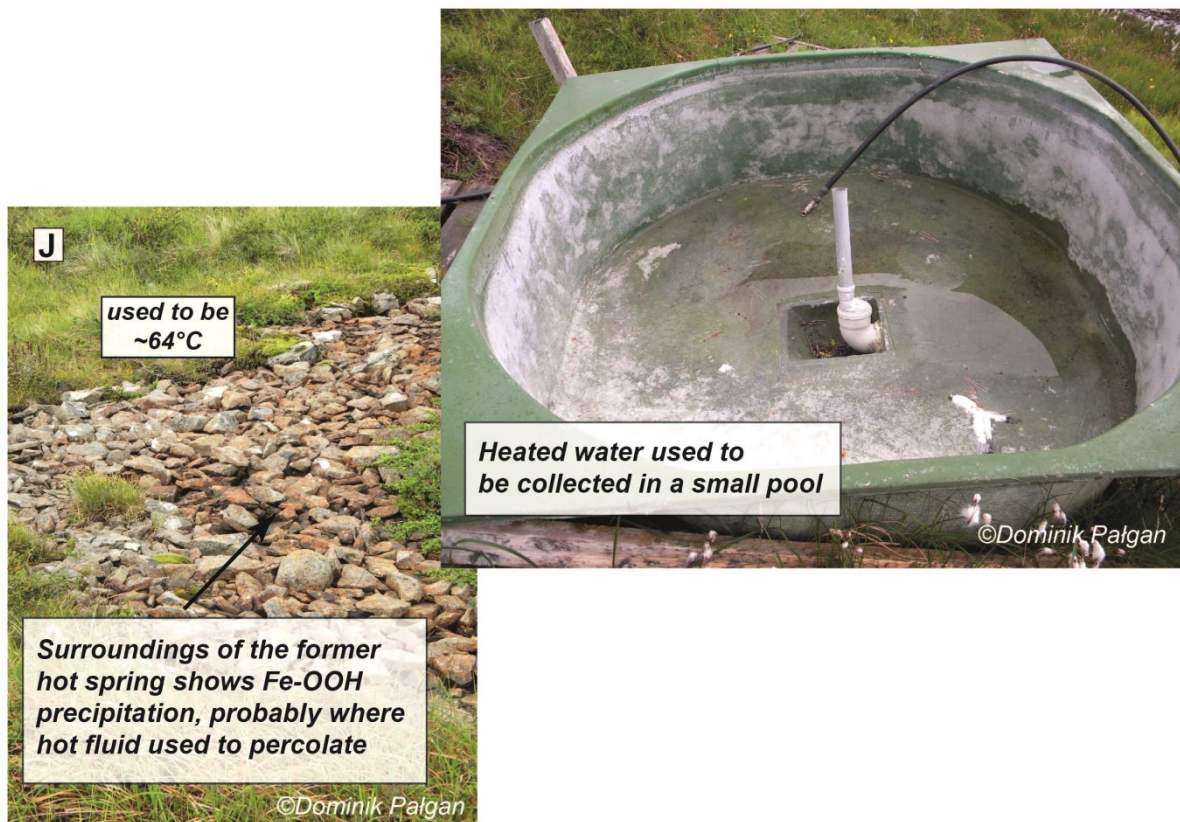












Surroundings of the former hot spring shows Fe-OOH precipitation, probably where hot fluid used to percolate

Fig. 21 Examples of hot springs from the Westfjords for which the correlation with geological features could not be made. They are usually man-made wells, swimming pools or small manifestations not adapted to commercial use. They are: (A) Rauðsdalur; (B) Kross; (C) Reykjarfjörður; (D) Hvítanes; (E) Botn A; (F) Botn B; (G) Gestir; (H) Gjörðidalur; (I) Nauteyri and (J) Rauðamýri. On each panel a maximum or approximate measured temperature is given, based on *Torfason (2003b)*.

## 2.3 Field season 2014

Following the fieldwork in 2013, a second visit in the field was carried out in 2014. The rationale was driven by the surprising results of the first field season where the major finding was that off-axis hydrothermal activity in Westfjords is almost exclusively controlled by off-axis dikes (see Chapter 3). Westfjords still remain the least studied region in Iceland with geological mapping only performed in several locations where eroded and exposed central volcanoes of Tertiary age have been mapped (e.g., Kristjánsson and Jóhannesson, 1996; Hald et al., 1971). Especially little is known about the dike intrusions, particularly their age, origin in on-/off-axis environment and potential role in supporting hydrothermal activity (e.g., permeability).

This field season had two main goals:

- To collect samples of dikes in order to determine their age and potential on- or off-axis origin and to put constraints on how long dike margins may remain open for hydrothermal circulation.
- To investigate the petrology and mineralogy of sampled dikes (especially the secondary mineralization) to examine a) conditions during hydrothermal activity, fluid properties, b) the overall impact of hydrothermal activity on their permeability and petrology, and c) potential impact of hydrothermal alteration on  $^{40}\text{Ar}/^{39}\text{Ar}$  dating of these samples.

### 2.3.1 Methods and preliminary results

Many of the dikes in Westfjords are observed along the coasts of fjords and where they are exposed due to strong differential weathering (mainly by the roads, within fjord valleys and near waterfalls). Therefore, fieldwork required locating the outcrops along the coasts of Isafjardardjup and Arnarfjörður in order to sample for further investigations. Only the freshest looking outcrops were sampled in order to avoid influence of alteration on the  $^{40}\text{Ar}/^{39}\text{Ar}$  dating results. In general, 17 of the least-altered dikes were sampled. Unfortunately, only 7 samples delivered enough material (i.e., plagioclase) for further  $^{40}\text{Ar}/^{39}\text{Ar}$  dating (see Chapter 4). The locations of seven intrusions outcrops are presented in Fig. 22. All seven dikes belong to the tholeiitic series which are, in general, low in potassium. Therefore, up to 5 kg of sample had to be taken in order to provide the minimum material necessary for  $^{40}\text{Ar}/^{39}\text{Ar}$  dating. The general information on geometry of the dikes is presented in Table 1, while the photographs of the outcrops are presented in Fig. 23. The laboratory methodology



(including sample preparation for  $^{40}\text{Ar}/^{39}\text{Ar}$  dating and mineralogical descriptions), results and interpretations of both  $^{40}\text{Ar}/^{39}\text{Ar}$  dating and mineralogical investigations are presented in Chapter 4.

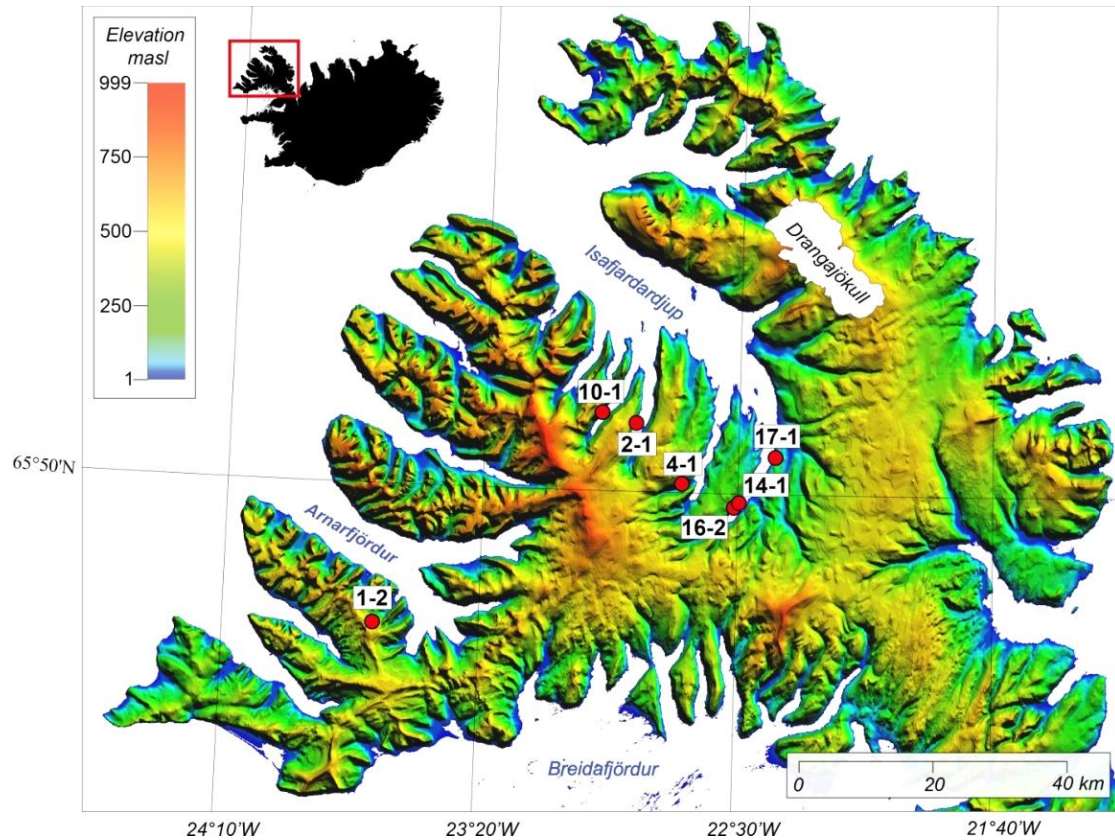
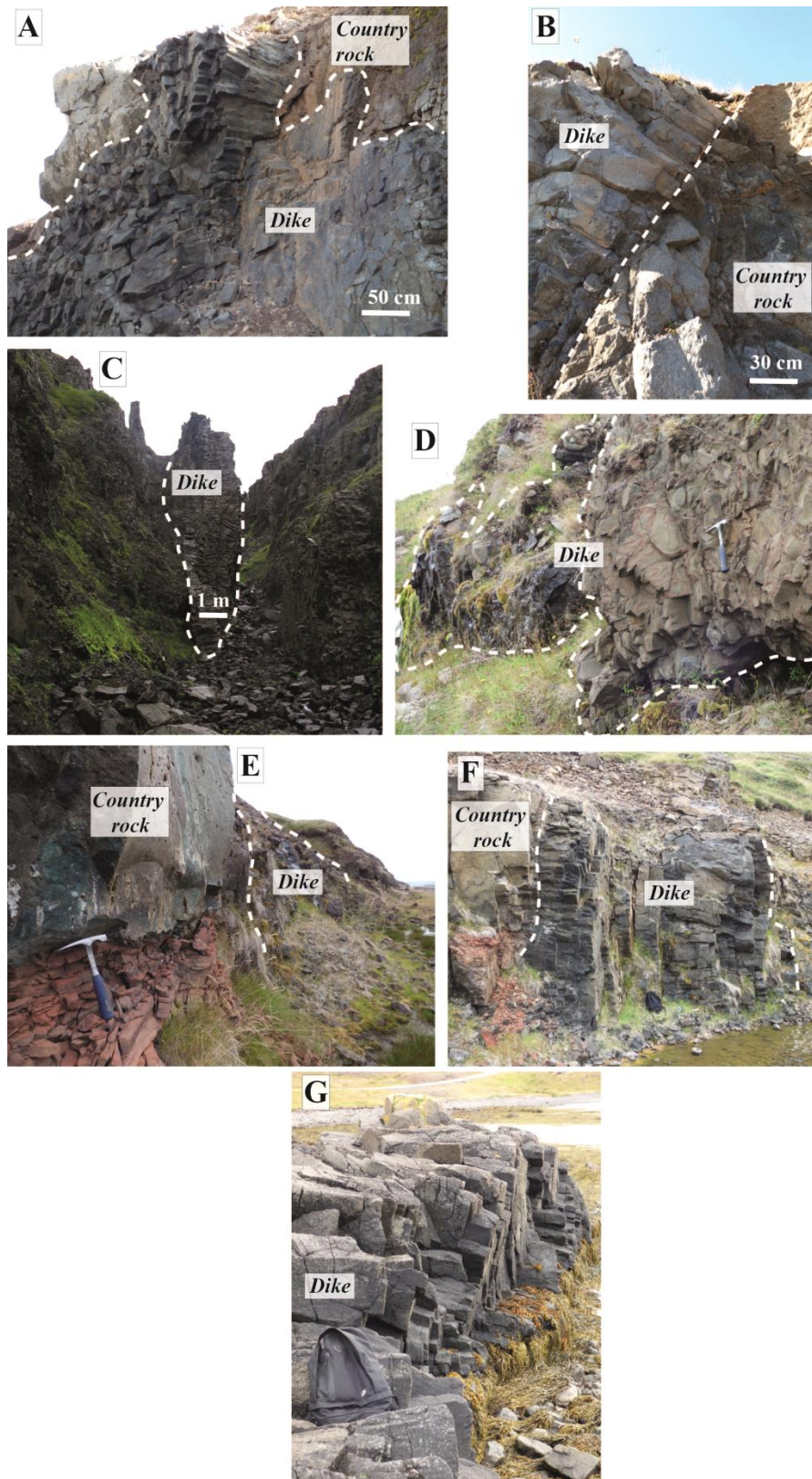


Fig. 22 Locations of the dikes outcrops visited in the Westfjords (NW Iceland) and subsequently sampled for  $^{40}\text{Ar}/^{39}\text{Ar}$  dating and mineralogical analyses. Observed dikes are usually exposed along the coastline, near waterfalls, roads, local airports and construction sites.

Table 1 Location, strike and dip of the 7 dikes sampled in the Westfjords, Iceland

Dike Sample	Latitude	Longitude	Strike (°)	Dip (°)	Comment
1-2	N 65° 38' 47.15"	W 23° 40' 38.93"	84	90	30 cm from the rim
10-1	N 65° 56' 17.81"	W 22° 57' 2.7"	40	90	Rim, reddish alteration on the cooling joints
2-1	N 65° 55' 30.18"	W 22° 50' 19.14"	6	70	Cooling joint
4-1	N 65° 50' 42.54"	W 22° 41' 3.12"	6	80	Rim, exposed in canyon in Heydalur
16-2	N 65° 48' 52.88"	W 22° 30' 44.53"	4	87	Middle of the dike
14-1	N 65° 49' 16.43"	W 22° 29' 46.57"	4	87	Rim, outcrop located by the 'submerged hydrothermal mound'
17-1	N 65° 52' 58.55"	W 22° 22' 47.24"	20	89	Rim, outcrop by the beach



**Fig. 23** Photographs of the seven dike outcrops sampled during the 2014 field season; A) Sample 1-2. Total thickness unmeasurable; B) Sample 2-1. Total thickness unmeasurable; C) Sample 4-1. Measured total thickness is ~3 m. More detailed setting of this dike is given in Chapter 3; D) Sample 10-1. Total thickness unmeasurable; E) Sample 14-1. Measured total thickness is 13 m. More detailed setting of this dike is given in Chapter 3; F) Sample 16-2. Measured total thickness is 6 m; G) Sample 17-1. Measured total thickness is 3 m.

## 2.4 References

- Arnórsson, S., Axelsson, G., and Sæmundsson, K., 2008, Geothermal systems in Iceland: Jökull, v. 58, p. 269–302.
- Bonini, M., Corti, G., Innocenti, F., Manetti, P., Mazzarini, F., Abebe, T., and Pecskey, Z., 2005, Evolution of the Main Ethiopian Rift in the frame of Afar and Kenya rifts propagation: *Tectonics*, v. 24, doi: 10.1029/2004TC001680.
- Breusing, C., Johnson, S.B., Tunnicliffe, V., and Vrijenhoek, R.C., 2015, Population structure and connectivity in Indo-Pacific deep-sea mussels of the *Bathymodiolus septemdiarum* complex: *Conservation Genetics*, v. 16, p. 1415–1430, doi: 10.1007/s10592-015-0750-0.
- Camitz, J., Sigmundsson, F., Foulger, G., Jahn, C.-H., Völksen, C., and Einarsson, P., 1995, Plate boundary deformation and continuing deflation of the Askja volcano, North Iceland, determined with GPS, 1987-1993: *Bulletin of Volcanology*, v. 57, p. 136–145, doi: 10.1007/BF00301404.
- DeMets, C., Gordon, R.G., Argus, D.F., and Stein, S., 1990, Current plate motions: v. 101, p. 425–478, doi: 10.1111/j.1365-246X.1990.tb06579.x.
- Foulger, G., Bilham, R., and Morgan, W.J., 1987, The Iceland GPS Geodetic Field Campaign 1986: *Eos*, v. 68, p. 1809–1818, doi: 10.1029/EO068i052p01809-02.
- Geirsson, H., Árnadóttir, Þ., Sturkell, E., Sigmundsson, F., Einarsson, P., Villemin, T., Árnadóttir, Þ., Geirsson, H., and Bergsson, B.H., 2002, Continuous GPS Measurements in Iceland 1999-2002: American Geophysical Union, Fall Meeting 2002, Abstract #G22A-05.
- Hackman, C.M., King, G.C.P., and Bilham, R., 1990, The Mechanics of the South Iceland Seismic Zone: *Journal of Geophysical Research*, v. 95, p. 17339–17351, doi: 10.1029/JB095iB11p17339.
- Hald, N., Noe-Nygaard, A., and Pedersen, A.K., 1971, The Króksfjörður central volcano in northwest Iceland: *Acta Naturalia Islandica*, v. II, pp. 29.
- Heki, K., Foulger, G.R., Julian, B.R., and Jahn, C.-H., 1993, Plate dynamics near divergent plate boundaries: Geophysical implications of post-rifting crustal deformation in NE Iceland: *Journal of Geophysical Research: Solid Earth*, v. 98, p. 14279–14297, doi: 10.1029/93JB00781.
- Hreinsdóttir, S., Einarsson, P., and Sigmundsson, F., 2001, Crustal deformation at the oblique spreading Reykjanes Peninsula, SW Iceland: GPS measurements from 1993 to 1998: *Journal of Geophysical Research Solid Earth*, v. 106, p. 13803–13816, doi: 10.1029/2001JB000428.
- Jahn, C.H., 1990, A highly precise GPS-epoch measurement in the northeast volcanic zone of Iceland, In: Paquet, J.P., Flick, J., and Ducarme, B. [Eds.], *Cahiers du Centre Européen de Géodynamique et de Sismologie*, Luxembourg, pp. 292–304.

- Kjartansson, G., 1969, Geological Map of Iceland, Sheet 1: North-West Iceland [Map]: 1:250 000, National Land Survey of Iceland, Reykjavik.
- Kristjánsson, L., and Jóhannesson, H., 1996, Stratigraphy and Paleomagnetism of the Lava Pile South of Ísafjarðardjúp, NW- Iceland: *Jökull*, v. 44, p. 3–16.
- Pałgan, D., Devey, C.W., and Yeo, I.A., 2016, Dike control of hydrothermal circulation in the Tertiary Icelandic crust and implications for cooling of the seafloor: *Journal of Volcanology and Geothermal Research*, v. 316, p. 22–33, doi: 10.1016/j.jvolgeores.2016.02.021.
- Russel-Smith, A., 1984, The environment of the Ethiopian Rift Valley compared to other areas of Africa: *ILCA Bulletin*, v. 17, p. 20–36.
- Sæmundsson, K., 1979. Outline of the geology of Iceland. *Jökull* 29, 7–28.
- Sæmundsson, K., Hjartarson, Á., Kaldal, I., Sigurgeirsson, M.A., Kristinsson, S.G., and Vikingsson, S., 2012, Geological Map of the Northern Volcanic Zone, Iceland [Map], 1:100 000: Iceland GeoSurvey and Landsvirkjun, Reykjavik.
- Sæmundsson, K., Jóhannesson, H., Hjartarson, Á., Kristinsson, S.G., and Sigurgeirsson, M.A., 2010, Geological Map of the Southwest Iceland [Map], 1:100 000, Iceland GeoSurvey, Reykjavik.
- Sigmundsson, F., Einarsson, P., and Bilham, R., 1992, Magma chamber deflation recorded by the global positioning system: The Hekla 1991 Eruption: *Geophysical Research Letters*, v. 19, p. 1483–1486, doi: 10.1029/92GL01636.
- Sigmundsson, F., Einarsson, P., Bilham, R., and Sturkell, E., 1995, Rift-transform kinematics in South Iceland: deformation from Global Positioning System measurements, 1986 to 1992: *Journal of Geophysical Research Solid Earth*, v. 100, p. 6235–6248, doi: 10.1029/95JB00155.
- Sturkell, E., Sigmundsson, F., Einarsson, P., and Bilham, R., 1994, Strain accumulation 1986–1992 across the Reykjanes peninsula plate boundary, Iceland, determined from GPS measurements: *Geophysical Research Letters*, v. 21, p. 125–128, doi: 10.1029/93GL03421.
- Torfason, H., 2003a, Geothermal Map of Iceland [Map], 1: 500 000, Náttúruminjasafn Íslands og Orkustofnun, Reykjavik.
- Torfason, H., 2003b, Jarðhitakort af Íslandi og gagnasafn urn jarðhita [in Icelandic], Orkustofnun Report OS-2003/062, Reykjavik, pp. 168.

## Chapter 3

### Dike control of hydrothermal circulation in the Tertiary Icelandic crust and implications for cooling of the seafloor

This chapter consists of a manuscript published in *Journal of Volcanology and Geothermal Research*.

Palgan, D., Devey, C.W., and Yeo, I.A., 2016, Dike control of hydrothermal circulation in the Tertiary Icelandic crust and implications for cooling of the seafloor: *Journal of Volcanology and Geothermal Research*, v. 316, p. 22–33, doi: 10.1016/j.jvolgeores.2016.02.021.

Declaration of contributions: C.W.D. proposed the study. D.P. defined the research area, prepared and carried field work in Iceland, interpreted the results and wrote the manuscript. All co-authors and external reviewers contributed discussions and revisions which improved the manuscript.



### **3 Dike control of hydrothermal circulation in the Tertiary Icelandic crust and implications for cooling of the seafloor**

#### **Abstract**

Hydrothermal activity along the Mid-Atlantic Ridge is predominantly high-temperature venting controlled by volcano-tectonic processes confined to the ridge axis and neotectonic zone, which extends ~20km on each side of the axis (e.g., TAG or Logatchev 1). These vents cannot, however, account for all the heat which needs to be removed to cool the plate and a significant amount of heat is probably removed in the off-axis regions as well. These regions have previously not been systematically surveyed for hydrothermal activity due to a lack of predictive models for its nature, location or controlling structures. Here we use hot springs in the Tertiary Westfjords of Iceland as onshore analogues for hydrothermal activity along the off-axis Mid-Atlantic Ridge to better understand tectonic and volcanological controls on their occurrence, as well as the processes which support hydrothermal circulation. Our results show that even crust  $\geq 10$  Ma has abundant low-temperature hydrothermal activity. We show that 66% of hot springs investigated, and 100% of those for which a detailed geological setting could be determined, are associated with basaltic dikes cross-cutting the sub-horizontal lava sequence. This is in strong contrast to on-axis springs, which are known (both from underwater and on land) to be predominantly associated with faults. Absence of earthquakes in Westfjords suggests the faults there are no longer active and possibly sealed by secondary minerals, suppressing fluid circulation. In such a situation, the jointed and fractures dike margins may provide the major pathways for fluid circulation. Extrapolating this idea to the off-axis regions of the Reykjanes Ridge, we suggest, based on bathymetric maps, potential sites for future exploration for off-axis hydrothermal systems.

**Key words:** Iceland, Westfjords, Dikes, Hydrothermal Activity, Reykjanes Ridge, Mid-Atlantic Ridge

#### **3.1 Introduction**

From its production at magmatic temperatures, the oceanic crust cools over millions of years by both conduction and advective hydrothermal cooling. Two main types of hydrothermal venting are recognized on the seafloor: focused high-temperature venting which produces a narrow buoyant plume in the water column connected to a large neutrally-buoyant plume at some height above the seafloor and low-temperature venting which appears to be more widespread but whose effect on the water column is much more subtle. Particularly the neutrally buoyant plumes from high-temperature venting are detectable chemically and even



thermally in the water column (e.g., Baker et al., 2001; Baker et al., 2004; German et al., 1991; German et al., 1994; German et al., 1998; German et al., 2008;). Almost 20 years ago Baker et al. (1996) proposed a linear correlation between high-temperature hydrothermal vent frequency and spreading rate. However, whether the abundance of such systems along an axis is sufficient to cool newly formed crust remains unclear (e.g., Baker et al., 1996; Wilcock and Delaney, 1996 and Coogan et al., 2005). For example, the only confirmed hydrothermal field (Steinahóll 63°03'N) on the ~800km long Reykjanes Ridge does not discharge enough heat to cool such a long ridge segment (German et al., 1994). Seems that additional mechanism, besides on-axis black smoker vents, is needed to dissipate magmatic heat, which until now has remained undetected. Widespread (i.e., off-axis) and low-temperature venting would appear to be the simplest explanation, and some authors have estimated that up to 90% of hydrothermal heat could be transported to the oceans by low-temperature venting (e.g., Barriga et al., 1998; German et al., 1996; Gracia et al., 2000; Melchert et al., 2008; Devey et al., 2010). But few techniques for prospecting for low-temperature ("diffuse") venting other than visual survey currently exist – such surveys have been carried out over much less than 1% of the ridge axis itself and almost nowhere in the near- or off-axis regions. If our knowledge of the distribution of high-temperature vents and the geological features which control their location, even within the ridge axis, can be said to be patchy at best; we have almost no information about the regional or global distribution of, nor the controls on, low-temperature venting, either on-or off-axis.

Iceland, as the only subaerial part of the Mid-Atlantic Ridge, provides unique access to such on- and off-axis areas, allowing direct observations of volcanic and tectonic controls on hydrothermal systems over a range of crustal ages. Assuming that Icelandic hot springs are onshore analogs, at least in terms of their controlling structures, of hydrothermal systems on the ocean floor, understanding the geological framework of onshore systems can help guide models to predict hydrothermal vent occurrence along mid-ocean ridges.

Arnórsson et al. (2008) defined low-temperature Icelandic systems as being vents with temperatures <150°C, anything above that temperature was classified as high-temperature. We will follow that definition here. The location of high-temperature systems in Iceland is restricted to the neovolcanic zones (Fig. 24), where shallow magma chambers and fissure swarms provide heat and pathways for hydrothermal circulation (Arnórsson, 1995a). Low-temperature Icelandic systems are more widespread and are found as far west as the Westfjords, where hot springs occur in Tertiary lava formations (ca. 12–16 Ma, see below) even though the area is located far from spreading centers and magmatic activity (Fig. 24).

Many researchers have studied low-temperature systems on Iceland (e.g., Árnason, 1977; Böldvarsson, 1983; Axelsson, 1985; Björnsson et al., 1990; Arnórsson, 1995b; Arnórsson et al., 2008; Axelsson et al., 2010) (Fig. 24), yet one generally applicable conceptual model explaining the geological framework of Icelandic low-temperature systems has yet to be presented (Arnórsson, 1995b).

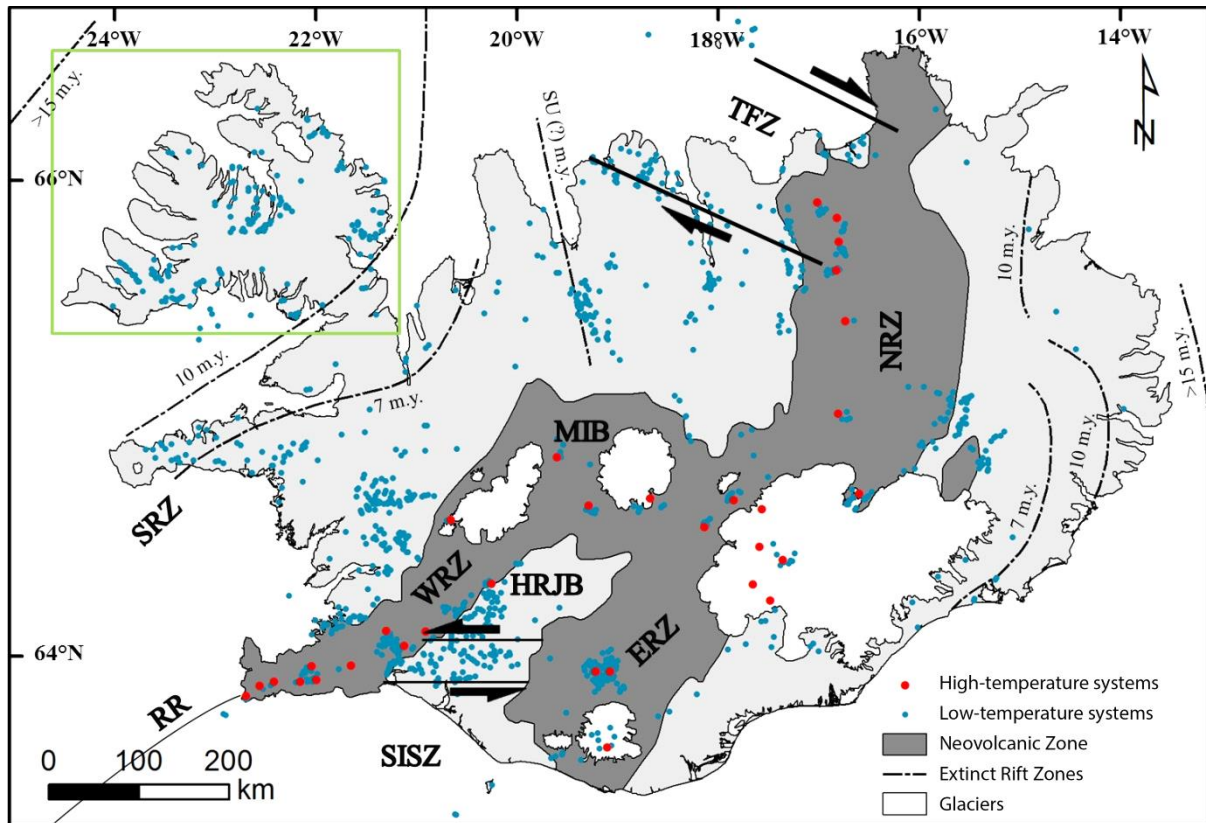


**Fig. 24** Map of Iceland showing its main tectonic elements (modified from (Johannesson and Sæmundsson, 2009), the distribution of high- and low-temperature geothermal sites (modified after Torfason (2003a)) and extinct rift zones (modified after Sæmundsson (1979)). The green box shows the Westfjords study area. Abbreviations are: SRZ Snæfellsnes Rift Zone; WRZ: Western Rift Zone; ERZ: Eastern Rift Zone; NRZ: North Rift Zone; TFZ: Tjörnes Fracture Zone; SU: Skagafjörður Unconformity; SISZ: South Iceland Seismic Zone; HRJB: Hreppar Rift-Jump Block; MIB: Mid-Icelandic Belt, RR: Reykjanes Ridge.

### 3.2 Geological setting of Westfjords low-temperature hydrothermal systems

The Westfjords Peninsula is the biggest peninsula of Iceland (Fig. 24) and forms the westernmost part of the country, constructed of Tertiary, mainly tholeiitic basaltic lava flows. With a few exceptions (e.g., Kristjánsson, 1968; Kjartansson, 1969), very little detailed mapping has been performed in Westfjords. Eroded central volcanoes can be observed in several locations across the peninsula (e.g., Kristjánsson and Jóhannesson, 1996), however, only one has been mapped in detail (Hald et al., 1971). These extinct edifices are characterized by the presence, in addition to basalts, of intermediate and acid rocks, with gabbro and granophyre plutons in the deeper sections. Such plutons have also been

recognized in eastern Iceland, where they represent the uppermost parts of shallow magma chambers (Gudmundsson, 1990).

The entire Westfjords lava plateau dips slightly ( $\leq 10^\circ$ ) to the SE (Sæmundsson, 1979). K–Ar dating of rocks collected in the westernmost part of the peninsula yield average ages of  $16.0 \pm 0.3$  Ma, making them the oldest exposed rocks in Iceland (Moorbath et al., 1968). In the central part of the Westfjords the age of lavas has been estimated as between 13.7 and 12.0 Ma (Kristjánsson and Jóhannesson, 1996). In various locations up to 15m thick lava sequences are separated by thin red interbeds of volcanic and eolian origin. Different alteration mineral assemblages in the rocks record a wide range of temperatures and may indicated the depths at which alteration took place (Sæmundsson, 1979; Ármannsson et al., 1987; Thordarson and Höskuldsson, 2002). In Iceland, especially in high-temperature systems, hydrothermal alteration shows depth–zonal distribution (Ármannsson et al., 1987).

The Westfjords lava plateau is cut by numerous faults that strike between NE and N (Gudmundsson et al., 1996). Throws on the faults range from 0.5 m to 25 m with an average of 5 m. In many cases, breccia composed of fine grained matrix and angular fragments of the host rock is observed on the fault surface.

Numerous lineaments cross-cutting the plateau can be observed in aerial photographs and satellite images of the southern and southwestern parts of the peninsula. Extensive field studies along the fjords have revealed that a great majority of them are exposed basaltic dikes (Gudmundsson, 1984). More than half of the dikes strike between NE and E, with NE and NNE directions being also common in the northern part of the studied area. The dikes have an average measured thickness of 4.3 m and many show signs of polyphase intrusions, consisting of up to ten sets of clearly distinguishable columnar rows within a single dike, suggesting successive magma pulses occurring over a period of several hundred days (Gudmundsson, 1984). The lineaments also cross the central part of the peninsula; however no ground–truthing of their geological nature has yet been carried out.

### **3.3 Methods**

We aimed to characterize the geological setting of Westfjords hot springs in order to determine whether any systematic associations between volcanic or tectonic structures and the locations of springs were visible. We used the coordinates of all known Westfjords hot springs from Torfason (2003b) to guide geological field mapping. All sites were visited and the nature of the hydrothermal manifestation and its geological environment determined. Where possible, for each natural hot spring we determined its exact location in relation to

topography, faults/fractures, lava flows or dikes. In some cases not all of these features could be determined. All hot springs and their geological settings were photographed for further interpretation. In some cases the "springs" are in reality artificial, drilled wells – we excluded such wells from further investigation. Multiple natural hot springs within a radius of 50m are usually summarized by Torfason (2003a) into so-called clusters and only one set of coordinates is given. This method was developed to ensure clarity of maps at the 1:500 000 scale, although the individual clusters themselves were defined based on maps at scale 1:50 000 (Torfason, 2003a).

Freely available online aerial images (provided by the National Land Survey of Iceland) are of sufficiently high resolution to allow most lineaments in Westfjords to be recognized. Ground-truthing field observations, similar to those undertaken by Sigurdsson (1967) and Gudmundsson (1983 and 1984), showed that most of them are dike intrusions.

### **3.4 Results**

Despite being 150–180 km away from the neovolcanic zone, low-temperature geothermal activity is abundant in the Westfjords (Fig. 24). Of all springs studied there, only three locations show fluid discharge with temperatures reaching 90°–100°C, the rest are <60°C. The hot springs normally occur at low points in the topography, along coastlines and within valleys of glacial origin, adjacent to the fjords (Torfason, 2003a).

In total, 32 geothermal manifestations were visited in the Westfjords region: 23 located in the central, 6 in the southern and 3 in the eastern part of the peninsula. Correlation with geological features was impossible in several cases, due to erosion (e.g., those in coastal areas, river valleys, estuaries or post-glacial valleys). The manifestations of the individual springs range in size from small vents a few tens of centimeters in size up to pools several meters in diameter. Others emerge from the bases of the steep slopes of fjords and one spring occurs as a “submersed” mound periodically exposed during low tide.

#### **3.4.1 Reykjanes Peninsula, Westfjords**

We examined 7 manifestations in the Reykjanes Peninsula area (Fig. 25A). Five of the hot springs align along a NNW trending line (Fig 25A). One (altered beach cluster A) deviates and is located 800 m to the north of this trend, where it occurs along a beach, periodically flooded by tide (Fig. 25B). In several places, hot fluid flows out of small pools (up to 20 cm in diameter). The isolated cluster of vents along the beach (A) is characterized by temperatures between 80–90°C (Torfason, 2003a). Associated with these vents are areas of

discoloration within the host basalts, where the basaltic matrix appears to have been replaced by a friable assemblage of quartz, calcite and Fe-hydroxides, presumably as the result of interaction between hot fluid and the surrounding basalts (Fig. 25B). Massive regions of basalts are also cut by mineral veins which fill small fractures and cracks. The highest temperatures (90–100°C) were measured in hot spring *B* (Torfason, 2003a).

The entire Reykjanes region is strongly weathered by glacial and fluvioglacial erosion and/or frost shattering. We mapped two dike walls in the vicinity of the line connecting six of the springs (Fig. 25C-E). The visible outcrop of the northern dike (Fig. 25C, D) is approximately 10 m long and strikes NNE. Measurement of dike thickness was not possible as only one contact is exposed. This contact is characterized by cooling joints (Fig. 25D) that rapidly narrow as they approach the margin of the dike. The dike is not overlain by lava flows, nor does it cut or blend into a lava flow, suggesting that the upper limit of the dike is exposed here.

Hot spring (*B*) is located 150 m NW of the northern end of the outcrop. Rocks around the spring are covered with silica deposits. The outcrop of the southern dike (Fig. 25E) is located 140 m SW of the southernmost hydrothermal manifestation on the Reykjanes Peninsula. This approximately 300 m long wall strikes NNE and stretches along the nearby runway. Thickness measurements were not possible. Unlike the northern dike, cooling joints here have a wide spacing (up to 40 cm) and the rock is not as weathered. The increased joint spacing indicates that the outcrop comes from a central part of the dike. All the warm springs along the alignment in Fig. 25A are characterized by temperatures ranging from 10 to 60°C. The spring located the closest to the southern dike (*E*) has a temperature of 10–20°C and is the smallest pond. The surroundings of the three springs located between the observed dike walls (*C*) are characterized by silica deposits and have temperatures between 50–60°C. The temperature of fluids decreases along the peninsula from north (90–100°C) to south (10–20°C). Lower temperature manifestations (<10–20°C) show no silica deposits in their surroundings and the fluid flow is less vigorous.



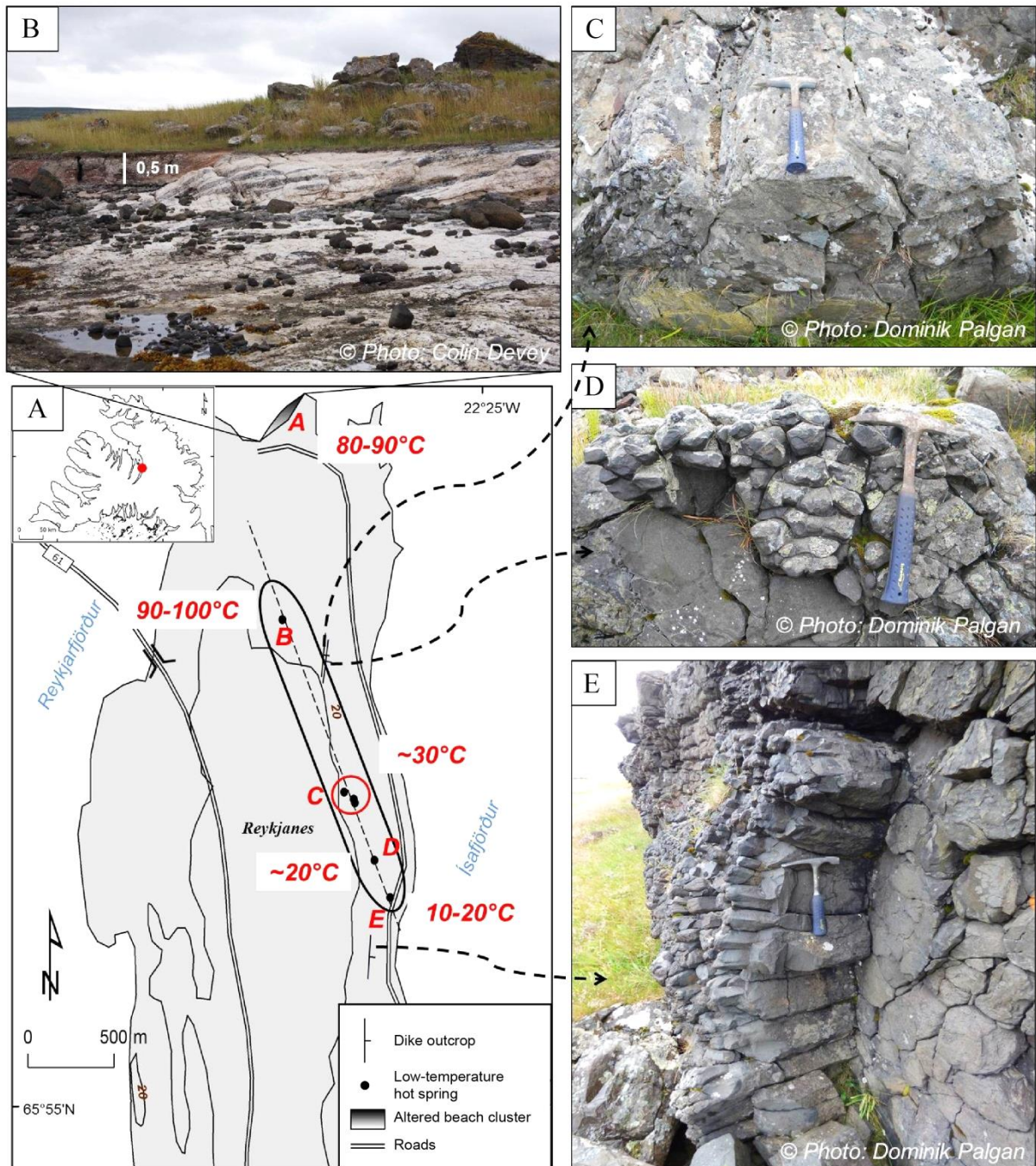


**Fig. 25** (A) Hot springs mapped on the Reykjanes Peninsula (Westfjords). (B) White mineral and iron-oxide beach deposits along northernmost hydrothermal cluster. Deposits formed due to relatively high temperature alteration of tholeiitic lava flows. Mineral veins fill fractures and cracks. (C) Highly weathered outcrop of northern dike striking NNE with relatively small cooling joints. Viewing direction is onto the top of the cooling polygons. (D) Southern continuation of (c) outcrop with even smaller cooling joints. (E) Less weathered outcrop of southern dike, striking NNE. Outcrop is characterized by progressively smaller cooling joints. The smallest joints are remnants of the location of cooling surface of the hosting rock. Viewing is from the S.

### 3.4.2 Heydalur

Two hot springs are located in Heydalur Valley (Fig. 26A). Spring B has a temperature of 40–50°C (Torfason, 2003a) and feeds a pool with a diameter of 2 m. Hot water and bubbles rise through permeable rocks on the floor of the pool and the pool overflow drains into a

nearby river. The rocks around the pool and in the warmer parts of the stream are covered by silica deposits, similar to ponds with comparable temperatures from the Reykjanes Peninsula. The temperature in pool *A* appears similar to pool *B* although it is not defined by Torfason (2003). Both manifestations align along a 1.25 m long lineament visible in aerial images, which we confirmed during field observations (Fig. 26A). Hot spring *C* is also aligned with this lineaments further downslope. Gudmundsson (1984) found similar lengths for lineaments in southern Westfjords measured from aerial photographs. The incised river valley which defines the lineament exposes a broad dike showing multiple internal contacts (Fig. 26B, C) of which we mapped physical parameters for 12. The average strike of the dike is NNW, similar to the orientations measured on Reykjanes Peninsula. The thickness of the individual intrusions ranges from several cm to >1 m. All observed outcrops have tetragonal to hexagonal cooling joints and show cooling contact relationships to the surrounding Tertiary basalts. In several cases, we observed dikes intersecting layers of red mineral deposits lying between lava sequences (Fig. 26D). Additionally, we identified red pigmentation in narrow gaps between joints and fractured Tertiary basalts. In one case, weathering exposed the contact wall between the dike and its cooling surface to the host rock (Fig. 26E) which is characterized by the presence of visible red pigmentation and green mineralization, located in cracked hosting basalt.

### **3.4.3. Submerged mound (N65°49.248' W22°29.762')**

We observed two hydrothermal manifestations located on the west shore of Ísafjörður (Fig. 27A). Water from hot spring *A* flows from boulders piled under the road located just above the beach. Manifestation *B* is a hydrothermal mound (Fig. 27C, D) located on the beach, below the high-tide mark, making it only visible at low tide. Measured temperatures in both springs are 40–50°C (Torfason, 2003a). Rocks around the upper manifestation are covered with white silica deposits. The mound itself has an irregular shape, approximately 4 x 5 m. Both observed hot springs are associated with a vertical basaltic dike (Fig. 27B). The lineament it generates in the landscape can also be distinguished on aerial images, extending approx. 2 km away to the NNE. Where exposed, the dike strikes almost N–S and is 13 m thick. The dike cuts a red interbed on one side (Fig. 27E), but the continuation of this layer is not visible on the other side of the intrusion, suggesting perhaps some vertical movement along the dike plane.



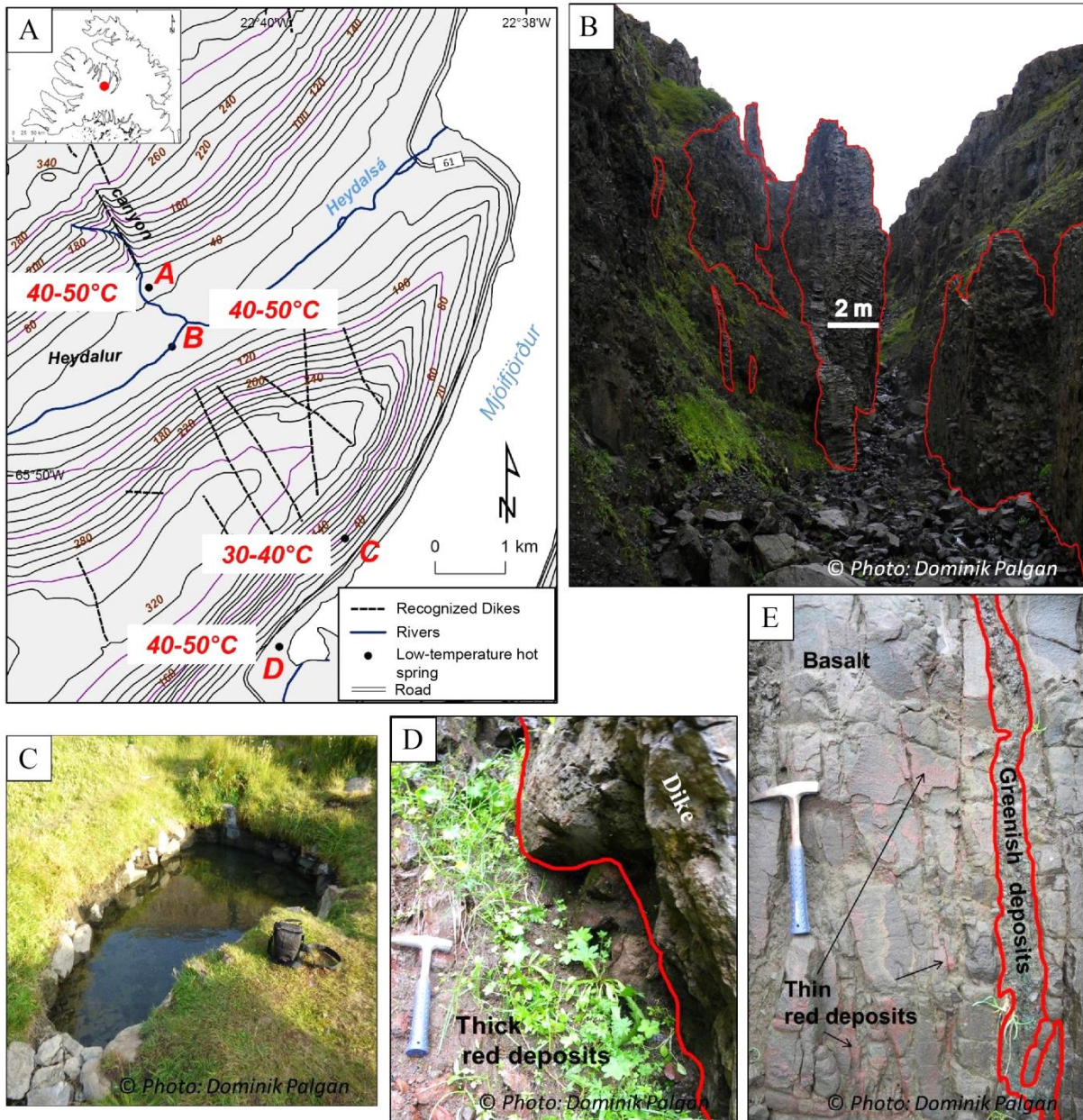


**Fig. 26** (A) Location of three hot springs in Heydalur. Manifestations align along lineament interpreted from satellite image and recognized in the field as multiple dikes. (B, C) Dike intrusions (outline in red) exposed in canyon located on the northern slope of a table mountain in Heydalur valley. (D) Layer of thick red deposits intersected by one of the observed dikes (outline in red). Red pigmentation is also present in small fractures in the dike's cooling joints. (E) Basaltic contact wall (cooling surface) exposed after weathering of associated dike. Thin layers of red pigmentation in cracks are also present together with a few centimeters thick layer of grey–green colored precipitates (most likely celadonite).



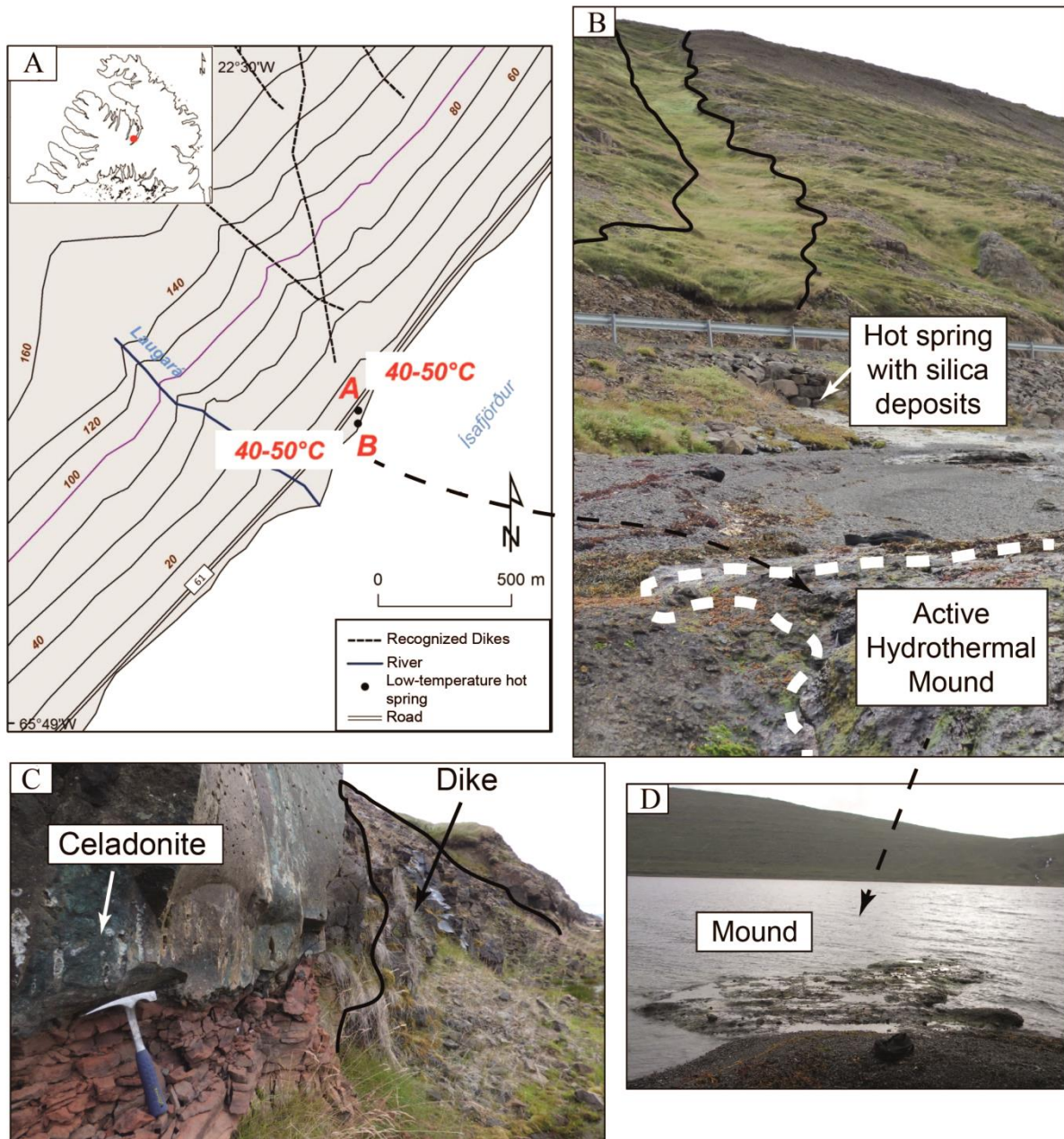


**Fig. 27** (A) Two hot springs located along west coast of Ísafjörður. (B) Both springs manifest on the extension of a NNE-striking dike (marked with black lines). White silica deposits occur near hot spring A. (C) Close-up of the alteration and thin red interbedded layer directly adjacent to the dike. Celadonite identification is based on hand-specimen color. (D) Hydrothermal mound (B) observed at low tide along the extension of the dike. The mound has approximate dimensions  $4 \times 5$  m and vents vigorously from the top and sides. Backpack for scale.

#### 3.4.4 Hamarsháls Peninsula

We observed three manifestations in the eastern part of the Westfjords, along the coast of Hamarsháls Peninsula (Fig. 28A). Two natural springs have been adapted for swimming by the local community (A) and one is a man-made well. The measured temperature in cluster A is  $70\text{--}80^\circ\text{C}$  (Torfason, 2003a). The direct vicinity of the cluster (Fig. 28C) is covered by white silica precipitates. Strong steaming is also evident. Both springs lie some 75 m NNW from the outcrop of a dike striking NE, which is also visible in the aerial photographs and easy to reach



in the field. The outcrop (Fig. 28B, D) is approx. 200 m long and 5–6 m thick. This dike is characterized by relatively large cooling joints (approximately 25 cm), comparable with the southern outcrop in Reykjanes (see above). We did not observe interaction between the dike and red interbeds, nor any indications of green discoloration which may indicate celadonite growth.

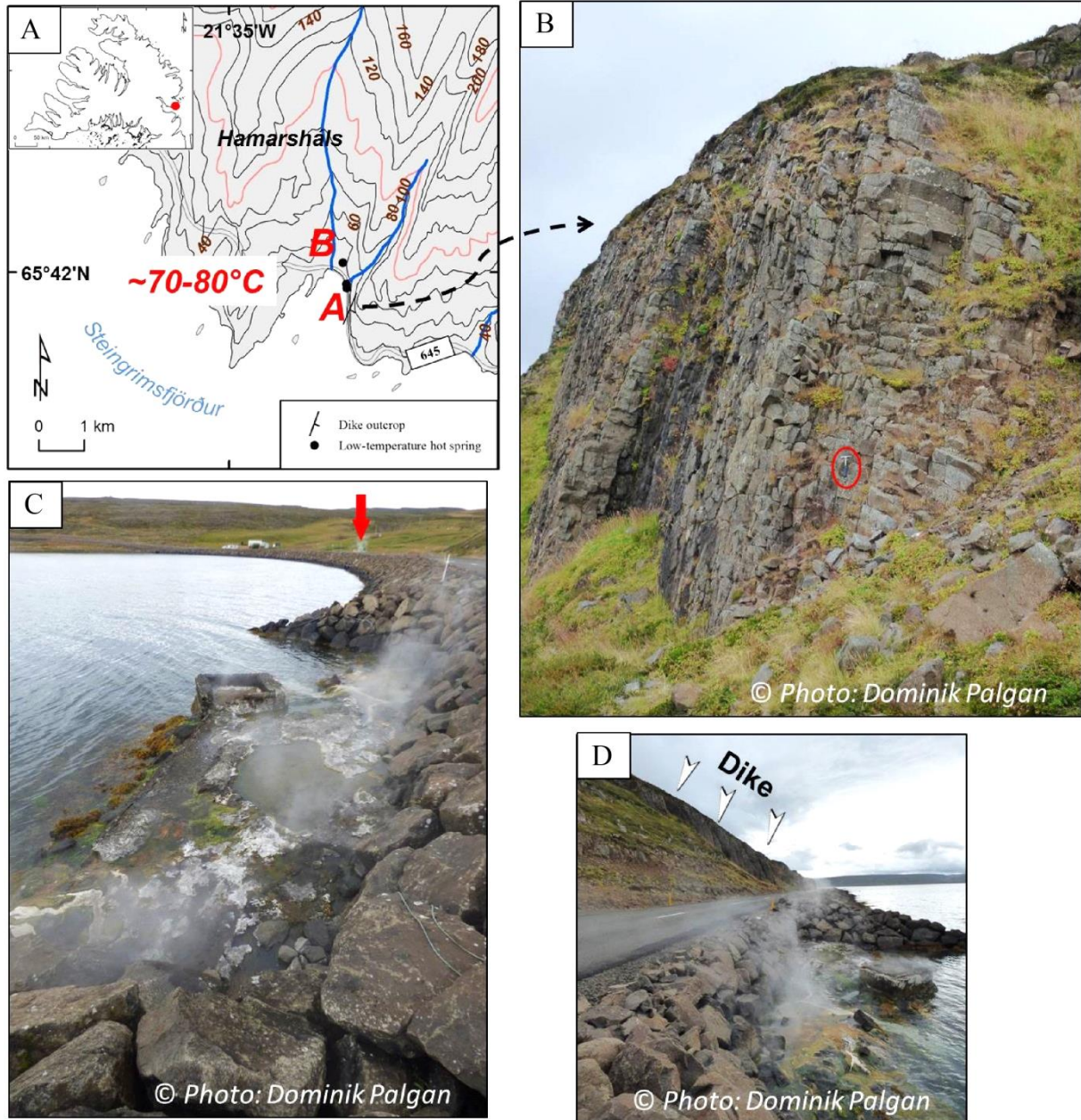


**Fig. 28** (A) Three hot springs located along coast of Hamarshál Peninsula. (B) Dike outcrop exposed approx. 75 m SSE away from cluster A. Viewing direction is to N. Hammer in red circle for scale. (C) Three observed manifestations (red arrow – man-made well) located by the coast. Visible are white silica deposits and associated strong steaming. Viewing direction is to N. (D) Location of the springs in vicinity of the dike. Viewing direction is to S.

### 3.5 Discussion

#### 3.5.1 Present low-temperature activity – dike-controlled hydrothermal circulation

The generally accepted model for the generation of hot springs on Iceland uses theoretical calculations based on Bodvarsson (1983) and modeled by Axelsson (1985). It assumes that regional tectonic and volcanological structures, such as faults and dikes/fractures, are the main geological features controlling low-temperature hydrothermalism (Fig. 29).

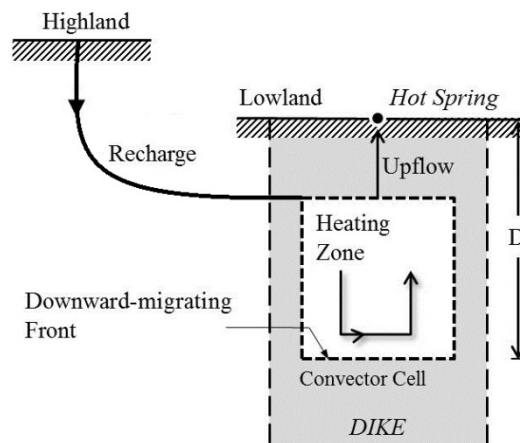


**Fig. 29 Model of heat source mechanism for low-temperature systems in Iceland. Abbreviation: D: Depth; based on Bodvarsson (1983).**

In the model, atmospheric precipitation migrates downhill along shallow paths where it gains a little heat. Additional heat is obtained when fluids encounter a hydrothermally active dike where they sink; mining heat from the deep rock as it is cracked by thermal contraction along a cooling front in a manner termed conductive downward migration (CDM) along the dike wall and associated fractures. After reaching depths of a few kilometers, the heated fluids ascend along the dike walls (Bodvarsson, 1983). This model does not explain why hot springs occur in the Westfjords, where magmatism is assumed to have been extinct for >10 Ma, nor does it explain why dikes, rather than faults, are the preferred paths for fluid migration.

Of all the hydrothermal manifestations we observed in Westfjords, 66% are confined to dike intrusions (e.g., Heydalur and Reykjanes) or occupy secondary fractures in their direct vicinity, while the remaining springs are either man-made wells or could not be associated with any evident geological features. Moreover, Bodvarsson (1983) noted similar behavior in boreholes drilled in low-temperature systems in Iceland, where the vast majority of produced thermal water is obtained from fractures found along the dike margins. This is in stark contrast to the active spreading axis, where faults are known to control hydrothermal circulation in the southern part of Iceland (Khodayar et al., 2005; Khodayar et al., 2010 and

Khodayar and Björnsson, 2014), on the Mid–Atlantic Ridge (e.g., Petersen et al., 2009) and on active oceanic–spreading axes in general.

On Iceland, Sæmundsson (1979) has suggested that the Westfjords lavas were never buried deeply and that very little of the stratigraphic succession has been lost to erosion. In this situation, many of the dikes visible in aerial photographs and which we have found to be providing pathways for hydrothermal circulation could be late feeder dikes. Many of the studied dikes trend NNW while, in general, the neovolcanic zone on Iceland trends NE–SW to N–S. It seems that these dikes reflect the main trajectories of the off-rift stress field from about 7 Ma ago (Gudmundsson et al., 1996) when the active rift zone (Snæfellsnes Rift Zone) was located south of the peninsula (see Fig. 24). This may indicate that they intruded off-axis during these unique stress conditions, but our observations (and the lack of radiometric dating) are insufficient to provide exact ages or relationships of the dikes to the rift zone.

Propagating dikes cause changes within the stress field both above and in front of the dike, initiating opening of fractures and cracks (e.g., Björnsson et al., 1979; Pollard et al., 1983; Axelsson, 1985; Rubin, 1992; Curewitz and Karson, 1998; Bohnenstiehl and Kleinrock, 2000; Gudmundsson, 2003; Qin and Buck, 2008; White et al., 2011). The average 1-m-basaltic dike (~1200°C) intruding wet basaltic lavas will have a major thermal effect both on the host rock (within 2 m of its margin) and itself (Delaney, 1987). Solidification and contraction of the dike results in the formation of joints (see, e.g., Figs 25C, D and 28B), forming pathways for fluids to migrate along the dike margins. Fracturing associated with dikes intruding into the oceanic crust has been shown to create a high permeability zone near the dike (Curewitz and Karson, 1998), sufficient to support hydrothermal circulation not only at the time of injection but also long after the dike cooled. This has also been observed along the intermediate–spreading Juan de Fuca Ridge (Cherkaoui et al., 1997), and is probably the case on mid-ocean ridges at all spreading rates. Furthermore, in terrain dissected by dikes, dikes may support both downward migration of water and ascent of heated fluids as shown schematically in Fig. 30.

In the seismically-active regions of Iceland (Fig. 31), hydrothermalism is almost always associated with faulting, with clear links between earthquakes and geothermal activity (e.g., Khodayar et al., 2006), Khodayar et al., 2010), Khodayar and Björnsson, 2014)). Earthquakes appear to actively generate permeable pathways for hydrothermal circulation with, for example, historic reports showing that hot springs aligned along the source fault for the largest earthquake in recorded Icelandic history (1784, M7.5–8.0) experienced pressure changes and increases in activity (Tryggvason, 1973).



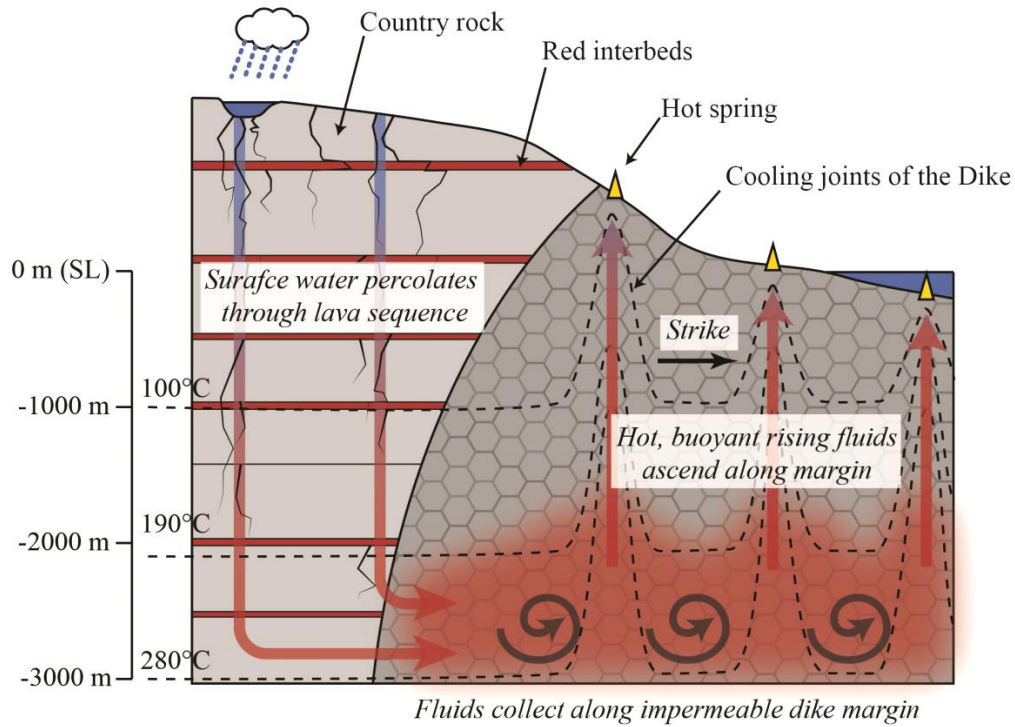


**Fig. 30** 2Dmodel (cut through fjord valley, parallel to the strike of the dike and right through its margin, exposing the cooling surface) showing dike-controlled hydrothermal circulation in Westfjords. The glassy margin of the dike is shown by the darker gray area with hexagons representing cooling joints formed perpendicular to the maximum cooling surface. Subsurface dike shape reflects the approximate expected shape of dike ends at depth (e.g., Behn et al., 2006). Atmospheric precipitation and ground-water trapped in lavas reaches 3–4 km depth. Heated fluids ascend along dike margins and associated fractures (damage zones) and reach the surface at the bottom of the fjord valley. Isotherm trajectories are based on geothermal gradient measurements in 3 drillholes (Palmason et al., 1979) and are perturbed by the hydrothermal circulation.

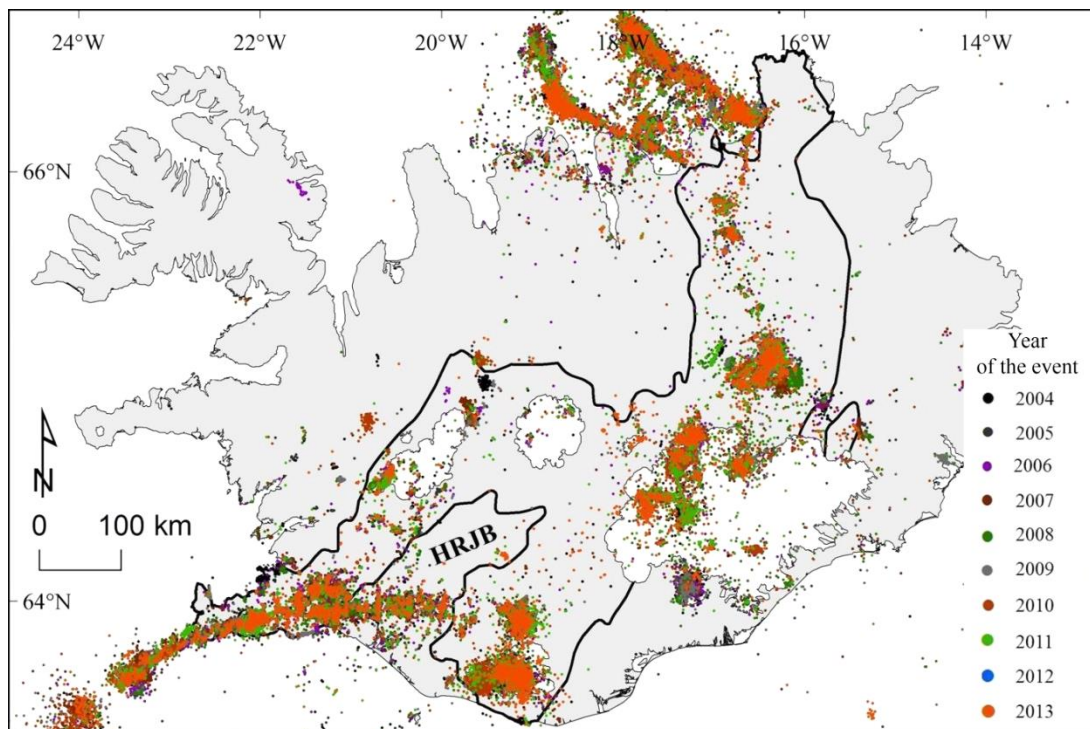


**Fig. 31** Seismic activity in Iceland in years 2004–2013. Epicenters deduced by the South Iceland Lowland (SIL) seismic network operated by Icelandic Meteorological Office. Abbreviation: HRJB: Hreppar Rift-Jump Block. For other tectonic elements see Fig. 1.

Compared to these on-axis regions, the Westfjords Peninsula shows very low levels of seismic activity (Fig. 31), implying that most of the faults there are inactive. Fault permeability is closely linked to seismic activity – the fault core, where most slip occurs, is usually characterized by the presence of breccia and cataclasites which have low permeability during interseismic periods, while the surrounding damage zone, intersected by secondary faults and fractures, has much greater permeability (Gudmundsson, 2000). But high-temperature fluids can quickly precipitate hydrous minerals and/or amorphous solids in faults and associated fractures which then block permeable pathways and restrain fluid flow (e.g. Hannington et al., 1995). It is likely, therefore, that once a fault becomes inactive its permeability, and hence its ability to channel hydrothermal fluid, will quickly be lost. Fontaine et al. (2001) suggested that the discharge of fluids with temperatures of 220–290°C can last for 1000 years if the fault hosting venting slips repeatedly. However, if the same fault shows no activity, it can support the circulation for no longer than 300 years. We believe that this is the explanation for the absence of fault control on the location of hot springs in the Westfjords and that an interplay between grain size, initial permeability and fluid temperatures favor the sealing of faults over dike margins. Our model is as follows: At the active plate boundary, we expect that repeated movement on faults keeps them highly permeable and the high-temperature fluids which characterize these active magmatic regions will be channeled preferentially (possibly exclusively) into faults. The high surface area/volume ratio of the fault gouges means that they will react rapidly with circulating fluid. Little high-temperature fluid will migrate along dike margins as they are much less permeable than the active faults. As a result, the dikes suffer little fracture-clogging by secondary mineral precipitation – the impermeability of the joint-bounded blocks at the dike margins also reduces mineral–fluid interaction. As the system migrates away from the active tectonic and magmatic region, fault permeability will become progressively clogged. Moreover, as the temperature of fluids fall, the amount of dissolved minerals being transported will decrease, and therefore, precipitation rate falls as well. At some point outside the neo-tectonic and – volcanic region, the dikes (and especially their jointed margins and the surrounding fractures) become the more permeable channels, and hydrothermal fluid circulation is concentrated there. As the circulating fluids are now cooler and the circulation is less vigorous, the rate of clogging of permeability will drop significantly, meaning dike margins provide long-term aquifers for rising hydrothermal fluids.

Low-temperature (<100°C) geothermal activity is significantly more abundant than high-temperature venting in Iceland (Arnórsson, 1995b) with possibly ~95% of all hot spring

in Iceland being low-temperature (Fig. 24). Bodvarsson (1961), however, estimated that the heat output of low-temperature hot springs in Iceland accounted only for ~10% of total hydrothermal heat output. Estimates of the ratio of high-temperature to low-temperature heat output made on the seafloor (Ramondenc et al., 2006) give the opposite result, with the heat flux related to low-temperature venting estimated to be at least 10 times that related to high-temperature vents. Bodvarsson's (1961) calculations were based only on measurements from the 5 biggest low-temperature systems located at the edges of neovolcanic zones and neglect many systems located away from it such as the Westfjords hot springs. Measurements of temperature and flow rate of all known low-temperature hot springs on Iceland are needed before an accurate estimation of their total heat output can be made and their role in heat removal from the crust evaluated. In the Westfjords, results from drillholes show the local geothermal gradient to be around 90°C/km (Palmason et al., 1979), much higher than that predicted by a half-space ocean-plate conductive cooling model such as that presented by Turcotte and Schubert (1982), in which (assuming:  $T_0 = 0^\circ\text{C}$ ,  $T_m = 1100^\circ\text{C}$ , thermal diffusivity ( $\kappa$ ) =  $8 \cdot 10^{-7} \text{ m}^2\text{s}^{-1}$  and thermal conductivity ( $k$ ) =  $3.3 \text{ W m}^{-1}\text{C}^{-1}$ ) the depth to the 200°C isotherm at 12 Ma should be 5.3 km, with a geothermal gradient of 37°C/km. The reason for this high geothermal gradient in the Westfjords is unknown – there is no evidence for recent volcanism in the region that could have recently reheated the lithosphere. With such a high gradient, water found in the Westfjords hot spring systems does not need to have penetrated to depths greater than 2–4 km to attain its measured temperature, consistent with previous conclusions of Einarsson (1942) and Arnórsson (1995). Moreover, it is likely that circulation at depth is restricted to a given dike margin as the only available permeable pathway in the given region. Using the measured temperatures and flow-rates of venting water (Torfason, 2003b) and assuming the specific heat of water  $C_p=4,187 \text{ kJ/kgK}$  (Petrucci et al., 2011)), the heat output of the Westfjords hot springs studied here ranges between 0.002  $\text{MW}_t$  (Heydalur) and 5.83  $\text{MW}_t$  (Reykjanes).

If Icelandic hot springs are directly comparable to those on submerged parts of the Mid-Atlantic Ridge, low-temperature venting may not only play an important role in heat removal from the oceanic crust but also be the key factor controlling biogeography of the deep ecosystems in the northern Atlantic Ocean.

### 3.5.2 Former hydrothermal activity associated with dikes in Westfjords?

In some locations in Westfjords, the lava pile hosting dikes is characterized by the presence of celadonite (Fig. 26E and 27E) filling many of the fractures, cracks and vesicles.



Celadonite is mostly formed in the marine environment or as a result of interaction with sea water, which provides the K and Mg needed for its formation (Baker et al., 2012). Celadonite alteration occurs mainly in oxidation haloes where it forms under oxidizing conditions at low-temperature (<50°C) (Alt et al., 1992; Schramm, 2004). In basalts, celadonite occurs along with other products of alteration, e.g., quartz, calcite, saponite or minerals from the zeolite group (Andrews, 1980). Neuhoff et al. (1999) was the first to recognize celadonite in Icelandic basalts and showed that the near-surface environment (fresh water) can also provide chemical components (K and Mg) necessary for its formation.

Our observations show that celadonite occurs only in the country rock hosting the dikes (e.g., Fig. 27E) but never in the dikes themselves. Moreover, lava piles that have never been intruded by dikes show no visible celadonite. Taken together, this evidence suggests that it is the lavas which were broken and highly fractured during dike emplacement which are acting as conduits for fluids rather than the permeability created by cooling joints in the dike itself.

### **3.5.3 Can we predict the locations of hydrothermal activity along slow-spreading ridges – case for the Reykjanes Ridge?**

#### ***3.5.3.1 Comparison of Westfjords and off-axis Reykjanes Ridge***

We suggest that our observations in Westfjords can help us predict the locations of hydrothermal venting along off-axis regions of the Reykjanes Ridge (Fig. 32). The Reykjanes Ridge (Fig. 32) extends for ~800 km between the Reykjanes Peninsula in SW Iceland and the Bight Fracture Zone at 56°50'N (e.g., Talwani et al., 1971; Searle et al., 1994). It is characterized by abnormally thick crust (decreasing from ~21 km near the Reykjanes Peninsula to ~10 km at 62°40'N (Weir et al., 2001)), an oblique spreading direction and geochemical hotspot indicators for ~550 km of its length (between Iceland and 60°N (Schilling, 1973)). The incidence of high-temperature hydrothermal sites along Reykjanes Ridge is, as for all shallow ridges, very low, with only one hydrothermal field, Steinahóll (63°06'N), having been confirmed along the whole length despite extensive prospection (German et al., 1994).

Westfjords and off-axis regions of the Reykjanes Ridge show several similarities: (1) the crust was formed at a slow-spreading mid-ocean ridge axis and has typical oceanic crustal structure; (2) the crust at both sites is abnormally thick; (3) they are located >300 km from the center of Icelandic hot spot, (4) both areas show no recent volcanic activity; (5) both sites are presently inactive seismically. Therefore, despite their different subaqueous or subaerial

settings, we expect similar processes to be supplying the heat and providing the permeability to allow hydrothermal fluid circulation both in the Westfjords and on the flanks of the Reykjanes Ridge.

Since the neotectonic zone along slow-spreading ridges is determined by the zone of seismic activity associated with active faulting (Wolfe et al., 1995), the neotectonic zone on Reykjanes Ridge can be defined as extending ~20 km on each side of the axis (as the majority of seismic events cluster there, Fig. 32). At a half-spreading rate of 1 cm/yr (Lawver and Müller, 1994), a 20 km wide zone is equivalent to 0–2 Ma crust, and we can say that our observations in Westfjords are relevant to oceanic crust older than 2 Ma on the Reykjanes Ridge.

### ***3.5.3.2 Prediction of hydrothermal activity along the Reykjanes Ridge***

Numerous researchers have studied the influence of hot spots on hydrothermal activity on the ocean floor (e.g., German et al., 1996; Langmuir et al., 1997; Baker and German, 2004; Haymon et al., 2007; Baker et al., 2014) and have found that hot spot influenced ridges have a lower incidence of high-temperature venting than expected for their spreading rate. This is especially surprising because the thickened oceanic crust in these regions should require more heat to be removed by hydrothermal activity than at normal slow-spreading ridges. For example, assuming a heat output typical for black smokers of 200 to 500 MW (e.g., Becker and Herzen, 1996; Kelley et al., 2002) for Steinahóll means it could only cool ~50 km of the 800-km-long ridge. Haymon et al. (2008) suggested that one of the reasons for the apparent reduced abundance of hydrothermal vents along hot spot influenced ridges could be intensive low-temperature cooling of the crust. However, the discrete sampling they carried out and the fact that their detection methods were not sensitive to low-temperature plumes means little evidence was presented to support this hypothesis. Devey et al. (2010) suggested a model in which hydrothermal activity along very shallow axes (e.g., the Reykjanes Ridge) may be reduced where temperatures in the crust are so high that most deformation is ductile, preventing the formation of deep and porous fractures. In both cases, incidences of high-temperature hydrothermal activity are thought to be reduced by the presence of a hotspot, and in both cases excess heat could be removed by off-axis hydrothermal venting. Our results from Westfjords suggest that this venting will occur in dike–margin hosted settings and that we should expect to find one vent every 13km<sup>2</sup>.

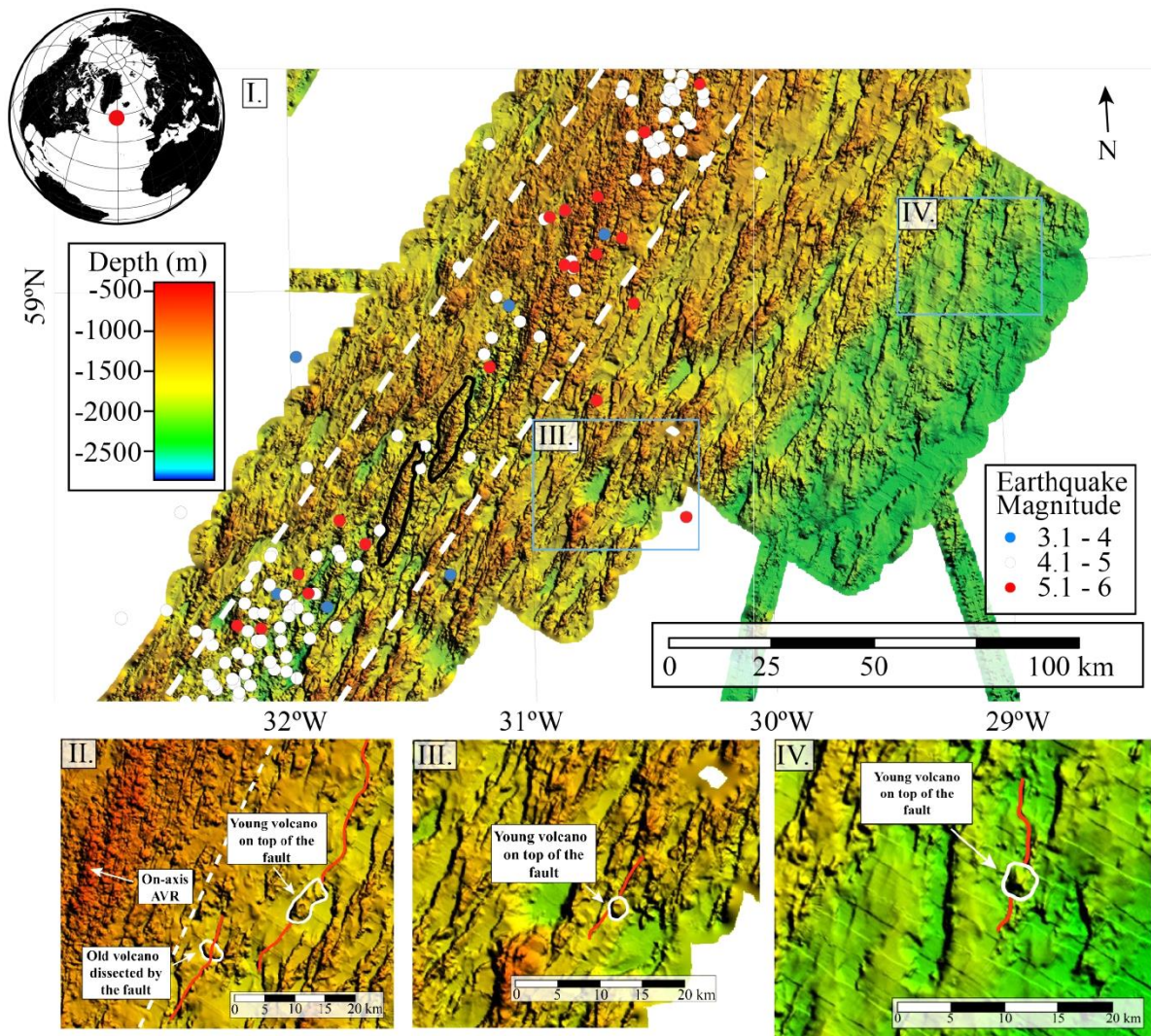


**Fig. 32** Location of earthquakes epicenters along a section of the Reykjanes Ridge in the years 1995–2014 (based on USGS Earthquake Hazard Program 2013) (Box I). The vast majority of the events are confined to a ~40 km wide neotectonic zone (white dashed lines) and neovolcanic zone i.e., Axial Volcanic Ridges (black outlines). Inset boxes: White outlines are off-axis volcanoes. Red lines represent lineaments either dissecting or underlying younger volcanoes. Box II. (located 30 km NE of the northern part of the enlarged ridge section) also shows a fault-dissected volcano for comparison between older and younger edifices. The glob shows location of the Reykjanes Ridge SW of Iceland. Bathymetry from Searle et al. (1994).

In the subaerial Westfjords, hot springs occur in the valleys (topographic lows). This is in contrast to the majority of submarine hydrothermal vents, which are located at local bathymetric highs along the mid-ocean ridges. Haymon et al. (1991) proposed that in young upper crust of the East Pacific Rise dike intrusions (also in off-axis regions (e.g., Fouquet et al., 1996)) reach a few hundred meters below the surface and hydrothermal vents often develop near elevations they create on the seafloor. If such dikes extended to the seafloor, they would like form small volcanoes. Modeling by Bani-Hassan et al. (2012) has shown that submarine venting is naturally focused towards bathymetric highs due to temperature-induced pressure variations within the systems and Titarenko and McCaig (2015) concluded that some hydrothermal systems located at bathymetric highs could be driven by modest basal heat flow

if fluids can penetrate deeply enough to gain heat from hotter layers. So finding vents in the off-axis regions of the Reykjanes Ridge will mean finding the youngest volcanic features, as these should be fed by dikes that reach the surface, providing the best pathways for fluids to traverse the lava pile. On bathymetric maps these off-axis young volcanoes will show, for example, no visible faults and high acoustic backscatter. In Fig. 32II, III and IV we show three potential sites using the available bathymetric data from the Reykjanes Ridge. In all three cases, the young volcanoes are located on top of lineaments striking roughly parallel to the ridge axis, reflecting the main extensional direction.

Of course Iceland and Reykjanes Ridge are high melt supply endmembers of the slow-spreading ridges and, therefore, are not typical for the slow-spreading mid-ocean ridges in general. Nevertheless, even in normal mid-ocean ridge settings, hydrothermal activity is apparently insufficient to cool the crust (e.g., Hannington et al., 2010) and substantial off-axis venting may be required. Our observation may, therefore, be valid not only for other hot spot influenced slow-spreading ridges, such as Mid-Atlantic Ridge south of the Azores or near Ascension Island, but also on ridge flanks in general.

### **3.6 Conclusions**

Our data show that even old Tertiary crust on Iceland (>12.0 Ma) is hydrothermally active, characterized by numerous sites of low-temperature venting (<100°C), and that these vents are linked to dikes which cut the lava pile, in strong contrast to the fault-controlled hydrothermal activity typically seen in on-axis regions. This contrast is probably related to a cross-over in the permeability of fault and dike margins as the plate migrates from an on-axis to an off-axis position. On the axis, the high permeability of active faults makes them the preferred pathways for high temperature fluid circulation above active magma chambers. Off-axis (i.e., outside the seismically-defined neovolcanic zone), the permeability of the now inactive fault surfaces quickly drops as the fine-grained fault gouge reacts with fluids to form secondary minerals. The inherently less permeable but also much less reactive jointed margins and damage zones around dikes then become the primary pathways for vertical fluid ascent. These fluids, having lower temperatures, flow-rates and dissolved species load lead to negligible sealing of the permeable zones even over millions of years. These results can be used to predict the locations of hydrothermal venting on the adjacent, submarine Reykjanes Ridge, whose neovolcanic zone is known to show a paucity of high-temperature vents. Bathymetric maps show numerous young volcanic cones outside the neotectonic zone located on top of lineaments striking almost parallel to ridge axis, which represent the best targets for

hydrothermal exploration. Given the density of low-temperature hydrothermal systems in Westfjords and the lack of known high-temperature hydrothermal sites on the Reykjanes Ridge, we would expect at least one low-temperature site for every 13km<sup>2</sup> of >2 Ma crust.

### Acknowledgments

We would like to thank Práinn Friðriksson and Bryndís Brandsdóttir for all the help associated with field work on Iceland and Keith Louden for discussions. We thank reviewers Kathi Faak and Andrew McCaig for their valuable comments which helped greatly improved this paper. Financial support through the Helmholtz graduate school HOSST is gratefully acknowledged.

### 3.7 References

- Alt, J.C., France-Ianord, C., Floyd, P.A., Castillo, P., and Galy, A., 1992, Low-temperature hydrothermal alteration of Jurassic ocean crust, Site 801: Proceedings of the Ocean Drilling Program, Scientific Results, v. 129, p. 415–427, doi: 10.2973/odp.proc.sr.129.132.1992.
- Andrews, A.J., 1980, Contributions to Mineralogy and Saponite and Celadonite in Layer 2 Basalts, DSDP Leg 37: Contributions to Mineralogy and Petrology, v. 73, p. 323–340, doi: 10.1007/BF00376627.
- Ármannsson, H., Gudmundsson, Á., and Steingrímsson, B.S., 1987, Exploration and development of the Kraftla geothermal area: Jökull, v. 37, p. 13–30.
- Árnason, B., 1977, Hydrothermal systems in Iceland traced by deuterium: Geothermics, v. 5, p. 125–151, doi: 10.1016/0375-6505(77)90015-3.
- Arnórsson, S., 1995a, Geothermal systems in Iceland: Structure and conceptual models–I. High-temperature areas: Geothermics, v. 24, p. 561–602, doi: 10.1016/0375-6505(95)00025-9.
- Arnórsson, S., 1995b, Geothermal systems in Iceland: Structure and conceptual models–II. Low-temperature areas: Geothermics, v. 24, no. 5-6, p. 603–629, doi: 10.1016/0375-6505(95)00026-7.
- Arnórsson, S., Axelsson, G., and Sæmundsson, K., 2008, Geothermal systems in Iceland: Jökull, v. 58, p. 269–302.
- Axelsson, G., 1985, Hydrology and thermomechanics of liquid-dominated hydrothermal systems in Iceland: Oregon State University.
- Axelsson, G., Gunnlaugsson, E., Jónasson, T., and Ólafsson, M., 2010, Low-temperature geothermal utilization in Iceland – Decades of experience: Geothermics, v. 39, p. 329–338, doi: 10.1016/j.geothermics.2010.09.002.



- Baker, E.T., Chen, J.Y., and Morgan, J.P., 1996, The relationship between near-axis hydrothermal cooling and the spreading rate of mid-ocean ridges: *Earth and Planetary Science Letters*, v. 142, p. 137–145, doi: 10.1016/0012-821X(96)00097-0.
- Baker, E., Christophe, H., Chen, Y., Briais, A., Scheirer, D., Walker, S., and Wang, T., 2014, Correlated patterns in hydrothermal plume distribution and apparent magmatic budget along 2500 km of the Southeast Indian Ridge: *Geochemistry, Geophysics, Geosystems*, v. 15, p. 3198–3211, doi: 10.1002/2014GC005344.
- Baker, E.T., Cormier, M.-H., Langmuir, Charles, H., and Zavala, K., 2001, Hydrothermal plumes along segments of contrasting magmatic influence, 15°20'–18°30'N, East Pacific Rise: Influence of axial faulting: *Geochemistry, Geophysics, Geosystems*, v. 2, doi: 10.1029/2000GC000165.
- Baker, E.T., Edmonds, H.N., Michael, P.J., Bach, W., Dick, H.J.B., Snow, J.E., Walker, S.L., Banerjee, N.R., and Langmuir, C.H., 2004, Hydrothermal venting in magma deserts: The ultraslow-spreading Gakkel and Southwest Indian Ridges: *Geochemistry, Geophysics, Geosystems*, v. 5, no. 8, doi: 10.1029/2004GC000712.
- Baker, E.T., and German, C.R., 2004, On the Global Distribution of Hydrothermal Vent Fields, *in* German, C.R., Lin, J., and Parson, L.M. (eds.), *Mid-Ocean Ridges*, American Geophysical Union, p. 245–266.
- Baker, L.L., Rember, W.C., Sprenke, K.F., and Strawn, D.G., 2012, Celadonite in continental flood basalts of the Columbia River Basalt Group: *American Mineralogist*, v. 97, p. 1284–1290, doi: 10.2138/am.2012.4129.
- Bani-Hassan, N., Iyer, K., Rüpke, L.H., and Borgia, A., 2012, Controls of bathymetric relief on hydrothermal fluid flow at mid-ocean ridges: *Geochemistry, Geophysics, Geosystems*, v. 13, p. Q05002, doi: 10.1029/2012GC004041.
- Barriga, F.J.A., Fouquet, Y., Almeida, A., Biscoito, M.J., Charlou, J.-L., Costa, R.L.P., Dias, A., Marques, A.M.S., Miranda, J.M.A., Olu, K., Porteiro, F., and Queiroz, M.G.P.S., 1998, Discovery of the Saldanha Hydrothermal Field on the FAMOUS Segment of the MAE (36°30'N): *Eos Transactions AGU*, v. 79.
- Becker, K., and Herzen, R.P. Von, 1996, Pre-drilling observations of conductive heat flow at the TAG active mound using Alvin: *Proceedings of the Ocean Drilling Program, Initial Reports*, v. 158, p. 23–29.
- Behn, M.D., Buck, W.R., and Sacks, I.S., 2006, Topographic controls on dike injection in volcanic rift zones: *Earth and Planetary Science Letters*, v. 246, p. 188–196, doi: 10.1016/j.epsl.2006.04.005.
- Bjornsson, A., Johnsen, G., Sigurdsson, S., Thorbergsson, G., and Tryggvason, E., 1979, Rifting of the plate boundary in north Iceland 1975–1978: *Journal of Geophysical Research*, v. 84, p. 3029–3038, doi: 10.1016/0198-0254(79)90771-4.
- Bodvarsson, G., 1982, Glaciation and geothermal processes in Iceland: *Jökull*, v. 32, p. 21–28.

- Bodvarsson, G., 1961, Physical characteristics of natural heat resources in Iceland: *Jökull*, v. 11, p. 29–38.
- Bodvarsson, G., 1983, Temperature/flow statistics and thermomechanics of low-temperature geothermal systems in Iceland: *Journal of Volcanology and Geothermal Research*, v. 19, p. 255–280, doi: 10.1016/0377-0273(83)90114-2.
- Bohnenstiehl, D.R., and Kleinrock, M.C., 2000, Fissuring near the TAG active hydrothermal mound , 26N on the Mid-Atlantic Ridge: *Journal of Volcanology and Geothermal Research*, v. 98, p. 33–48, doi: 10.1016/S0377-0273(99)00192-4.
- Cherkaoui, A.S.M., Wilcock, W.S.D., and Baker, E.T., 1997, Thermal fluxes associated with the 1993 diking event on the CoAxial segment, Juan de Fuca Ridge: A model for the convective cooling of a dike: *Journal of Geophysical Research*, v. 102, p. 24,887–24,902, doi: 10.1029/97JB02123.
- Coogan, L., Kasemann, S., and Chakraborty, S., 2005, Rates of hydrothermal cooling of new oceanic upper crust derived from lithium-geospeedometry: *Earth and Planetary Science Letters*, v. 240, p. 415–424, doi: 10.1016/j.epsl.2005.09.020.
- Curewitz, D., and Karson, J.A., 1998, Geological Consequences of Dike Intrusion at Mid-Ocean Ridge Spreading Centers, *in* Buck, R., Karson, J.A., and Lagabrielle, Y. (eds.), *Faulting and Magmatism at Mid-Ocean Ridges*, Geophysical Monograph 106, p. 117–137.
- Delaney, P.T., 1987, Heat transfer during emplacement and cooling of mafic dykes, *in* Halls, H.C. and Fahrig, W.F. (eds.), *Mafic Dyke Swarms*, Geological Association of Canada, p. 31–46.
- Devey, C.W., German, C.R., Haase, K.M., Lackschewitz, K.S., and Melchert, B., 2010, The relationships between volcanism , tectonism , and hydrothermal activity on the southern equatorial Mid-Atlantic Ridge, *In*: Rona, P., Devey, C. W., Dymont, J., and Murton, B., [Eds.], *Diversity of hydrothermal systems on slow spreading ocean ridges*, American Geophysical Union, Washington D.C., p. 133–152, doi: 10.1029/GM188.
- Einarsson, T., 1942, Über das Wesen der Heissen Quellen Islands: mit einer Übersicht über die Tektonik des mittleren Nordislands: *Soc. Sci. Islandica*, v. 26, pp. 91.
- Fontaine, F.J., Rabinowicz, M., and Boulègue, J., 2001, Permeability changes due to mineral diagenesis in fractured crust: implications for hydrothermal circulation at mid-ocean ridges: *Earth and Planetary Science Letters*, v. 184, p. 407–425, doi: 10.1016/S0012-821X(00)00332-0.
- Fouquet, Y., R. Knott, R., Cambon, P., Fallick, A., Rickard, D. and Desbruyeres, D., 1996, Formation of large sulfide mineral deposits along fast spreading ridges. Example from off-axial deposits at 12°43'N on the East Pacific Rise: *Earth and Planetary Science Letters*, v. 144, p. 147–162, doi: 10.1016/0012-821X(96)00142-2..
- German, C.R., Baker, E.T., Mevel, C., Tamaki, K., and Team, the F.S., 1998, Hydrothermal activity along the southwest Indian ridge: *Nature*, v. 395, p. 490–493, doi: 10.1038/26730.

- German, C.R., Bennett, S. a., Connelly, D.P., Evans, A.J., Murton, B.J., Parson, L.M., Prien, R.D., Ramirez-Llodra, E., Jakuba, M., Shank, T.M., Yoerger, D.R., Baker, E.T., Walker, S.L., and Nakamura, K., 2008, Hydrothermal activity on the southern Mid-Atlantic Ridge: Tectonically- and volcanically-controlled venting at 4–5°S: *Earth and Planetary Science Letters*, v. 273, p. 332–344, doi: 10.1016/j.epsl.2008.06.048.
- German, C.R., Briem, J., Chin, C., Danielsen, M., Holland, S., James, R., Jónsdóttir, A., Ludford, E., Moser, C., Ólafsson, J., Palmer, M.R., and Rudnicki, M.D., 1994, Hydrothermal activity on the Reykjanes Ridge: the Steinahóll vent-field at 63°06'N: *Earth and Planetary Science Letters*, v. 121, no. 3-4, p. 647–654, doi: 10.1016/0012-821X(94)90098-1.
- German, C., Campbell, A.C., and Edmond, J.M., 1991, Hydrothermal scavenging at the Mid-Atlantic Ridge: Modification of trace element dissolved fluxes: *Earth and Planetary Science Letters*, v. 107, p. 101–114, doi: 10.1016/0012-821X(91)90047-L.
- German, C.R., Parson, L.M., and Team, H.S., 1996, Hydrothermal exploration near the Azores Triple Junction: tectonic control of venting at slow-spreading ridges?: *Earth and Planetary Science Letters*, v. 138, p. 93–104, doi: 10.1016/0012-821X(95)00224-Z.
- Gracia, E., Charlou, J.-L., Radford-Knoery, J., and Parson, L.M., 2000, Non-transform offsets along the Mid-Atlantic Ridge south of the Azores (38°N–34°N): ultramafic exposures and hosting of hydrothermal vents: *Earth and Planetary Science Letters*, v. 177, p. 89–103, doi: 10.1016/S0012-821X(00)00034-0.
- Gudmundsson, A., 2000, Active fault zones and groundwater flow: *Geophysical Research Letters*, v. 27, no. 18, p. 2993–2996, doi: 10.1029/1999GL011266.
- Gudmundsson, A., 1990, Dyke emplacement at divergent plate boundaries, *in* Parker, A.J., Rickwood, P.C., and Tucker, D.H., (eds.), *Mafic Dykes and Emplacement Mechanisms, Project 257: Publication*, Balkema, Rotterdam, p. 47–62.
- Gudmundsson, A., 1983, Form and dimensions of dykes in eastern Iceland: *Tectonophysics*, v. 95, p. 295–307, doi: 10.1016/0040-1951(83)90074-4.
- Gudmundsson, A., 2003, Surface stresses associated with arrested dykes in rift zones: *Bulletin of Volcanology*, v. 65, p. 606–619, doi: 10.1007/s00445-003-0289-7.
- Gudmundsson, A., 1984, Tectonic aspect of dykes in northwestern Iceland: *Jökull*, , no. 34, p. 81–96.
- Gudmundsson, A., Bergerat, F., and Angelier, J., 1996, Off-rift and rift-zone palaeostresses in Northwest Iceland: *Tectonophysics*, v. 255, p. 211–228.
- Hald, N., Noe-Nygaard, A., and Pedersen, A.K., 1971, The Króksfjörður central volcano in northwest Iceland: *Acta Naturalia Islandica*, v. II, p. 40.
- Hannington, M.D., Jamieson, J.W., Monecke, T., and Petersen, S., 2010, Modern seafloor massive sulfides and base metal resources: toward an estimate of global seafloor massive sulfide potential: *Society of Economic Geologists Special Publication*, v. 15, p. 317–338.

- Hannington, M.D., Jonasson, I.R., Herzig, P.M., and Petersen, S., 1995, Physical and chemical processes of seafloor mineralization at mid-ocean ridges, *in* Humphirs, S.E., Zierenberg, R.A., Mullineaux, L.S., and Thomson, R.E. eds., *Seafloor Hydrothermal Systems: Physical, Chemical, Biological, and Geological Interactions*, AGU Geophys. Monogr. 91, p. 115–157.
- Haymon, R.M., Baker, E.T., Resing, J.A., White, S.M., Macdonald, K.C., and TEAM, T.G., 2007, Hunting for Hydrothermal Vents Along the Galápagos Spreading Center: *Oceanography*, v. 20, p. 100–107.
- Haymon, R.M., Fornari, D.J., Edwards, M.H., Carbotte, S., Wright, D., and Macdonald, K.C., 1991, Hydrothermal vent distribution along the East Pacific Rise crest (9°09 “-54” N) and its relationship to magmatic and tectonic processes on fast-spreading mid-ocean ridges: *Earth and Planetary Science Letters*, v. 104, p. 513–534, doi: 10.1016/0012-821X(91)90226-8.
- Haymon, R.M., White, S.M., Baker, E.T., Anderson, P.G., Macdonald, K.C., and Resing, J. A., 2008, High-resolution surveys along the hot spot-affected Galápagos Spreading Center: 3. Black smoker discoveries and the implications for geological controls on hydrothermal activity: *Geochemistry, Geophysics, Geosystems*, v. 9, p. Q120006, doi: 10.1029/2008GC002114.
- Johannesson, H., and Sæmundsson, K., 2009, *Geological Map of Iceland: Tectonics [Map]*, 1: 600 000, Náttúruminjasafn Íslands, Reykjavík.
- Kelley, D.S., Baross, J. a., and Delaney, J.R., 2002, Volcanoes, Fluids, and Life At Mid-Ocean Ridges Spreading Centers: *Annual Review of Earth and Planetary Sciences*, v. 30, p. 385–491, doi: 10.1146/annurev.earth.30.091201.141331.
- Khodayar, M., and Björnsson, S., 2014, Fault ruptures and geothermal effects of the second earthquake, 29 May 2008, South Iceland Seismic Zone: *Geothermics*, v. 50, p. 44–65, doi: 10.1016/j.geothermics.2013.07.002.
- Khodayar, M., Björnsson, S., Einarsson, P., and Franzson, H., 2010, Effect of tectonics and earthquakes on geothermal activity near plate boundaries: A case study from South Iceland: *Geothermics*, v. 39, no. 3, p. 207–219, doi: 10.1016/j.geothermics.2010.06.003.
- Khodayar, M., Markusson, S.H., and Einarsson, P., 2006, GPS-mapping of geothermal areas in West Iceland and tectonic interpretation, Phase 2: Klettur-Runnar - An overview: *Orkustofnun Report ISOR-06038*, Reykjavík, pp.13.
- Kjartansson, G., 1969, *Geological map of Iceland; Sheet 1: North-West Iceland [Map]*, 1: 250 000, Náttúruminjasafn Íslands, Reykjavík.
- Kristjánsson, L., 1968, The Paleomagnetism and Geology of North-Western Iceland: *Earth and Planetary Science Letters*, v. 4, p. 448–450, doi: 10.1016/0012-821X(68)90022-8.
- Kristjánsson, L., and Jóhannesson, H., 1996, Stratigraphy and Paleomagnetism of the Lava Pile South of Ísafjarðardjúp, NW- Iceland: *Jökull*, v. 44, p. 3–16.

- Langmuir, C., Humphris, S., Fornari, D., Van Dover, C., Von Damm, K., Tivey, M.K., Colodner, D., Charlou, J.-L., Desonie, D., Wilson, C., Fouquet, Y., Klinkhammer, G., and Bougault, H., 1997, Hydrothermal vents near a mantle hot spot: the Lucky Strike vent field at 37°N on the Mid-Atlantic Ridge: *Earth and Planetary Science Letters*, v. 148, p. 69–91, doi: 10.1016/S0012-821X(97)00027-7.
- Lawver, L.A., and Müller, D.R., 1994, Iceland hotspot track: *Geology*, v. 22, p. 311–314, doi: 10.1130/0091-7613(1994)022<0311:IHT>2.3.CO;2.
- Melchert, B., Devey, C.W., German, C.R., Lackschewitz, K.S., Seifert, R., Walter, M., Mertens, C., Yoerger, D.R., Baker, E.T., Paulick, H., and Nakamura, K., 2008, First evidence for high-temperature off-axis venting of deep crustal/mantle heat: The Nibelungen hydrothermal field, southern Mid-Atlantic Ridge: *Earth and Planetary Science Letters*, v. 275, p. 61–69, doi: 10.1016/j.epsl.2008.08.010.
- Moorbath, S., Sigurdsson, H., and Goodwin, R., 1968, K-Ar ages of the oldest exposed rocks in Iceland: *Earth and Planetary Science Letters*, v. 4, p. 197–205, doi: 10.1016/0012-821X(68)90035-6.
- Neuhoff, P.S., Fridriksson, T., Arnórsson, S., and Bird, D.K., 1999, Porosity evolution and mineral paragenesis during low-grade metamorphism of basaltic lavas at Teigarhorn, eastern Iceland: *American Journal of Science*, v. 299, p. 467–501, doi: 10.2475/ajs.299.6.467.
- Palmason, G., Arnórsson, S., Fridleifsson, I.B., Kristmannsdóttir, H., Sæmundsson, K., Stefansson, V., Steingrímsson, B., Tomasson, J., Kristjánsson, L., and Temp, C., 1979, The Iceland crust: Evidence from drillhole data on structure and processes, *in* *Deep Drilling Results in the Atlantic Ocean: Oceanic Crust*, American Geophysical Union, Maurice Ewing Ser., p. 43–65.
- Petersen, S., Kuhn, K., Kuhn, T., Augustin, N., Hékinian, R., Franz, L., and Borowski, C., 2009, The geological setting of the ultramafic-hosted Logatchev hydrothermal field (14°45'N, Mid-Atlantic Ridge) and its influence on massive sulfide formation: *Lithos*, v. 112, p. 40–56, doi: 10.1016/j.lithos.2009.02.008.
- Petrucci, R.H., Herring, G.F., Madura, J.D., and Bissonette, C., 2011, *General Chemistry: Principles and Modern Applications*: Pearson Prentice Hall, New York.
- Pollard, D.D., Delaney, P.T., Duffield, W.A., Endo, E.T., and Okamura, A.T., 1983, Surface deformation in volcanic rift zones: *Tectonophysics*, v. 94, no. 1-4, p. 541–584, doi: 10.1016/0040-1951(83)90034-3.
- Qin, R., and Buck, W.R., 2008, Why meter-wide dikes at oceanic spreading centers?: *Earth and Planetary Science Letters*, v. 265, p. 466–474, doi: 10.1016/j.epsl.2007.10.044.
- Ramondenc, P., Germanovich, L.N., Von Damm, K.L., and Lowell, R.P., 2006, The first measurements of hydrothermal heat output at 9°50'N, East Pacific Rise: *Earth and Planetary Science Letters*, v. 245, p. 487–497, doi: 10.1016/j.epsl.2006.03.023.
- Rubin, M., 1992, Dike-induced faulting and graben subsidence in volcanic rift zones: *Journal of Geophysical Research*, v. 97, p. 1839–1858, doi: 10.1029/91JB02170.



- Sæmundsson, K., 1979, Outline of the geology of Iceland: Jökull, v. 29, p. 7–28.
- Schilling, J.-G., 1973, Iceland Mantle Plume: Geochemical Study of Reykjanes Ridge: Nature, v. 242, p. 565–571, doi: 10.1038/242565a0.
- Schramm, B., 2004, Color atlas of low-temperature alteration features in basalts from the Southern East Pacific Rise: Geochemistry, Geophysics, Geosystems, v. 5, p. Q06006, doi: 10.1029/2003GC000665.
- Searle, R.C., Field, P.R., and Owens, R.B., 1994, Segmentation and nontransform ridge offset on the Reykjanes Ridge near 58°N: Journal of Geophysical Research, v. 99, p. 159–172, doi: 10.1029/94JB01549.
- Sigurdsson, H., 1967, Dykes, fractures and folds in the basalt plateau of western Iceland, in Björnsson, S. ed., Iceland and Mid-ocean Ridges, Vísindafélag Íslendinga, Soc. Sci. Islandica, p. 162–169.
- Talwani, M., Windisch, C.C., and Langseth, M.G., 1971, Reykjanes Ridge crest: A detailed geophysical study: Journal of Geophysical Research, v. 76, p. 473–577, doi: 10.1029/JB076i002p00473.
- Thordarson, T., and Höskuldsson, Á., 2002, Iceland: Classic Geology in Europe 3, Terra, Harpenden, pp. 200.
- Titarenko, S.S., and McCaig, A.M., 2015, Modelling the Lost City hydrothermal field: influence of topography and permeability structure: Geofluids, pp. 15, doi: 10.1111/gfl.12151.
- Torfason, H., 2003a, Geothermal Map of Iceland [Map], 1: 500 000, Náttúruminjasafn Íslands og Orkustofnun, Reykjavík.
- Torfason, H., 2003b, Jarðhitakort af Íslandi og gagnasafn um jarðhita: Orkustofnun Report OS-2003/062, Reykjavík, pp. 168.
- Tryggvason, B.Y.E., 1973, Seismicity, earthquake swarms, and plate boundaries in the Iceland region: Bulletin of the Seismological Society of America, v. 63, no. 4, p. 1327–1348.
- Turcotte, D.L., and Schubert, G., 1982, Geodynamics: Applications of Continuum Physics to Geological Problems: John Wiley & Sons, New York.
- Weir, N.R., White, R.S., Brandsdóttir, B., Einarsson, P., Shimamura, H., Shiobara, H., and Team, R.F., 2001, Crustal structure of the northern Reykjanes Ridge and Reykjanes Peninsula, southwest Iceland: Journal of Geophysical Research, v. 106, p. 6347–6368, doi: 10.1029/2000JB900358.
- White, R.S., Drew, J., Martens, H.R., Key, J., Soosalu, H., and Jakobsdóttir, S.S., 2011, Dynamics of dyke intrusion in the mid-crust of Iceland: Earth and Planetary Science Letters, v. 304, no. 3-4, p. 300–312, doi: 10.1016/j.epsl.2011.02.038.

- Wilcock, W.S.D., and Delaney, J.R., 1996, Mid-ocean ridge sulfide deposits: Evidence for heat extraction from magma chambers or cracking fronts?: *Earth and Planetary Science Letters*, v. 145, p. 49–64, doi: 10.1016/S0012-821X(96)00195-1.
- Wolfe, C.J., Purdy, G.M., Toomey, R., and Solomon, C., 1995, Microearthquake characteristics and crustal velocity structure at 29°N on the Mid-Atlantic Ridge: The architecture of a slow spreading segment: *Journal of Geophysical Research*, v. 100, p. 24449–24472, doi: 10.1029/95JB02399.



## Chapter 4

$^{40}\text{Ar}/^{39}\text{Ar}$  dating of dikes from the Westfjords, Iceland: insights into timing of hydrothermal activity in the off-axis oceanic crust

This chapter consists of a manuscript which will be submitted at the Journal of Geophysical Research: Solid Earth.

Authors: Pałgan Dominik<sup>1\*</sup>, Devey Colin W.<sup>1</sup> and Wartho Jo-Anne<sup>1</sup>,

<sup>1</sup>GEOMAR, Helmholtz Centre for Ocean Research Kiel, Wischhofstr. 1–3, 24148, Kiel, Germany

Declaration of contributions: C.W.D. and D.P. proposed the study. D.P. carried field work in Iceland, collected and prepared samples for  $^{40}\text{Ar}/^{39}\text{Ar}$  dating and wrote the manuscript. J-.A.W. analyzed the samples and calculated the  $^{40}\text{Ar}/^{39}\text{Ar}$  ages. All co-authors discussed the results, interpreted them and contributed to the discussion in the manuscript.

## 4 $^{40}\text{Ar}/^{39}\text{Ar}$ dating of dikes from the Westfjords, Iceland: insights into timing of hydrothermal activity in the off-axis oceanic crust

### 4.1 Introduction to $^{40}\text{Ar}/^{39}\text{Ar}$ dating

The K-Ar and  $^{40}\text{Ar}/^{39}\text{Ar}$  dating techniques are based upon a decay of the naturally occurring radioactive isotope of potassium ( $^{40}\text{K}$ ) to  $^{40}\text{Ca}$  (89.5%) and  $^{40}\text{Ar}$  (10.5%) (Merrhue and Turner, 1966). The K-Ar dating technique was developed in the 1950's and requires analysis of two aliquots of the same sample for (1) photometry/atomic absorption spectroscopy measurement of  $^{40}\text{K}$ , and (2) for ultra-high vacuum heating and noble gas mass spectrometry measurement of the atmospheric and radiogenic isotopes of argon ( $^{36}\text{Ar}$ ,  $^{38}\text{Ar}$  and  $^{40}\text{Ar}$ ). In contrast to the K-Ar method, the  $^{40}\text{Ar}/^{39}\text{Ar}$  dating technique only requires one aliquot of a geological sample. To achieve this, the K-bearing geological samples are irradiated with fast neutrons in a nuclear reactor, whereby another isotope of potassium ( $^{39}\text{K}$ ) is converted to  $^{39}\text{Ar}$ , with a half-life of 269 years, thus becoming a proxy-parent for  $^{40}\text{K}$ . Other Ar isotopes are produced by interfering reactions in the reactor (e.g.,  $^{37}\text{Ar}$  from calcium, and  $^{38}\text{Ar}$  from chlorine), which requires monitoring via the irradiation of pure Ca- and K-bearing salts and glasses, to allow corrections to be applied to the data (e.g., McDougall and Harrison, 1999). The irradiation flux duration is optimized for the age and K- and Ca-contents of the samples, and appropriate age standards are included in the canisters with the unknown samples.

The K-Ar and  $^{40}\text{Ar}/^{39}\text{Ar}$  dating techniques yield cooling ages, defined by the different Ar closure temperatures for each mineral, which is also grain size and cooling rate dependent (Dodson, 1973). The validity of  $^{40}\text{Ar}/^{39}\text{Ar}$  cooling ages is dependent on a number of assumptions: 1) the decay of the parental nuclide ( $^{40}\text{K}$ ) is independent of its physical state and is not affected by pressure and temperature; 2) all the radiogenic  $^{40}\text{Ar}$  ( $^{40}\text{Ar}^*$ ) comes from the radioactive decay of active  $^{40}\text{K}$  since the “K-Ar decay clock” became closed, with no subsequent gain/loss of  $^{40}\text{K}$  or  $^{40}\text{Ar}$ ; 3) the  $^{40}\text{K}/\text{K}$  ratio is constant in samples; 4) any non-radiogenic  $^{40}\text{Ar}$  in terrestrial samples can be determined by assuming a constant atmospheric  $^{40}\text{Ar}/^{36}\text{Ar}$  ratio of 295.5, which can be monitored using isochron and inverse isochron plots (e.g., Steiger and Jäger, 1977; McDougall and Harrison, 1999).

The  $^{40}\text{Ar}/^{39}\text{Ar}$  age calculation is described by the equation:

$$t = \frac{1}{\lambda} \ln \left[ 1 + J \frac{^{40}\text{Ar}^*}{^{39}\text{Ar}} \right] \quad (1)$$



where  $t$  is the time since Ar closure,  $\lambda$  is the total decay constant of  $^{40}\text{K}$  to  $^{40}\text{Ar}$ ,  $^{40}\text{Ar}^*/^{39}\text{Ar}$  is the ratio of the radiogenic daughter product ( $^{40}\text{Ar}^*$ ) to the proxy-parent ( $^{39}\text{Ar}_K$ ) isotope, and  $J$  is a dimensionless irradiation-related parameter that is determined from analyses of a mineral standard with a known age, thus monitoring the neutron flux variation along a canister during fast-neutron irradiation.

It is important to stress that step-heating and single crystal fusion  $^{40}\text{Ar}/^{39}\text{Ar}$  ages are calculated by assuming that all the  $^{40}\text{Ar}^*$  in the sample was derived from the decay of  $^{40}\text{K}$ , after correcting for (1) mass spectrometer detector baselines, (2) mass spectrometer and extraction line blanks, (3) interfering argon isotopes produced via fast neutron interactions with Ca, K, Ar and Cl in the sample during irradiation, and (4) for the presence of atmospheric  $^{40}\text{Ar}$ . Correcting for the presence of atmospheric  $^{40}\text{Ar}$  in a sample to yield the quantity of  $^{40}\text{Ar}^*$  is undertaken by measuring the  $^{36}\text{Ar}$  peak signal of the sample and using the atmospheric  $^{40}\text{Ar}/^{36}\text{Ar}$  ratio of air (i.e., 295.5; Steiger & Jäger, 1977), according to the following equation:

$$^{40}\text{Ar}^* = ^{40}\text{Ar}_{\text{total}} - (^{36}\text{Ar} \times 295.5) \quad (2)$$

However, not all samples contain a simple mix of atmospheric and radiogenic  $^{40}\text{Ar}$ , as excess  $^{40}\text{Ar}$  can also be present. Excess argon is defined as a component of argon incorporated into the sample by processes other than in situ radioactive decay of  $^{40}\text{K}$ . It commonly comes from Ar-saturated fluids that interact with the sample (e.g., Cumbest et al., 1994). The term “trapped argon” is commonly used to define a mix of atmospheric argon, with or without excess argon (e.g., Kuiper, 2002). Therefore, the simple “trapped argon = atmospheric argon” assumption used for the determination of  $^{40}\text{Ar}/^{39}\text{Ar}$  step-heating and total fusion ages, can be verified using both normal and inverse isochron plots. Normal isochron plots display the  $^{39}\text{Ar}/^{36}\text{Ar}$  ratio on the x-axis and the  $^{40}\text{Ar}/^{36}\text{Ar}$  ratio on the y-axis, with  $^{36}\text{Ar}$  as the common denominator. Inverse isochron plots instead show the  $^{39}\text{Ar}/^{40}\text{Ar}$  ratio on the x-axis, and the  $^{36}\text{Ar}/^{40}\text{Ar}$  ratio on the y-axis for each of the analyses, using  $^{40}\text{Ar}$  as the divisible denominator (a hypothetical example is shown in Fig. 33).  $^{36}\text{Ar}$  in samples is commonly present in low concentrations, hence any uncertainties in the measurements introduces large errors on both axes of normal isochron plots, where  $^{36}\text{Ar}$  is used as the denominator. For this reason, inverse isochron plots, which use  $^{40}\text{Ar}$  as the denominator, where  $^{40}\text{Ar}$  is commonly the largest argon peak measured with the smallest uncertainties, are preferred over normal isochron plots in  $^{40}\text{Ar}/^{39}\text{Ar}$  dating of terrestrial samples.

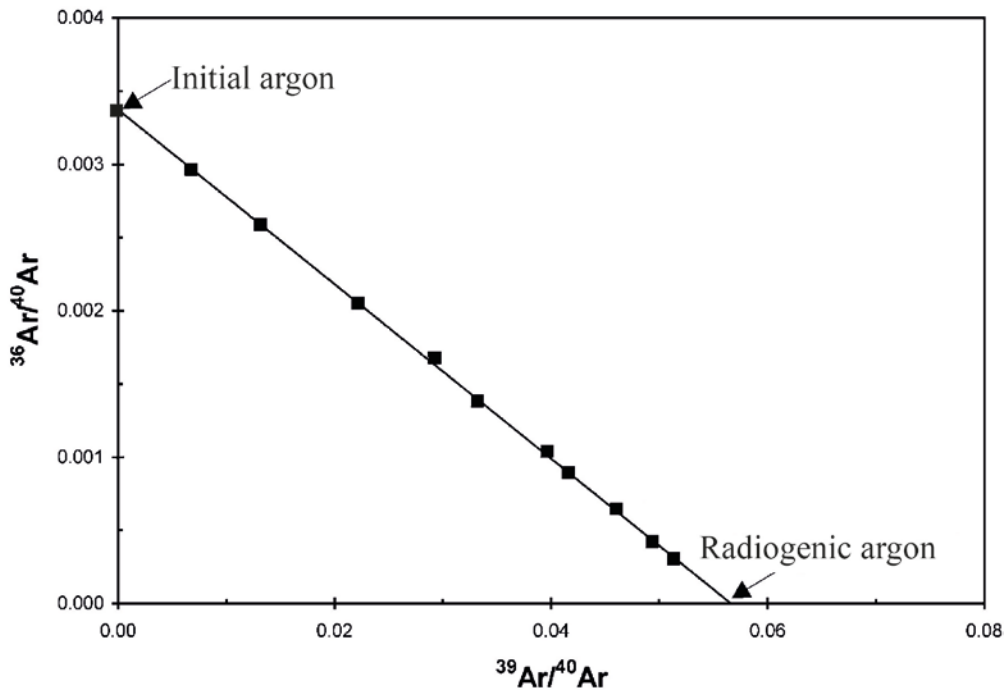


Fig. 33 Example of a hypothetical inverse isochron plot used for  $^{40}\text{Ar}/^{39}\text{Ar}$  dating determination. The isochron regression line intercept with the y-axis represents the trapped initial  $^{36}\text{Ar}/^{40}\text{Ar}$  argon component of the sample (atmospheric and excess Ar), while the intercept with the x-axis represents the radiogenic Ar component, yielding a  $^{39}\text{Ar}/^{40}\text{Ar}$  ratio from which the inverse isochron age can be calculated. Figure modified from Kuiper (2002).

Each individual point on an inverse isochron plot represents a different temperature step analysis from a step-heating experiment performed on the sample (Fig. 33). The position of each of the analyses depends on the ratio of trapped argon relative to radiogenic argon. Therefore, measurements with a high radiogenic component plot close to the  $^{39}\text{Ar}/^{40}\text{Ar}$  x-axis, while measurements with a high trapped component plot close to the  $^{36}\text{Ar}/^{40}\text{Ar}$  y-axis (Fig. 33). If the gas released during the step-heating experiment is a simple two-component mixture of trapped and radiogenic argon then the points will plot along a line, and the data can be regressed and an isochron line can be fitted (Fig. 33 and Kuiper, 2002). If the intercept of the isochron line with the  $^{36}\text{Ar}/^{40}\text{Ar}$  axis (i.e., at  $^{39}\text{Ar}/^{40}\text{Ar} = 0$ ) occurs within  $2\sigma$  errors on an initial  $^{36}\text{Ar}/^{40}\text{Ar}$  ratio of 1/295.5 (the composition of atmospheric argon, Steiger and Jäger, 1977), then all the trapped  $^{40}\text{Ar}$  has an atmospheric origin. In this case, the inverse isochron age will match the  $^{40}\text{Ar}/^{39}\text{Ar}$  step-heated ages. However, if the  $^{36}\text{Ar}/^{40}\text{Ar}$  ratio of the isochron line intercept is lower, yielding an inverted initial  $^{40}\text{Ar}/^{36}\text{Ar}$  ratio of  $>295.5$ , then excess  $^{40}\text{Ar}$  is present in the sample, in addition to atmospheric argon (Kuiper, 2002). Therefore, if excess  $^{40}\text{Ar}$  is homogeneously distributed within a  $^{40}\text{Ar}/^{39}\text{Ar}$  step-heated sample, its effects can be identified using inverse isochron plots and thus an “excess  $^{40}\text{Ar}$  corrected age” can be determined. In this case, the determined inverse isochron age will be younger than the  $^{40}\text{Ar}/^{39}\text{Ar}$  step-heated ages, which are calculated assuming that no excess Ar is present.

However, if excess  $^{40}\text{Ar}$  is heterogeneously distributed within the sample, a precise age determination is impossible using inverse isochron plots (e.g., Pickles et al., 1997).

Excess  $^{40}\text{Ar}$  belongs to a broader group of potential  $^{40}\text{Ar}/^{39}\text{Ar}$  dating complications, termed extraneous  $^{40}\text{Ar}$ , that also includes inherited  $^{40}\text{Ar}$  (McDougall and Harrison, 1999 and references therein). Inherited  $^{40}\text{Ar}$  is defined as being derived from the incorporation of older xenocrystic material into a sample, thus yielding older or mixed origin  $^{40}\text{Ar}/^{39}\text{Ar}$  ages. For example, Devey and Stephens (1992) showed that Deccan (60 Ma) dikes intruded into Seychelles (2000 Ma) crust all have probably inherited  $^{40}\text{Ar}$  from the surrounding country bedrock and all pre-existing radiogenic argon failed to completely outgas probably because these dikes have not reached the surface. However, McDougall et al. (1984) suggested that such degassing failure does not seem to be the problem with Icelandic lavas.

$^{40}\text{Ar}/^{39}\text{Ar}$  ages can also be affected by  $^{37}\text{Ar}$  and  $^{39}\text{Ar}$  recoil in samples, which occurs during the transmutation reaction ( $^{39}\text{K}(\text{n,p})^{39}\text{Ar}$ , where (n,p) is 'neutron in, proton out') from fast-neutron bombardment, with resulting recoil distances of up to  $\sim 0.4\ \mu\text{m}$  in fine-grained or interlayered minerals (Turner and Cadogan, 1974). This effect is mostly observed in  $^{40}\text{Ar}/^{39}\text{Ar}$  measurements of fine-grained clay minerals (Foland et al., 1983), altered minerals (Lo and Onstott, 1989), and basaltic rocks (Féraud and Courtillot, 1994).  $^{39}\text{Ar}$  and  $^{37}\text{Ar}$  recoil effects can be minimized by careful evaluation and selection of material during sample preparation.

The  $^{40}\text{Ar}/^{39}\text{Ar}$  furnace or laser step-heating  $^{40}\text{Ar}/^{39}\text{Ar}$  dating technique can allow the identification of different K-bearing mineral phases within a sample as a result of the minerals different breakdown temperatures over temperatures of  $\sim 300$  to  $>1500^\circ\text{C}$ , and by examination of the  $^{37}\text{Ar}_{\text{Ca}}/^{39}\text{Ar}_{\text{K}}$  and  $^{38}\text{Ar}_{\text{Cl}}/^{39}\text{Ar}_{\text{K}}$  ratios from each analysis. Step-heating of  $^{40}\text{Ar}/^{39}\text{Ar}$  samples can result in the decrepitation of excess- $^{40}\text{Ar}$ -bearing fluids inclusions within a sample at low temperatures, which can result in high initial  $^{40}\text{Ar}/^{39}\text{Ar}$  ages observed in some age spectra. In addition, melt and solid inclusions are degassed at high temperatures and can be responsible for the release of the excess  $^{40}\text{Ar}$ , which causes the high-temperature older ages in an age spectrum (Boven et al., 2001). Samples with low potassium contents (e.g., plagioclases and amphiboles) are extremely susceptible to the effects of excess  $^{40}\text{Ar}$ , and many samples preserve disturbed or 'U-shaped'  $^{40}\text{Ar}/^{39}\text{Ar}$  age spectra (e.g., Wartho et al., 1996), for example, because of the Ar solubility and partitioning behavior between different fluids, melts and minerals, melt and fluid inclusions can contain  $\sim 4\ 000$  and  $\sim 500\ 000$  times more  $^{40}\text{Ar}$ , respectively, than hosting plagioclase crystals, even though the phases all crystallized from the same source (Kelley, 2002; Wartho et al., 2013).

Plagioclases in igneous rocks have been widely and successfully dated using both the K-Ar and  $^{40}\text{Ar}/^{39}\text{Ar}$  dating methods to reveal geologically meaningful ages (e.g., McDougall and Harrison, 1999). The low potassium contents of plagioclases (typically <0.01 to ~0.5%) make them easily susceptible to excess  $^{40}\text{Ar}$  effects, however, plagioclases have been successfully  $^{40}\text{Ar}/^{39}\text{Ar}$  dated from dredged and altered seafloor basalt samples (e.g., Pringle et al., 1991).

## 4.2 Previous dating work in Westfjords

The first attempt to date rocks of the Westfjords peninsula were undertaken by Moorbath et al. (1968). They used the K-Ar method to date 4 samples from a borehole located just west of the Isafjörður town (Fig. 34). Rocks were collected from 500-600 m above sea level (above the zeolite alteration zone) and as deep as 1000 m above the base of the exposed succession of the peninsula. The K-Ar ages from the 4 samples (each sample was dated in duplicate) ranged from  $14.2 \pm 2.0$  to  $16.5 \pm 2.0$  Ma ( $2\sigma$  errors) yielding a weighted mean age from 3 samples of  $16.0 \pm 0.6$  Ma ( $2\sigma$ ). Using the  $^{40}\text{K}$  decay constants and  $^{40}\text{K}/\text{K}$  ratio of Steiger and Jäger (1977) and the ArAR age conversion software of Mercer and Hodges (2016), this Moorbath et al. (1968)  $16.0 \pm 0.6$  Ma average age was converted to  $16.4 \pm 0.6$  Ma ( $2\sigma$ ) and will be quoted from here onwards. This K-Ar age was significantly younger than expected, which opened the discussion about the formation genesis of Iceland. Despite this early sensational finding, very few radiometric ages have been obtained from the region. The most extensive dating study, along with the stratigraphic mapping, of the lava pile across Westfjords was carried out by McDougall et al. (1984). They mapped a ~7 km thick lava sequence along the western and eastern peninsulas and obtained K-Ar ages of >70 lava flows (in 19 short profiles), and the average ages are shown in Fig. 34. Although some of the samples were difficult to analyze, especially from the western side of the NW peninsula, McDougall et al. (1984) concluded that the investigated sequence was erupted between  $13.60 \pm 0.58$  Ma (west) and  $8.00 \pm 0.52$  Ma (east) ( $2\sigma$ ). Later, Kristjánsson and Jóhannesson (1996) estimated that the lava sequence located along a 35 km profile, located south of Isafjardardjup fjord (the A'-B' profile in Fig. 34), was erupted between  $13.57 \pm 0.60$  Ma (location A') and  $11.78 \pm 0.38$  Ma (location B',  $2\sigma$ ). They used paleomagnetic polarity patterns, the petrography of the lava flows, and sedimentary horizons (previously dated at ~12 Ma, McDougall et al., 1984) that are exposed below the location B and B' lavas; Fig. 34) to correlate a ~2.6 km composite section located further east (profile A-B on Fig. 34) with the central 2.8 km profile (A'-B' profile in Fig. 34) of a total 4.1 km thick segment of the western peninsula studied by McDougall et al. (1984). A detailed description of the correlations can

be found in Kristjánsson and Jóhannesson (1996). In the latest dating study, Riishuus et al. (2013) obtained >50 new  $^{40}\text{Ar}/^{39}\text{Ar}$  lava whole rock ages across the peninsula, including the rocks originally investigated by Moorbath et al. (1968). Riishuus et al. (2013) concluded that the lavas located both below and above the previously-mentioned sedimentary horizon/unconformity were erupted between ~17-16 Ma and ~15.0-14.5 Ma, respectively. The Riishuus et al. (2013) reference is only a short American Geophysical Union abstract, and does not list errors on the ages or the decay constants used, etc. However, the  $^{40}\text{Ar}/^{39}\text{Ar}$  analyses were undertaken at the Oregon State University Geochronology Laboratory, and a co-author publication from the same year (Duncan and Al-Amri, 2013) lists the  $^{40}\text{K}$  decay constants used. Therefore, the Riishuus et al. (2013) age ranges of 17-16 Ma and 14.5-15.0 Ma have been recalculated to 16.8-15.8 Ma and 14.8-14.3 Ma, respectively, using the Steiger and Jäger (1977) decay constants and the ArAr computer software of Mercer and Hodges (2016). The new below-unconformity 16.8-15.8 Ma  $^{40}\text{Ar}/^{39}\text{Ar}$  ages are similar to the K-Ar age of  $16.4 \pm 0.6$  Ma ( $2\sigma$ ) from a borehole sample presented by Moorbath et al. (1968). However, these 16.8-15.8 Ma K-Ar and  $^{40}\text{Ar}/^{39}\text{Ar}$  ages are ~0.5-1.5 Ma older than the oldest below-unconformity K-Ar age of  $15.32 \pm 0.34$  Ma, reported by McDougall et al. (1984) in this region (Fig. 34). In addition, the above-unconformity 14.8-14.3 Ma ages of Riishuus et al. (2013) are also ~0.7-1.2 Ma older than the oldest above-unconformity McDougall et al. (1984) K-Ar lava age of  $13.60 \pm 0.58$  Ma from the NW Peninsula. This may suggest that the McDougall et al. (1984) K-Ar ages from older studies should perhaps be re-determined using the  $^{40}\text{Ar}/^{39}\text{Ar}$  dating technique and the previous polarity correlations of Kristjánsson and Jóhannesson (1996) should be reassessed. Dike intrusions have never been dated in Westfjords, therefore, until now their ages could only be estimated based on the determined or extrapolated ages of the hosting lava flows determined or estimated from previous studies.



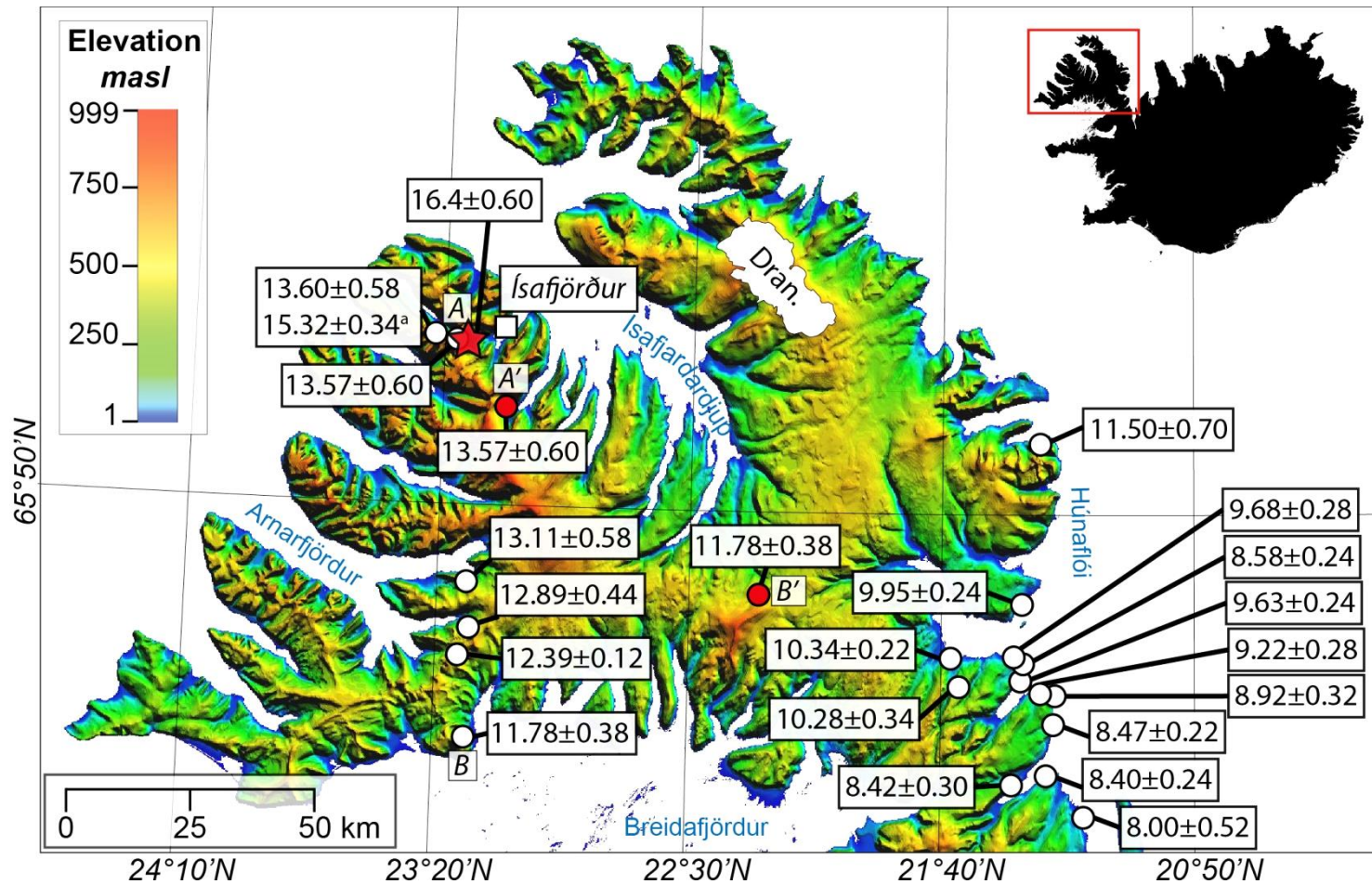


Fig. 34 The Westfjords Peninsula, NW Iceland, showing location and mean ages (in Ma with  $2\sigma$  errors) of lavas dated in the area. The first K-Ar dating in the region by Moorbath et al. (1968) is shown by blue star (with age recalculated using the values of Steiger and Jäger (1977)). Later, Riishuus et al. (2013) dated lavas from the same location using the  $^{40}\text{Ar}/^{39}\text{Ar}$  method and yielded similar ages to Moorbath et al. (1968), i.e., 16.8-15.8 Ma. Along the west and east parts of the peninsula, McDougall et al. (1984) dated ~7 km thick lava piles using the K-Ar method (white dots) along profile A-B. They determined the oldest age (below the unconformity) as  $15.32 \pm 0.34$  Ma (<sup>a</sup> on the figure and details in text). Kristjánsson and Jóhannesson (1996) correlated magnetic polarity and other stratigraphical observations, with the geochronological studies of McDougall et al. (1984) along profile A-B (white dots and K-Ar ages), to estimate the ages of a ~2.6 km thick lava sequence along the coast of Isafjardardalur (profile A'-B' with red dots and correlated K-Ar ages). Dran: Drangajökull.

## 4.3 Methods

### 4.3.1 $^{40}\text{Ar}/^{39}\text{Ar}$ dating

#### 4.3.1.1 *Sample preparation*

During the 2014 field season, seven dikes across the Westfjords peninsula were sampled for  $^{40}\text{Ar}/^{39}\text{Ar}$  dating (see Fig. 22). To ensure high sample quality and to provide sufficient material for dating, each collected sample weighed between 1-5 kg. The samples were crushed using a jaw crusher and dry sieved using mesh sizes ( $\phi$ ) of  $\geq 1$  mm, 500, 250, 125, 63 and  $\leq 63$   $\mu\text{m}$ . Based on thin section and crushed sample observations, only the 250 and 125  $\mu\text{m}$  fractions were used for  $^{40}\text{Ar}/^{39}\text{Ar}$  sample preparation. After dry sieving, each sample was cleaned using distilled water in an ultrasonic bath to remove fine-grained dust particles. The samples were run through a Frantz magnetic mineral separator in order to isolate the non-magnetic felsic from the mafic magnetic minerals, which significantly accelerated the subsequent process of hand picking of the plagioclase separates under the binocular microscope. The overall summary of the material picked (including total weights of the plagioclases) is presented in Table 2. Overall, hand-picking of clean and high quality plagioclases proved to be difficult. Most of the minerals show variable levels of alteration or fluid/melt inclusions (see section 4.5.1). For this reason and the overall lack of bigger grains, plagioclases from sample 14-1 were picked from the finer 125  $\mu\text{m}$  grain size fraction. Feldspars from the remaining six samples were hand-picked from the 250  $\mu\text{m}$  fractions. To remove and minimize alteration within the samples, each plagioclase sample was treated with 3% HCl for 10 minutes to remove any carbonates and then washed with distilled water. Then each plagioclase sample was leached with 5% hydrofluoric acid for 10 minutes in order to help remove fine-grained alteration products, and was then washed in distilled water using an ultrasonic stick. The samples were dried in a 50°C oven overnight. Samples prepared for  $^{40}\text{Ar}/^{39}\text{Ar}$  dating weighed between 7.7-39.9 mg. Each unknown sample was loaded into appropriately sized holes in small 99.999% aluminium disks, which were stacked and bolted together, and then placed in a 99.9% Al canister to make up the irradiation package. Grains of Taylor Creek sanidine (TCR-2) age standard ( $27.87 \pm 0.04$  Ma,  $1\sigma$  error (Lanphere, pers. comm.), calibrated to SB-3 biotite standard (Lanphere and Dalrymple, 2000)) were regularly interspersed in the aluminium disks with the unknown samples to monitor the fast neutron gradient. The irradiation package was irradiated with fast neutrons in the Cadmium-Lined In-Core Irradiation Tube (CLICIT) reactor core position for 4 hours at the Oregon State University nuclear reactor, Corvallis, USA.

**Table 2** General summary of seven samples prepared for the  $^{40}\text{Ar}/^{39}\text{Ar}$  dating experiments.

Sample	Unit	Rock type	Fraction ( $\mu\text{m}$ )	Material	Mass of hand-picked plagioclase separates (mg)	Quality
1-2	Dike	Basalt	250	Plagioclase	31.2	Good
10-1	Dike	Basalt	250	Plagioclase	26.1	Good
2-1	Dike	Basalt	250	Plagioclase	36.2	Good
4-1	Dike	Basalt	250	Plagioclase	12.9	Good
16-2	Dike	Basalt	250	Plagioclase	13.7	Good
14-1	Dike	Basalt	125	Plagioclase	7.7	Good
17-1	Dike	Basalt	250	Plagioclase	39.9	Good

#### 4.3.1.2 Analytical methods

Upon return of the irradiation canister, single age standard grains and unknown sample separates were loaded into variously sized aluminium laser palettes. A laser palette and glass coverslips were loaded into an ultra-high vacuum 4.5" laser chamber with a Kovar viewport that was baked at 230°C, and the whole extraction line was baked in an oven at 195°C for 8 hours, and then pumped for 2 days to remove adsorbed atmospheric argon from the samples and chamber walls.

A 25 W Coherent Sabre 25TSM argon ion laser ( $\lambda = 455\text{-}515$  nm), with a computer-controlled X-Y stage, was used to incrementally heat the unknown samples or totally fuse the age standard single grains for 45 seconds, with a 0.25-1.0 mm diameter laser beam. The laser system was fitted with a binocular microscope and light source for sample illumination and X-Y stage calibration, and a camera for video recording of the laser heating of each sample.

The gases released by laser heating were cleaned for 3 minutes using an automatically-refilling liquid nitrogen Dewar attached to a glass finger, and two SAES AP10 getter pumps (one at 400°C and one at room temperature) to remove all active gases. The remaining noble gases were equilibrated into a high sensitivity Mass Analyzer Products (MAP) 216 mass spectrometer, containing a Bauer-Signer-type source, with a mass resolution of 239, operated at a 240  $\mu\text{A}$  emission current, with a Becton Dickinson MM-1 Mesh electron multiplier, and a mass spectrometer sensitivity of  $2.70 \times 10^{-10}$   $\text{cm}^3/\text{V}$  ( $1.203 \times 10^{-14}$  moles/V) using the normal operating gain value.

The five Ar isotopes ( $^{36}\text{Ar}$ ,  $^{37}\text{Ar}$ ,  $^{38}\text{Ar}$ ,  $^{39}\text{Ar}$  and  $^{40}\text{Ar}$ ) and baselines for the system blanks, age standards and unknown samples were measured via peak-hopping using a single electron multiplier with variable gain. The fully automated laser heating, X-Y stage movement, automated valves operation, and data acquisition were computer controlled using a Turbo Pascal program.

The unweighted mean extraction system blank Ar isotope measurements obtained during the unknown sample analyses were  $1.20 \times 10^{-13}$ ,  $3.09 \times 10^{-13}$ ,  $5.46 \times 10^{-14}$ ,  $7.49 \times 10^{-14}$ , and  $1.73 \times 10^{-12} \text{ cm}^3 \text{ STP}$  (standard temperature and pressure) for  $^{36}\text{Ar}$ ,  $^{37}\text{Ar}$ ,  $^{38}\text{Ar}$ ,  $^{39}\text{Ar}$ , and  $^{40}\text{Ar}$ , respectively. Unknown analyses were corrected for mass spectrometer discrimination using a  $^{40}\text{Ar}/^{36}\text{Ar}$  ratio of 285.9, yielding a linear law mass discrimination value of 1.008304 per atomic mass unit, which was calculated from air pipette shots and zero-age glasses, and nuclear interference reaction correction factors of  $^{40}\text{Ar}/^{39}\text{Ar}_{\text{K}} = 7.30 \times 10^{-4}$ ,  $^{36}\text{Ar}/^{37}\text{Ar}_{\text{Ca}} = 2.65 \times 10^{-4}$ , and  $^{39}\text{Ar}/^{37}\text{Ar}_{\text{Ca}} = 7.02 \times 10^{-4}$  from Renne et al. (2013; 2015) were used. Errors are quoted at  $1\sigma$  and  $2\sigma$  levels, and the  $^{40}\text{Ar}/^{39}\text{Ar}$  ages were calculated using the decay constants and  $^{40}\text{K}/\text{K}$  ratio of Steiger and Jäger (1977). The  $J$  values and errors are noted in the sample  $^{40}\text{Ar}/^{39}\text{Ar}$  data tables (Appendix B).

All the plots and plateau and inverse isochron age determinations were made using the Excel Isoplot macro v. 4.15 (Ludwig, 2011). Plateau ages were determined using the criteria of Lanphere and Dalrymple (1978), where a significant proportion of the  $^{39}\text{Ar}$  release ( $> 50\%$ ) is represented in the plateau steps.

Ar diffusion modelling of plagioclase grains was done using the MathCAD program (Jo-Anne Wartho, pers. comm.) and the Ar diffusion parameters of Wartho et al. (2013).

#### 4.3.2 Chemistry of plagioclase phenocrysts and overall alteration of dikes

Chemical composition (e.g., potassium content) of plagioclase phenocrysts and overall level of alteration of the seven dikes studied here was investigated in order to determine the quality of plagioclase separates later hand-picked for  $^{40}\text{Ar}/^{39}\text{Ar}$  dating and to evaluate the potential impact of hydrothermal alteration on the applicability of  $^{40}\text{Ar}/^{39}\text{Ar}$  method for age determinations of basaltic dikes from Iceland.

Seven dike samples were thoroughly washed and dried in oven to remove any unwanted mud, clay or other contamination. Then the most representative rocks were cut and thin sections have been prepared. These thin sections were then examined to determine the rock type (texture, presence of phenocrysts and their volume), abundance, number of generations and freshness of plagioclase phenocrysts. The overall level and type of alteration of the rocks was also investigated to evaluate the potential impact of alteration on  $^{40}\text{Ar}/^{39}\text{Ar}$  dating method and give approximate conditions during the alteration.

The Electron Microprobe (EMP) analyses were performed to determine the potassium content in plagioclase phenocrysts prior to the  $^{40}\text{Ar}/^{39}\text{Ar}$  dating. For these measurements, the method from Kutterolf et al. (2011) was adjusted. The Electron Microprobe Jeol JXA-8200

wavelength dispersive “Superprobe” at GEOMAR was used to analyze major elements (Na, K, Fe, Mn, Si, Ca, Mg, Al and Ti) using a focused beam (reduced to 1  $\mu\text{m}$ ), an acceleration voltage of 15 kV and a beam current of 20 nA. Measurements were calibrated with international natural and synthetic standards, and minor deviations have been corrected. Each of the plagioclase feldspars had 6 measurements: 3 in the core and 3 close to the rim. The number of analyzed feldspars was determined by the minimum number of feldspar found in one of the samples. Hence, in dike 4-1 only 6 suitable feldspars were found, each dike sample had 36 measurements.

## **4.5 Results**

### **4.5.1 Petrography of the dikes, chemical composition of plagioclases and hydrothermal alteration**

Seven dikes studied here are tholeiitic basalts with the overall total alkali concentrations <3%, which does not differ from the earlier investigations of lava types in Westfjords, conducted by McDougall et al. (1984) and Kristjánsson and Jóhannesson (1996). Table 3 summarizes the most important observations from the examinations of the thin sections and EMP measurements. It includes types of observed phenocrysts (with sizes and proportion in sample), phenocrysts composition, average potassium concentration in plagioclase >250  $\mu\text{m}$ , state of the alteration of both phenocrysts and groundmass, and types of alteration observed. Detailed EMP results are given in tables (separately for each sample) in Appendix A. The most representative photomicrographs of the samples are also shown in Figure 35.

Among the seven dikes, dikes 2-1 and 17-1 appear the freshest (Tab. 3). In the remaining intrusions alteration is dominated by smectite (montmorillonite, saponite and bowlingite) and later overprinting by Fe-OOH. Secondary minerals completely or partly replace primal phases in the groundmass (e.g., no fresh volcanic glass has been observed) but also precipitate in the fractures of phenocrysts. Thus, many plagioclase phenocrysts have fractures and cracks filled with smectite and Fe-OOH (Fig. 35). Moreover, alteration has overall impact on the color of these minerals causing apparent shift from white in the hand specimen or colorless in thin sections to yellow-brownish in both hand specimen and thin sections.

**Table 3 Summary of the results of thin sections examinations and EMP measurements from the seven studied dikes.**

Sample	Phenocrysts: petrography <sup>1</sup>	Phenocrysts: composition	wt. %K <sub>2</sub> O in Pl	Alteration state <sup>2</sup>	Type of secondary minerals	Vesicles <sup>3</sup>	Crystal clots <sup>4</sup>	Melt/fluid inclusions in Pl
1-2	Pl (≤4 mm, 30%) Cpx (≤1 mm, 10%)	Pl (By, Lab) Cpx (Aug/Di)	0.071	Pl = 2, Cpx = 2, Ol = 4, G <sub>mass</sub> = 2	Sme (Mnt, Sap), Fe-OOH	Yes = 2 (Zeo, Fe-OOH)	Yes (Pl)	Yes
10-1	Pl (≤3 mm, 10%) Cpx (≤1 mm, <5%)	Pl (By, Lab) Cpx (Aug/Di)	0.079	Pl = 3, Cpx = 2, G <sub>mass</sub> = 3	Sme (Mnt), Fe-OOH	Yes = 2 (Sme, Fe-OOH)	Yes (Pl)	Yes
2-1	Pl (≤3 mm, ~20%) Cpx (≤1 mm, ~10%) Ol (≤500 μm, <<1%)	Pl (By, Lab) Cpx (Aug) Ol (Fo)	0.066	Pl = 1, Cpx = 2, Ol = 2, G <sub>mass</sub> = 1	Fe-OOH	Yes = 1	Yes (Pl)	Rare
4-1	Pl (≤3 mm, 5%) Cpx (≤500 μm, <<1%) Ol (< 1 mm, <<1%)	Pl (An, By, Lab), Cpx (Aug/Di), Ol (Fo)	0.061	Pl = 3, Cpx = 2, Ol = 3, G <sub>mass</sub> = 3	Sme (Mnt, Bw), Fe- OOH,	No	Yes (Pl, Ol)	Rare
16-2	Pl (≤5 mm, 25%) Cpx (≤1 mm, ~5%)	Pl (By, Lab, And) Cpx (Aug/Di)	0.09	Pl = 3, Cpx = 2, Ol = 4, G <sub>mass</sub> = 3,	Sme (Mnt, Bw), Fe- OOH,	Yes = 2 (Sme, Fe-OOH)	No	Rare
14-1	Pl (≤5 mm, <5%)	Pl (An, By, Lab)	0.097	Pl = 3	Sme, Fe-OOH	No	Yes (Pl)	Rare
17-1	Pl (≤8 mm, 30%) Cpx (≤ 1mm, ~5%)	Pl (By, Lab) Cpx (Aug)	0.12	Pl = 1, Cpx = 2	Sme, Fe-OOH	No	Yes (Pl, Cpx)	Yes

**Abbreviations:** Pl: plagioclase, An: anorthite, By: bytownite, Lab: labradorite, And: andesine, Cpx: clinopyroxene, Aug: augite, Di: diopside, Ol: olivine, Fa: fayalite, Fo: forsterite, Sme: smectite, Mnt: montmorillonite, Sap: saponite, Bw: bowlingite, Zeo: zeolites, G<sub>mass</sub>: groundmass.

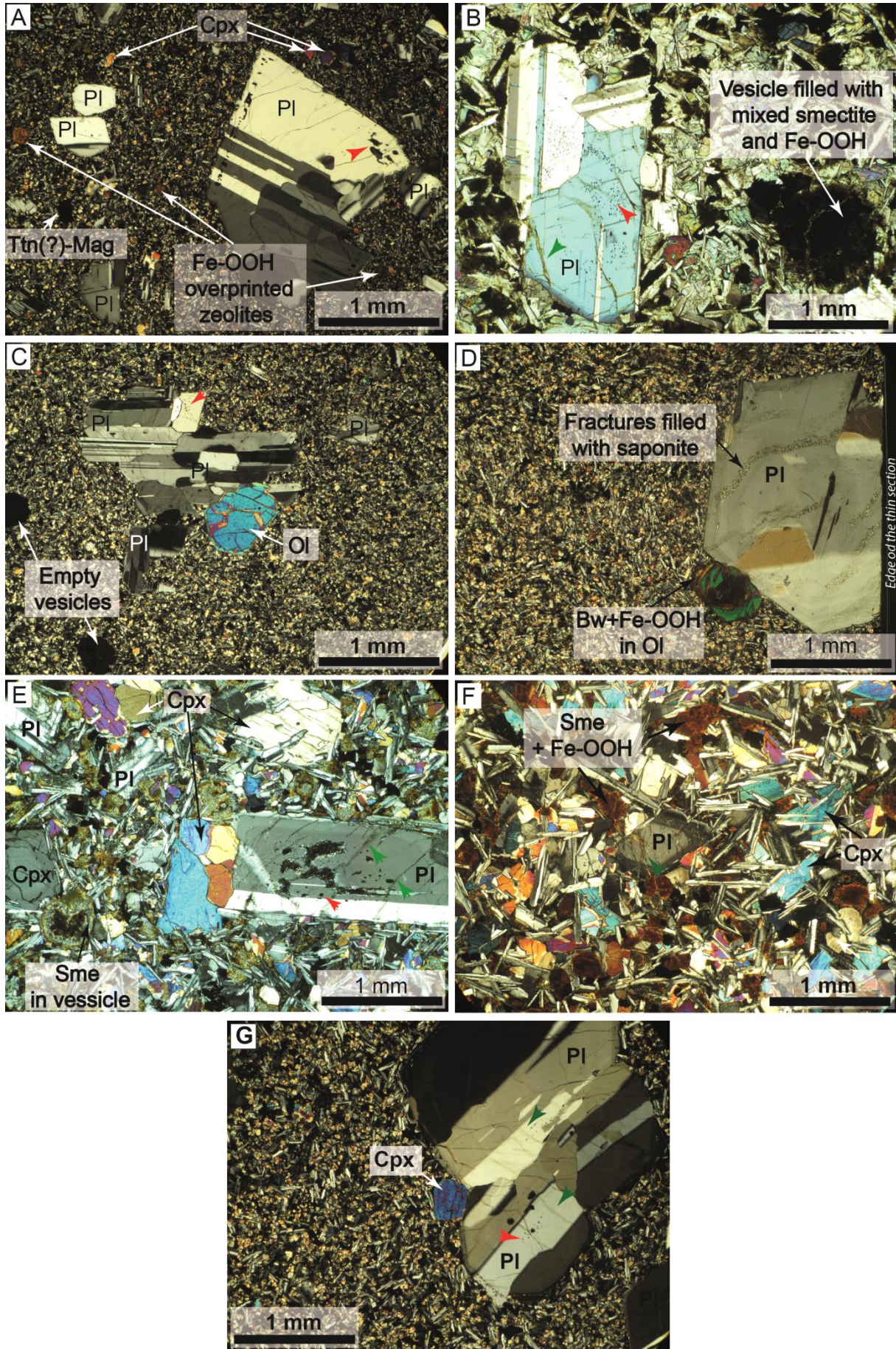
<sup>1</sup> Type (size, volume percent).

<sup>2</sup> Fresh = 1; Little alteration = 2; High alteration = 3; Very high alteration = 4.

<sup>3</sup> Empty = 1; Filled = 2 + (Type).

<sup>4</sup> Types of minerals present in mineral clots (when observed).







### 4.5.2 $^{40}\text{Ar}/^{39}\text{Ar}$ dating

Outcrops of the dikes visited in the 2014 field during season showed relatively high levels of alteration (Fig. 35), with minor amounts of relatively unaltered plagioclase. Therefore, only 7 samples were collected that delivered sufficient good quality material necessary for  $^{40}\text{Ar}/^{39}\text{Ar}$  dating. The overall results of the plagioclase step-heating experiments are summarized in Table 4 and plotted on an overview map of the samples locations (Fig. 36). Detailed results of the  $^{40}\text{Ar}/^{39}\text{Ar}$  laser step-heating analyses are separately presented below in the following sub-sections for each of the 7 samples. They include plateau ages, inverse isochron ages, %K<sub>2</sub>O concentrations (measured using the Electron Microprobe) and the  $^{37}\text{Ar}/^{39}\text{Ar}$  Alteration Index values for each heating step, which gives an indication of the quality (fresh/altered) of the plagioclases heating steps. The  $^{37}\text{Ar}/^{39}\text{Ar}$  Alteration Index (*AI*) values for each heating step is calculated according to Baksi (2007) and are shown in Tables in below sub-chapters for each sample separately. *AI* values of  $>0.00006$  are used to indicate alteration of the plagioclase, whereas values of  $\leq 0.00006$  are used to suggest fresh material. The age spectra and inverse isochron results (for two aliquots, where applicable) are plotted individually.

---

**Fig. 35 (Previous page) Representative photomicrographs of thin sections of seven dikes from this study. (A) Slightly altered sample 1-2 with plagioclase (Pl) and clinopyroxene (Cpx) phenocrysts, Fe-OOH overprinted zeolites and opaques. Clot of Pl crystals also visible. View in XPL; (B) Highly altered sample 10-1 with Pl phenocrysts (with melt/fluid inclusion and smectite (Sme) filled fractures). Vesicles partly or completely filled with dark-colored alteration (Sme and Fe-OOH) are also observed; (C) Fresh sample 2-1 with Pl phenocrysts with melt/fluid inclusion. Some fractures show Sme precipitation. Vesicles are completely empty; (D) Altered sample 4-1 with Pl, Cpx and Olivine (Ol) phenocrysts. The Pl shows smooth oscillatory zoning and melt/fluid inclusions. Fractures in many Pl are filled with Sme. Ol shows partial alteration to bowlingite (Bw) and Fe-OOH; (E) Highly altered sample 16-2 with Pl and Cpx phenocryst. Pl show Sme filled fractures. Some Cpx show alteration rims; (F) Highly altered sample 14-1 with Pl phenocrysts. Many of these phenocrysts have Sme filled fractures. Groundmass is highly altered to Sme and Fe-OOH; (G) Fresh sample 17-1 with Pl and Cpx phenocrysts clustered in a clot. Pl has little alteration (Sme) and melt/fluid inclusions while Cpx shows slight alteration along the rim. All photomicrographs are in XPL.**

The  $^{40}\text{Ar}/^{39}\text{Ar}$  laser step-heating analyses were performed on plagioclase separates for 20 incrementally heated steps until the sample was totally fused. Heating steps for which the  $^{39}\text{Ar}$  isotope measurements showed negative or  $<2$  times the  $^{39}\text{Ar}$  blank levels were rejected and are not shown. Two aliquots of samples 1-2, 2-1, 10-1 and 17-1 were step-heated, however the second aliquots contained fewer steps (see Tables 5-11 and Appendix B). Samples 4-1, 14-1 and 16-2 contained too little original hand-picked material to allow 2 aliquots to be analyzed. Plateau ages are determined from the error-weighted mean of at least three consecutive steps carrying  $>50\%$  of the total released  $^{39}\text{Ar}$ , overlapping in age within  $2\sigma$  errors levels (Lanphere and Dalrymple, 1978). The statistical relevance of the plateau ages and inverse isochron ages is tested by the calculation of a Mean Square of Weighted Deviation (MSWD) and probability of fit ( $P$ ) values to determine whether the scatter of the data is compatible with the measured analytical errors. Hence, the MSWD of the measurements should yield values  $<2$ , and the  $P$  values should be  $>0.05$  (i.e., 5%). All subsequent quoted plateau ages are quoted with  $2\sigma$  errors, and all inverse isochron ages with 95% confidence errors.

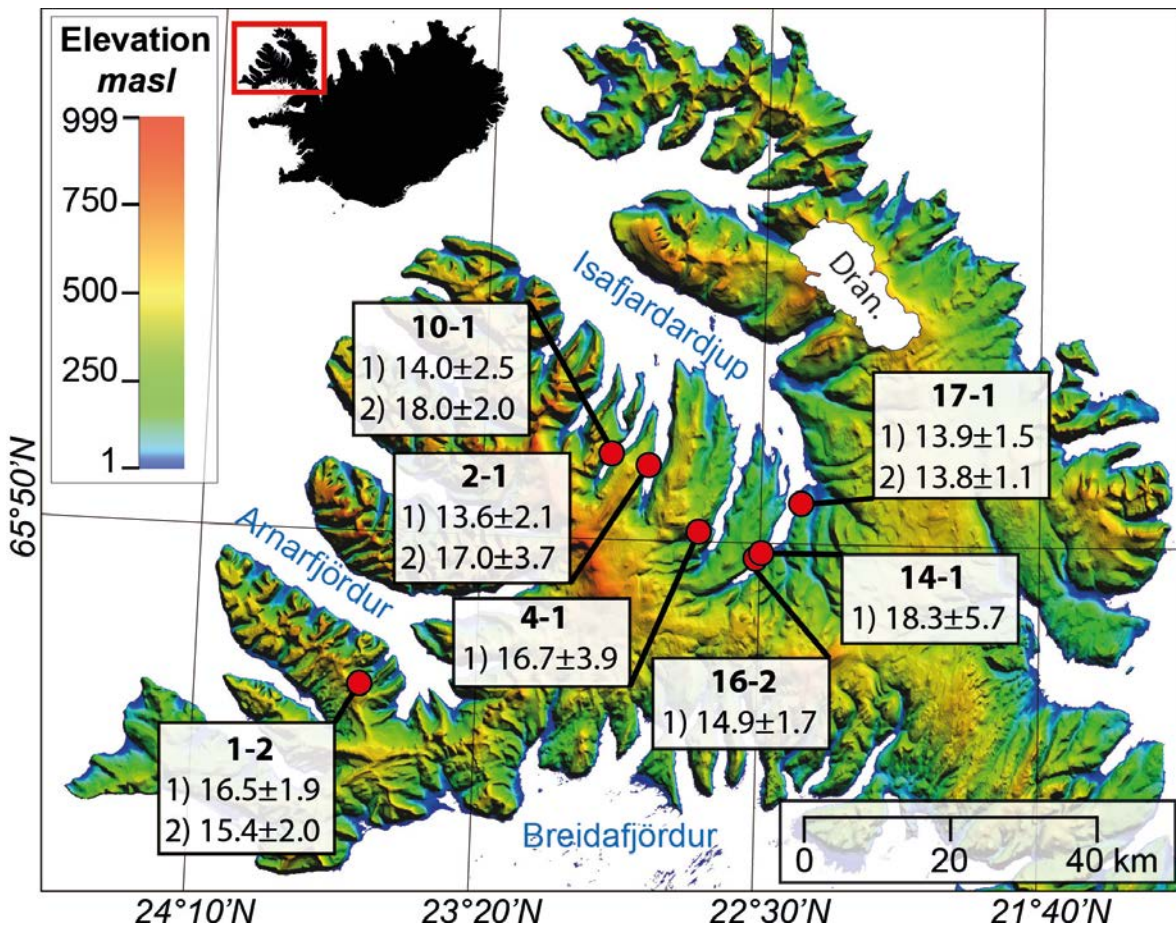


Fig. 36 The  $^{40}\text{Ar}/^{39}\text{Ar}$  step-heating ages (in Ma with  $2\sigma$  errors) from the seven dikes studied in Westfjords, Iceland. Where analyzed, results from two aliquots are shown. Dran: Drangajökull.

**Table 4 Summary of  $^{40}\text{Ar}/^{39}\text{Ar}$  dating of 7 dikes from Westfjords studied consisting of plateau and inverse isochron ages with additional statistical information. Abbreviation: Pl: Plagioclase.**

Sample number	Mineral picked	Grain size	Mass (mg)	Plateau ages (Ma, $2\sigma$ )	% $^{39}\text{Ar}$ in plateau	MSWD (< 2)	P (> 0.05)	Inverse isochron age (Ma, 95% conf., plateau steps)	Initial $^{40}\text{Ar}/^{36}\text{Ar}$	MSWD (< 2)	P (> 0.05)
1-2 (aliqu. 1)	Pl	250 $\mu\text{m}$	9.756	16.5 $\pm$ 1.9	66.2	0.81	0.58	17.5 $\pm$ 2.4	292.1 $\pm$ 4.4	0.46	0.84
1-2 (aliqu. 2)	Pl	250 $\mu\text{m}$	5.763	15.4 $\pm$ 2.0	60.2	0.26	0.77	14.5 $\pm$ 3.9	302 $\pm$ 18	0.032	0.86
10-1 (aliqu. 1)	Pl	250 $\mu\text{m}$	9.579	14.0 $\pm$ 2.5	61.3	0.94	0.45	11.9 $\pm$ 6.0	323 $\pm$ 45	0.67	0.61
10-1 (aliqu. 2)	Pl	250 $\mu\text{m}$	9.070	18.0 $\pm$ 2.0	99.96	0.83	0.62	15.6 $\pm$ 6.2	322 $\pm$ 49	0.70	0.74
2-1 (aliqu. 1)	Pl	250 $\mu\text{m}$	10.278	13.6 $\pm$ 2.1	100	0.49	0.94	14.8 $\pm$ 5.8	292 $\pm$ 15	0.50	0.93
2-1 (aliqu. 2)	Pl	250 $\mu\text{m}$	2.313	17.0 $\pm$ 3.7	100	0.60	0.73	21 $\pm$ 12	265 $\pm$ 49	0.41	0.84
4-1	Pl	250 $\mu\text{m}$	8.350	16.7 $\pm$ 3.9	100	0.89	0.57	16.4 $\pm$ 4.2	296.0 $\pm$ 1.4	1.07	0.38
16-2	Pl	250 $\mu\text{m}$	9.296	14.9 $\pm$ 1.7	66.7	1.60	0.12	17.4 $\pm$ 4.2	264 $\pm$ 38	1.14	0.34
14-1	Pl	125 $\mu\text{m}$	5.954	18.3 $\pm$ 5.7	93.8	0.50	0.92	18.3 $\pm$ 7.7	295.5 $\pm$ 2.3	0.54	0.88
17-1 (aliqu. 1)	Pl	250 $\mu\text{m}$	9.213	13.9 $\pm$ 1.5	96.9	0.55	0.86	14.3 $\pm$ 1.8	292.8 $\pm$ 4.1	0.35	0.96
17-1 (aliqu. 2)	Pl	250 $\mu\text{m}$	10.679	13.8 $\pm$ 1.1	100	0.64	0.84	13.6 $\pm$ 1.2	297.1 $\pm$ 2.4	0.41	0.97

#### 4.5.2.1 Sample 1-2

Sample 1-2 is the most western sample dated in this study and was sampled near the coast of Arnarfjörður (Fig. 36). Plagioclase crystals were relatively abundant and clean (some showed minor alteration or melt/fluid inclusions – see Table 3). After the rejection of  $^{39}\text{Ar}$ -poor steps, 15 of 20 steps remain in the first aliquot, while 8 of 10 steps remain in the second aliquot. The aliquot 1  $^{40}\text{Ar}/^{39}\text{Ar}$  plateau age is  $16.5 \pm 1.9$  Ma (MSWD = 0.81, P = 0.58), containing 66.2% of the released  $^{39}\text{Ar}$  (steps 6-13), and agrees within error with the inverse isochron age of  $17.5 \pm 2.4$  Ma (MSWD = 0.46, P = 0.84; Fig. 37 and Tabs. 4 and 5) obtained from the plateau steps, with an initial  $^{40}\text{Ar}/^{36}\text{Ar}$  ratio of  $292.1 \pm 4.4$  (Tab. 4). Aliquot 2 yields a younger plateau age of  $15.4 \pm 2.0$  Ma (MSWD = 0.25, P = 0.77) with 60.2% of the released  $^{39}\text{Ar}$  (steps 4-6), with an inverse isochron age of  $14.5 \pm 3.9$  Ma (MSWD = 0.032, P = 0.86) and an initial  $^{40}\text{Ar}/^{36}\text{Ar}$  ratio of  $302 \pm 18$  Ma. However, in aliquot 2 only 3 of 8 heating steps are used to calculate the plateau and inverse isochron ages, and therefore, aliquot 1 (which contained 8 plateau steps) is determined to have a more robust age. The initial  $^{40}\text{Ar}/^{36}\text{Ar}$  ratios in both aliquots overlap within error with the atmospheric  $^{40}\text{Ar}/^{36}\text{Ar}$  value of 295.5 (Steiger and Jäger, 1977), which suggests no excess  $^{40}\text{Ar}$  component. Based on the plagioclase *AI*, values of aliquot 1, the low temperature steps (1-6) and the last step (15) show alteration effects, while steps 7-14 contain fresh material. In the aliquot 2 only three steps show fresh material (4-7) while the low temperature and last steps (1-3, 8) contain alteration (Tab. 5).

**Table 5 Summary of the results of  $^{40}\text{Ar}/^{39}\text{Ar}$  dating of sample 1-2 including plateau and inverse isochron ages, weights of the samples, average potassium concentration, and Alteration Index values.**

					Alteration Index (cut-off = <0.00006) <sup>2</sup>	
Sample (aliquot)	Plateau ages (Ma, 2 $\sigma$ )	Inverse isochron age (Ma, 2 $\sigma$ )	Mass (mg)	wt.%K <sub>2</sub> O <sup>1</sup>	Steps showing Fresh	Steps showing Alteration
<b>1-2 (1)</b>	$16.5 \pm 1.9$	$17.5 \pm 2.4$	9.756	0.071	7-14	1-6; 15
<b>1-2 (2)</b>	$15.4 \pm 2.0$	$14.5 \pm 3.9$	5.756		4-7	1-3; 8

<sup>1</sup>see Appendix A

<sup>2</sup>after Baksi (2007)

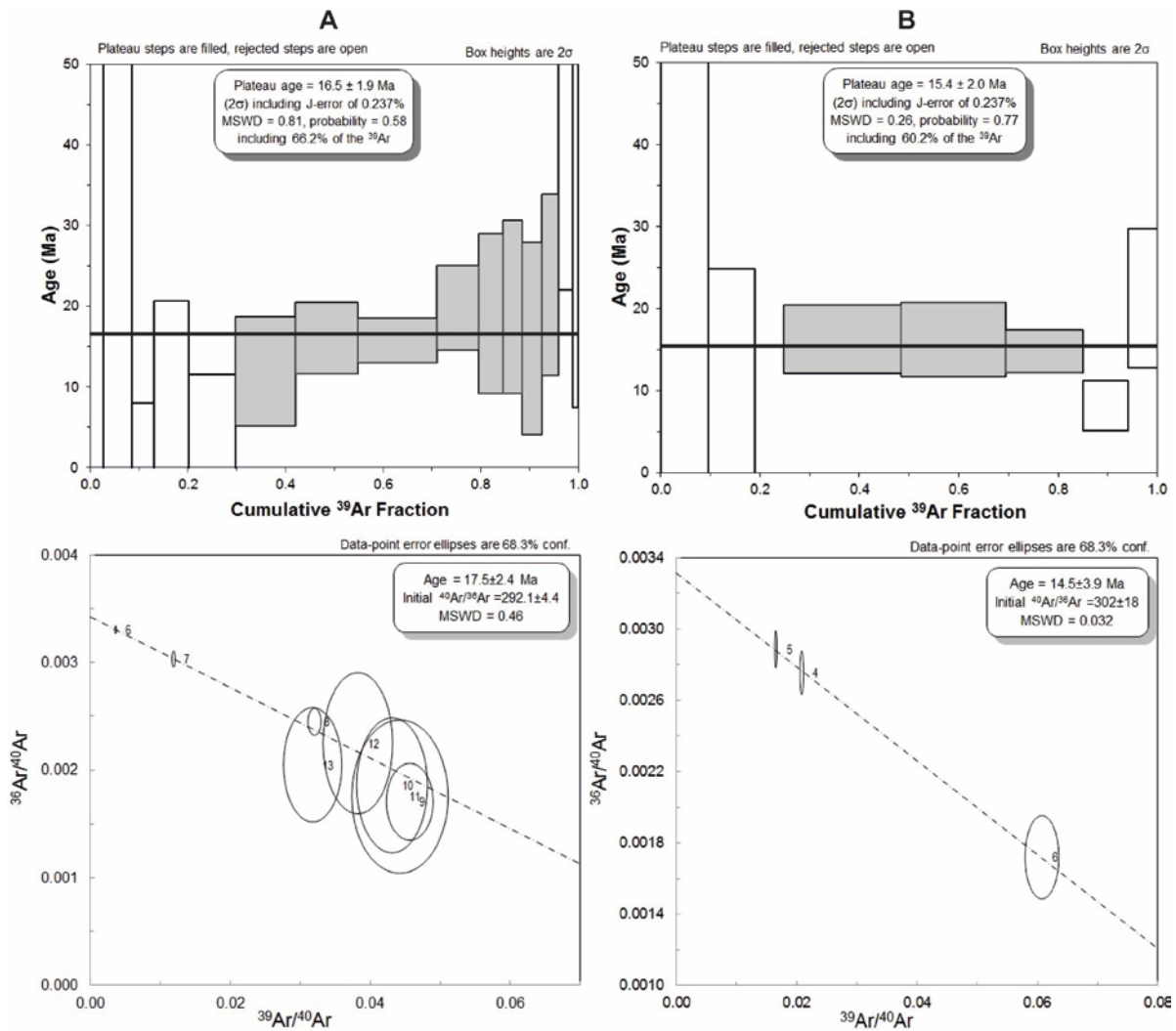


**Fig. 37** Age spectra (top) and inverse isochron diagrams (bottom) from the  $^{40}\text{Ar}/^{39}\text{Ar}$  step heating experiments on sample 1-2: (A) aliquot 1 and (B) aliquot 2. The age spectrum apparent age error bars are  $2\sigma$  and the inverse isochron error ellipses are 68.3% confidence. The plateau steps are shown in grey while rejected steps are white. The black line on each age spectrum represents the error-weighted mean plateau age. The inverse isochron line fit is shown by a black dashed line.

#### 4.5.2.2 Sample 10-1

Sample **10-1** is located 46.5 km NE of sample 1-2 along the southern coast of Isafjardardjup (Fig. 36). Overall, fewer clean and fresh plagioclase crystals were found in this sample compared to sample 1-2. Some heating steps have been rejected due to very low  $^{39}\text{Ar}$  yields and, therefore, the age spectra and inverse isochron ages have been calculated based on 13 and 14 of 20 steps of aliquots 1 and 2, respectively. Aliquot 1 yields a plateau age of  $14.0 \pm 2.5$  Ma (MSWD = 0.94,  $P = 0.45$ ) containing 61.3% of the  $^{39}\text{Ar}$  (steps 1-6), which is supported by an inverse isochron age of  $11.9 \pm 6.0$  Ma (MSWD = 0.67,  $P = 0.61$ ), with an initial  $^{40}\text{Ar}/^{36}\text{Ar}$  ratio of  $323 \pm 45$ . Aliquot 2 shows a significantly older plateau age of  $18.0 \pm 2.0$  Ma (MSWD = 0.83,  $P = 0.62$ ) containing 99.96% of the  $^{39}\text{Ar}$  (steps 2-14), which is



supported by an inverse isochron age of  $15.6 \pm 6.2$  Ma (MSWD = 0.70, P = 0.74; Fig. 38 and Tabs. 4 and 6), with an initial  $^{40}\text{Ar}/^{36}\text{Ar}$  ratio of  $322 \pm 49$ . Although the initial  $^{40}\text{Ar}/^{36}\text{Ar}$  ratios are high, they are still within error of the atmospheric  $^{40}\text{Ar}/^{36}\text{Ar}$  ratio of 295.5. The large errors on these two initial  $^{40}\text{Ar}/^{36}\text{Ar}$  ratios is caused by close clustering of some steps on the inverse isochrons (4 of a total of 6 steps, and 9 of a total of 13 steps for aliquots 1 and 2, respectively; Fig. 38). The AI values from both aliquots show that low temperature heating steps (steps 1 or 1-2 for aliquots 1 and 2, respectively) indicate the presence of alteration while the remaining steps seem to be from fresh material (Tab. 6).

**Table 6 Summary of the results of  $^{40}\text{Ar}/^{39}\text{Ar}$  dating of sample 10-1 including plateau and inverse isochron ages, weights of the samples, average potassium concentration, and Alteration Index values.**

					Alteration Index (cut-off = <0.00006) <sup>2</sup>	
Sample (aliquot)	Plateau ages (Ma, 2 $\sigma$ )	Inverse isochron age (Ma, 2 $\sigma$ )	Mass (mg)	wt. %K <sub>2</sub> O <sup>1</sup>	Steps showing Alteration	Steps showing Fresh
<b>10-1 (1)</b>	14.0±2.4	11.9±6.0	9.579	0.079	1	2-13
<b>10-1 (2)</b>	18.0±2.0	15.6±6.2	9.070		1-2	3-14

<sup>1</sup>see Appendix A

<sup>2</sup>after Baksi (2007)

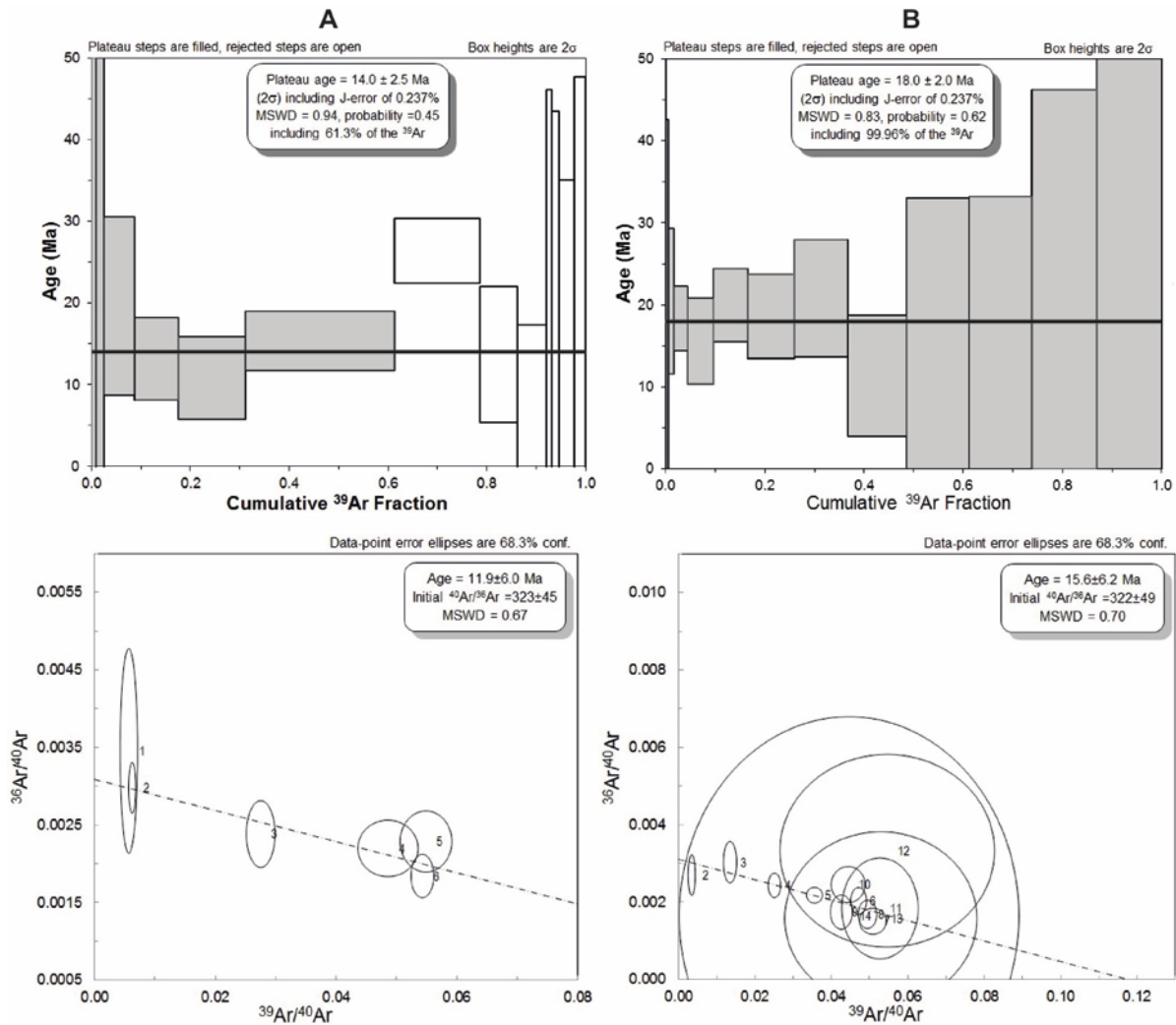


**Fig. 38** Age spectra (top) and inverse isochron diagrams (bottom) derived from the  $^{40}\text{Ar}/^{39}\text{Ar}$  step heating experiments on sample 10-1: (A) aliquot 1 and (B) aliquot 2. The age spectrum apparent age error bars are  $2\sigma$  and the inverse isochron error ellipses are 68.3% confidence. The plateau steps are shown in grey while rejected steps are white. The black line on each age spectrum represents the error-weighted mean plateau age. The inverse isochron line fit is shown by a black dashed line.

#### 4.5.2.3 Sample 2-1

Sample 2-1 was collected 5.3 km SE from the dike 10-1 and is also located at the southern coast of Isafjardardjup (Fig. 36). The abundance of relatively fresh plagioclases allowed ~16 mg of material to be hand-picked for the step-heating experiments and two aliquots of this sample were  $^{40}\text{Ar}/^{39}\text{Ar}$  dated (see Appendix B). After the rejection of steps with very low  $^{39}\text{Ar}$  yields, aliquot 1 contained 15 of 20 steps. However, only 5.8 mg was analyzed for aliquot 2, therefore the number of heating steps was reduced resulting in only 7 of 10 useable steps. Results from aliquot 1 yield a plateau age of  $13.6 \pm 2.1$  Ma (MSWD = 0.49,  $P = 0.94$ , containing 100% of the  $^{39}\text{Ar}$  (steps 1-15)), which overlaps with the inverse isochron age of  $14.8 \pm 5.8$  Ma (MSWD = 0.50,  $P = 0.93$ ; Fig. 39 and Tabs. 4 and 7), with an initial  $^{40}\text{Ar}/^{36}\text{Ar}$  ratio of  $292 \pm 15$ , within error of the atmospheric  $^{40}\text{Ar}/^{36}\text{Ar}$  ratio. Aliquot 2

has an older plateau ( $17.0 \pm 3.7$  Ma, MSWD = 0.60, P = 0.73, containing 100% of the  $^{39}\text{Ar}$  (steps 1-7)) and inverse isochron ( $21.0 \pm 12.0$  Ma, MSWD = 0.41, P = 0.84) ages. The results from the smaller aliquot 2 have significantly higher scatter and errors; however, both aliquots will be used in our discussion. The *AI* values indicates that the low temperature steps (1-5) from aliquot 1 indicate degassing from altered regions of the samples, while the remaining steps are derived from fresh material, whereas for aliquot 2 all the 7 steps indicate fresh material (Tab. 7).

**Table 7 Summary of the results of  $^{40}\text{Ar}/^{39}\text{Ar}$  dating of sample 2-1 including plateau and inverse isochron ages, weights of the samples, average potassium concentration, and Alteration Index values.**

					<b>Alteration Index (cut-off = &lt;0.00006)<sup>2</sup></b>	
<b>Sample (aliquot)</b>	<b>Plateau ages (Ma, 2<math>\sigma</math>)</b>	<b>Inverse isochron age (Ma, 2<math>\sigma</math>)</b>	<b>Mass (mg)</b>	<b>wt.%K<sub>2</sub>O<sup>1</sup></b>	<b>Steps showing Alteration</b>	<b>Steps showing Fresh</b>
<b>2-1 (1)</b>	$13.6 \pm 2.1$	$14.8 \pm 5.8$	10.278	0.066	1-5	6-15
<b>2-1 (2)</b>	$17.0 \pm 3.7$	$21 \pm 12.0$	2.313		-	1-7

<sup>1</sup>see Appendix A

<sup>2</sup>after Baksi (2007)

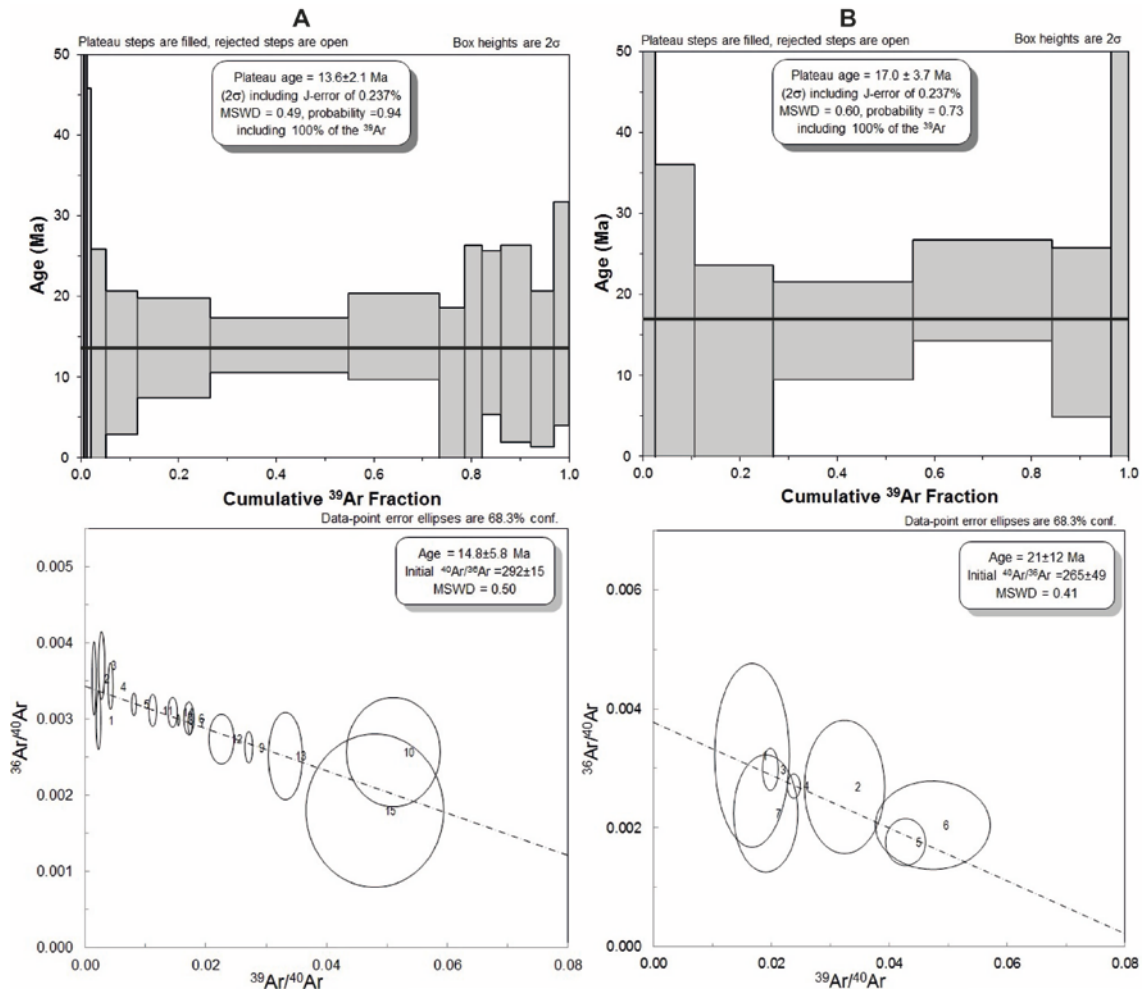


**Fig. 39** Age spectra (top) and inverse isochron diagrams (bottom) derived from the  $^{40}\text{Ar}/^{39}\text{Ar}$  step heating experiments on sample 2-1: (A) aliquot 1 and (B) aliquot 2. The age spectrum apparent age error bars are  $2\sigma$  and the inverse isochron error ellipses are 68.3% confidence. The plateau steps are shown in grey while rejected steps are white. The black line on each age spectrum represents the error-weighted mean plateau age. The inverse isochron line fit is shown by a black dashed line.

#### 4.5.2.4 Sample 4-1

Sample **4-1** was collected from the dike located ~11.4 km SE from the sample 2-1. The outcrop is exposed in a narrow canyon in Heydalur valley near Isafjardardjup, ~2.2 km away from the coastline (Fig. 36). Overall, fewer fresh plagioclases in this sample have been found compared to sample 2-1 allowing 12.90 mg of material to be hand-picked for the step-heating experiments and one aliquot was  $^{40}\text{Ar}/^{39}\text{Ar}$  dated (see Appendix B). After rejection of Ar-poor steps, 14 of 20 steps remained and yield a plateau age of  $16.7 \pm 3.9$  Ma (MSWD = 0.89,  $P = 0.57$ , containing 100% of the  $^{39}\text{Ar}$  (steps 1-14)) and is supported by the inverse isochron age of  $16.4 \pm 4.2$  Ma ((MSWD = 1.07,  $P = 0.38$ ; Fig. 40 and Tabs. 4 and 8), with an initial  $^{40}\text{Ar}/^{36}\text{Ar}$  ratio of  $296 \pm 1.4$ , within error of the atmospheric  $^{40}\text{Ar}/^{36}\text{Ar}$  ratio. The  $AI$  values in this sample indicate that the low temperature steps (1-6) and the highest step (14)

represent degassing from altered regions of the sample while the remaining steps appear to be from fresh material (Tab. 8).

**Table 8 Summary of the results of  $^{40}\text{Ar}/^{39}\text{Ar}$  dating of sample 4-1 including plateau and inverse isochron ages, weights of the samples, average potassium concentration, and Alteration Index values.**

					Alteration Index (cut-off = $<0.00006)^2$	
Sample (aliquot)	Plateau ages (Ma, $2\sigma$ )	Inverse isochron age (Ma, $2\sigma$ )	Mass (mg)	wt.% $\text{K}_2\text{O}^1$	Steps showing Alteration	Steps showing Fresh
4-1 (1)	16.7 $\pm$ 3.9	16.4 $\pm$ 4.2	8.350	0.061	1-6,14	7-3

<sup>1</sup>see Appendix A

<sup>2</sup>after Baksi (2007)

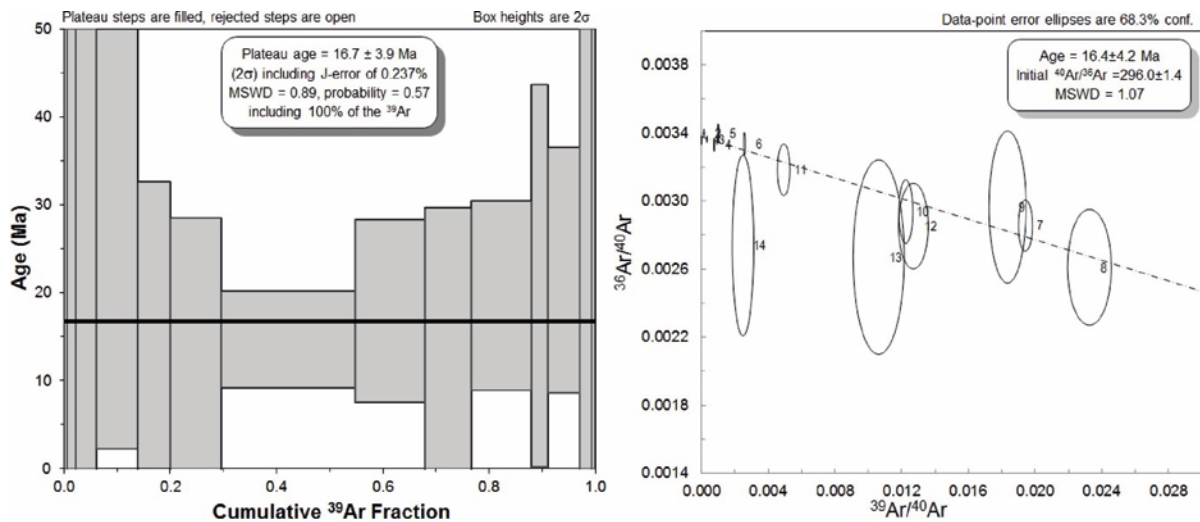


**Fig. 40** Age spectra (left) and inverse isochron (right) ages derived from the  $^{40}\text{Ar}/^{39}\text{Ar}$  step heating experiments on sample 4-1. The age spectrum apparent age error bars are  $2\sigma$  and the inverse isochron error ellipses are 68.3% confidence. The plateau steps are shown in grey while rejected steps are white. The black line on each age spectrum represents the error-weighted mean plateau age. The inverse isochron line fit is shown by a black dashed line.

#### 4.5.2.5 Sample 16-2

Sample **16-2** is located 8.5 km SE from the sample 4-1 where it is exposed along the coast of Isafjardardjup (Fig. 36). Plagioclase crystals were abundant (e.g., in comparison to sample 4-1) but show higher levels of alteration and melt/fluid inclusions. This allowed 13.7 mg of material to be hand-picked for the step-heating experiments and one aliquot of this sample was  $^{40}\text{Ar}/^{39}\text{Ar}$  dated (see Appendix B). The first 6 low-temperature steps were rejected due to very low  $^{39}\text{Ar}$  yields, and therefore, 14 of 20 steps were used. The  $^{40}\text{Ar}/^{39}\text{Ar}$  plateau age is  $14.9 \pm 1.9$  Ma, containing 66.7% of total released  $^{39}\text{Ar}$  (steps 6-13), and is supported by

the inverse isochron age of  $17.4 \pm 4.2$  Ma (MSWD = 1.60,  $P = 0.12$ ; Fig. 41 and Tabs. 4 and 9), with an initial  $^{40}\text{Ar}/^{36}\text{Ar}$  ratio of  $264 \pm 38$ , which is within error of the atmospheric  $^{40}\text{Ar}/^{36}\text{Ar}$  ratio. The large error on the initial  $^{40}\text{Ar}/^{36}\text{Ar}$  ratio is caused by the some clustering of some steps on the inverse isochron (5 of 8 steps). The plagioclase *AI* index shows that the low temperature steps and the last step (1-5 and 14) indicate the effect of degassing from alteration, while the middle steps (6-13) appear to degas from fresh material (Tab. 9).

**Table 9 Summary of the results of  $^{40}\text{Ar}/^{39}\text{Ar}$  dating of sample 16-2 including plateau and inverse isochron ages, weights of the samples, average potassium concentration, and Alteration Index values.**

Sample (aliquot)	Plateau ages (Ma, $2\sigma$ )	Inverse isochron age (Ma, $2\sigma$ )	Mass (mg)	wt. % $\text{K}_2\text{O}^1$	Alteration Index (cut-off = $<0.00006$ ) <sup>2</sup>	
					Steps showing Alteration	Steps showing Fresh
16-2 (1)	$14.9 \pm 1.7$	$17.4 \pm 4.2$	9.296	0.090	1-5, 14	6-13

<sup>1</sup>see Appendix A

<sup>2</sup>after Baksi (2007)

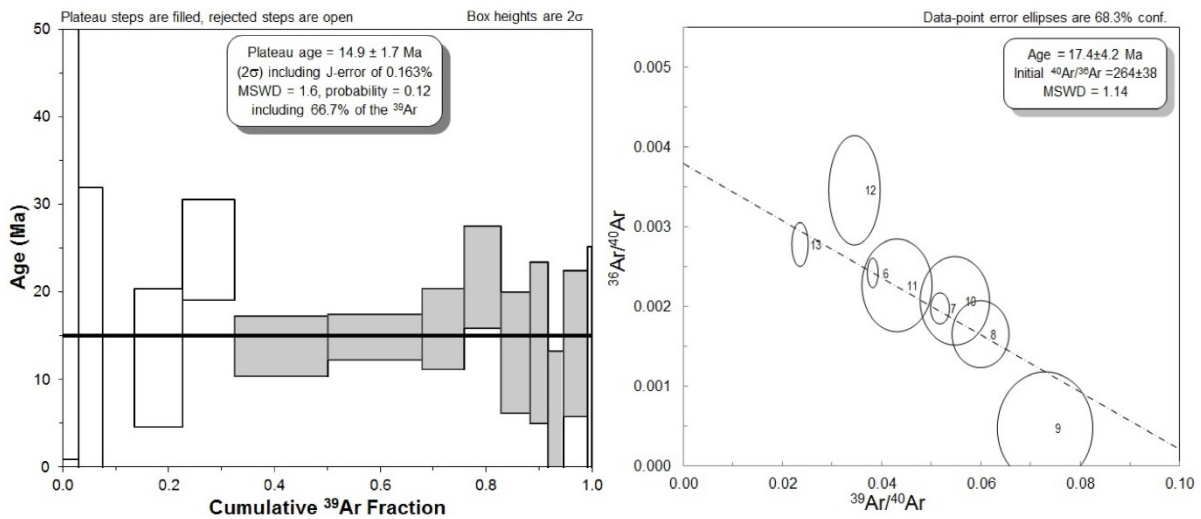


**Fig. 41 Age spectra (left) and inverse isochron diagrams (right) derived from the  $^{40}\text{Ar}/^{39}\text{Ar}$  step heating experiments on sample 16-2. The age spectrum apparent age error bars are  $2\sigma$  and the inverse isochron error ellipses are 68.3% confidence. The plateau steps are shown in grey while rejected steps are white. The black line on each age spectrum represents the error-weighted mean plateau age. The inverse isochron line fit is shown by a black dashed line.**

#### 4.5.2.6 Sample 14-1

Sample **14-1** was collected from the dike exposed along the coast of Isafjardardjup, ~1.1 km NE of the dike 16-2 (Fig. 36). Very few plagioclases were found in the 250  $\mu\text{m}$  fraction; therefore the 125  $\mu\text{m}$  fraction was used. The fine-grained plagioclase fraction showed relatively high levels of alteration, allowing only 5.954 mg of material to be hand-



picked for one  $^{40}\text{Ar}/^{39}\text{Ar}$  step-heating experiment. The first 5 steps yielded very low  $^{39}\text{Ar}$  values and have been rejected leaving 15 of 20 steps to be used in the age calculations. This yielded a plateau age of  $18.3 \pm 5.7$  Ma (MSWD = 0.50, P = 0.92, containing 93.8% of the total  $^{39}\text{Ar}$  (steps 2-14)), which is supported by an inverse isochron age of  $18.3 \pm 7.7$  Ma (MSWD = 0.54, P = 0.88), with an initial  $^{40}\text{Ar}/^{36}\text{Ar}$  ratio of  $295.5 \pm 2.3$  Ma, which overlaps within an error of the atmospheric  $^{40}\text{Ar}/^{36}\text{Ar}$  of 295.5 proposed by Steiger and Jäger (1977) (Fig. 42 and Tabs. 4 and 10). Based on the Alteration Index values, a significant number of the lower temperature steps (1-8 and 10) show alteration effects, while steps 9 and 11-15 appear to contain fresh material (Tab. 10).

**Table 10** Summary of the results of  $^{40}\text{Ar}/^{39}\text{Ar}$  dating of sample 14-1 including plateau and inverse isochron ages, weights of the samples, average potassium concentration, and Alteration Index values.

Sample (aliquot)	Plateau ages (Ma, $2\sigma$ )	Inverse isochron age (Ma, $2\sigma$ )	Mass (mg)	wt. % $\text{K}_2\text{O}^1$	Alteration Index (cut-off = $<0.00006$ ) <sup>2</sup>	
					Steps showing Alteration	Steps showing Fresh
14-1 (1)	$18.3 \pm 5.7$	$18.3 \pm 7.7$	5.954	0.097	1-8,10	9,11-15

<sup>1</sup>see Appendix A

<sup>2</sup>after Baksi (2007)

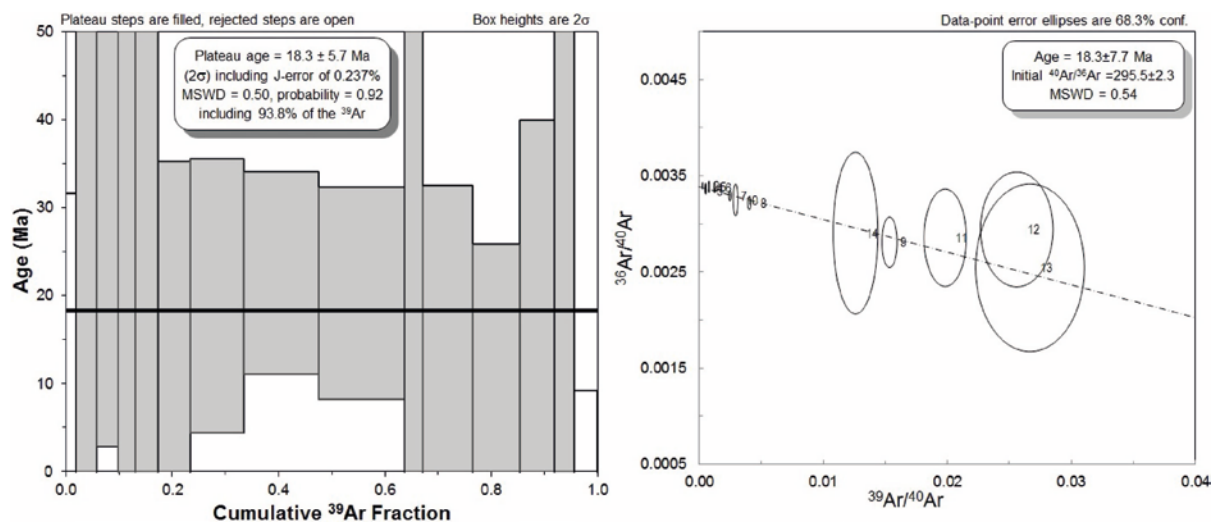


**Fig. 42** Age spectra (left) and inverse isochron diagrams (right) derived from the  $^{40}\text{Ar}/^{39}\text{Ar}$  step heating experiments on sample 14-1. The age spectrum apparent age error bars are  $2\sigma$  and the inverse isochron error ellipses are 68.3% confidence. The plateau steps are shown in grey while rejected steps are white. The black line on each age spectrum represents the error-weighted mean plateau age. The inverse isochron line fit is shown by a black dashed line.

#### 4.2.2.7 Sample 17-1

Sample **17-1** is the eastern most sample dated in this study and was sampled ~8.5 km NE of the dike sample 14-1 along the coast of Isafjardardjup (Fig. 36). The abundance of fresh plagioclases of desired size allowed > 39 mg of material to be hand-picked for the step-heating experiments and two aliquots of this sample were  $^{40}\text{Ar}/^{39}\text{Ar}$  dated (see Appendix B). After rejection of  $^{39}\text{Ar}$ -poor steps, 13 of 20 steps remain in aliquot 1, while 16 of 20 steps remain in aliquot 2. Results from aliquot 1 yielded a plateau age of  $13.9 \pm 1.5$  Ma (MSWD = 0.55,  $P = 0.86$ , containing 96.9% of the total  $^{39}\text{Ar}$  (steps 3-13)), which overlaps with the inverse isochron age of  $14.3 \pm 1.8$  Ma (MSWD = 0.35,  $P = 0.96$ ; Fig. 43 and Tabs. 4 and 11), with an initial  $^{40}\text{Ar}/^{39}\text{Ar}$  ratio of  $292 \pm 4.1$  Ma, within error of the atmospheric  $^{40}\text{Ar}/^{39}\text{Ar}$  ratio. Aliquot 2 yielded very similar to aliquot 1 plateau age of  $13.8 \pm 1.1$  Ma (MSWD = 0.64,  $P = 0.84$ , containing 100% of the total  $^{39}\text{Ar}$  (steps 1-16)), which is also very well supported by the inverse isochron of  $13.6 \pm 1.2$  Ma (MSWD = 0.41,  $P = 0.97$ ; Fig. 43 and Tab. 11), with an initial  $^{40}\text{Ar}/^{39}\text{Ar}$  ratio of  $297.1 \pm 2.4$  Ma, within error of the atmospheric  $^{40}\text{Ar}/^{39}\text{Ar}$  ratio of 295.5 (Steiger and Jäger, 1977). The overlap of the initial  $^{40}\text{Ar}/^{36}\text{Ar}$  ratios with the atmospheric ratio in both aliquots suggests that no excess  $^{40}\text{Ar}$  component was present in this sample. Similarly to the previous samples from this study, the calculated *AI* values indicate that the low temperature steps (1-4) from aliquot 1 represent degassing from the altered regions of the sample, while the remaining steps (5-13) are derived from fresh material. In the aliquot 2, the low temperature steps (1-3) show the same effect of degassing from alteration, whereas the remaining steps (4-16) represent fresh material (Tab. 11).

**Table 11** Summary of the results of  $^{40}\text{Ar}/^{39}\text{Ar}$  dating of sample 14-1 including plateau and inverse isochron ages, weights of the samples, average potassium concentration, and Alteration Index values.

					Alteration Index (cut-off = $<0.00006$ ) <sup>2</sup>	
Sample (aliquot)	Plateau ages (Ma, $2\sigma$ )	Inverse isochron age (Ma, $2\sigma$ )	Mass (mg)	wt.%K <sub>2</sub> O <sup>1</sup>	Steps showing Alteration	Steps showing Fresh
<b>17-1 (1)</b>	13.9±1.5	14.3 ± 1.8	9.213	0.120	1-4	5-13
<b>17-1 (2)</b>	13.8±1.1	13.6 ± 1.2	10.679		1-3	4-16

<sup>1</sup>see Appendix A

<sup>2</sup>after Baksi (2007)

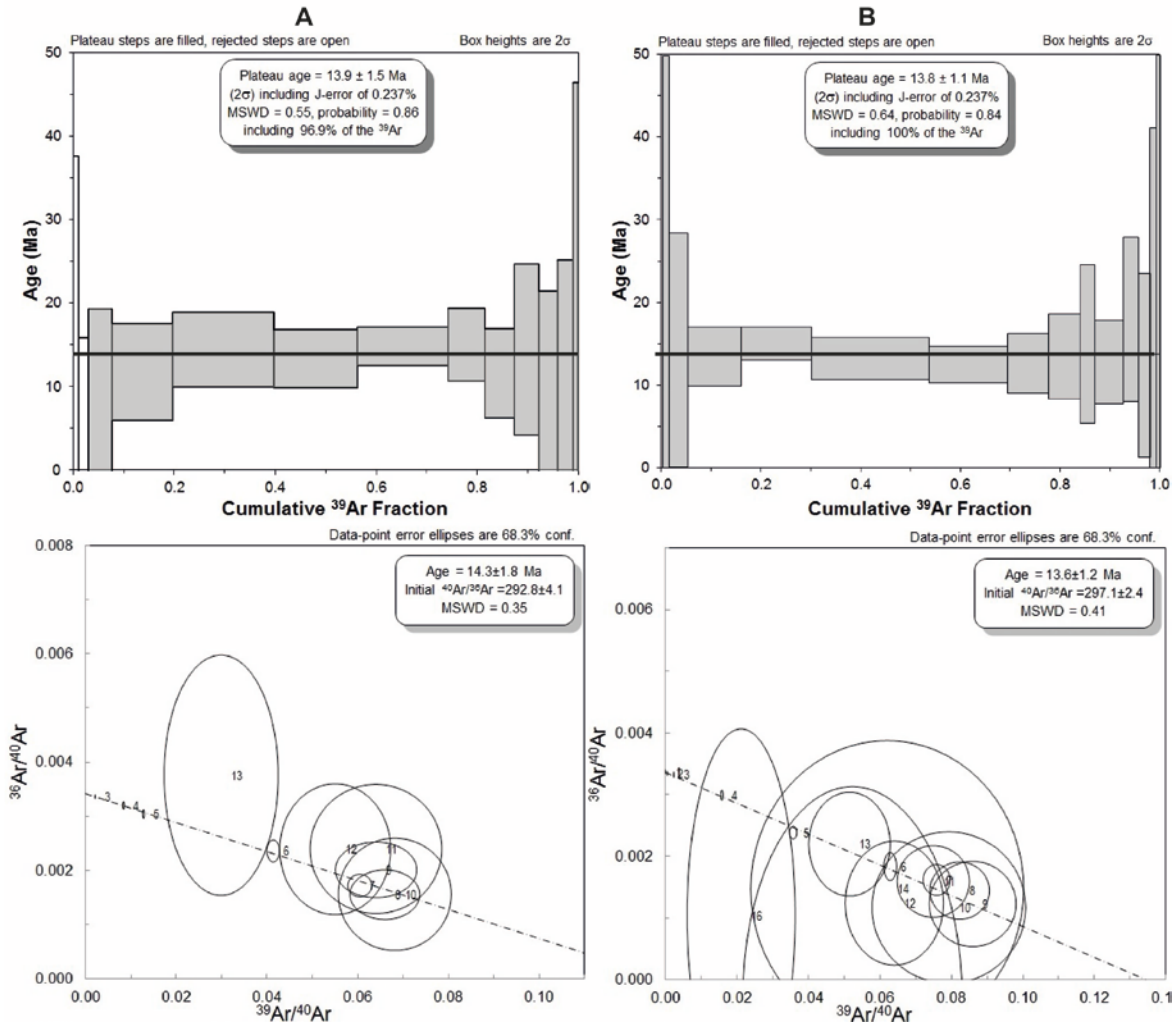


**Fig. 43** Age spectra (top) and inverse isochron diagrams (bottom) derived from the  $^{40}\text{Ar}/^{39}\text{Ar}$  step heating experiments on sample 17-1: (A) aliquot 1 and (B) aliquot 2. The age spectrum apparent age error bars are  $2\sigma$  and the inverse isochron error ellipses are 68.3% confidence. The plateau steps are shown in grey while rejected steps are white. The black line on each age spectrum represents the error-weighted mean plateau age. The inverse isochron line fit is shown by a black dashed line.

All the  $^{40}\text{Ar}/^{39}\text{Ar}$  plagioclase ages presented in this study have large individual step, plateau and inverse isochron errors, with common plateau age  $2\sigma$  errors of 8-23%. This is due to combination of factors, that include: a) the very low%  $\text{K}_2\text{O}$  concentrations of all the analyzed plagioclase separates (0.061-0.120%) in these low K-bearing dike rocks (Tables 5-11), and b) the maximum diameter of the argon ion laser beam used to  $^{40}\text{Ar}/^{39}\text{Ar}$  step-heat these plagioclases has a laser palette hole size/weight limit of 10 mg, to allow even heating of the material during lasing. For low K-bearing plagioclases, it is advisable to analyze 50-100 mg of material (i.e., 5-10 times more sample than was used in this study) from ~14 Ma old, 0.061-0.120%  $\text{K}_2\text{O}$  plagioclases to obtain precise measurable quantities of  $^{40}\text{Ar}^*$  for 20 heating steps using a MAP 216 mass spectrometer. However, this was not possible with the current experimental setup in the GEOMAR Ar-Ar dating laboratory. For example, McDougall et al. (1984) obtained <4.5%  $2\sigma$  precision on their K-Ar ages for whole rock

basalt samples containing higher wt. %K<sub>2</sub>O values of 0.1421-0.7063%, plus they utilized 10-20 g of sample to obtain the argon isotope measurements, and 30 mg of material for the K determinations. However, the validity of presented here dike plagioclase <sup>40</sup>Ar/<sup>39</sup>Ar ages is not diminished by these large errors, and this study represents the first <sup>40</sup>Ar/<sup>39</sup>Ar dating study of these Westfjords dikes.

## **4.6 Discussion**

### **4.6.1 Alteration of the dikes and its impact on the plagioclase phenocrysts**

The dikes from this study show moderate to relatively high level of alteration implying rather extensive hydrothermal activity associated with them after they intruded into the lava sequence of Westfjords (section 4.5.1). The dominance of clay minerals from the smectite group (montmorillonite, saponite and bowlingite) suggests a maximum temperature of the hydrothermal fluids to be ~250°C (Fig. 35 and Velde, 1985) and shows that the dikes were subjected to intermediate argillic alteration (e.g., Guilbert and Park, 1986). Montmorillonite forms in less leached rocks which still have abundant silica and cations, especially Al and Mg (Millot, 1970). Moreover, both montmorillonite and saponite are early alteration products which form in a low water/rock ratio environment and slightly reduced conditions at the time of alteration (Andrews, 1980; Alt et al., 1992). Thus, our observations indicate that the dikes were affected by slightly acidic hydrothermal fluids causing H<sup>+</sup> metasomatism (Pirajno, 2009). It appear that the hydrothermal activity associated with these seven dikes was sufficient to 1) completely replace all of the phase the least resistant to hydrothermal alteration, i.e., volcanic glass, in all samples except 2-1 and 17-1 which still appear much fresher; and 2) partly-to-completely replace the slightly more resistant olivine (e.g., dikes 1-2 and 16-2). However, plagioclase phenocrysts, the most resistant to alteration of all basaltic primary phases (Millot, 1970) show only slight alteration (change in color to yellow-brownish) and secondary minerals are only present in fractures and cracks (Fig. 35). Overall, the observed secondary minerals and generally high (but not complete) level of alteration overprinting suggest that alteration due to hydrothermal activity occurred relatively early after the dike emplacement events. However, the fact the rocks are not completely overprinted and clogged with secondary mineralization typical for lower temperatures (<250°C) shows that they retained some of their original permeability and suggests that hydrothermal cooling was only a contribution to a conductive-dominated cooling of the dikes against the host rocks (Delaney, 1988).

The microprobe analyses showed that no leaching of mobile elements (e.g., Na or K) occurred over the plagioclase grains boundaries (see Appendix A). Therefore, the wt. %K<sub>2</sub>O appears to reflect the original potassium content in these plagioclase phenocrysts indicating overall very low K content. Some potassium could be lost from the dikes due to, e.g., leaching from the volcanic glasses embedded in the groundmass, which in our samples have been completely replaced by smectite and Fe-OOH. However, measured wt. %K<sub>2</sub>O concentrations in Icelandic tholeiites are still very low, ranging from <<0.1% (in Tertiary formations) to 0.4% (closer to the hot spot) (e.g., Brouncea et al., 2012) which are similar to wt. %K<sub>2</sub>O concentrations in plagioclases used in this study. Therefore, it is most likely that the <sup>40</sup>Ar/<sup>39</sup>Ar dating of bulk rock would yield similar ages in comparison to ages determined with plagioclase indicating that plagioclase separates are probably the best material for <sup>40</sup>Ar/<sup>39</sup>Ar dating of altered basaltic dikes from Westfjords.

#### **4.6.2 Ages of the dikes and implications for off-axis hydrothermal activity**

The North American-Eurasian plate boundary is continuously migrating westwards (e.g., Burke et al., 1973) relative to a fixed Icelandic hot spot position (which is presently centered under the Vatnajökull glacier in the central-east part of the island (e.g., Fig. 9 in Chapter 1 and Sæmundsson, 1979)). Despite this migration, several rift-jumps throughout the geological history of Iceland have occurred to keep the hotspot ridge-centered, although few of the extinct rift zones such jumps produce have been recognized (Sæmundsson, 1979). The oldest extinct rift zone in Iceland, the North-West-Iceland Rift Zone, was located at what is now the westernmost part of the Westfjords Peninsula (Fig. 44) where, according to estimations, it was active until ~15 Ma ago. Later, rifting migrated eastwards to the Snæfellsnes–Skagi Rift Zone (SSRZ) (Fig. 44) where it was active until 7 Ma (Sæmundsson, 1979). Therefore, the Westfjords Peninsula is built of rocks which erupted between >15 and 7 Ma.

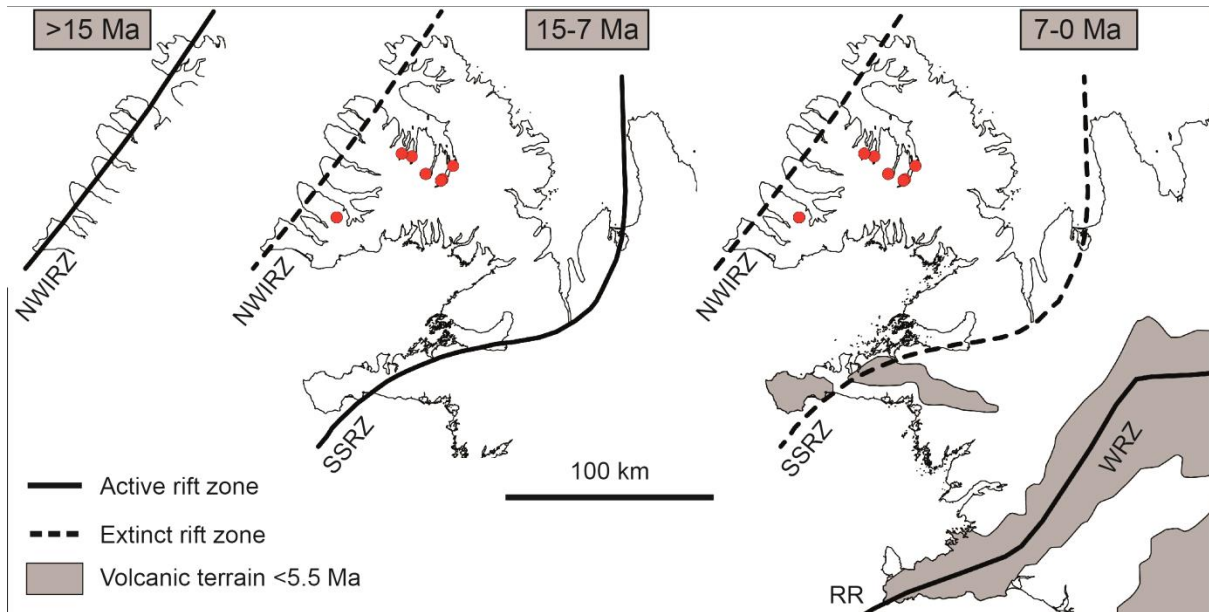


**Fig. 44** Geodynamic evolution of western Iceland during the past 15 Ma, modified from Martin et al. (2011). Westward migration of the plate boundary (away from the eastward migrating center of the hot spot (see Fig. 9 in Chapter 1)) resulted in a series of rift jumps (see text for details). Red dots show locations of dikes from this study (see Fig. 36 in this Chapter). Abbreviations: NWIRZ: North-West-Iceland Rift Zone; SSRZ: Snæfellsnes-Skagi Rift Zone; RR: Reykjanes Ridge; RRZ: Reykjanes Rift Zone.

Early age determinations from Moorbath et al. (1968) based on the K-Ar dating of whole rock basalts suggested that the oldest rock in Westfjords (see Fig. 34) had ages of  $16.4 \pm 0.6$  Ma (all the errors quoted in the discussion are  $2\sigma$ ). Unfortunately, the general geology and the ages of lavas in the Westfjords region are poorly known as few studies have been carried out. The most comprehensive K-Ar dating was performed by McDougall et al. (1984). Their results show that the complete  $\sim 7$  km thick sequence of flood basalt lavas along the western and eastern parts of the peninsula range in age from  $13.60 \pm 0.58$  Ma (near the base of the lava sequence in the western section) to about  $8.00 \pm 0.52$  Ma (near the top of the composite pile in the eastern section). Later, Kristjánsson and Jóhannesson (1996) indirectly dated lava piles located along the southern coast of Isafjardardjup by correlating the stratigraphic units and paleomagnetic polarities of the sequence in their profile with the results from the western profile from McDougall et al. (1984). However, no direct age measurements have been determined along the coast of Isafjardardjup and despite the lack of direct measurement, Kristjánsson and Jóhannesson (1996) concluded that the  $\sim 2.6$  km thick lava sequence in this region was erupted between  $13.57 \pm 0.60$  Ma and  $11.78 \pm 0.38$  Ma. However, more recently Riishuus et al. (2013) used the  $^{40}\text{Ar}/^{39}\text{Ar}$  dating method to re-evaluate the results from McDougall et al. (1984) and presented  $>50$  new age determinations. They showed that the oldest lavas, located below the oldest sediment horizon in Westfjords, were erupted between  $\sim 17.1$  and  $16.1$  Ma, which is significantly older than previously thought



(Moorbath et al., 1968; Sæmundsson, 1979), and is also older than the K-Ar ages of the surface lavas along southern coast of Isafjardardjup of  $13.57 \pm 0.60$  to  $11.78 \pm 0.38$  (McDougall et al. 1984, Kristjánsson and Jóhannesson, 1996).

The  $^{40}\text{Ar}/^{39}\text{Ar}$  ages of the dikes studied here overlap within  $2\sigma$  errors with the overall age of the peninsula, as they all yield  $^{40}\text{Ar}/^{39}\text{Ar}$  ages  $>7$  Ma (see Tab. 3).  $^{40}\text{Ar}/^{39}\text{Ar}$  ages calculated in our study range from  $13.6 \pm 2.1$  Ma (sample 2-1) to  $18.3 \pm 5.7$  Ma (sample 14-1), which means that they all are older than 7 Ma (except of sample 10-1 aliquot 2 with calculated age of  $18.0 \pm 2.0$  Ma) and most likely older than 10 Ma. This, together with the fact that all the dikes are located between the two extinct rift zones (NWIRZ and SSRZ, Fig. 44) may suggest that they were all intruded along the SSRZ, before the rift jumped into its current position (WRZ, Fig. 44). Our  $^{40}\text{Ar}/^{39}\text{Ar}$  dating results suggest that all the studied dikes intruded roughly at the same time, as their plateau ages all overlap with each other within  $2\sigma$  errors (see Tab. 3), most likely within the neovolcanic zone of one of the extinct axes; however, with our data we are unable to put any further constraints on the potential extent of this neovolcanic zone (its width, for example, in comparison to currently active Icelandic neovolcanic zones (RRZ and ARZ, Fig. 10 in Chapter 1).

The correlation of stratigraphy and paleomagnetic polarity presented by Kristjánsson and Jóhannesson (1996) for lavas sampled near the area studied here suggested that the exposed lava pile was erupted between  $13.57 \pm 0.60$  Ma and  $11.78 \pm 0.38$  Ma, which would make this a maximum age limit for the intruded dikes. We note that the absolute ages used by Kristjánsson and Jóhannesson (1996) were determined by McDougall et al. (1984) using the K-Ar method on whole rock basalts and that more recently, Riishuus et al. (2013), using the more precise  $^{40}\text{Ar}/^{39}\text{Ar}$  method to re-date the oldest rocks previously dated by McDougall et al. (1984) found them to yield ages  $\sim 0.5$ - $1.5$  Ma older than generated by the K-Ar method. In view of this uncertainty in the accuracy of the older K-Ar dates, it is difficult to use them as a geological constraint on the quality of the dikes dating presented here. We note, however, that most dike ages overlap within  $2\sigma$  errors with the maximum lava ages, with two dike samples (Sample 1-2 aliquot 1;  $16.5 \pm 1.9$  Ma and Sample 10-1 aliquot 2;  $18.0 \pm 2.0$  Ma) giving a significantly older, geologically unreasonable, values. The possible explanation for older ages in these two dikes will be discussed later.

The primal motivation for  $^{40}\text{Ar}/^{39}\text{Ar}$  dating of the dikes from Westfjords was to evaluate whether they were intruded on-axis in the neovolcanic zone (dikes age  $\approx$  lavas) or off-axis events of rejuvenated volcanism in Westfjords (dikes age  $<$  lavas)? This could help us understand if the widespread low-temperature hydrothermal activity observed in Westfjords

(this thesis, Chapter 3) can be sustained for a very long time even away from the neovolcanic zone and derive heat from hot rocks at depth or if younger off-axis volcanism (intraplate) is necessary for such support. Our results show that the dikes we dated are not significantly younger than their host lavas. As we mentioned above, all the dikes from our study intruded roughly at the same time (probably within the neovolcanic zone of the extinct SSRZ) and their  $^{40}\text{Ar}/^{39}\text{Ar}$  ages overlap within  $2\sigma$  errors with the maximum age of the hosting lava pile (i.e.,  $15.37 \pm 0.34$  Ma, McDougall et al., 1984) and extrapolated ages of the lava pile of the southern coast of Isafjardardjup (i.e.,  $13.57 \pm 0.60$ - $11.78 \pm 0.38$  Ma, McDougall et al., 1984). This suggests that they intruded coevally with the hosting lavas, and therefore, are not younger, off-axis events. This has major implications for the hydrothermal circulation in the Westfjords but perhaps also in other off-axis regions of the global mid-ocean ridge system. Our results suggest that there was no volcanic rejuvenation of the crust in the Westfjords significantly after the lavas were erupted on-axis, and certainly not since 7 Ma, when the currently extinct SSRZ jumped to its present position along the WRZ and RRZ. Geological mapping (this thesis, i.e., Pałgan et al., 2016, Chapter 3) showed that the abundant low-temperature hydrothermal activity scattered across the Westfjords region is exclusively controlled by dikes rather than by faults, which are known to focus hydrothermal flow in on-axis settings of the modern neovolcanic zones of mid-ocean ridges (reviewed in German et al., 2016). Therefore, our results show that, despite most likely being older than 10 Ma (all samples are  $>10$  Ma within  $2\sigma$  errors) and most certainly older than 7 Ma, such old dikes and dike margins still remain open conduits for hydrothermal flow. Yang and Shen (2005) noted a low-velocity anomaly underneath western Iceland (eastern Westfjords) associated with relatively thin (15-20 km) crust in comparison to elsewhere in Iceland (e.g., Allen et al., 2002). They suggested that the large reduction in velocity in western Iceland, similarly to central Iceland, reflects the presence of partial melt and a residual mantle upwelling beneath a failed spreading center of the SSRZ. Therefore, if a thin lithosphere extends from the western Westfjords to the present location of the hot spot (potentially along the hot spot track, see Fig. 9 in Chapter 1), the shallow crust-mantle boundary may act as a heat extractor and a pathway for the buoyant mantle flow away from the present hot spot (Yang and Shen, 2005). Hence, it is likely that such flow is at-depth heat source for the low-temperature hot spring in Westfjords while the dikes provide permeable vertical pathways for ascending heated fluids. Similar mantle flow pathways may be present along the Reykjanes Ridge, other hot spot-influenced ridges or even non-hot spot-influenced ridges. Therefore, it appears that along axis magmatic system of the mid-ocean ridges may be sufficient to sustain even far off-axis

hydrothermal circulation up to 15 Ma old crust but the hydrothermal activity will most likely be low-temperature (<150°C). In an earlier study (this thesis, i.e., Pałgan et al., 2016, Chapter 3), the Westfjords were compared to >2 Ma old crust of the adjacent Reykjanes Ridge (south of Iceland). In the view of these comparisons and the above results showing that >7 Ma old dikes can still support low-temperature hydrothermal circulation, we suggest that the situation may be similar on the >2 Ma old crust of the Reykjanes Ridge. However, recognizing surface expressions of old dikes in off-axis regions along the flanks of the Reykjanes Ridge could be difficult taking into account relatively high sedimentation coverage there (Litvin, 1984). However, off-axis and young volcanoes (without tectonic deformation) sitting on top of older faults have been recognized in a central section (this thesis, i.e., Pałgan et al., 2016) and along the southern part of the ridge (Hey et al., 2010; Martinez and Hey, 2017). If such dikes are exposed in areas where sediments do not accumulate, e.g., steep slopes of volcanic edifices or fault scarps (e.g., Auzende et al., 1989) they may still support hydrothermal discharge.

#### 4.6.3 Quality and reliability of $^{40}\text{Ar}/^{39}\text{Ar}$ dating method for dating Icelandic dikes

The dikes examined in this study were sampled along the southern coast of Isafjardardjup, near the area studied by Kristjánsson and Jóhannesson (1996), where the correlation of stratigraphy and paleomagnetic polarity suggests that the exposed lava pile was erupted between  $13.57 \pm 0.60$  Ma and  $11.78 \pm 0.38$  Ma. Even though the majority of the  $^{40}\text{Ar}/^{39}\text{Ar}$  dike ages from this study overlap within  $2\sigma$  errors with the projected maximum  $13.57 \pm 0.60$  Ma K-Ar age of surface lava sequence (Kristjánsson and Jóhannesson, 1996), two samples ages (sample 1-2 aliquot 1 =  $16.5 \pm 1.9$  Ma and sample 10-1 aliquot 2 =  $18.0 \pm 2.0$  Ma) give older ages. There are a few possible explanations for this slight mismatch that can be related to the different geochronological methodologies, differences in the compositions of the two rock units (host rock/dikes), what material was dated (whole rock basalt versus plagioclase separates), and the overall freshness of the samples and any hydrothermal overprinting, etc. The use of different  $^{40}\text{K}$  to  $^{40}\text{Ar}$  decays constants between our  $^{40}\text{Ar}/^{39}\text{Ar}$  study compared to the McDougall et al. (1984) study can be ruled out, as both the McDougall et al. (1984) and this study employ the same decay constants,  $^{40}\text{K}/\text{K}$  production ratio and atmospheric  $^{40}\text{Ar}/^{36}\text{Ar}$  ratio of Steiger and Jäger (1977).

It is possible that the dikes (especially the ones with ages that do not overlap with other samples ages within  $2\sigma$  errors, i.e., sample 1-2 aliquot 1 and sample 10-1 aliquot 2) entrained some older sub-surface plagioclase xenocrysts (e.g., Gardner et al., 2002, Santo et al., 2011) as they intruded into the overlying younger lava pile (Fig. 44 and Foulger and

Anderson, 2005). Two types of plagioclase crystals are preserved in these dikes: a) normally zoned plagioclase found in the altered groundmass, and b) oscillatory zoned plagioclase that often form rounded clusters or clots of crystals (see Fig. 35). Sano et al. (2011) found similar plagioclase crystal clots in the 1256D IODP hole of the East Pacific Rise, and based on the size and occurrence of the oscillatory zoned plagioclases, their different zoning patterns, and the chemical disequilibria between the An-rich cores and the host liquids, they concluded that their plagioclase clots are xenocrysts. In addition, Gardner et al. (2002) found similar crystal clots of hornblende and plagioclase in the 74 ka Toba tuff, which preserved  $^{40}\text{Ar}/^{39}\text{Ar}$  hornblende and plagioclase ages up to 1.5 Ma in age. Unfortunately, the oscillatory zoned plagioclases in our study were not analyzed using the EMP, plus the groundmass of these dike samples is too altered to preserve any original basaltic melt to see if the normally-zoned and oscillatory-zoned plagioclases were in disequilibria. However, based on the different zoning in the two generations of plagioclases in these dike samples, and the occurrence of the oscillatory-zoned plagioclases crystal clots, it is possible that these crystals are xenocrysts.

The plagioclase separates used in this study were prepared by jaw crushing of the whole rock dike samples, which means that the plagioclase crystals in the crushed material could come from a variety of different sized plagioclase crystals. The average grain diameter of the groundmass plagioclase phenocrysts is 125  $\mu\text{m}$ , whereas the grain diameter of the plagioclases from the crystal clots is larger (250  $\mu\text{m}$  to 3 mm). Therefore, it is probable that the predominantly 250-500  $\mu\text{m}$  sieved fractions used to hand-pick the  $^{40}\text{Ar}/^{39}\text{Ar}$  plagioclase separates contained xenocrysts derived from these large crystal clots. If this is the case, it may explain the older  $^{40}\text{Ar}/^{39}\text{Ar}$  plagioclase ages of the dikes (from  $18.3 \pm 5.7$  to  $13.8 \pm 1.1$  Ma), when compared to the  $13.57 \pm 0.60$  Ma to  $11.78 \pm 0.38$  Ma estimated ages of the host lavas suggested by Kristjánsson and Jóhannesson (1996), as the dikes may have incorporated some older plagioclase xenocrystic material from the >15 Ma sub-surface lava sequence underlying Westfjords (Foulger and Anderson, 2005).

Using an author-written MathCAD program (J-A. Wartho, pers. comm., 2017) it was possible to model the effects of  $^{40}\text{Ar}^*$  loss in 250  $\mu\text{m}$  and 3 mm diameter plagioclase grains, assuming a spherical diffusion geometry and using the Ar diffusion parameters of plagioclase of Wartho et al., (2013). A very simple assumption is made that the plagioclase crystals in these dikes linearly cooled from 1200°C to 20°C over a period of 2-3 years. This cooling rate is based on a 1 m wide basaltic dike from Curewitz and Karson (1998), which would be applicable to my Icelandic dikes as they all have widths of >1 m. This would result in 100% resetting of any older xenocrystic  $^{40}\text{Ar}/^{39}\text{Ar}$  ages in 250  $\mu\text{m}$  diameter plagioclase grains.

However, the larger 3 mm diameter plagioclase grains would only lose a maximum of ~10-17% of their original  $^{40}\text{Ar}^*$  via cooling over 2 and 3 years, respectively, resulting in the potential preservation of older pre-dike-intrusive, partially-reset  $^{40}\text{Ar}/^{39}\text{Ar}$  ages in these larger plagioclase xenocrysts. However, more detailed chemical composition studies are required in the future to determine if the larger oscillatory-zoned plagioclases and crystal clots, observed in the thin sections of our dikes, are xenocrysts.

The  $^{40}\text{Ar}/^{39}\text{Ar}$  method only requires one small aliquot of a sample to obtain a geochronological age (e.g., tens to hundreds of milligrams for basalt samples of this age), whereas the K-Ar dating technique requires two aliquots (e.g., hundreds of milligrams to grams of material is required), and these two aliquots are assumed to be homogenous with respect to the  $^{40}\text{K}$  and  $^{40}\text{Ar}^*$  contents. In addition, K-Ar dating only yields a single age for each 2 aliquots of sample analyzed, whereas the  $^{40}\text{Ar}/^{39}\text{Ar}$  dating technique commonly uses a step-heating technique, obtaining a series of 10-20 step ages from the same aliquot, thus yielding much more age and chemical composition information from the sample. For these reasons, the  $^{40}\text{Ar}/^{39}\text{Ar}$  dating technique is generally considered to yield more accurate and precise ages compared to the K-Ar geochronological method. The early ages from McDougall et al. (1984), later quoted by Kristjánsson and Jóhannesson (1996) were determined by the K-Ar method on whole rock basalts while in a more recent attempt, Riishuus et al. (2013) used more precise  $^{40}\text{Ar}/^{39}\text{Ar}$  method to re-date the oldest rocks previously dated by McDougall et al. (1984), yielding ages ~0.5-1.5 Ma older. This suggests that, in order to accurately determine the age of lava pile of Westfjords (including southern coast of Isafjardardjup), the earlier K-Ar results may need to be analyzed using the  $^{40}\text{Ar}/^{39}\text{Ar}$  method. However, our study is currently the only direct attempt to directly date the dike intrusions in Westfjords. Hence, we see no reason to not rely on these preliminary geochronological results, which despite their large errors, are accurate and geologically meaningful. Nevertheless, the errors on plagioclase  $^{40}\text{Ar}/^{39}\text{Ar}$  ages in this study are large and the reasons for this should be addressed.

The potassium content of plagioclases used for  $^{40}\text{Ar}/^{39}\text{Ar}$  dating is crucial in order to yield measureable  $^{40}\text{Ar}^*$  concentrations that are at least 5 times higher than the system blank  $^{40}\text{Ar}$  values, thus minimizing errors and keeping the highest possible precision and accuracy of the age measurements. The rock types analyzed by McDougall et al. (1984) in western and eastern Westfjords were tholeiites, olivine tholeiites, porphyritic basalts and intermediate to acidic lavas. The weight % concentrations of  $\text{K}_2\text{O}$  in the whole rock samples they analyzed are relatively high for the rock types they studied and range from 0.1421 to as high as 0.7063% (McDougall et al., 1984). Along the southern coast of Isafjardardjup, Kristjánsson

and Jóhannesson (1996) additionally recognized some compound lavas and basaltic icelandites. In addition, the whole rock K-Ar dating approach of McDougall et al. (1984) was possible due to the overall freshness of their whole rock samples, and hence they obtained K-Ar whole rock ages with majority of the errors ( $2\sigma$ ) on the order of  $< 5\%$  (with only two ages with errors of 6%). In contrast to the McDougall et al. (1984) K-Ar dating project, our study of 7 basaltic dike samples indicated that they are relatively highly altered (see section 4.5.1) and, therefore, the  $^{40}\text{Ar}/^{39}\text{Ar}$  dating method could not be used on the highly altered whole rock or groundmass material. Plagioclases are moderately abundant in our dikes and they appeared to be fresh and relatively unaltered, hence they were hand-picked for  $^{40}\text{Ar}/^{39}\text{Ar}$  analyses. Subsequent electron microprobe analyses showed that these plagioclase weight % $\text{K}_2\text{O}$  concentrations range from 0.061% (Sample 4-1) to 0.120% (Sample 17-1), which is summarized in Table 2. Overall, it is observed that the smallest  $^{40}\text{Ar}/^{39}\text{Ar}$  age errors are obtained for samples with the highest K plagioclase concentrations, e.g., sample 17-1 (wt. % $\text{K}_2\text{O}$  = 0.120) has plateau age errors of 8% (aliquot 2) and 11% (aliquot 1). This is in line with the general assumptions of  $^{40}\text{Ar}/^{39}\text{Ar}$  dating method and observations from earlier studies on plagioclase samples (e.g. Boven et al., 2001).

Hydrothermal alteration may have a significant impact on the  $^{40}\text{Ar}/^{39}\text{Ar}$  ages determined using the plagioclase separates as, for example, excess Ar may reside in hydrothermal alteration minerals filling fractures (Verati et al., 2013) or mobile elements (e.g., Na or K) may be leached from the plagioclase (Humphris, 1978). Moreover, investigations of the thin sections of our dikes show in the majority of the dikes plagioclase crystals display different levels of alteration: from almost no alteration (e.g., sample 2-1) to high alteration (e.g., sample 14-1). However, microprobe analysis of the plagioclase boundaries showed no leaching of K (see section 4.5.1) and all the plagioclase separates have been treated with hydrofluoric acid to remove alteration products. Acid treatment proved to be relatively successful as no visible alteration has been observed in the plagioclase separates under the binocular microscope after the acid treatment. Nevertheless, some degassing from alteration material has been observed during the step-heating experiments (see Tables 5-11 in section 4.5.2). If  $^{40}\text{Ar}^*$  was lost (e.g., due to later hydrothermal alteration or diffusion via grain boundaries) the determined  $^{40}\text{Ar}/^{39}\text{Ar}$  ages would be younger than expected. However, this is not the case for these dike plagioclase samples; therefore, it appears that hydrothermal alteration had minor impact on the calculated  $^{40}\text{Ar}/^{39}\text{Ar}$  ages of the Westfjords dike samples.

Therefore, in summary the main reasons for obtaining large errors on the individual step and plateau  $^{40}\text{Ar}/^{39}\text{Ar}$  ages from the 7 basalt plagioclase samples include: (1) low



potassium contents of the analyzed plagioclase samples and (2) the scarcity of good-quality plagioclases in some of the samples so that 10 mg of material could not be prepared.

## 4.7 Conclusions

To summarize, it has been shown that the dikes from Westfjords can be dated using the  $^{40}\text{Ar}/^{39}\text{Ar}$  method on plagioclase separates in hydrothermally-altered basalt dike samples. Our  $^{40}\text{Ar}/^{39}\text{Ar}$  plagioclase ages yielded high errors on individual step and plateau ages, which mainly resulted from the overall very low K concentrations in the plagioclases, low quantities of the material, and the overall degrees of alteration in the dike samples. Despite these high errors, the majority of the obtained  $^{40}\text{Ar}/^{39}\text{Ar}$  plagioclase ages overlap within  $2\sigma$  errors with previous K-Ar whole rock ages of the hosting lava pile along the southern coast of Isafjardardjup (McDougall et al., 1984). This suggests that the dikes were emplaced shortly after extrusion of the surrounding lava flows, which occurred along SSRZ before the rift jump relocated it to its current position along the WRZ at 7Ma. All the  $^{40}\text{Ar}/^{39}\text{Ar}$  dike ages overlap with each other within  $2\sigma$  errors, suggesting that they all intruded roughly at the same time, most likely within the neovolcanic zone of the SSRZ. This, together with the overlapping age of these dikes with the hosting lava pile, suggests that they are not younger, off-axis volcanic episodes and Westfjords have not been volcanically rejuvenated at least over the past 7 Ma. Nevertheless they support low-temperature hydrothermal circulation at the present day. This implies that old rift-related dikes remain open and penetrable for the hydrothermal fluids flow up to 15 Ma after they left the neovolcanic zone. Similar situation to the one observed in Westfjords may occur on the Reykjanes Ridge, where low-temperature hydrothermal activity controlled by old dikes may be widespread in  $>2$  Ma crust. These dikes can be recognized in the off-axis regions of the Reykjanes Ridge as volcanoes sitting on top of faults, or where they are exposed on unsedimented seafloor, e.g., steep slopes of volcanic edifices or fault scarps.

## 4.8 References

- Allen, R.M., Nolet, G., Morgan, W.J., Vogfjörd, K., Nettles, M., Ekström, G., Bergsson, B.H., Erlendsson, P., Foulger, G.R., Jakobsdottir, S., Julian, B.R., Pritchard, M., Ragnarsson, S., and Stefansson, R., 2002, Plume-driven plumbing and crustal formation in Iceland: *Journal of Geophysical Research*, v. 107, p. 1–19, doi: 10.1029/2001JB000584.
- Alt, J.C., France-lanord, C., Floyd, P.A., Castillo, P., and Galy, A., 1992, Low-temperature hydrothermal alteration of Jurassic ocean crust, Site 801: *Proceedings of the Ocean Drilling Program, Scientific Results*, v. 129, p. 415–427, doi: 10.2973/odp.proc.sr.129.132.1992.

- Andrews, A.J., 1980, Saponite and Celadonite in Layer 2 Basalts , DSDP Leg 37: Contributions to Mineralogy and Petrology, v. 73, p. 323–340, doi: 10.1007/BF00376627.
- Auzende, J.-M., Bideau, D., Bonatti, E., Cannat, M., Honnorez, J., Lagabrielle, Y., Malavieille, J., Mamaloukas-Frangoulis, V., and Mevel, C., 1989, Direct observation of a section through slow-spreading oceanic crust: *Nature*, v. 337, p. 726–729, doi: 10.1038/337726a0.
- Baksi, A.K., 2007, A quantitative tool for detecting alteration in undisturbed rocks and minerals – I: water , chemical weathering and atmospheric argon: *Geological Society of America, Special Papers*, v. 430, p. 285–303, doi: 10.1130/2007.2430(15).
- Boven, A., Pasteels, P., Kelley, S.P., Punzalan, L., Bingen, B., and Demaiffe, D., 2001,  $^{40}\text{Ar}/^{39}\text{Ar}$  study of plagioclases from the Rogaland anorthosite complex (SW Norway); an attempt to understand argon ages in plutonic plagioclase: *Chemical Geology*, v. 176, p. 105–135, doi: 10.1016/S0009-2541(00)00372-7.
- Brouncea, M., Feinmana, M., LaFemina, P., and Gurenko, A., 2012, Insights into crustal assimilation by Icelandic basalts from boron isotopes in melt inclusions from the 1783–1784 Lakagígar eruption: *Geochimica et Cosmochimica Acta*, v. 94, p. 164–180, doi: 10.1016/j.gca.2012.07.002.
- Burke, K., Kidd, W.S.F., and Wilson, J.T., 1973, Plumes and concentric plume traces of the Eurasian Plate: *Nature*, v. 241, p. 128–129, doi: 10.1038/physci241128a0.
- Cumbest, R.J., Johnson, E.L., and Onstott, T.C., 1994, Argon composition of metamorphic fluids: Implications for  $^{40}\text{Ar}/^{39}\text{Ar}$  geochronology: *Geological Society of America Bulletin*, v. 106, p. 942–951, doi: 10.1130/0016-7606(1994)106<0942:ACOMFI>2.3.CO;2.
- Curewitz, D., and Karson, J.A., 1998, Geological Consequences of Dike Intrusion at Mid-Ocean Ridge Spreading Centers, In: Buck, R., Karson, J.A., and Lagabrielle, Y. [Eds.], *Faulting and Magmatism at Mid-Ocean Ridges*, *Geophysical Monograph* 106, p. 117–137, doi: 10.1029/GM106p0117
- Dalrymple, G.B., and Moore, J.G., 1966, Argon 40: Excess in Submarine Pillow Basalts from Kilauea Volcano, Hawaii: *Science*, v. 161, p. 1132–1135, doi: 10.1126/science.161.3846.1132.
- Delaney, P.T., 1988, FORTRAN 77 programs for conductive cooling of dikes with temperature-dependent thermal properties and heat of crystallization: *Computers & Geosciences*, v. 14, p. 181–212, doi: 10.1016/0098-3004(88)90004-0.
- Devey, C.W., and Stephens, W.E., 1992, Deccan-related magmatism west of the Seychelles-India rift, In: Storey, B.C., Alabaster, T., and Pankhurst, R.J. [Eds.], *Magmatism and the causes of continental break-up: Geological Society London Special Publications* 68, p. 271–291, doi: 10.1144/GSL.SP.1992.068.01.17.

- Dodson, M.H., 1973, Closure temperature in cooling geochronological and petrological systems: *Contributions to Mineralogy and Petrology*, v. 40, p. 259–274, doi: 10.1007/BF00373790.
- Duncan, R.A., and Al-Amri, A.M., 2013, Timing and composition of volcanic activity at Harrat Lunayyir, western Saudi Arabia: *Journal of Volcanology and Geothermal Research*, v. 260, p. 103–116, doi: 10.1016/j.jvolgeores.2013.05.006.
- Féraud, G., and Courtillot, V., 1994, Comment on: “Did Deccan volcanism pre-date the Cretaceous-Tertiary transition?” *Earth and Planetary Science Letters*, v. 122, p. 259–262, doi: 10.1016/0012-821X(94)90068-X.
- Foland, K.A., Linder, J.S., Laskowski, T.E., and Grant, N.K., 1983,  $^{40}\text{Ar}/^{39}\text{Ar}$  dating of glauconites: Measured  $^{39}\text{Ar}$  recoil loss from well-crystallized specimens: *Chemical Geology (Isotope Geoscience Section)*, v. 2, p. 241–264.
- Foulger, G.R., and Anderson, D.L., 2005, A cool model for the Iceland hotspot: *Journal of Volcanology and Geothermal Research*, v. 141, p. 1–22, doi: 10.1016/j.jvolgeores.2004.10.007.
- Gardner, J.E., Layer, P.W., and Rutherford, M.J., 2002, Phenocrysts versus xenocrysts in the youngest Toba Tuff: Implications for the petrogenesis of 2800 km<sup>3</sup> of magma: *Geology*, v. 30, p. 347–350, doi: 10.1130/0091-7613(2002)030<0347:PVXITY>2.0.CO;2.
- German, C.R., Petersen, S., and Hannington, M.D., 2016, Hydrothermal exploration of mid-ocean ridges: Where might the largest sulfide deposits be forming?: *Chemical Geology*, v. 420, p. 114–126, doi: 10.1016/j.chemgeo.2015.11.006.
- Guilbert, J.M., and Park, C.F., 1986, *The Geology of Ore Deposits*: W. H. Freeman, New York, pp. 985
- Hey, R., Martinez, F., Höskuldsson, Á., and Benediktsdóttir, Á., 2010, Propagating rift model for the V-shaped ridges south of Iceland: *Geochemistry, Geophysics, Geosystems*, v. 11, p. Q03011, doi: 10.1029/2009GC002865.
- Humphris, S.E., 1978, The hydrothermal alteration of oceanic basalts by seawater: *Geochimica et Cosmochimica Acta*, v. 42, p. 107–125, doi: 10.1016/0016-7037(78)90221-1.
- Kelley, S., 2002, K-Ar and Ar-Ar Dating, In: Porcelli, D., Ballentine, C.J., and Wieler, R., [Eds.], *Nobles Gases in Geochemistry and Cosmochemistry*, *Reviews in Mineralogy and Geochemistry*, v. 47, p. 785–818, doi: 10.2138/rmg.2002.47.17.
- Kristjánsson, L., and Jóhannesson, H., 1996, Stratigraphy and Paleomagnetism of the Lava Pile South of Ísafjarðardjúp, NW- Iceland: *Jökull*, v. 44, p. 3–16.
- Kuiper, Y.D., 2002, The interpretation of inverse isochron diagrams in  $^{40}\text{Ar}/^{39}\text{Ar}$  geochronology: *Earth and Planetary Science Letters*, v. 203, p. 499–506, doi: 10.1016/S0012-821X(02)00833-6.

- Kutterolf, S., Freundt, A., and Burkert, C., 2011, Eruptive history and magmatic evolution of the 1.9 kyr Plinian dacitic Chiltepe Tephra from Apoyeque volcano in west-central Nicaragua: *Bulletin of Volcanology*, v. 73, p. 811–831, doi: 10.1007/s00445-011-0457-0.
- Lanphere, M.A., and Dalrymple, G., 2000, First-principles calibration of  $^{38}\text{Ar}$  tracers: implications for the ages of  $^{40}\text{Ar}/^{39}\text{Ar}$  fluence monitors: United States Geological Survey Professional Paper, v. 1621, p. 1–10.
- Lanphere, M.A., and Dalrymple, G.B., 1978, The use of  $^{40}\text{Ar}/^{39}\text{Ar}$  data in evaluation of disturbed K-Ar systems: Geological Survey Open-File Report, v. 78-701, p. 141–148.
- Litvin, V.M., 1984, The Structure of Sedimentary Series and its Role in the Morphostructure of the Ocean Floor, In: Litvin, V.M. [Ed.], *The Morphostructure of the Atlantic Ocean Floor*, Springer Netherlands, p. 51–76, doi: 10.1007/978-94-009-6245-3\_3.
- Lo, C., and Onstott, T.C., 1989,  $^{39}\text{Ar}$  recoil artifacts in chloritized biotite: *Geochemica et Cosmochimica Acta*, v. 53, p. 2697–2711, doi: 10.1016/0016-7037(89)90141-5.
- Ludwig, K.R., 2011, Users manual for Isoplot 4.15: A geochronological toolkit for Microsoft Excel: Special Publication 4, Berkeley Geochronology Centre, Berkeley, CA.
- Martin, E., Paquette, J.L., Bosse, V., Ruffet, G., Tiepolo, M., Sigmarsson, O., Magmas, L., Pascal, U.B., and Ferrand, C., 2011, Geodynamics of rift-plume interaction in Iceland as constrained by new  $^{40}\text{Ar}/^{39}\text{Ar}$  and in situ U-Pb zircon ages: *Earth and Planetary Science Letters*, v. 311, p. 28–38, doi: 10.1016/j.epsl.2011.08.036.
- Martinez, F., and Hey, R., 2017, Propagating buoyant mantle upwelling on the Reykjanes Ridge: *Earth and Planetary Science Letters*, v. 457, p. 10–22, doi: 10.1016/j.epsl.2016.09.057.
- McDougall, I., and Harrison, T.M., 1999, *Geochronology and Thermochronology by the  $^{40}\text{Ar}/^{39}\text{Ar}$  method*: Oxford University Press, New York, pp. 269.
- McDougall, I., Kristjánsson, L., and Sæmundsson, K., 1984, Magnetostratigraphy and geochronology of northwest Iceland: *Journal of Geophysical Research*, v. 89, no. B8, p. 7029–7060, doi: 10.1029/JB089iB08p07029.
- Mercer, C.M., and Hodges, K. V., 2016, ArAR - A software tool to promote the robust comparison of K-Ar and  $^{40}\text{Ar}/^{39}\text{Ar}$  dates published using different decay, isotopic, and monitor-age parameters: *Chemical Geology*, v. 440, p. 148–163, doi: 10.1016/j.chemgeo.2016.06.020.
- Merrill, C., and Turner, G., 1966, Potassium-argon dating by activation with fast neutrons: *Journal of Geophysical Research*, v. 71, no. 11, p. 2852–2857, doi: 10.1029/JZ071i011p02852.
- Millot, G., 1970, *Geology of clays: weathering, sedimentology, geochemistry*: Springer-Verlag, New York, pp. 430, doi: 10.1007/978-3-662-41609-9.

- Moorbath, S., Sigurdsson, H., and Goodwin, R., 1968, K-Ar ages of the oldest exposed rocks in Iceland: *Earth and Planetary Science Letters*, v. 4, p. 197–205, doi: 10.1016/0012-821X(68)90035-6.
- Pałgan, D., Devey, C.W., and Yeo, I.A., 2016, Dike control of hydrothermal circulation in the Tertiary Icelandic crust and implications for cooling of the seafloor: *Journal of Volcanology and Geothermal Research*, v. 316, p. 22–33, doi: 10.1016/j.jvolgeores.2016.02.021.
- Person, R.C., Hedge, C.E., Thomas, H.H., and Stern, T.W., 1966, Geochronology of the St. Kevin Granite and Neighboring Precambrian Rocks, Northern Sawatch Range, Colorado: *Geological Society of America Bulletin*, v. 77, p. 1109–1120, doi: 10.1130/0016-7606(1966)77[1109:GOTSKG]2.0.CO;2.
- Pickles, C.S., Kelley, S.P., Reddy, S.M., and Wheeler, J., 1997, Determination of high spatial resolution argon isotope variations in metamorphic biotites: *Geochimica et Cosmochimica Acta*, v. 61, p. 3809–3833, doi: 10.1016/S0016-7037(97)00289-5.
- Pirajno, F., 2009, Hydrothermal Processes and Wall Rock Alteration, In: Pirajno F. [Ed.], *Hydrothermal Processes and Mineral Systems*: Springer Netherlands, Amsterdam, p. 73–164, doi: 978-1-4020-8613-7.
- Pringle, M.S., Staudigel, H., and Gee, J., 1991, Jasper Seamount: Seven million years of volcanism: *Geology*, v. 19, p. 364–368, doi: 10.1130/0091-7613(1991)019<0364:JSSMYO>2.3.CO;2.
- Renne, P.R., Deino, A.L., Hilgen, F.J., Kuiper, K.F., Mark, D.F., Iii, W.S.M., Morgan, L.E., Mundil, R., and Smit, J., 2013, Time scales of critical events around the Cretaceous-Paleogene boundary: *Science*, v. 339, p. 684–687, doi: 10.1126/science.1230492.
- Renne, P.R., Sprain, C.J., Richards, M.A., Self, S., Vanderkluysen, L., and Pande, K., 2015, State shift in Deccan volcanism at the Cretaceous-Paleogene boundary, possibly induced by impact: *Science*, v. 350, p. 76–78, doi: 10.1126/science.aac7549.
- Riishuus, M.S., Duncan, R.A., and Kristjansson, L., 2013, Revised Geochronology and Magnetostratigraphy of Northwest Iceland: American Geophysical Union, Fall Meeting 2013, abstract #GP43A-1196.
- Sæmundsson, K., 1979, Outline of the geology of Iceland: *Jökull*, v. 29, p. 7–28.
- Sano, T., Sakuyama, T., Ingle, S., Rodriguez, S., and Yamasaki, T., 2011, Petrological relationships among lavas, dikes, and gabbros from Integrated Ocean Drilling Program Hole 1256D: Insight into the magma plumbing system beneath the East Pacific Rise: *Geochemistry, Geophysics, Geosystems*, v. 12, p. Q06013, doi: 10.1029/2011GC003548.
- Steiger, R.H., and Jäger, E., 1977, Subcommittee on geochronology: Convention on the use of decay constants in geo- and cosmochronology: *Earth and Planetary Science Letters*, v. 36, p. 359–362, doi: 10.1016/0012-821X(77)90060-7.

- Turner, G., and Cadogan, P.H., 1974, Possible effects of  $^{39}\text{Ar}$  recoil in  $^{40}\text{Ar}/^{39}\text{Ar}$  dating: *Geochimica et Cosmochimica Acta*, v. 5, p. 1601–1615.
- Velde, B., 1985, *Clay minerals: A physico-chemical explanation of their occurrence*: Elsevier, Amsterdam, pp. 248.
- Verati, C., Patrier-Mas, P., Lardeaux, J.M., and Bouchot, V., 2013, Timing of geothermal activity in an active island-arc volcanic setting: First  $^{40}\text{Ar}/^{39}\text{Ar}$  dating from Bouillante geothermal field (Guadeloupe, French West Indies): In: Jourdan, F., Mark, D.F., and Verati, C. [Eds.], *Advances in  $^{40}\text{Ar}/^{39}\text{Ar}$  Dating: From Archaeology to Planetary Sciences*, Geological Society, London, Special Publications, v. 378, p. 285–295, doi: 10.1144/SP378.19.
- Wartho, J.-A., Kelley, S.P., and Elphick, S.C., 2013, Ar diffusion and solubility measurements in plagioclases using the ultra-violet laser depth-profiling technique, In: Jourdan, F., Mark, D.F., and Verati, C. [Eds.], *Advances in  $^{40}\text{Ar}/^{39}\text{Ar}$  Dating: From Archaeology to Planetary Sciences*, Geological Society, London, Special Publications, v. 378, p. 137–154, doi: 10.1144/SP378.13.
- Wartho, J.-A., Rex, D.C., and Guise, P.G., 1996, Excess argon in amphiboles linked to greenschist facies alteration in the Kamila Amphibolite Belt, Kohistan island arc system, northern Pakistan: insights from  $^{40}\text{Ar}/^{39}\text{Ar}$  step-heating and acid leaching experiments: *Geological Magazine*, v. 133, p. 595–609, doi: 10.1017/S0016756800007871.
- Yang, T., and Shen, Y., 2005, P-wave velocity structure of the crust and uppermost mantle beneath Iceland from local earthquake tomography: *Earth and Planetary Science Letters*, v. 235, p. 597–609, doi: 10.1016/j.epsl.200.





# Chapter 5

## Volcanism and hydrothermalism on a hot spot-influenced ridge: Comparing Reykjanes Peninsula and Reykjanes Ridge, Iceland

This chapter consists of a manuscript currently being under review at the Journal of Volcanology and Geothermal Research.

Authors: Dominik Pałgan<sup>1\*</sup>, Colin W. Devey<sup>1</sup> and Isobel A. Yeo<sup>1,2</sup>

<sup>1</sup>GEOMAR, Helmholtz Centre for Ocean Research Kiel, Wischhofstr. 1–3, 24148, Kiel, Germany

<sup>2</sup>National Oceanography Centre Southampton, Waterfront Campus, European Way, Southampton SO14 3ZH, United Kingdom

\* Corresponding author ([dpalgan@geomar.de](mailto:dpalgan@geomar.de))

Declaration of contributions: D.P. and I.A.Y. proposed the study. D.P. carried field work in Iceland, acquired bathymetric data from the Marine Research Institute in Iceland, interpreted the data and wrote the manuscript. All co-authors further contributed to the interpretation and discussion of the results in the manuscript.

## **5 Volcanism and hydrothermalism on a hot spot–influenced ridge: Comparing Reykjanes Peninsula and Reykjanes Ridge, Iceland**

### **Abstract**

High-temperature hydrothermal venting along the mid-ocean ridges is one of the primary pathways for the heat extraction from the Earth's mantle accounting for ~25% of the total heat loss. Early estimates indicate that the number of high temperature vents – 1 per 100 km of axial length – scales with spreading rate and should scale with crustal thickness, as thicker crust contains more magmatic heat. But up to present, shallow ridge axes underlain by thick crust show anomalously low incidences of high-temperature activity. Here we compare the Reykjanes Ridge, an abnormally shallow ridge with thick crust and only one high-temperature vent known over 900 km axial length, to the adjacent subaerial Reykjanes Peninsula, which is characterized by high-temperature geothermal sites confined to four volcanic systems (each showing relatively young (Holocene) volcanic activity) transected by fissure swarms consisting of multiple faults, cracks and fissures, and showing high seismicity. New high-resolution bathymetry of the Reykjanes Ridge between 62°30'N and 63°30'N shows seven Axial Volcanic Ridges (AVR) which are, based on their morphology, mechanism of formation and tectonic regime equivalents to the fissure swarms on land. We investigate in detail the volcano-tectonic features of all mapped AVRs. Based on our observations and interpretations we expect all of these segments to be hydrothermally active. We suggest that combined CTD and autonomous vehicles surveys are probably the most efficient methods in this region for hydrothermal exploration, as the unique morphological and hydrographic setting of Reykjanes Ridge causes hydrothermal plumes to be quickly dispersed and diluted due to exposure of the ridge axis to strong bottom currents.

**Key words:** Reykjanes Peninsula, Reykjanes Ridge, Mid-Atlantic Ridge, Axial Volcanic Ridge, Hydrothermal activity, Steinahóll Vent Field

### **5.1 Introduction**

Early estimates of Baker and German (2004) and later of German et al. (2016) predict the incidence of high-temperature hydrothermal venting along slow-spreading ridges should be >1 vent field per 100 km of the ridge axis and be correlated with spreading rate. On hot spot-influenced sections of ridge, higher incidences are expected due to higher magma (and hence heat) fluxes. On the hot spot-influenced Mid-Atlantic Ridge (MAR) south of the Azores this effect is observed, with 1 vent field every ~25–30 km (German et al., 1996), a

much denser spacing than would be expected for a slow-spreading ridge. In contrast, the Reykjanes Ridge (RR), which lies close to the Iceland hot spot, has to date only one discovered system, the Steinahóll Vent Field (German et al., 1994), along ~950 km of its axis. This is surprising considering that the adjacent, subaerial Reykjanes Peninsula has ~6 fields per 100 km of axis (e.g., Torfason, 2003). It is unclear if this apparent paucity of vents is because they are not present (and the ridge-axis is being cooled by mechanisms other than high-temperature venting) or if they have just not yet been detected. Beside the implications for the thermal balance of such shallow ridges, determining how and where the Reykjanes Ridge loses its heat also has implications for marine mineral prospecting and chemosynthetic biogeography.

The subaerial Reykjanes Peninsula (RP), a direct on land continuation of the Reykjanes Ridge, provides a unique opportunity to observe directly the interaction between volcanic, tectonic and hydrothermal processes on the divergent plate boundary. It constitutes a subaerial extension of the RR and is similar to it in terms of geomorphology, mechanisms of volcanic activity, tectonism and seismicity. Conducting fieldwork on land is easier than in the deep ocean, as large areas can be covered more quickly and detailed information on the topography is available from satellite imagery. This allows us to map the areas and assess the geological setting of hydrothermalism on a geologically similar ridge segment much more quickly and easily than would be possible using research vessels. Hence, extrapolation of controls of venting on the RP combined with interpretation of high-resolution ship-based bathymetry can help us better predict locations of new hydrothermal systems on the RR.

## **5.2 Datasets and methods**

The Digital Elevation Model (DEM) of the Reykjanes Peninsular used in this study is a smoothed, accurately relocated iteration of data collected during the 2000 Shuttle Radar Topography Mission (SRTM) re-worked by Aleksandr Yashin (pers. comm.) and has a resolution of 100 m. The ship-based multibeam bathymetry of the RR between 62°30'N and 63°30'N was collected by the Marine Research Institute (MIR) in Reykjavik on board *R/V Árni Friðriksson* during the cruise A8-2006 in summer 2006 using the onboard Simrad EM 300 multibeam echosounder. The data were gridded at 60 m resolution using the QPS Fledermaus and DMagic software. The maps presented here were produced from this data using a combination of shaded relief and the Terrain Texture Shader (TTS) applications in Global Mapper. The TTS is a tool that enhances the DEMs with increased contrast and detail,

and no bias on the illumination direction. Acoustic backscatter information from the same survey is presently undergoing re-processing at MIR and is not presented in this study.

The locations of earthquake hypocenters along the RP and RR for the years 1950–2015 were extracted from the International Seismic Center (ISC) on-line bulletin. The location of earthquakes with magnitudes higher than 4 are well-constrained teleseismically from the arrival times of P and S phases reported both to the ISC and NEIC (US Geological Survey's National Earthquake Information Center). These events have been relocated using, in addition, the arrival times of *PKiKP* and *PKP<sub>df</sub>* and the depth phases *pP*, *pwP*, and *sP* (Engdahl et al., 1998).

The locations of geothermal fields on the RP were taken from (Torfason, 2003) and our own field observations; the location of the Steinahóll Vent Field on the RR was taken from German et al. (1994) and the InterRidge Vents Database Ver. 3.3. The geological map of the RP is based on the Geological Map of Southwest Iceland produced at a scale of 1:100 000 (Sæmundsson et al., 2010) and enhanced by additional interpretation of the DEM. The geological map of the RR was produced in ArcMap 10.1. ArcMap was also used to measure the geometry of features and eruption volumes.

In the interpretations given below, the term "eruptive fissure" is used to refer to the sites of the rejuvenated and/or youngest volcanism. From bathymetric data alone there are some clear criteria which allow us to distinguish such fissures from fault blocks. To classify a feature as an eruptive fissure we require them: (1) to be linear or sinuous in shape, (2) to be  $\leq 1$  km wide, (3) to form local highs (mostly  $>20$  m above the surrounding seafloor), (4) to have no significant depth offsets along their length and (5) to have distinct outward-facing slopes on both sides with slope angles between  $5^\circ$  and  $28^\circ$  (shallower than in case of faults). Examples of bathymetric profiles showing these features are given in Figure 45.

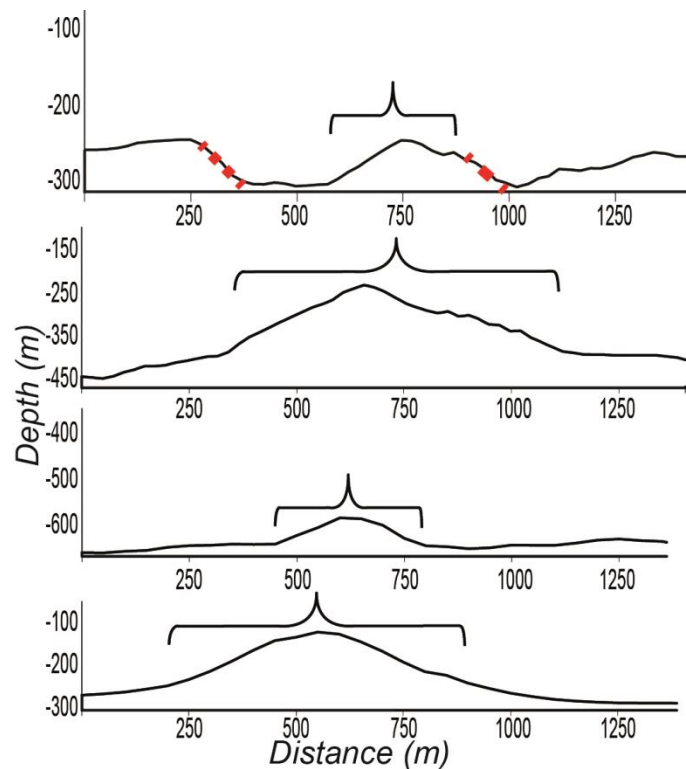


**Fig. 45** Profiles across four examples of eruptive fissures (marked by brackets) mapped along the Reykjanes Ridge. These examples illustrate their characteristic width (shown by brackets), the fact that they form local highs and allow them to be clearly distinguished from faulted blocks (e.g., red dashed lines in upper panel). The profiles have no vertical exaggeration.

## 5.3 Geological setting

### 5.3.1 Reykjanes Peninsula

The RP is a direct subaerial continuation of the RR (Fig. 46A), part of the northern MAR. The bedrock comprises basalts of Pleistocene age, covered by later postglacial and historic lava flows (Johannesson, 2014). Most of the Pleistocene rocks are hyaloclastite ridges, table mountains (tuyas) and basaltic lava flows (Gudmundsson, 1987). The RP has been an active spreading zone for the last 6–7 Ma, when the spreading axis jumped there from its previous location on the Snæfellsnes Peninsula (Sæmundsson, 1979; Johannesson, 1980). Few historic eruptions (younger than AD 871) have been mapped in the area (Johannesson, 2014).



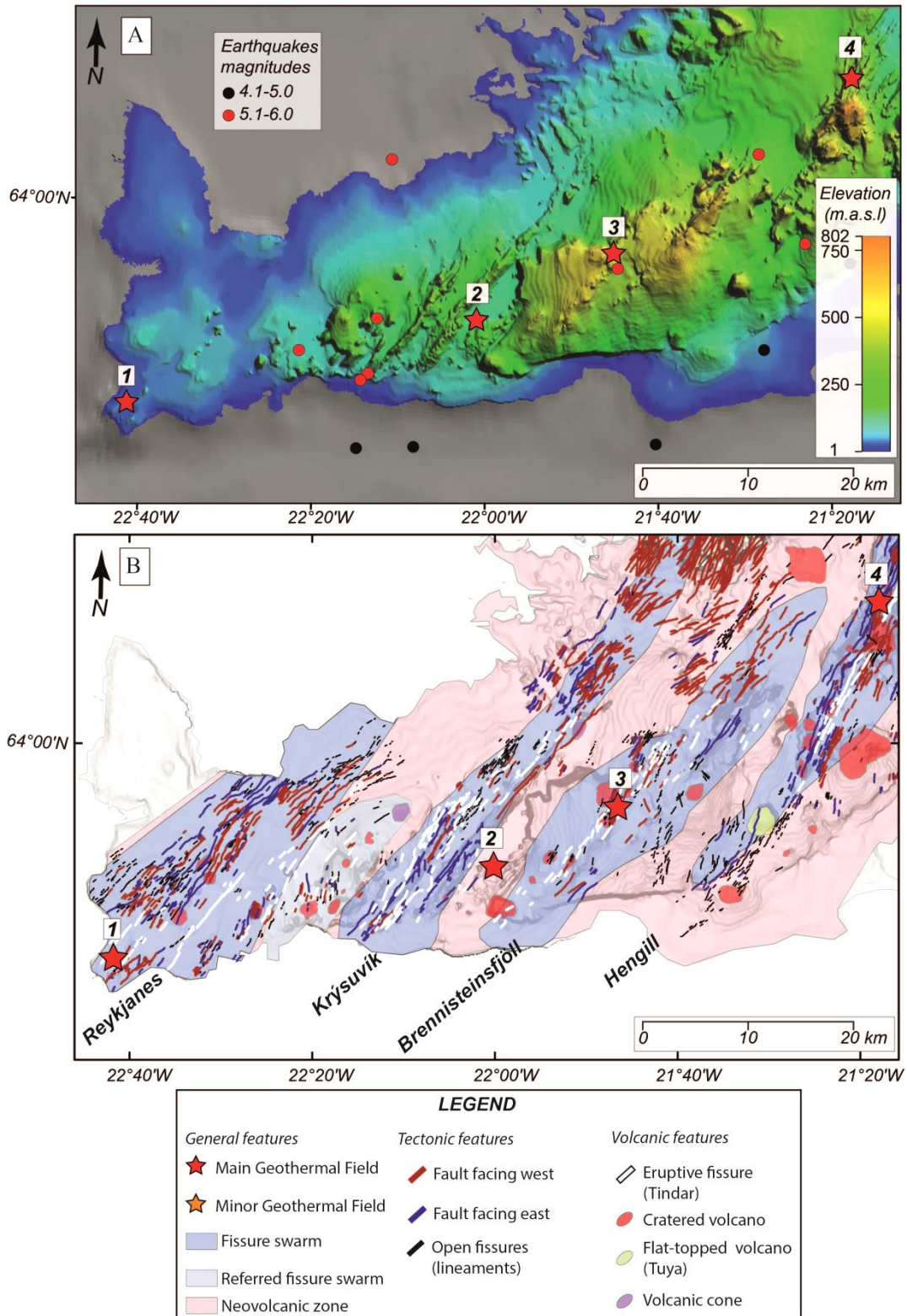


**Fig. 46** The general geological setting of the Reykjanes Peninsula (SW Iceland) and associated hydrothermal systems. (A) Topography of the peninsula based on the Digital Elevation Model (DEM) gridded at 100 m. The area is a direct, onshore prolongation of the Reykjanes Ridge. Seven major earthquakes ( $M_1 > 4$ ) occurred here between 1950 and 2015 (red dots). In general, the Reykjanes Peninsula has 4 major high-temperature (red stars) and 4 much smaller geothermal fields (orange stars). The four high-temperature fields are: 1 – Reykjanes, 2 – Krýsuvík, 3 – Brennisteinsfjöll and 4 – Nesjavellir (Hengill). (B) Simplified geological map of the peninsula based on Sæmundsson et al. (2010). The area is characterized by four distinctive fissure swarms (named underneath each swarm) each with multiple eruptive fissures, faults, fractures, volcanic edifices and an associated high-temperature geothermal field.

The peninsula consists of 4 major right stepping en echelon fissure swarms (e.g., Sæmundsson, 1979) consisting of tensional fractures, normal and/or strike-slip faults, and volcanic or tectonic fissures (Sæmundsson, 1979; Clifton and Kattenhorn, 2006). From west to east they are: Reykjanes, Krýsuvík, Brennisteinsfjöll, and Hengill (Fig. 46). Each fissure swarm is approximately 15–40 km long, 7–15 km wide and on average strikes N40° E (Sæmundsson, 1979). Each of these fissure swarms is transecting volcanic systems (where only Hengill has developed a central volcano) distinguished from each other by chemically and spatially constrained magma source. Moreover, all of these volcanic systems host geothermal activity (Fig. 46); hence, 4 high-temperature geothermal fields can be distinguished on the peninsula over a distance of ~80 km.

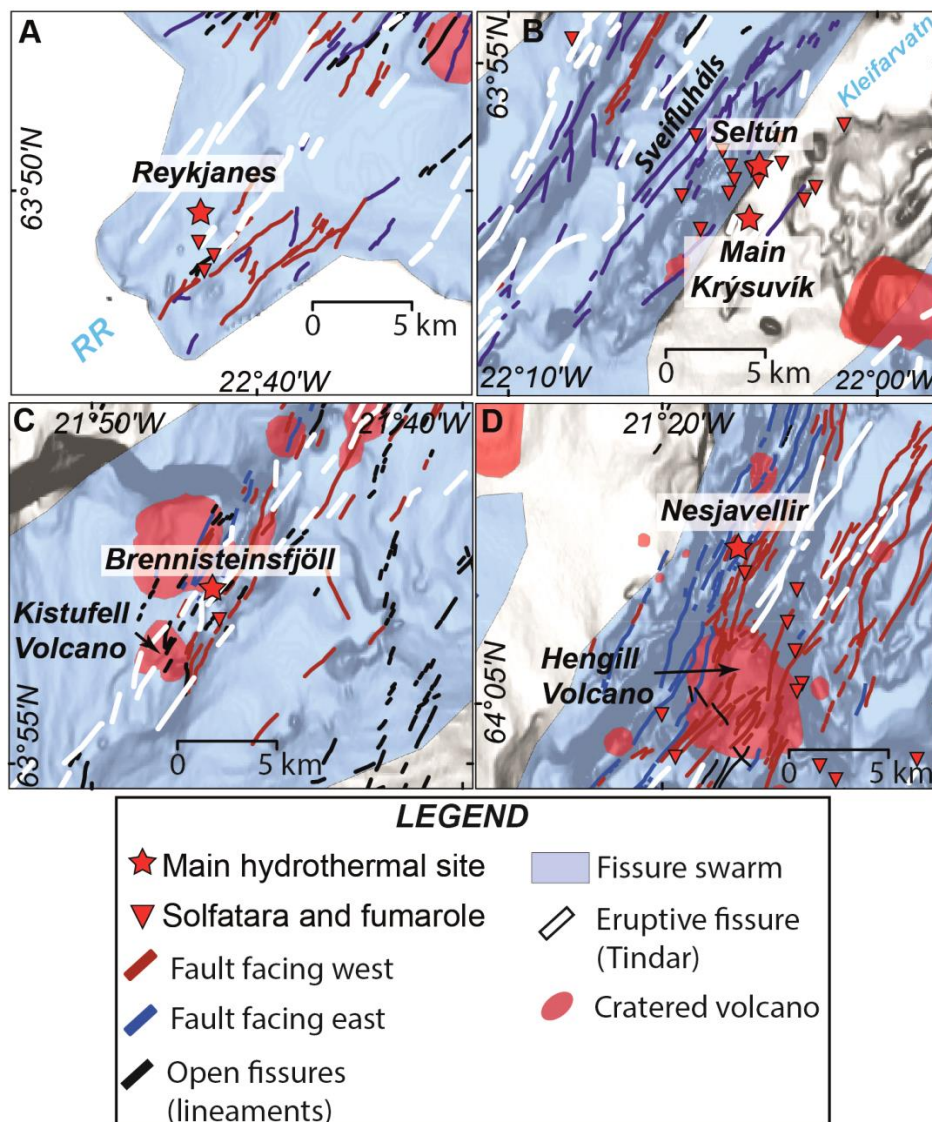
The **Reykjanes geothermal field** is located at the southwest tip of the peninsula (Fig. 47A). The temperature of the reservoir is between 250 and 290°C at a depth of a few hundreds of meters. The fluids have similar salinities to seawater although intense interaction with the host basaltic rocks has led to differences in concentrations of some other ions (increased K, Ca, SiO<sub>2</sub>, Fe, and Al; and decreased SO<sub>4</sub> and Mg) (Björnsson et al., 1970; Arnórsson, 1995). The Reykjanes site covers about 1 km<sup>2</sup>. The surface manifestations of the geothermal activity are saline hot springs, steam vents, mud springs, hot ground and solfataras (e.g., Björnsson et al., 1970). Due to its saline fluid composition, the Reykjanes geothermal site is a clear analog for shallow submarine hydrothermal systems although under lower hydrostatic pressure (Fowler et al., 2015).

The **Krýsuvík geothermal field** is located in the central part of the peninsula (Fig. 47B), on the eastern side of the Sveifluháls hyaloclastic ridge and surrounded by many faults. Most likely the heat driving geothermal activity in Krýsuvík area is linked to the historic eruption located just west of the Sveifluháls ridge while tectonic features provide permeable conduits (Sæmundsson et al., 2010). Detailed mapping of hydrothermal alteration suggests that this field covers about 40–60 km<sup>2</sup> (Mawejje, 2007). The surface manifestations here are: acid surface alteration, steam vents, steam-heated hot springs, mud pots and hot ground. The main surface activity is visible near the Sveifluháls hyaloclastic ridge area, especially within the small sub-areas of the field known as Seltún and Main Krýsuvík (Mawejje, 2007; Markússon and Stefánsson, 2011).

The **Brennisteinsfjöll geothermal field** (Fig. 47C) is associated with two lava flows of different ages that have erupted from the Kistufell volcano. The area is characterized by many fumaroles which seem to be more intense in the older lava. The entire presently active geothermal field covers only about 0.01 km<sup>2</sup>. However, evidence of hydrothermal alteration

can be observed beyond the boundaries of the lava flows and ancient manifestations can be found on a fault about 1 km north of the main field, where hydrothermal clays, gypsum and sulphur deposits have been observed, suggesting former high-temperature activity (Jónsson, 1978; Maochang, 2001).

The **Hengill** is located at the triple-junction between the Reykjanes Rift Zone, the West Volcanic Zone and the South Iceland Seismic Zone (e.g., Ingólfsson et al., 2008). The high-temperature geothermal field **Nesjavellir** (Fig.47D) is located where the Hengill fissure swarm intersects with the Hengill central volcanic system (Sæmundsson, 1992; Clifton et al., 2002). Observational and modeling studies suggest that heated groundwater migrates from a heat source under the central volcano and rises along fissures, dikes and associated fractures towards the southwest and northeast, feeding the Nesjavellir system (Franzson et al., 2010) and numerous smaller manifestations around it. The temperature of the Nesjavellir geothermal reservoir is  $> 200^{\circ}\text{C}$  at a depth of 1 km (Haraldsdóttir et al., 2012).



The plate boundary exposed along the RP is characterized by a ~2–5 km wide zone of high seismicity (e.g., Klein et al., 1977; Jakobsdóttir, 2008). The zone trends approximately N80°E in the central part of the peninsula and bends south in the western–most part of the peninsula. Seven seismometer stations installed on the peninsula have been continuously monitoring seismic activity since 1993 (Stefánsson et al., 1993), recording thousands of earthquakes (Jakobsdóttir, 2008). Older stations distributed across the country have recorded seven earthquakes with  $M_I$  greater than 5 (Fig. 46A) between 1950 and 2015 (based on International Seismic Center (ISC) Bulletin Database and relocated according to Engdahl et al., 1998).

### 5.3.2. Reykjanes Ridge

The Reykjanes Ridge (Fig. 48A) is an oblique and ~ 900 km long segment of the northern Mid-Atlantic Ridge, located between Iceland and the Bight Fracture Zone (57°N), spreading at 1 cm yr<sup>-1</sup> half rate (e.g., Talwani et al., 1971; Vogt, 1971; Keeton et al., 1997; Searle et al., 1998). It is the longest V-shaped and hot spot-influenced ridge in the world (Ito, 2001) with some unique characteristics listed below. The depth of the ridge axis gradually increases from sea level at the coast to about 2600 m near the Bight Fracture Zone and the axis is characterized by two distinct morphologies. South of 59°N, a median valley typical of slow-spreading ridges (~2.5 km deep and ~15 km wide) is present. It has been suggested that this marks the maximum extent of the Iceland hotspot influence (Talwani et al., 1971; Searle et al., 1994; Peirce et al., 2005; Peirce and Sinha, 2008). North of 59°N, the ridge is characterized by an axial high more typical for intermediate and fast spreading ridges like the Juan de Fuca Ridge or East Pacific Rise (e.g., Talwani et al., 1971). Crustal thicknesses vary from 7–7.5 km near 57°45'N (Sinha et al., 1998), a value typical of oceanic crust uninfluenced by hotspot activity elsewhere in the oceans, to 10.6 km at 62°40'N, 14 km at the tip of the Reykjanes Peninsula and ~21 km at Hengill (Weir et al., 2001). The entire length of

---

**Fig. 47 (Previous page) Detailed locations of the four main high-temperature hydrothermal fields on the Reykjanes Peninsula in relation to geological features. Blue polygons are fissure swarms, red polygons are volcanic cones, blue and red lines are minor faults facing east and west, respectively; (A) The Reykjanes Field is located at the SW tip of the peninsula, covers 1 km<sup>2</sup> and shows few fumarole around it; (B) The Krýsuvík Field is located at the eastern side of the Sveifluháls hyaloclastic ridge. The area has 2 major hydrothermal sites, Seltún and Main Krýsuvík, and many fumaroles in close proximity; (C) The Brennisteinsfjöll Field is located NE of the Kistufell volcano where solfataras, fumaroles and former high-temperature hydrothermal alteration occupies older and younger lava flows and some faults; (D) The Nesjavellir Field is located in the Hengill area and associated with the Hengill central volcano. The area is strongly tectonized which, together with the heat source from the volcano, seems to be controlling the hydrothermal circulation. Many solfataras and fumaroles are present around the volcano, along faults and associated fractures.**

the ridge is devoid of first-order offsets (Searle et al., 1994), however, it is constructed of individual en echelon Axial Volcanic Ridges (AVRs) separated from each other by 3–10 km of flatter seafloor with (lava flows), hummocky terrain and sparse volcanic cones (Fig. 48A). Each AVR is 20–30 km long, 3–6 km wide and 200–500 m high (Parson et al., 1993; Searle et al., 1998; Keeton et al., 1997). The AVRs trend  $\sim 015^\circ$ , oblique to the overall Reykjanes Ridge orientation but almost perpendicular to the spreading direction. Each AVR contains conical-, fissure- and shield-like volcanoes up to several kilometers in diameter (Höskuldsson et al., 2007). Searle et al. (1998) mapped 40 AVRs between  $58^\circ\text{N}$  and  $62^\circ\text{N}$ , while between  $63^\circ10'\text{N}$  and Iceland, Höskuldsson et al. (2007) distinguished 10 AVR and 3 large seamounts. These offshore features are often referred to as morphological analogues of the fissure swarms, conical, cratered and flat-topped (tuya) volcanoes and eruptive fissures observed on the subaerial RP (Fig. 46A and B) (e.g., Jakobsson et al., 1978; Murton and Parson, 1993). However, the formation of on-land tuyas is a result of interaction between volcanism and ice caps, while the mechanism of the formation of seafloor flat-topped volcanoes is still poorly understood.

Hydrothermal plume hunting along the RR during the cruise number B8 on board *R/V Bjarni Sæmundsson* led to the discovery of only one active high-temperature vent field – Steinahóll ( $63^\circ06'\text{N}$ ) (German et al., 1994). This vent site is located in only 250–300 m water depth (Fig. 48A) and has plume properties (high dissolved  $\text{CH}_4$ ,  $\text{H}_2$ , Si and dissolvable Mn) similar to plumes of some black smokers found along the MAR. The location of this vent site at such shallow depth gives rise to a bubble-rich buoyant plume which was detected by a high frequency (38 kHz) echosounder on board.

Seismic activity along the RR is mostly confined to the ridge axis and neotectonic zone where it occurs in a band paralleling the axial volcanic highs (e.g., Fig. 48A). Earthquakes usually occur in swarms and cluster in small (2–5 km wide) areas and extend  $\sim 20$  km on each side of the ridge axis (Francis, 1973; Lilwall et al., 1980; Crane et al., 1997; Mochizuki et al., 2000; Goslin et al., 2005). Events with magnitudes higher than 4 are detectable teleseismically and are listed, along with epicenter locations, by the International Seismological Centre.



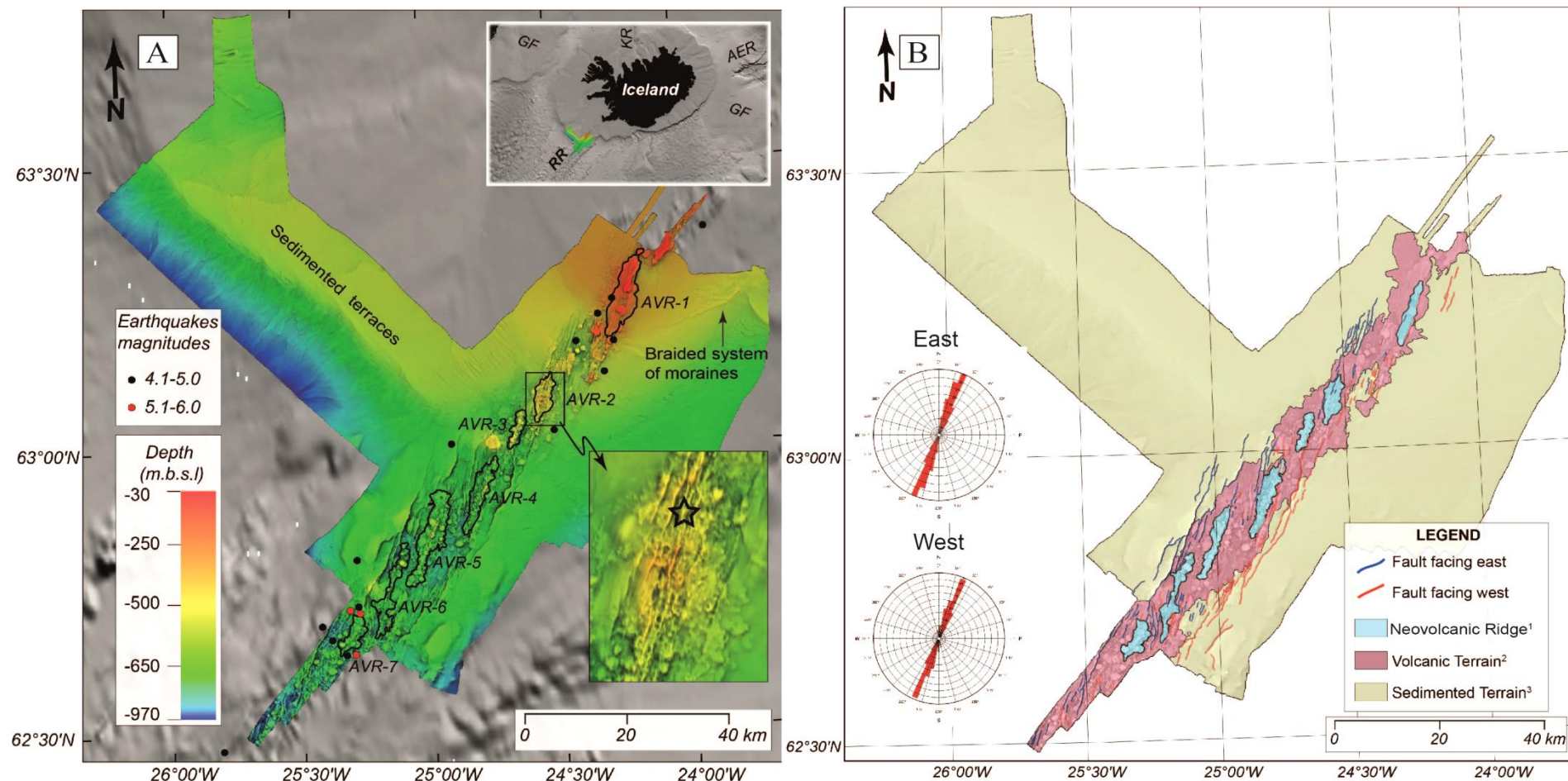


Fig. 48 (A) Multibeam bathymetry map of the Reykjanes Ridge gridded at 60 m. Black and red dots indicate the relocated earthquake epicenters for 1950-2015 from the ISC (Engdahl et al., 1998). Black open star in the inset box marks the location of Steinahóll Vent Field (from German et al., 1994). The top inset box shows the general tectonic setting of the area – RR: Reykjanes Ridge; KR: Kolbeinsey Ridge; GF: Greenland-Faroes Ridge; AER: extinct Aegir Ridge; (B) The simplified geological map produced based on the interpretation of multibeam data from A. The area is characterized by seven Axial Volcanic Ridges (discussed in more detail in section 5.4); <sup>1</sup>The youngest seafloor where robust magmatic activity is located, <sup>2</sup>Terrain where volcanic edifices like hummocky terrain, older eruptive fissures, coned-, cratered and flat-topped volcanoes can be distinguished. The rose diagrams represent directions of east and west facing faults and have intervals of 15°.



## 5.4 Results and interpretations

### 5.4.1 General morphology of the spreading axis

The RR axis is bordered by sedimented seafloor with thickness ranging from <200 m on the crust <5 Ma to ~1 km on 10–12 Ma old crust (Ruddiman, 1972). Both ridge flanks are characterized by smooth terrain with a few features resembling old volcanic edifices covered by sediments (e.g., southern part around 25°W, Fig. 48A). Our data confirm that the region of the RR studied is uninterrupted by any first- or second-order offsets. The median valley is on average 13 km wide and bounded by inward-facing normal faults with throws ranging from > 50 to > 100 m. This median valley appears to host the majority of the present volcanic and tectonic activity (Fig. 48B and section 5.4). Most faults (both major and minor) are ridge-parallel and strike NNE–SSW with only a few striking N-S or NNW-SSE (Fig. 48B). Overall, we mapped 119 faults with scarps facing east (nine with throws >100 m) and 98 faults with scarps facing west (six with throws >100 m). These faults have wide spectrum of length ranging from ~0.5 to 16.2 km. North of about 63°N, no major faults (throws >100 m) bounding the ridge axis are visible and the ridge axis forms a prominent high elevated above the surrounding seafloor.

The ridge axis is characterized by multiple linear and usually AVR-parallel volcanic edifices we interpreted as eruptive fissures. They rise from ~20 to >100 m above the surrounding seafloor and range in length from ~0.2 to 7.0 km. We can see that in many cases they connect circular volcanic edifices (cone-, crater- and/or flat-topped volcanoes) indicating that multiple volcanic edifices may be constructed in a single volcanic even and may be fed by a single underlying dike. Moreover, we mapped 55 volcanic cones (covering areas from 0.05 to 3.00 km<sup>2</sup>), 69 cratered volcanoes (covering areas from 0.04 to 8.67 km<sup>2</sup>) and 36 flat-topped volcanoes (covering areas from 0.31 to 8.93 km<sup>2</sup>). The most distinctive seamount within the neovolcanic zone is ~3.1 km in diameter flat-topped volcano located near 63°00'N and 24°45'W. Its summit is dissected by both east and west facing minor faults (throws < 100 m) and its highest point reaches ~210 mbsl (Fig. 48A).

### 5.4.2 Morphology of the AVRs

The resolution of the bathymetric data allows us to identify an en echelon array of 7 right stepping AVRs between 62°30'N and 63°30'N (Fig. 48A). The main properties of the AVRs are summarized in Table 12. All AVRs have a similar strike with an average azimuth of N22.2°E. The length/width aspect ratios of the neovolcanic zones differ from each other with 3 having low (<4) and 4 having high (>7) aspect ratios. The total length of the AVRs

ranges from 8.0 to 19.8 km, while their total width ranges from 1.8 to 3.1 km (with AVR-6 being the longest and AVR-2 being the widest). Moreover, AVR-4 covers the most area – 42.4 km<sup>2</sup> and in some regions rises >300 m above the surrounding seafloor, making it the highest among the all seven mapped. On the other hand, the neovolcanic zone of AVR-7 is almost half of the size of AVR-4 and covers only 20.8 km<sup>2</sup>. The AVR-3 is the shortest (8.0 km long) while AVR-1 is the narrowest (1.8 km wide). Moreover, AVR-6 rises only ~ 90 m above the surrounding seafloor making it the least tall. The spacing between the AVRs ranges from 1.5 to 12.3 km and AVR-1/AVR-2 and AVR-3/AVR-4 do not overlap. Otherwise, AVRs overlap over a distance of 1/3 of their length, which is typical for the Reykjanes Ridge and was also observed in the north (Höskuldsson et al., 2007) and south (e.g., Searle et al., 1998).

**Table 12** Main geometric characteristics of 7 AVRs located on the Reykjanes Ridge between 62°30'N and 63°20'N

AVR	Length of NVZ* (km)	Width of NVZ* (km)	L/W Ratio full AVR	Area of NVZ* (km <sup>2</sup> )	Strike
AVR-1	13.3	1.8	7.4	23.0	N23,3° E
AVR-2	10.2	3.1	3.3	23.4	N19,1° E
AVR-3	8.0	2.2	3.6	29.5	N21,8° E
AVR-4	16.8	2.4	7.0	42.4	N22,9° E
AVR-5	15.5	2.0	7.8	27.3	N19,4° E
AVR-6	19.8	2.2	9.0	29.3	N18,9° E
AVR-7	8.7	2.8	3.1	20.8	N29,9° E

\*NVZ - Neovolcanic Zone

### 5.4.3 Seismic activity

There is no permanent seafloor seismometer network in the studied region. Only earthquakes with magnitudes >4 can be detected teleseismically by international monitoring systems. Hence, the micro-seismic activity on the Reykjanes Ridge still remains largely unknown. In the International Seismological Center database of relocated epicenters of earthquakes from 1950 to 2015 with magnitudes >4 (Fig. 48A), the area is characterized by less earthquake activity compared with areas further south on the axis (e.g., Parnell–Turner et al., 2013). Earthquakes are confined to the neotectonic zone and do not extend more than 9 km from the ridge axis. The majority of events have magnitudes between 4.1 and 5.0. The

biggest earthquake (M5.2) was recorded in August 1986 near 62°43'N and 25°19'W. Two other events with  $M > 5.0$  occurred in this vicinity on the same day.

#### 5.4.4 Interpretations

An evolutionary model for the growth and decline of an AVR on the RR has been previously proposed by Murton and Parson (1993) and Parson et al. (1993) based on relatively low-resolution bathymetric information. They suggested that each AVR went through a 4-stage history, beginning with (1) eruptions along fissures, followed by the development of (2) conical and then (3) shield-like volcanoes. Their last proposed stage was (4) tectonic dismemberment which the authors attributed to the consequence of a rapidly decreasing magma supply. Our new bathymetric data allow a more detailed examination of the evolution of the AVRs and shows them to have a much less linear evolution than Murton and Parson (1993) and Parson et al. (1993) suggest. To illustrate this, an interpretation of the locus and intensity of volcanism on the 7 AVRs mapped here is given below.

The **AVR-1** (Fig. 49) has the smoothest surface in comparison to the remaining six AVRs studied here which, on first appearances, might suggest that it has experienced much less volcanism in recent times than the others. This conclusion may, however, be erroneous as the surface of AVR-1 has probably been subjected to either (1) intensive glacial and/or fluvio-glacial erosion smoothing the surface or (2) high sedimentation rates masking volcanic surface roughness. The former seems most likely as, although sedimentary structures (e.g., channels engraved in sediments, Fig. 48A) are visible on the eastern side of the ridge, we see no such features on top of the AVR and its seamounts. Egloff and Johnson (1979) and later Hubbard et al. (2006) showed through modelling that the ice sheets during the Last Glacial Maximum (LGM) could have extended as far south from Iceland as  $\sim 63^{\circ}10'N$ , making sub-glacial erosion a viable process on AVR-1. The present neovolcanic zone appears to be concentrated in the axial part of the AVR where hummocks, eruptive fissures and smooth/irregular volcanoes are concentrated within a 1.5 km-wide valley bounded by inward-facing minor faults (Fig. 49). Five large smoothed volcanoes there seem to be connected by multiple eruptive fissures (Fig. 49A). In three cases (marked by *a* on Fig. 49B) these eruptive fissures sit on top of the volcanoes implying that they formed most recently. The high level of smoothing and general lack of cross-cutting (e.g., tectonic deformation or overlapping) interactions between features in the northern part makes it very difficult to determine any relative ages. Tectonically dissected volcanic cones located just E of the neovolcanic zone suggest that in the past such volcanoes were building this AVR (Fig. 49B). It seems that,

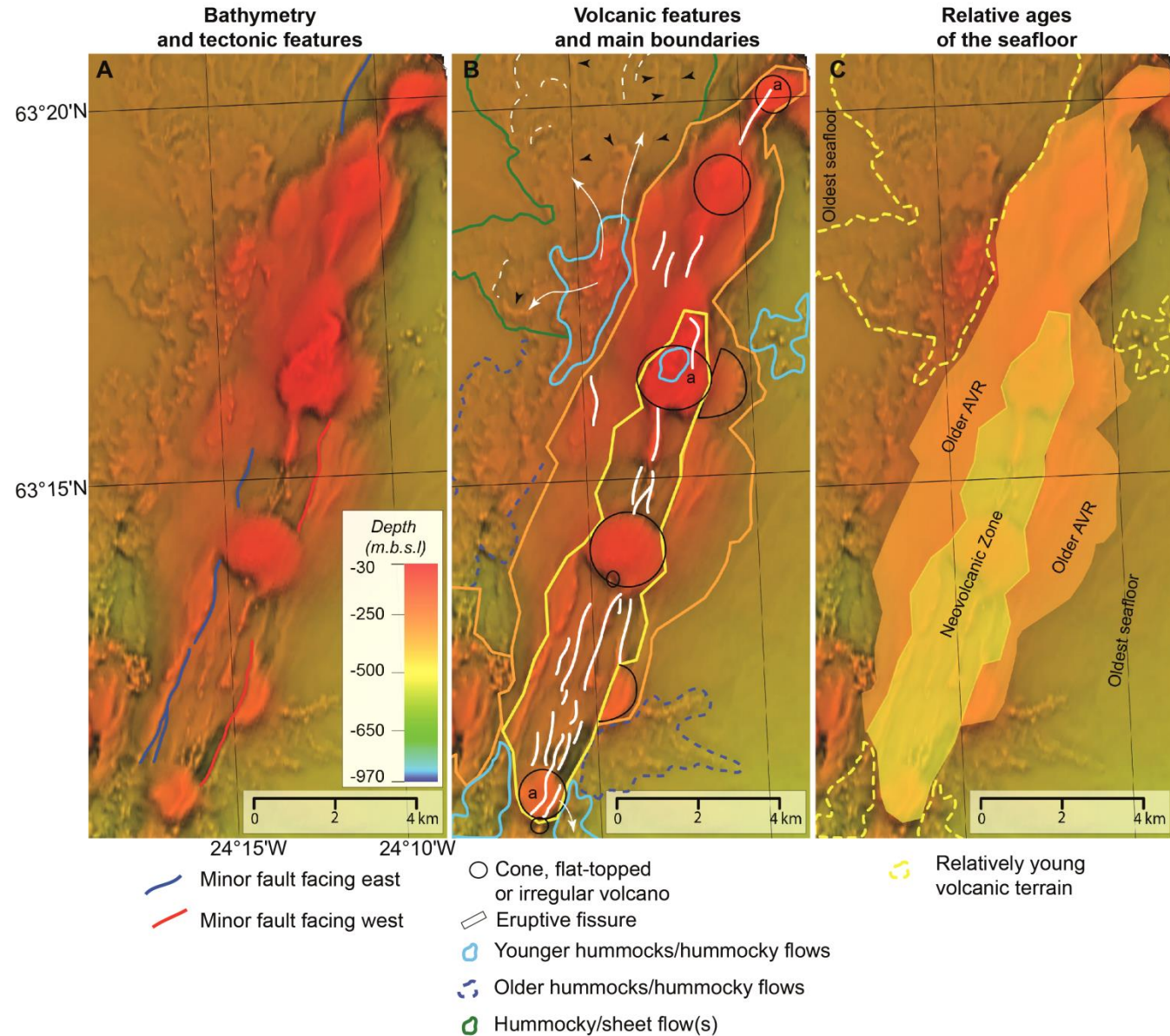
presently, AVR-1 is constructed by eruptions from multiple eruptive fissures located mostly in the central and southern part of the AVR. Moreover, a large lava flow with what we interpret as prominent lava flow front is present NW of the AVR-1 (Fig. 49B). Orientation and shape of these fronts suggest that the flow might have erupted from hummocky volcanoes located just W of the AVR. The lack of tectonic deformation in both the area between flow and source hummocks, and lava flow itself may suggest it is relatively young. However, with this data set we are unable to determine whether these hummocky volcanoes are of similar age as the eruptive fissures within the neovolcanic zone. If the axial valley is located directly at the plate boundary and a  $1 \text{ cm yr}^{-1}$  half-spreading rate of the RR has not changed significantly over the last few hundred thousand years (what we also assume for the remaining AVRs), the "spreading age" (i.e., the age of the outermost structures assuming axisymmetric spreading at constant rate) of the valley is  $\sim 17\,000$  years. Our interpretation suggests that presently volcanic activity is concentrated in the central and southern parts of AVR-1 but it is possible that some activity also takes place outside the neovolcanic zone on the flanks of the AVR.

The AVR-2, similarly to AVR-1, is a subtle axial high rising above (rather smooth) surrounding seafloor (Fig. 50). We interpret that based on the terrain roughness, strong topographic relief and presence of some tectonic deformation the presently active neovolcanic zone is surrounded by the remains of an older AVR. The latter is characterized by smoothed volcanic cones (Fig. 50B) and smoother hummocky terrain/hummocky flows (slightly tectonized in SE and SW parts, Fig. 50A) while eruptive fissures are rare. However, the transition between the two generations is subtle (in comparison to sharp change in, e.g., AVR-3, see below); therefore, it seems that the two construction periods could have overlapped with each other and a period of relative magmatic quiescence have not occurred. The neovolcanic zone has overall rough hummocky terrain with eruptive fissures clustered near the segment's axis and cone/cratered volcanoes located both on and near the axis (Fig. 50B). Many of the eruptive fissures cut volcanic craters, implying that these eruptive fissures are the youngest features on AVR-2. Moreover, a ring-shaped and caldera-like subsidence structure,  $\sim 1.5$  km in diameter and  $\sim 30$ - $40$  m deeper than the surrounding seafloor, is present in the southern part of the neovolcanic zone. It is cut by three segment-parallel eruptive fissures suggesting that they formed after the subsidence. Similar subsidence occurred within the  $\sim 10$  km diameter Krafla caldera (on land, Iceland) linked to the last eruption in 1975-1984 (Björnsson et al., 1977; Tryggvason, 1980). The highest topographic feature on AVR-2 (reaching  $\sim 180$  mbsl, Fig. 50A) is an eruptive fissure located just north of the subsidence structure. Its southern tip seems to also overlap the edge of the subsidence structure and,

therefore, post-dates it. Our interpretation suggests that present volcanic activity on AVR-2 is confined to the neovolcanic zone and is concentrated in the area south of 63°05'N.

The **AVR-3** (Fig. 51) is the shortest among all seven studied AVRs (see Table 12). We recognize two principle relative seafloor ages on this AVR (Fig. 51C). The older AVR is characterized by eruptive fissures surmounted by cone/crater volcanoes on its western flank and by older eruptive fissures and cone/crater volcanoes with no relative age relationships in the east. This older AVR has been tectonized and dismembered and is split by the neovolcanic zone, which appears to be constructed of volcanic comes in its outer parts but by a prominent eruptive fissure along the axis (Fig. 51A and B). This fissure seems to cut some of the crater volcanoes in the northern part but has one large crater volcano built on top of it in the southern region. These cross-cutting relationships suggest that the present AVR began construction from cone/crater or flat-topped volcanoes in the north followed by the formation of a long (~4 km) eruptive fissure and development of large cratered volcano (~1.1 km in diameter). It is difficult to determine whether the hummocky terrain located in the southern part of the neovolcanic zone originated from the older eruptive fissure or the cratered volcano which presently sits on top of it. The northern part of the neovolcanic zone also shows a prominent caldera-like subsidence structure (similar to observed on AVR-2) which possibly formed after the formation of a long eruptive fissure (Fig. 51B). It appears that the present AVR is longer than the older one, as neovolcanic zone terrain is in direct contact with the oldest seafloor at the northern and southern AVR ends. This may indicate that presently more melt is being supplied to the segment, possibly in response to a pulse of hotter mantle material from the Icelandic plume (e.g., Poore et al., 2011). A higher melt supply may also be indicated by the general paucity of faulting within both the older AVR and the neovolcanic crust (Fig. 51A).

**Fig. 49 Detailed interpretation of volcano-tectonic status of the AVR-1; (A) The bathymetry and main tectonic features. Surface of the AVR shows relatively smooth terrain with concentrated along axis rough hummocky volcanoes and eruptive fissures. The axis has narrow (~1.5 km wide) valley bounded by inward-facing minor faults; (B) Volcanic features and main structural boundaries. A narrow valley is characterized by presence of eruptive fissures and cone volcanoes. A prominent lava flow extending outside the AVR is present in the NW region. It shows multiple lava channels (black arrows) and lava flow fronts (white dashed lines) which orientation suggest it originated from the hummocks located just W of the AVR (direction of flow showed by white arrows). Additionally, a hummocky flow is present in the southern region which probably originated from a young eruptive fissure. Annotation 'a' indicates locations of younger eruptive fissures on top of flat-topped seamounts; (C) Relative ages of the seafloor on and around the AVR-1. In the neovolcanic zone (youngest seafloor) eruptive fissures seem to be the youngest features as they cut some of the older volcanic cones. It is possible that the hummocks on the E, S and W of the AVR are also relatively young but with this data we cannot definitely conclude if that is the case.**





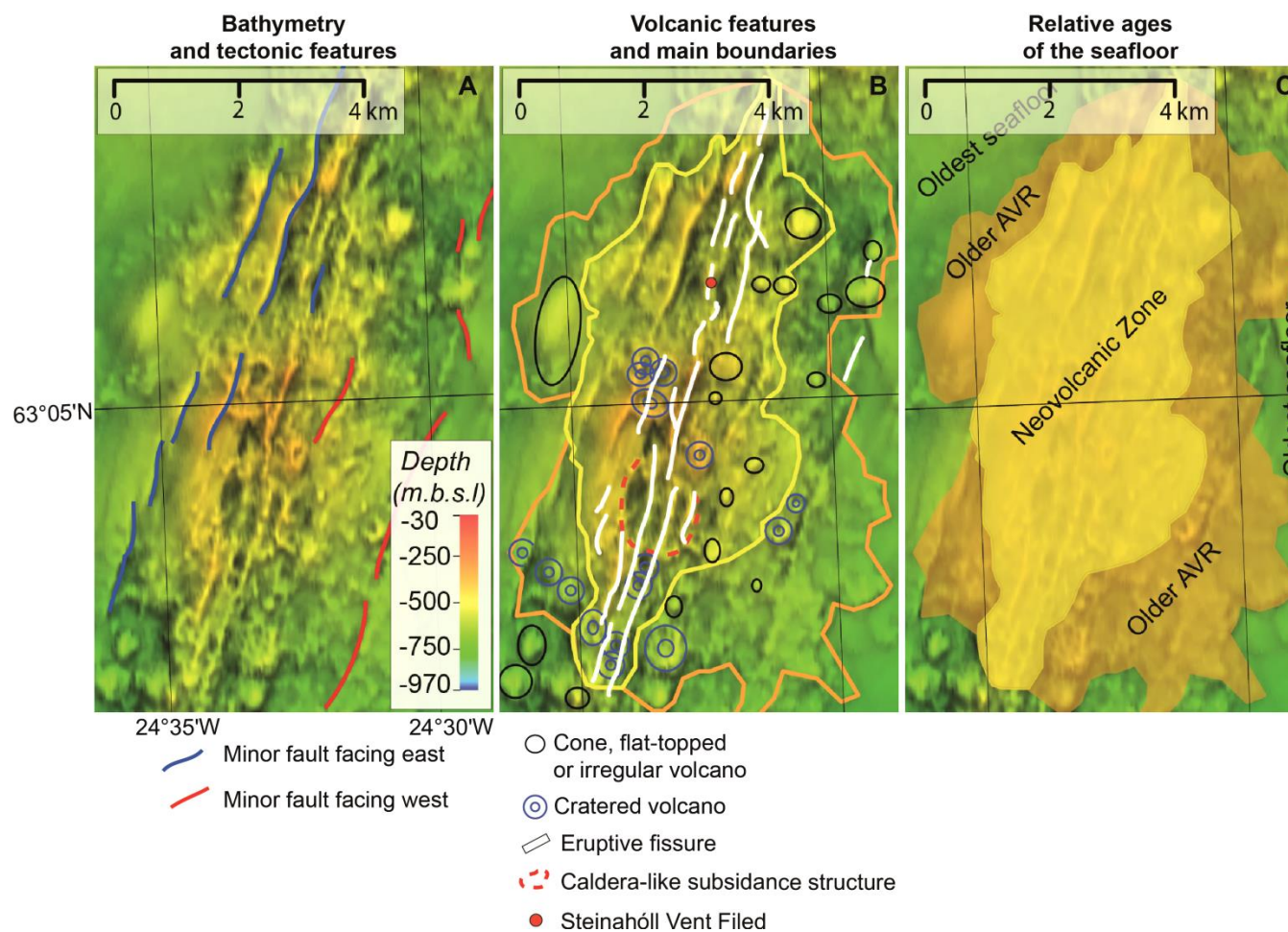


**Fig. 50** Detailed interpretation of volcano-tectonic status of the AVR-2; (A) The bathymetry and main tectonic features. The rough hummocky neovolcanic zone has cone/crater volcanoes located both near and away from the axis of neovolcanic zone and multiple eruptive fissures clustered along its axis; (B) Volcanic features and main structural boundaries. It appears that two generations of AVR can be recognized based on the overall smoothness of the seafloor, topographic relief and some tectonic deformation. Older AVR has mostly cone/crater volcanoes and eruptive fissures are rare. The neovolcanic zone has multiple axial eruptive fissures which often cut older cone/crater volcanoes. A prominent (~1.5 km in diameter) caldera-like subsidence structure is located in the southern part of the neovolcanic zone. The Steinahóll Vent Field is located on top of the >50 m high eruptive fissure, additionally associated with an east-facing fault; (C) Relative ages of the seafloor on and around the AVR-2.

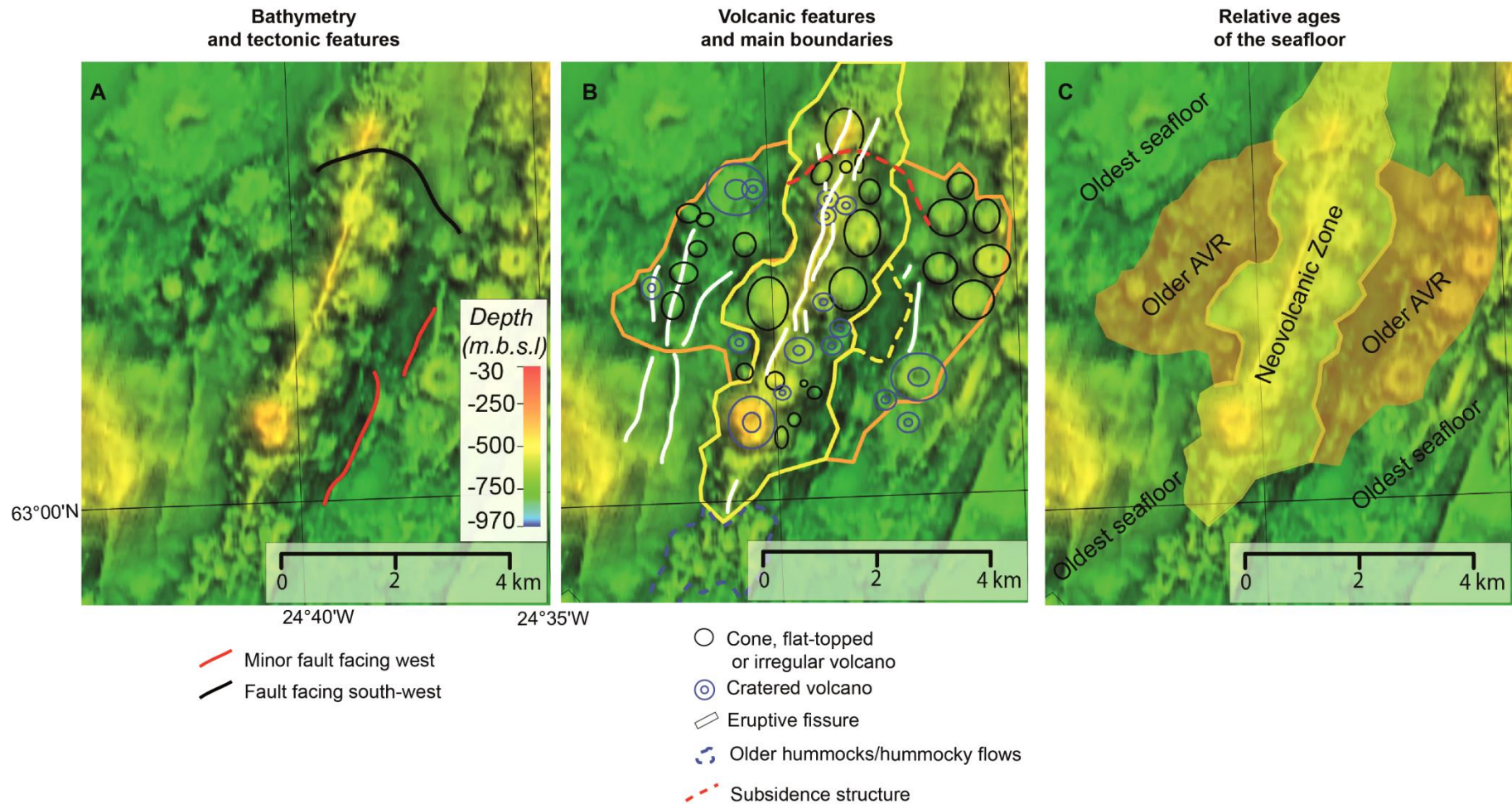


**Fig. 51** Detailed interpretation of volcano-tectonic status of the AVR-3; (A) The bathymetry and main tectonic features; Young and rough hummocky terrain is located along the segment's axis while away from it is much smoother; (B) Volcanic features and main structural boundaries. Two generations of AVR are recognized based on the overall smoothness of the seafloor and topographic relief. The neovolcanic zone has coned/cratered volcanoes located in its outer parts while a long eruptive fissure has developed along its axis. This eruptive fissure appears to cut some older conical volcanoes but in the southern part is overlapped by large cratered volcano. Older AVR (visible on E and W side of the neovolcanic zone) has older eruptive fissures and coned/cratered volcanoes sitting on top of them. A prominent boundary facing SW is present in the northern part of the neovolcanic zone which is probably a caldera-like subsidence structure similar to one observed on AVR-2; (C) Relative ages of the seafloor on and around the AVR-3.

The **AVR-4**, unlike the three previous AVRs described, is located in a ~3.3 km wide trough (between inward-facing minor faults) rather than forming an axial high rising above the surrounding seafloor (Fig. 52A). It is the closest AVR to Iceland which is located within a median valley. An older AVR can be observed on both flanks of the neovolcanic zone (Fig. 52B). The northern parts of this older AVR are characterized by the presence of large but tectonized flat-topped volcanoes while only some much smaller tectonized cones can be observed in the southern regions. Large underwater flat-topped volcanoes have been proposed to form during long-lived, steady, effusive, point source eruptions on gentle slopes (Clague et al., 2000). It seems that older AVR-4 has been built mostly by such eruptions (Fig. 52B). However, the area located S and SE of 62°55'N and 24°45'W is characterized by a very smooth surface with some collapse structures (white-dashed rectangles marked with 'a' in Fig. 52B). We interpret that as sheet flows and/or flat pillow flows which erupted during the formation of older AVR; however, higher resolution bathymetry is needed to confirm the diagnosis. These observations suggest that in the past volcanic activity on AVR-4 was mostly focused in the area north of 62°55'N with less activity in the southern region. The present neovolcanic zone of AVR-4 covers the largest area (42.4 km<sup>2</sup>) of all the seven studied AVRs and seems to have been built by multiple, rather short (in comparison to AVR-2 or AVR-3) eruptive fissures which are often observed to cut older coned/cratered volcanoes (Fig. 52B). Therefore, it seems that the neovolcanic zone has experienced a transition from cone/crater volcanoes followed by the development of multiple short eruptive fissures. This may reflect a reduction in effusion and eruption rates. No large flat-topped volcanoes appear to have formed recently on AVR-4. The higher density of eruptive fissures and volcanic cones in the neovolcanic zone north of 62°55'N implies that volcanic activity continues, as on the older AVR, to focus in this area.

The **AVR-5** is the longest (20 km) AVR in the study area (Fig. 53). Its structure is complex, and four generations of crustal production, an initial one with no clear AVR structure visible followed by three generations of AVR activity, can be recognized. In the past, volcanic activity in this region was dominated by longer-lived, steady-state, most likely sourced from segment's center volcanism, hence, at least four generations of a large, presently tectonically dismembered flat-topped volcano can be traced in the oldest seafloor, W of present neovolcanic zone (Fig. 53B and C). Hence, this early focusing of volcanism could have lasted for a minimum of 25 000 years before the AVR activity developed. The oldest AVR material ('Oldest AVR' in Figure 53C) is composed of hummocky terrain with some cone/crater volcanoes and rare eruptive fissures. The remains of one large cratered volcano,



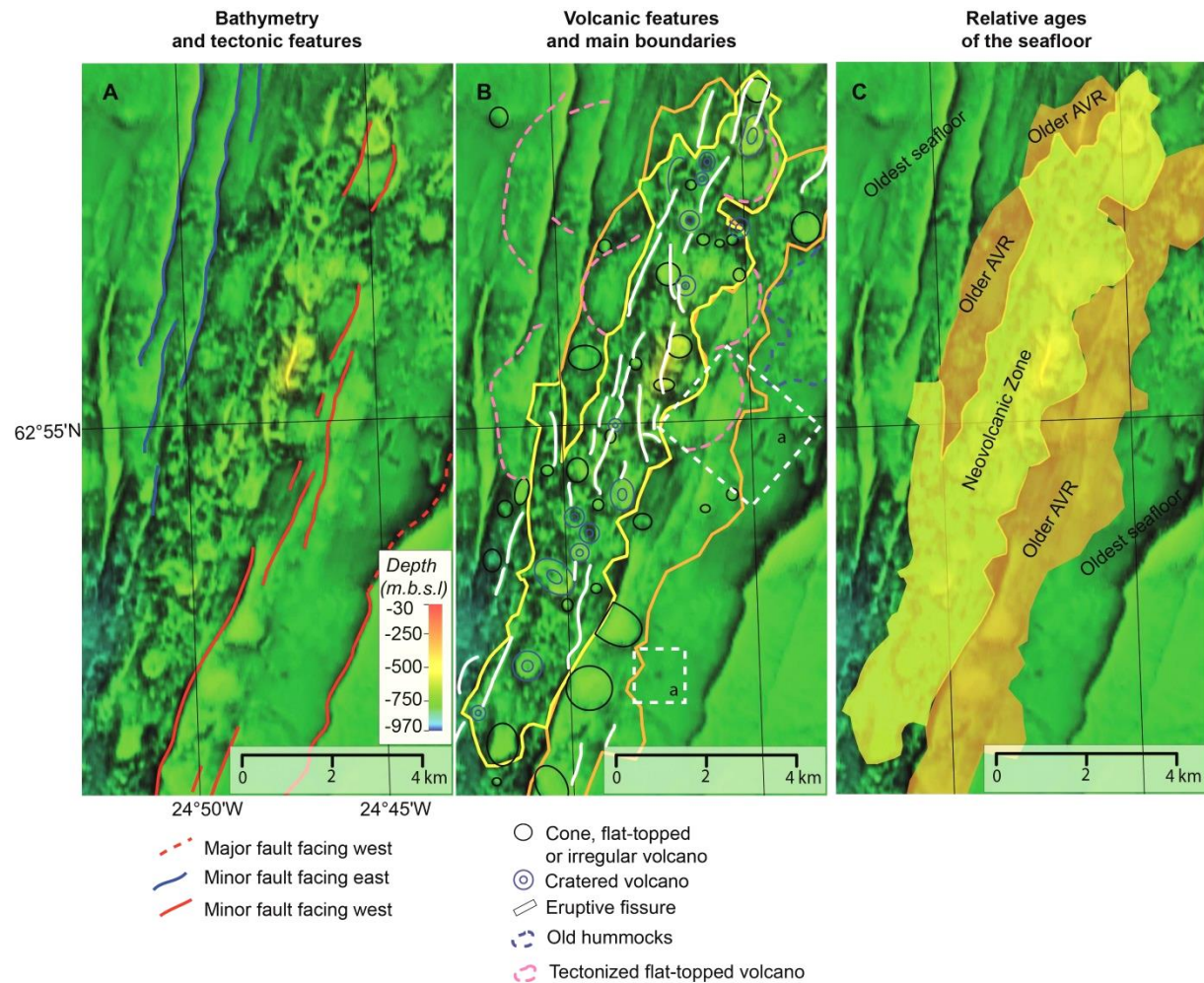


**Fig. 52 Detailed interpretation of volcano-tectonic status of the AVR-4; (A) The bathymetry and main tectonic features. AVR-4 appears to be located in a ~3.3 km wide trough; (B) Volcanic features and main structural boundaries. Older AVR appears to be constructed by large flat-topped volcanoes dismembered due to continuous spreading and smaller volcanic cones. Smooth terrain located E of the older AVR shows some collapse structures (white-dashed rectangles 'a') interpreted as sheet flows which origin remains unknown. The neovolcanic zone is constructed by volcanic cones often cut by younger eruptive fissures. An eruptive fissure overlapping older cones makes the topographic high which reaches depth of ~250 mbsl – similar to eruptive fissure observed on AVR-2 (C) Relative ages of the seafloor on and around AVR-4. Oldest seafloor is strongly tectonized by inward-facing minor and major faults.**



which has been partially covered by products from the next generation of AVR ('older' AVR on Fig. 9C), can be observed on the eastern side of the segment. The older AVR has significantly more volcanic cones indicating that, with time, point-source eruptions became predominant in constructing this AVR. An alignment of smaller hummocky and bigger cratered/flat-topped volcanoes can be observed on the eastern side of older AVR (white-dashed box *b* in Fig. 53B). Similar alignments have been recognized, for example, on the MAR near 29°N (Head et al., 1996) or the Gorda Ridge (Yeo et al., 2013), where they probably represents surface expression of an underlying dikes. It seems that the size of these edifices becomes bigger towards the center of the alignment. This may indicate that at the beginning, this alignment was built by eruptions evenly distributed along a fissure but gradual cooling of the magma at both ends while continuous melt supply to the segment led to focusing of flow in several discrete locations in the central part. Hence, larger edifices have been constructed over time. A large shield-like volcano (~3.5 km in diameter) showing a deep and irregularly-shaped crater marks the northern end of the older AVR. Its present surface is rather smooth indicating that it might be inactive for considerable amount of time. An eruptive fissure cuts the surface of this volcano just E of the crater. This fissure cannot be clearly assigned to the youngest, neovolcanic zone but may be the first indications of the shift in the volcanic style in this area related to the establishment of the neovolcanic zone (Fig. 53B). The southern part of the older AVR has some smaller volcanic cones suggesting many point-source eruption sites none of which reached the size of northern shield volcano. The neovolcanic zone of AVR-5 has rough hummocky terrain, volcanic cones/craters and flat-topped volcanoes distributed towards its margins along its entire length. In the central part hummocky terrain seems to be overlapped by a flat-topped volcano with a small conical summit. This volcano is then cut by eruptive fissures (white-dashed box *c* in Fig. 53B). This cross-cutting of the features indicates that the neovolcanic zone of AVR-5 was built up by multiple eruptions and shows that the eruptive fissures were the most recent. We observe a similar situation in other parts of the neovolcanic zone. The complex make-up of the seafloor on AVR-5 allows us to propose an evolution from focused magmatism at a large volcanic center (oldest seafloor). This volcano was then split by the development of a 20-km-long AVR, which initially was more active at its northern end, where it developed a large shield-like volcano. At present, volcanic activity seems to be migrating towards the center of the segment where the youngest eruptive fissures occur.



The **AVR-6** is located in a ~10 km wide trough between two inward-facing major faults (Fig. 54A). Outside the neovolcanic zone, in the central part of this segment, a large (~7.5 km wide), relatively smooth yet visibly tectonized flat-topped volcano can be traced for ~3 km to the W and E of the present neovolcanic zone suggesting it may have begun construction ~30 000 years ago. Remains of it are visible outside the axial trough, implying that focused point-source volcanism was present here even before the trough developed. Large central volcanoes like this require localized eruptions of large volumes of lava (often as sheet flows) over a protracted time period and are usually underlain by thickened crust and often have axial magma chambers (AMC) associated with them (Cannat et al., 1999a; Cannat et al., 1999b; Escartin et al., 2001; Sauter and Cannat, 2010; Escartín et al., 2014). In more recent times a ~1.5 km wide graben with hummocky terrain, eruptive fissures and volcanic cones has developed through the central part of this old seamount (Fig. 54A). Observations from the Lucky Strike central volcano (37°15'N, MAR) suggest that such structures develop in times of decreased melt supply to the segment (Escartín et al., 2014). Past volcanic output on Lucky Strike was sufficient to cover any tectonic features (faults/fractures) associated with spreading but presently the neovolcanic zone is confined to a narrow graben located at the volcano's summit. The seamount on AVR-6 shows some tectonic deformation, suggesting that volcanic output here was not sufficient to cover all faults/fractures, unlike at the Lucky Strike. Presently, the neovolcanic zone of AVR-6 is ~20 km long. In its southern part it has rough hummocky terrain with some coned/cratered volcanoes and very few eruptive fissures. In the central part a larger volcanic cone and more eruptive fissures can be distinguished. Towards the north, the highest density of eruptive fissures is seen, although coned/cratered and flat-topped volcanoes become most numerous features (Fig. 54B). This may indicate that, presently, volcanism on AVR-6 is migrating northwards where lower effusion rate eruptive fissures are being fed by laterally propagating dikes (originating from short-lived magma reservoirs) while circular edifices have higher effusion rates and may have more established magma reservoirs. The remains of two older generations of AVR can be observed SE of the present neovolcanic zone, where a few coned/cratered volcanoes are observed (Fig. 54B) implying that in the past more voluminous point-source eruptions constructed this AVR. The smoothed oldest seafloor around AVR-6 is probably old and slightly sedimented sheet flows, as Ruddiman (1972) and later Litvin (1984) suggested that sediments (which accumulation could significantly smoothed the seafloor) do not accumulate along the axis of the Reykjanes Ridge. Nevertheless, the origin and age of these sheet flows remains unknown.

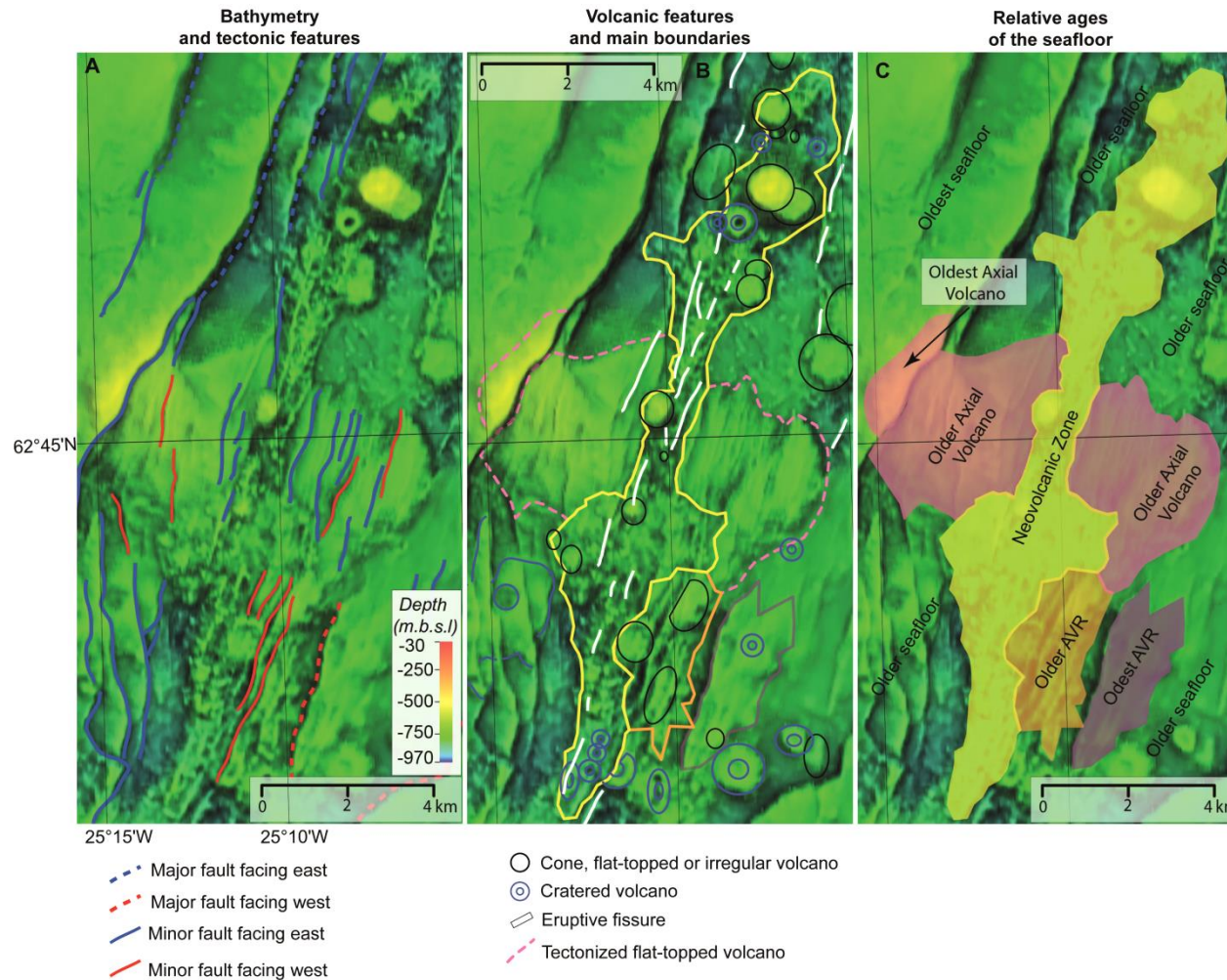


**Fig. 54 Detailed interpretation of volcano-tectonic status of the AVR-6; (A) The bathymetry and main tectonic features; (B) Volcanic features and main structural boundaries. A large (~ 7.5 km in diameter) and tectonically deformed seamount can be observed. Its remains are also visible outside bounded by inward-facing major faults trough. The neovolcanic zone here stretches for 19.8 km. In central part of the segment it cuts through the large seamount. Its southern part has few volcanic cones and eruptive fissures but number of volcanic features increases towards the northern part. Sections of older AVR are visible in SE part of the region. They are constructed by coned/cratered volcanoes. The area around AVR-6 is smooth and probably covered by sheet flows which originated from older generations of AVR, former large axial volcano or both; C) Relative ages of the seafloor on and around AVR-6.**

The **AVR-7** is comparable in length, width and surface morphology to AVR-3 (Fig. 55). The bathymetric coverage around this region is limited but it appears that AVR-7 is, as with AVR-5 and -6, an axial high located within a median valley. The surrounding seafloor is rougher in comparison to neighboring AVR-6 with one tectonized cratered volcano located between the two (Fig. 55B). The western flank of the AVR has an old eruptive fissure overlapped by a flat-topped volcano, which has a smaller cone on top (white-dashed box *a* in Fig. 11B, 62°40'39.63"N, 25°20'17.05"W). Eastern flank shows older tectonized volcanic cones and some volcanic craters (white-dashed rectangle *b* in Fig. 55B). These features probably belong to a former AVR which got split and dismembered by ongoing spreading. The alignment of features of the western flank of the AVR-7 resembles those observed on the eastern flank of AVR-5. The location of flat-topped volcanoes in the southern part of this older AVR suggests that volcanic activity migrated southwards in the past where point-source eruptions constructed early AVR-7 (Fig. 55B and C). The most recent accretion is dominated by magmatic processes, as the neovolcanic zone shows no tectonic deformation. Therefore, seismic activity that has been observed around the southern part of this segment (Mochizuki et al., 2000) may be related to magmatic rather than tectonic activity. The outer parts of the neovolcanic zone are constructed by coned/cratered volcanoes but a prominent eruptive fissure cutting older cones is present along the AVR's axis, north of 62°40'N (Fig. 55B). Moreover, this fissure may be source of hummocky flows extending NW and NE of it. A large (~1.8 km in diameter) flat-topped volcano with noticeable small cone on top is present at the SW extension of older eruptive fissure (SW of white-dashed rectangle *a*) and overlaps some cones of the oldest seafloor and eruptive fissures of the neovolcanic zone. This indicates that it is the youngest (latest formed) volcanic feature in the area. A small cone at its summit suggests single vent eruptions. Large axial volcanoes (e.g., Lucky Strike) show similar to observed here surface roughness at comparable bathymetry resolution. There are mostly built by high effusion rate sheet flows (Escartín et al., 2014); therefore, we suggests that the flat surface of the big volcano on this AVR may represent such sheet flows. Moreover, the position of this flat-top may imply that volcanism has migrated even further south from the older eruptive fissure (white-dashed rectangle *a* in Fig. 55B). A magma reservoir has probably developed under this volcano and continuous melt supply led to construction of this large edifice. Unfortunately, with our data we are unable to conclude whether the flat-topped volcano and young eruptive fissure stretched along the AVRs axis are of the same or similar age. However, because both the flat-topped volcano and the eruptive fissure appear to be younger than other parts of the AVR, it seems that the two eruption mechanisms (one

constructing flat-topped volcano and the other constructing hummocky terrain) can coexist and simultaneously erupt on one AVR at approximately the same time. A similar situation has been observed on an AVR located at 45°N on the Mid-Atlantic Ridge (Yeo and Searle, 2013).

## **5.5 Discussion**

### **5.5.1 Volcanism on Axial Volcanic Ridges**

Our interpretations (summarized in Tab. 13) based on the new high-resolution bathymetric data show that the 4-stage evolution model for AVRs (fissure → conical volcano → shield volcano → tectonic dismemberment) proposed by Murton and Parson (1993) and Parson et al. (1993) does not reflect the construction and status of volcanic activity of the AVRs studied here. Instead we conclude that the type of volcanic activity at the surface is closely linked to the volume of magma being delivered to relatively small/short-lived magma reservoirs (Smith and Cann, 1993; Sinha et al., 1998) and that the time-scales on which this supply operates will determine formation and status of volcanic activity on AVRs. This has been suggested for AVRs elsewhere on the Mid-Atlantic Ridge, e.g., near 45°N (Yeo, 2012), where it has been shown that one end of the AVR experienced robust volcanism (magmatic extension) while the other tectonic deformation (tectonic extension). These observations suggest that melt does not need to be equally available along the entire length of a segment and one AVR may display volcanic activity in multiple locations (e.g., not only at AVRs crest), at different times and by different eruption mechanisms (eruptive fissures or coned/cratered/flat-topped volcanoes). Therefore, our interpretations seem to agree with the observations of Yeo (2012). It appears that along some segments (AVR-2, AVR-4 and AVR-7) the availability of melt has not changed significantly over time, as the neovolcanic zones follow the patterns of former AVRs. However, in the case of AVR-1 and AVR-5 it seems that less melt may be being supplied to the segments at the present as their neovolcanic zones are shorter and narrower than the adjacent relicts of the former AVRs. In contrast, it appears that currently more melt may be being supplied to AVR-3 and AVR-6, where the neovolcanic zones are longer than those of former AVRs. Volcanism is not solely confined to the crest of the AVR but may also occur across the AVR, building, for example, young eruptive fissures or young volcanic cones on the margins of neovolcanic zones (e.g., AVR-2, AVR-3 and AVR-7). In some cases volcanic activity seems to be migrating along the segments, hence, on some AVRs robust volcanism is focused in central parts while in other cases it is concentrated at the segments ends. This suggests that melt supply to the segments is time-dependent, although with our data set we are unable to put further constraints on the time span involved.



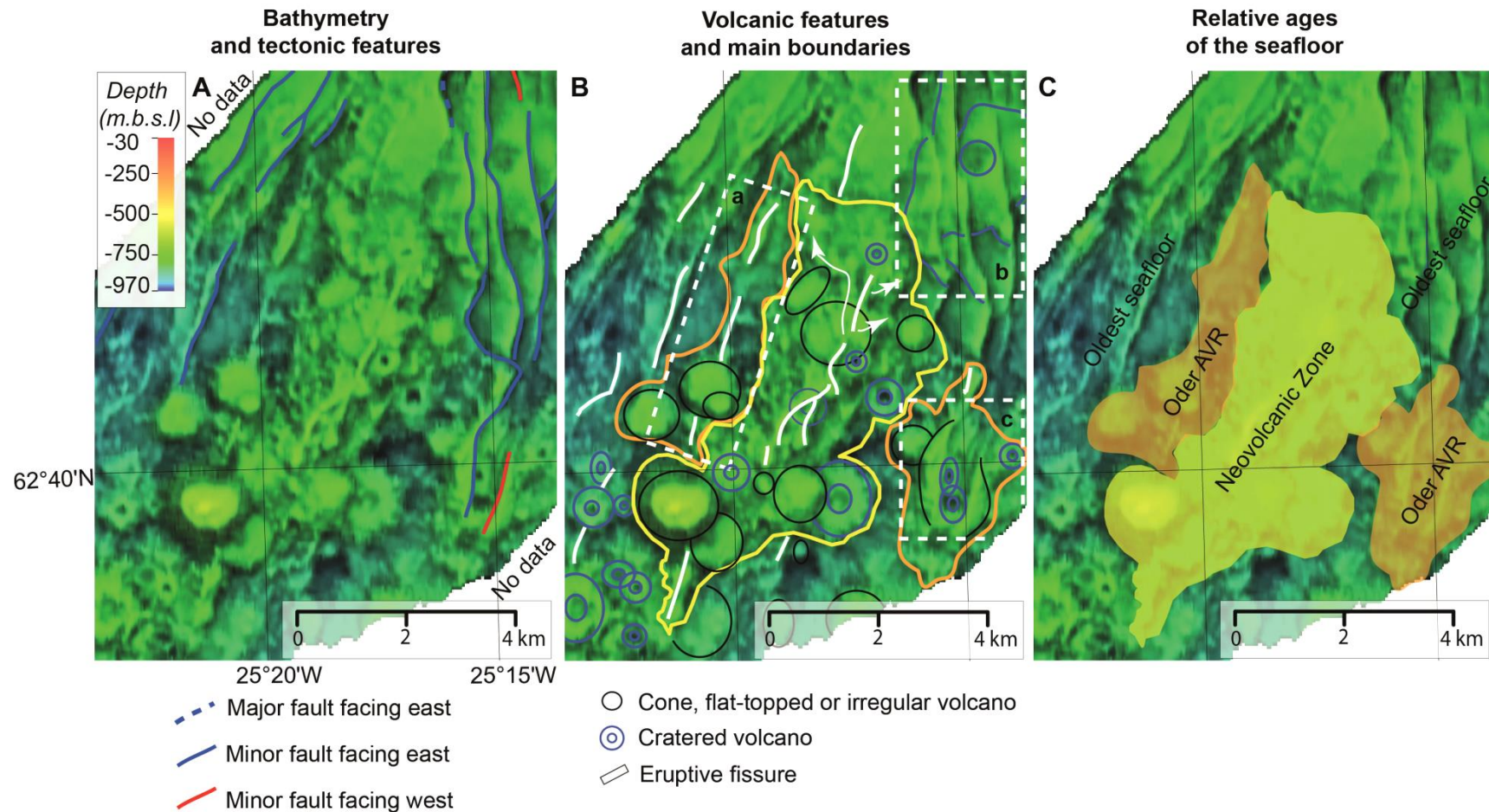


**Fig. 55** Detailed interpretation of volcano-tectonic status of the AVR-7; (A) The bathymetry and main tectonic features; (B) The volcanic features and main structural boundaries. Remains of a former AVR can be observed on the western and eastern flanks of the present AVR. It was constructed by coned/cratered volcanoes and an old eruptive fissure which has been overlapped by flat-topped volcanoes (white-dashed box a). White-dashed boxes b and c show tectonized terrain between AVR-7 and -6 and the older AVR-7, respectively. The present neovolcanic zone consists of coned/flat-topped volcanoes in its outer part and a prominent eruptive fissure which cuts some of the volcanic cones along the axis. The large (~1.8 km in diameter) flat-top volcano is present in the SW part of the neovolcanic zone (SW of the white-dashed box a) which is probably the locus of young point-source eruptions. Both, the flat-top and the eruptive fissure show relatively young ages suggesting that two eruption mechanisms may co-exist on AVR-7. Additionally, white arrows indicate origin and direction of axial hummocky flows; (C) Relative ages of the seafloor on and around AVR-7.

**Table 13 Summary of the observations and interpretations of the volcanic status of AVRs from this study. Abbreviations: EF – Eruptive fissures, CON – Coned volcanoes, CRA – Cratered volcanoes, FT – Flat-topped volcanoes; <sup>a</sup>No axial valley bounding faults visible, <sup>b</sup>No full bathymetric coverage.**

AVR	Maximum length (km)	Maximum width (km)	Axial valley width (km)	Present volcanic edifices	Locus of youngest (rejuvenated) volcanism	Youngest volcanic edifices	Generations of AVR	Tectonic deformation	Hydrothermal activity
AVR-1	13.3	2.6	(?) <sup>a</sup>	EF, FT	Center, South	Eruptive fissures	2	—	—
AVR-2	10.2	3.8	(?) <sup>a</sup>	EF, CON, CRA, FT, Caldera-like structure	Center	Eruptive fissures	2	+	+
AVR-3	8.0	2.4	8.4	EF, CON, CRA, FT, Caldera-like structure	Center	Cratered volcanoes	2	—	—
AVR-4	16.8	3.0	12.2	EF, CON, CRA, FT	Center	Eruptive fissures	2	+	—
AVR-5	15.5	2.8	12.8	EF, CON, CRA, FT, Shield-like volcano	Center	Eruptive fissures	3	—	—
AVR-6	19.8	3.7	11.0	EF, CON, CRA, FT, Tectonized flat-topped volcano	North, Center	Eruptive fissures / Flat-topped volcanoes	3	—	—
AVR-7	8.7	3.5	(?) <sup>b</sup>	EF, CON, CRA, FT,	Center, South-West	Eruptive fissures / Flat-topped volcano	2	—	—



### 5.5.2 Status of volcanic activity on the Reykjanes Peninsula

The geometry of the 4 segments on the Reykjanes Peninsula is thought to mirror the elongated magma reservoirs at the base of the crust (Gudmundsson, 1995) and stress regime within the spreading environment (Fujita and Sleep, 1978), while their morphology is controlled by the influence of the Icelandic hotspot and the last glaciation. Each fissure swarm has eruptive fissures confined to its central part and non-eruptive fissures, flat-topped and shield volcanoes on the peripheries (Jakobsson et al., 1978). Head et al. (1996) suggested that individual eruptions occur along the entire length of the fissure and gradually focus down to a few discrete points as the effusion rate wanes. This mechanism was also observed during the Bardarbunga-Holuhraun 2014-2015 rifting episode in Iceland (Sigmundsson et al., 2015). This may indicate an evolution of volcanic style from fissure (forming eruptive fissures) to point-source eruptions (forming conical or flat-topped volcanoes). However, only continuous melt supply would lead to development of large (higher eruptive rate) features like shields or flat-tops. Pedersen and Grosse (2014) divided volcanic edifices on the RP based on their shapes, average slope values and total volume, and showed that the ellipticity is a function of volume, suggesting that smaller edifices mainly erupt from fissures, while larger edifices are more circular and mostly erupt from central vents. The transition between the two lies in the volume range 0.01-0.1 km<sup>3</sup> which may also suggest evolutionary nature of eruptions from fissure eruptions to more point-source eruptions (Pedersen and Grosse, 2014).

Russell et al. (2014) and Pedersen and Grosse (2014) suggested that the shield volcanoes (also known as flat-topped tuyas or table mountains) and eruptive fissures (also called hyaloclastite ridges or tindars) on the RP have glaciovolcanic origin and formed through the interaction between volcanism and glaciers. However, Smellie (2007) and later Skilling (2009) argued that they can also form in other subaqueous environments like lakes or on the seafloor. Tindars from the RP formed in a single (Schopka et al., 2006) or multiple (Sæmundsson et al., 2010) eruptions when lava simultaneously erupted from many points of a fissure at once (Was et al., 2013). They are made of pillow lavas, sometimes covered by hyaloclastites or compound lavas. Hiatt et al. (2013) suggested that tindars from the Krýsuvík swarm formed under the pressure equivalent to 450-475 m of water depth. There is a strong correlation between elongation of tindars and arrangement of faults on the RP suggesting tectonic control of their formation. Hence, some tindars have used pre-existing faults/fractures as eruption conduits (e.g., Clifton and Kattenhorn, 2006). Tuyas from the RP consist of pahoehoe lava flows which extend radially from the central vent forming smooth and flat cones. They are surrounded by rather steep lava aprons (Rossi, 1996).

Jakobsson et al. (1978) suggested that on land fissure swarms are the equivalents of off shore AVRs as they have similar mechanism of formation and show similar surface morphologies. However, the eruption volumes of the on land tindars on the RP (0.0016-0.0822 km<sup>3</sup>, Pedersen and Grosse, 2014) are approximately ten times greater than those produced by submarine eruptive fissures studied here (0.0003-0.0139 km<sup>3</sup>). Moreover, our estimates overlap with the earlier estimates calculated for the transition between the smaller elongated and bigger circular edifices from the RP showed by Pedersen and Grosse, 2014.

The above observations allow subaerial observations on the RP to be used as a proxy for the submerged RR. We suggest that tuyas and tindars from the RP are equivalents of flat-topped volcanoes and eruptive fissures, respectively, from the RR. On land, tindars are mostly made of pillow lavas suggesting subaquatic origin and low effusion rates eruptions (e.g., Schopka et al., 2006). Similar observations have been collected along the MAR where eruptive fissures, often built by one or more hummocky ridges, consist of pillow lavas and elongated pillows (Yeo and Searle, 2013). Tuyas from RP have nearly circular shapes, flat tops and rarely develop a prominent central cone on top (e.g., Rossi, 1996). Flat-topped volcanoes on RR also are circular, have flat tops, follow the height to diameter ratio 1:10 typical for flat-topped seamounts (Magde and Smith, 1995) and sometimes have central cones on their flat summits (e.g., Fig. 55A). The tops of the Icelandic tuyas consist of smooth pahoehoe lava flows (Rossi, 1996) which is in line with the smooth sheet flows observed on surfaces of flat-topped volcanoes on the seafloor (Yeo and Searle, 2013). Therefore, the summits of flat-topped volcanoes from RR are probably covered by such sheet flows, which would explain their flatness and smoothness.

There is no direct evidence for the evolutionary progression of eruptions from eruptive fissures to centrally focused coned/cratered/flat-topped volcano on the Reykjanes Peninsula or elsewhere on Iceland. However, Pedersen and Grosse (2014) suggested that such a transition may occur based on the total volumes of tindars and tuyas on the RP although such evolution has not been directly observed. Our interpretations of the submarine AVRs indicate that such transition may be a valid process, as at several locations (e.g., Figs. 51, 53 or 55) we observed volcanic cones and flat-topped volcanoes developed directly on top of former eruptive fissures. However, at the same time we have observed younger eruptive fissures forming on top of the circular edifices which is contrary with the evolutionary hypothesis and shows that this is a more complicated process. Fissure eruptions are expected to be predominantly segment-parallel, reflecting the local stress regime (Fujita and Sleep, 1978). The extensional stress mostly builds up near the segment axes where a zone of crustal weakness (which along

the RR deforms as a response to oblique spreading) is bounded by the areas of relatively strong lithosphere (Tuckwell et al., 1998). This weak zone can develop in areas of recent and/or robust volcanism (thickened crust) or where dikes emplace at depth (e.g., Lee, 1995). The above conditions prevail along and across the AVRs which are surface expressions of robust volcanism and thickened crust. This suggests that the opening of new fissures (leading to formation of eruptive fissures) can occur at any location within the AVR; however, this seems to be only possible during periods of magmatic extension when melt is being supplied to the segment. Perhaps some fissures may open further away from the segments axes if thickening of the crust due to overflow of hummocky/sheet flows accommodates enough stress. This could explain development of younger eruptive fissures away from the segments axes or on top of coned/cratered/flat-topped volcanoes (e.g., Figs. 50, 52 or 53).

### **5.5.3 Volcanic control of venting at Steinahóll Vent Field and elsewhere**

The Steinahóll Vent Field is located in the northern part of AVR-2 (Figs. 48A, 50B) in an area characterized by a ~500 m long eruptive fissure located between 2 east-facing faults, although the site is not directly located on the scarp or extension of any fault (Figs. 48A and 50A). The area around the site seems to be rough volcanic terrain (eruptive fissures and hummocks). Our interpretation of the geological evolution of AVR-2 (see section 5.1) suggests that at least some of the eruptive fissures are the youngest features on this AVR, implying that venting at Steinahóll may be driven by heat input from dikes intruding along this segment. It is possible that the Steinahóll field is cooling this entire 10.2 km long segment by the system of sub-bottom faults and fractures, as it has been shown that one black smoker can cool up to 50 km of the spreading axis (e.g., Hannington et al., 2010).

Previously, authors have suggested that oceanic crust formed on the Reykjanes Ridge may be cooled by widespread off-axis ‘diffuse’ venting rather than on-axis focused high-temperature vents (German et al., 1994; Devey et al., 2010). Pałgan et al. (2016) proposed that such diffuse venting may be controlled by off-axis dike intrusions, as observed in off-axis regions of Iceland. However, evidence for such a cooling mechanism has not yet been found along the RR. The frequency of venting on a slow-spreading mid-ocean ridge should be at least 1 high-temperature hydrothermal field every ~100 km (Baker et al., 2004; German et al., 2016), although a hotspot-influenced ridge like RR should show an even higher incidence of hydrothermal vents than this, as seen in the Azores (German et al., 1996). On the RP, all fissure swarms have been volcanically active in the Holocene and each host at least one high-temperature hydrothermal system (Figs. 46 and 47), an incidence of 1 field every ~20 km. By

analogy, and in view of the similarities of AVRs to fissure swarms both tectonically and volcanologically, each of the seven AVRs mapped in this study should also host hydrothermal activity. Submarine hydrothermal venting naturally focuses towards topographic highs (Bani-Hassan et al., 2012; Titarenko and McCaig, 2015) or in regions where the most recent volcanic activity occurred or volcanic and/or tectonic features cross-cut. Taking this into account, Figure 56 shows sites along the RR between 62°30'N and 63°30'N where we postulate that sites of hydrothermal activity may be located.

On AVR-1, eruptive fissures are sites of the youngest volcanic activity and are probably post-glacial (younger than 12 000 years). They may host hydrothermal activity similarly to that seen at the Brennisteinsfjöll area on the RP. Despite one known hydrothermal field on AVR-2 (northern part) it appears that young eruptive fissures may be present in its southern region as well, where they cut a prominent caldera-like collapse structure. One of these fissures is the highest topographic feature on the AVR, reaching a depth of ~180 mbsl, making it a preferable location for a hydrothermal system to develop. On AVR-3 we predict that hydrothermal activity may be located in the southern part of the segment where a relatively large cratered volcano sits on top of a long eruptive fissure. The volcano's summit reaches depths of ~200-250 mbsl. At a similar depth to the Steinahóll field on AVR-2. High-temperature geothermal activity has been observed in areas of large caldera collapses in Iceland, e.g., Krafla (Arnórsson et al., 2008). Therefore, the two such features observed on AVR-2 and AVR-3 could be valid locations for the future hydrothermal exploration. On AVR-4 and AVR-5 hydrothermalism may be associated with eruptive fissures (the youngest volcanic features of these segments), reaching depth of ~250 mbsl (again similarly to Steinahóll) and ~300 mbsl, respectively. On AVR-6, volcanic activity seems to be migrating northwards, making the region north of 62°45'N a valid region for exploration. Particularly the shallow (~315 mbsl), flat-topped volcano with small summit cone near the northern end of the neovolcanic zone appears to be a strong target. Moreover, a strongly rifted and tectonized axial high on this AVR should form a site of increased crustal permeability and so also has high potential for development of a hydrothermal site such as those seen at Lucky Strike (Langmuir et al., 1997) or Menez Gwen (Fouquet et al., 1994). On AVR-7, both eruptive fissure (cutting older flat-topped volcano in the northern part) and a large flat-topped volcano (overlapping older eruptive fissures and volcanic cones) are the youngest volcanic features of similar age. However, the flat-topped volcano is the shallowest feature, reaching ~360 mbsl, making it the preferable location for a hydrothermal manifestation to develop. Major seismic activity (Fig. 48) on this segment in recent years reinforce this view: Mochizuki et al. (2000)

suggested that the micro seismicity near AVR-7 is closely related to hydrothermal activity, as earthquakes cluster near the flanks of the segment and similar patterns of activity have been reported in geothermal sites in Iceland (e.g., Khodayar et al., 2010).

Hydrothermal prospection on these sites will need to be adapted to the particular local conditions: the shallow setting of the whole area coupled with strong bottom currents associated with the North Atlantic Drift or Iceland-Scotland Overflow Water (Valdimarsson and Malmberg, 1999) and the general morphology of the plate boundary along the RR between  $\sim 59^\circ\text{N}$  and Iceland (a prominent axial high with only a very shallow axial trough) may lead to very fast dispersal and dilution of hydrothermal plumes. We propose that a combination of survey methods (including near-bottom use of autonomous vehicles) would be necessary to study the incidence of hydrothermal activity along the Reykjanes Ridge and perhaps on other hotspot influenced ridges.

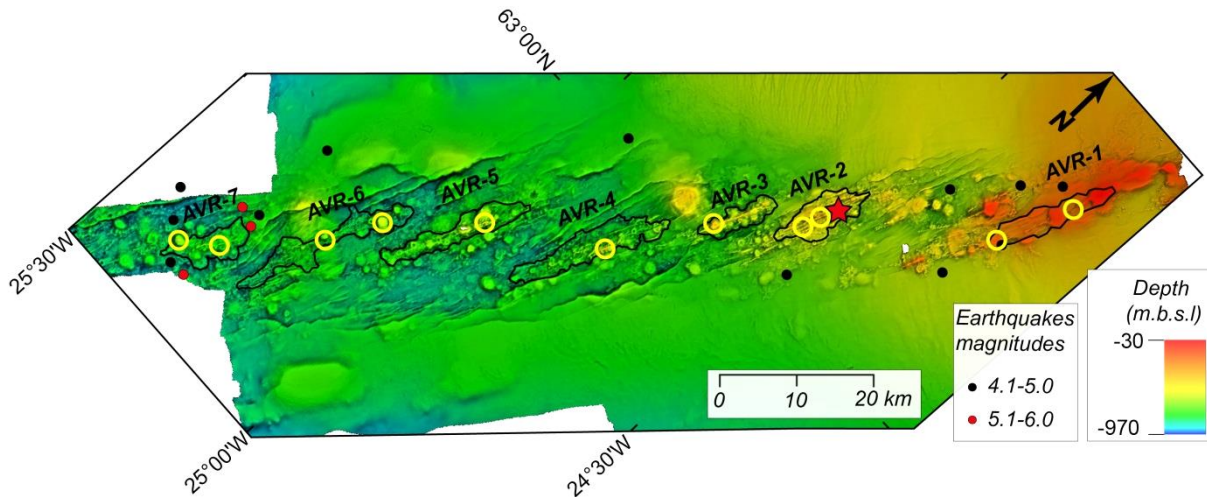


**Fig. 56** Predicted locations of new hydrothermal sites along the Reykjanes Ridge between  $62^\circ 30' \text{N}$  and  $63^\circ 30' \text{N}$ . Seven mapped AVRs are highlighted with black outlines. Red star indicates location of Steinahóll Vent Field while red and black dots represent epicenters of earthquake from years 1950-2015 (USGS). We predict 10 new sites of hydrothermal activity based on the interpretation of Steinahóll setting, on land observations from Reykjanes Peninsula and other parts of Iceland. Therefore, the youngest volcanic features are expected to host hydrothermal activity. These are eruptive fissures or coned/cratered volcanoes which tend to form local topographic highs. Additionally, two caldera-like structures observed on AVR-2 and AVR-3 also are taken into consideration.

#### 5.5.4 Signs of off-axis volcanism on the Reykjanes Ridge?

Although most crustal accretion occurs along the spreading axes, off- and near-axis eruptions may contribute significantly to the formation of new oceanic crust (Perfit and Chadwick, 1998). For example, fresh looking lavas have even been sampled along the flanks of ultraslow-spreading Southwest Indian Ridge between  $9\text{-}16^\circ\text{E}$  (Standish and Sims, 2010). Leroy et al. (2010) suggested that mantle plumes may cause off-axis volcanism on the flanks of slow-spreading ridges by channeling of melt along the ridge system and its distribution along the brittle-ductile boundary at depth. Off-axis eruptions may use pre-existing fractures

and faults as conduits (Standish and Sims, 2010) also observed on Iceland by Khodayar and Einarsson (2002) who showed examples of dikes intruded into faults on the flanks of the neovolcanic zones there.

The resolution of bathymetry presented in this paper allows us to point few locations along the flanks of the RR where off-axis magmatism may have occurred. Figure 57 shows three sites where hummocky volcanoes and elongated volcanic ridges striking parallel to the AVRs lie outside the ridge axis and away from the AVRs. In places hummocky ridges rise up to 50 m above the surrounding seafloor and seem to occupy minor faults. This may indicate that, similar to ridges of different spreading rates, off-axis volcanism along slow-spreading and hotspot-influenced ridges can occur where magma uses even far off-axis faults and fractures as conduits. In such cases, it is probable that faults on the flanks of RR reach the brittle-ductile boundary underneath the ridge where melt accumulates. Off-axis volcanic edifices are known to host active hydrothermal activity and hydrothermal deposits along the flanks of East Pacific Rise (EPR) near 9°28'N (Macdonald et al., 2002) but whether the three mentioned above locations are also hydrothermally active remains unknown. However, even if they are active they could not account for missing along the RR hydrothermal sites and heat output of this ridge. All three areas in Figure 57 are located near the margin of the neovolcanic terrain (e.g., Fig. 48) and ~5 km from the ridge axis. That distance is sufficient for a high-temperature system to develop away from the ridge axis as, for example, in Iceland the high-temperature sites of Krafla, Námafjall and Theistareykir are located at the margins of Northern Volcanic Zone, up to 21 km away from the ridge axis (Arnórsson et al., 2008). This implies that areas pointed here are also of relevance for hydrothermal prospection. The age of this eruptions is unknown and, therefore, we cannot put further constrains on the life span of any potential hydrothermal sites. However, overall lower eruption volumes in comparison to RP suggest less heat is supplied for the hydrothermal system and circulation may occur over shorter time (less magma = faster cooling = shorter hydrothermal cooling time = short life span of hydrothermal system). If the RR is similar to the EPR and NVZ in Iceland, off-axis volcanic activity may be important for the formation SMS deposits and/or locating old SMS deposits and the biogeography of northern MAR.



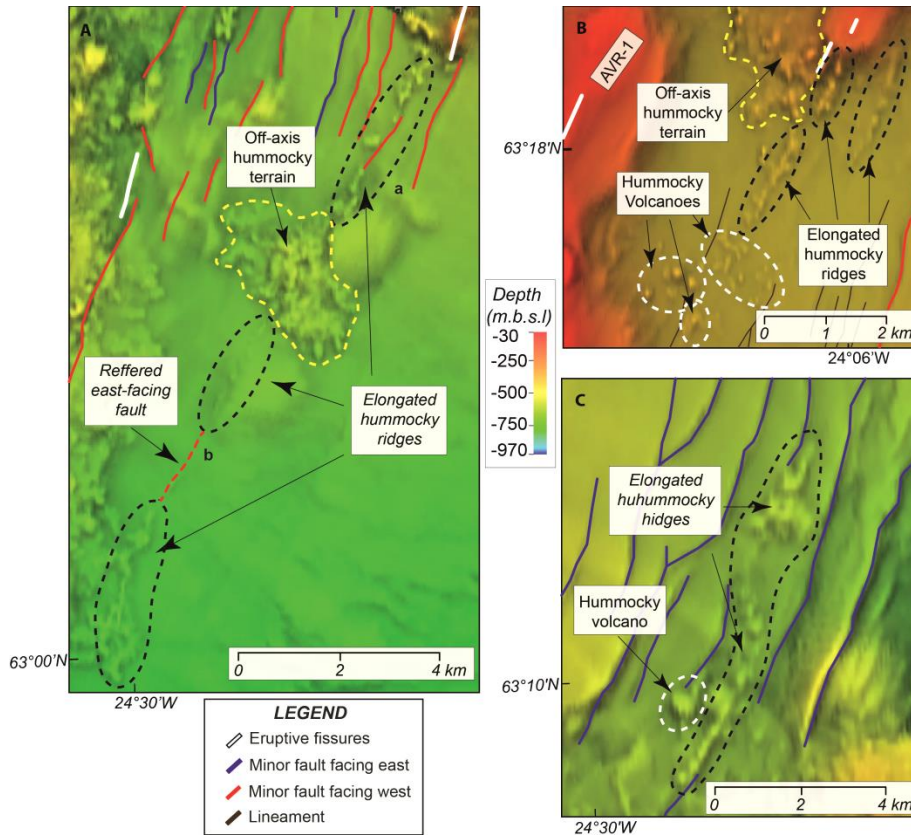


**Fig. 57** Suggested locations of off-axis eruption sites on the flanks of the Reykjanes Ridge between  $62^{\circ}30'N$  and  $63^{\circ}20'N$ ; (A) Eastern flank of the RR with 13 km long hummocky ridge rising up to 50 m above the surrounding seafloor. In the northern part (a) the ridge occupies the west-facing fault suggesting dike injection into the pre-existing fault. In the southern are (b) same fault emerges between two elongated hummocky ridges. The site is located  $\sim 5$  km away from the ridge axis; (B) Western flank of the RR with 5 km long hummocky ridge rising up to 30 m above the surrounding seafloor. Ridge seems to interact with east-facing fault again suggesting dike injection into the fault. The site is located  $\sim 5$  km away from the ridge axis; (C) Eastern flank of the RR near AVR-1 with elongated hummocky ridges (1-2 km long) and hummocky volcanoes ( $\sim 20$  m in diameter and  $\sim 20$  m high). Elongated ridges indicate eruptions along faults or fractures while hummocky volcanoes are more point-source eruptions. Black dashed-lines mark sites where elongated hummocky ridges interact with the tectonic features. White dashed lines mark more point-source hummocky volcanoes. Depth scale is applicable to all three panels.

## 5.6 Conclusions

The Reykjanes Ridge between  $62^{\circ}30'N$  and  $63^{\circ}30'N$  contains seven Axial Volcanic Ridges (AVRs) which, based on their morphology and geometry, are the equivalents of the adjacent on land fissure swarms on the Reykjanes Peninsula, Iceland. Interpretation of the volcano-tectonic setting allowed us to identify the sites of youngest volcanic activity on each of the seven AVRs. Magma does not seem to be evenly distributed along the entire length of the AVRs implying that formation of AVRs along the Reykjanes Ridge is more complex than the 4-stage model previously proposed. In some cases the youngest volcanism appears to be associated with elongated eruptive fissures up to 7 km in length suggesting strong tectonic control and low effusion-rate eruption mechanisms. However, on others the latest volcanic activity seems to have more point-source character implying longer-lived magma supply to

the systems and higher effusion rates. Our interpretation suggests that Steinahóll (the only known high-temperature hydrothermal field along the ~950 km long Reykjanes Ridge) is located on top of a young eruptive fissure (~250 mbsl). This distinctive morphology strongly resembles abundant tindars (also known as hyaloclastite ridges) which are known to host geothermal activity on the Reykjanes Peninsula (e.g., Krýsuvík or near Brennisteinsfjöll). Bathymetric features similar to those observed at Steinahóll are observed on shallow regions of all the AVRs, where sometimes they are the highest topographic features. The fact that hydrothermal systems have not also been previously detected there is probably due to the sensitivity of the instruments used to search for them - topographic highs on the axial ridges of the Reykjanes Ridge are the regions where strongest currents occur, probably causing plumes to be swept away from their source and dispersed rapidly, a situation requiring near-bottom prospection, ideally with autonomous and remote vehicles. Off-axis volcanism, which on Iceland has been shown to provide permeable pathways for off-axis hydrothermal circulation, has been detected on the flanks of the Reykjanes Ridge - it remains to be seen if it is also the site of hydrothermal circulation.

## 5.7 References

- Arnórsson, S., 1995, Geothermal systems in Iceland: Structure and conceptual models—I. High-temperature areas: *Geothermics*, v. 24, p. 561–602, doi: 10.1016/0375-6505(95)00025-9.
- Arnórsson, S., Axelsson, G., and Sæmundsson, K., 2008, Geothermal systems in Iceland: *Jökull*, v. 58, p. 269–302.
- Baker, E.T., Edmonds, H.N., Michael, P.J., Bach, W., Dick, H.J.B., Snow, J.E., Walker, S.L., Banerjee, N.R., and Langmuir, C.H., 2004, Hydrothermal venting in magma deserts: The ultraslow-spreading Gakkel and Southwest Indian Ridges: *Geochemistry, Geophysics, Geosystems*, v. 5, no. 8, doi: 10.1029/2004GC000712.
- Baker, E.T., and German, C.R., 2004, On the Global Distribution of Hydrothermal Vent Fields, In: German, C.R., Lin, J., and Parson, L.M. [Eds.], *Mid-Ocean Ridges*, American Geophysical Union, p. 245–266.
- Bani-Hassan, N., Iyer, K., Rüpke, L.H., and Borgia, A., 2012, Controls of bathymetric relief on hydrothermal fluid flow at mid-ocean ridges: *Geochemistry, Geophysics, Geosystems*, v. 13, p. Q05002, doi: 10.1029/2012GC004041.
- Björnsson, S., Arnórsson, S., and Tómasson, J., 1970, Exploration of the Reykianes Thermal Brine Area: *Geothermics*, v. 56, p. 2380–2391, doi: 10.1016/0375-6505(70)90491-8.

- Björnsson, A., Sæmundsson, K., Einarsson, P., Tryggvason, E., and Grönvold, K., 1977, Current rifting episode in North Iceland: *Nature*, v. 266, p. 318–323, doi: 10.1038/266318a0.
- Cannat, M., Briais, A., Deplus, C., Escartı, J., Georgen, J., Lin, J., Mercouriev, S., Meyzen, C., Muller, M., Pouliquen, G., and Rabain, A., 1999a, Mid-Atlantic Ridge - Azores hotspot interactions: along-axis migration of a hotspot-derived event of enhanced magmatism 10 to 4 Ma ago: *Earth and Planetary Science Letters*, v. 173, p. 257–269, doi: 10.1016/S0012-821X(99)00234-4.
- Cannat, M., Rommevaux-Jestin, C., Sauter, D., Deplus, C., and Mendel, V., 1999b, Formation of the axial relief at the very slow spreading Southwest Indian Ridge (49° to 69°E): *Journal of Geophysical Research: Solid Earth*, v. 104, p. 22825–22843, doi: 10.1029/1999JB900195.
- Clague, D.A., Moore, J.G., and Reynolds, J.R., 2000, Formation of submarine flat-topped volcanic cones in Hawai'i: *Bulletin of Volcanology*, v. 62, p. 214–233, doi: 10.1007/s004450000088.
- Clifton, A.E., and Kattenhorn, S.A., 2006, Structural architecture of a highly oblique divergent plate boundary segment: *Tectonophysics*, v. 419, p. 27–40, doi: 10.1016/j.tecto.2006.03.016.
- Clifton, A.E., Sigmundsson, F., Feigl, K.L., Gudmundsson, G., and Arnadottir, T., 2002, Surface effects of faulting and deformation resulting from magma accumulation at the Hengill triple junction, SW Iceland, 1994-1998: *Journal of Volcanology and Geothermal Research*, v. 115, p. 233–255, doi: 10.1016/S0377-0273(01)00319-5.
- Crane, K., Johnson, L., Appelgate, B., Nishimura, C., Buck, R., Jones, C., Vogt, P., and Rubin, K., 1997, Volcanic and Seismic Swarm Events on the Reykjanes Ridge and Their Similarities to Events on Iceland: Results of a Rapid Response Mission: *Marine Geophysical Researches*, v. 19, p. 319–338, doi: 10.1023/A:1004298425881.
- Devey, C.W., German, C.R., Haase, K.M., Lackschewitz, K.S., and Melchert, B., 2010, The relationships between volcanism, tectonism, and hydrothermal activity on the southern equatorial Mid-Atlantic Ridge, In: Rona, P., Devey, C. W., Dymont, J., and Murton, B., [Eds.], *Diversity of hydrothermal systems on slow spreading ocean ridges*, American Geophysical Union, Washington D.C., p. 133–152, doi: 10.1029/GM188.
- Egloff, J., and Johnson, G.L., 1979, Erosional and depositional structures of the southwest Iceland insular margin: thirteen geophysical profiles, In: Watkins, J.S., Montadert, L., and Dickerson, P.W. [Eds.], *Geological and Geophysical Investigations of Continental Margins*, Tulsa, Oklahoma, AAPG, p. 43–63.
- Engdahl, E.R., Hilst, R. Van Der, and Buland, R., 1998, Global Teleseismic Earthquake Relocation with Improved Travel Times and Procedures for Depth Determination: *Bulletin of the Seismological Society of America*, v. 88, p. 722–743.
- Escartin, J., Cannat, M., Pouliquen, G., Rabain, A., and Lin, J., 2001, Crustal thickness of V-shaped ridges south of the Azores; interaction of the Mid-Atlantic Ridge (36°-39°N) and

- the Azores hot spot: *Journal of Geophysical Research*, v. 106, p. 21719–21735, doi: 10.1029/2001JB000224.
- Escartín, J., Soule, S.A., Cannat, M., Fornari, D.J., Düşünür, D., and Garcia, R., 2014, Lucky Strike seamount: Implications for the emplacement and rifting of segment-centered volcanoes at slow spreading mid-ocean ridges: *Geochemistry, Geophysics, Geosystems*, v. 15, p. 4157–4179, doi: 10.1002/2014GC005477. Received.
- Fouquet, Y., Charlou, J.-L., Costa, I., Donva, J.P., Radford-Knoery, J., Pelle, H., Ondreas, H., Lourenço, N., Segonza, M., and Tivey, M.K., 1994, A Detailed Study of the Lucky Strike Hydrothermal Site and Discovery of a New Hydrothermal Site: Menez Gwen; Preliminary Results of the DIVA1 Cruise (5-24 May 1994): *InterRidge News*, v. 3, p. 14–17.
- Fowler, A.P.G., Zierenberg, R.A., Schiffman, P., Marks, N., and Friðleifsson, G.Ó., 2015, Evolution of fluid-rock interaction in the Reykjanes geothermal system, Iceland: Evidence from Iceland Deep Drilling Project core RN-17B: *Journal of Volcanology and Geothermal Research*, v. 302, p. 47–63, doi: 10.1016/j.jvolgeores.2015.06.009.
- Francis, T.J.G., 1973, The seismicity of the Reykjanes Ridge: *Earth and Planetary Science Letters*, v. 18, p. 119–123, doi: 10.1016/0012-821X(73)90042-3.
- Franzson, H., Gunnlaugsson, E., Árnason, K., Sæmundsson, K., Steingrímsson, B., and Hardarson, B.S., 2010, The Hengill Geothermal System, Conceptual Model and Thermal Evolution, *Proceedings of the 2010 World Geothermal Congress, Bali, Indonesia, 25-29 April*, p. 25–29.
- Fujita, K., and Sleep, N.H., 1978, Membrane stresses near mid-ocean intersections ridge-transform: *Tectonophysics*, v. 50, p. 207–221, doi: 10.1016/0040-1951(78)90136-1.
- German, C.R., Briem, J., Chin, C., Danielsen, M., Holland, S., James, R., Jónsdóttir, A., Ludford, E., Moser, C., Ólafsson, J., Palmer, M.R., and Rudnicki, M.D., 1994, Hydrothermal activity on the Reykjanes Ridge: the Steinahóll vent-field at 63°06'N: *Earth and Planetary Science Letters*, v. 121, p. 647–654, doi: 10.1016/0012-821X(94)90098-1.
- German, C.R., Parson, L.M., and Team, H.S., 1996, Hydrothermal exploration near the Azores Triple Junction: tectonic control of venting at slow-spreading ridges?: *Earth and Planetary Science Letters*, v. 138, p. 93–104, doi: 10.1016/0012-821X(95)00224-Z.
- German, C.R., Petersen, S., and Hannington, M.D., 2016, Hydrothermal exploration of mid-ocean ridges: Where might the largest sulfide deposits be forming?: *Chemical Geology*, v. 420, p. 114–126, doi: 10.1016/j.chemgeo.2015.11.006.
- Goslin, J., Lourenço, N., Dziak, R.P., Bohnenstiehl, D.R., Haxel, J., and Luis, J., 2005, Long-term seismicity of the Reykjanes Ridge (North Atlantic) recorded by a regional hydrophone array: *Geophysical Journal International*, v. 162, p. 516–524, doi: 10.1111/j.1365-246X.2005.02678.x.

- Gudmundsson, A., 1987, Geometry, formation and development of tectonic fractures on the Reykjanes Peninsula, southwest Iceland: *Tectonophysics*, v. 139, p. 295–308, doi: 10.1016/0040-1951(87)90103-X.
- Gudmundsson, A., 1995, Infrastructure and mechanics of volcanic systems in Iceland: *Journal of Volcanology and Geothermal Research*, v. 64, p. 1–22, doi: 10.1016/0377-0273(95)92782-Q.
- Hannington, M.D., Jamieson, J.W., Monecke, T., and Petersen, S., 2010, Modern seafloor massive sulfides and base metal resources: toward an estimate of global seafloor massive sulfide potential: *Society of Economic Geologists Special Publication*, v. 15, p. 317–338.
- Haraldsdóttir, H.S., Franzson, H., and Árnason, K., 2012, Preliminary study of down-hole resistivity from 72 boreholes in the S-Hengill Geothermal Field, SW-Iceland, with respect to surface resistivity data and alteration minerals, 37th Workshop on Geothermal Reservoir Engineering, Stanford University, Stanford, California, pp. 10.
- Head, W., Wilson, L., and Smith, D.K., 1996, Mid-ocean ridge eruptive vent morphology and substructure: Evidence for dike widths, eruption rates, and evolution of eruptions and axial volcanic ridges: *Journal of Geophysical Research Solid Earth*, v. 101, p. 28265–28280, doi: 10.1029/96JB02275.
- Höskuldsson, Á., Hey, R., Kjartansson, E., and Guðmundsson, G.B., 2007, The Reykjanes Ridge between 63°10'N and Iceland: *Journal of Geodynamics*, v. 43, p. 73–86, doi: 10.1016/j.jog.2006.09.003.
- Hubbard, A., Sugden, D., Dugmore, A., Norddahl, H., and Petrusson, H.G., 2006, A modelling insight into the Icelandic Last Glacial Maximum ice sheet: *Quaternary Science Reviews*, v. 25, p. 2283–2296, doi: 10.1016/j.quascirev.2006.04.001.
- Ingolfsson, O., Sigmarsson, O., Sigmundsson, F., and Símonarson, L., 2008, The dynamic geology of Iceland: *Jökull*, v. 58, p. 1–2.
- Ito, G., 2001, Reykjanes “V”-shaped ridges originating from a pulsing and dehydrating mantle plume: *Nature*, v. 411, p. 681–684, doi: 10.1038/35079561.
- Jakobsdóttir, S.S., 2008, Seismicity in Iceland: 1994 – 2007: *Jökull*, , no. 58, p. 75–100.
- Jakobsson, S.P., Jonsson, J., and Shido, F., 1978, Petrology of the Western Reykjanes Peninsula, Iceland: *Journal of Petrology*, v. 19, p. 669–705, doi: 10.1093/petrology/19.4.669.
- Johannesson, H., 1980, Evolution of rift zones in western Iceland [in Icelandic with an English summary]: *Naturufraedingurinn*, v. 50, p. 13–31.
- Johannesson, H., 2014, Geological Map of Iceland: Bedrock Geology: [Map], 1: 600 000, Náttúruminjasafn Íslands, Reykjavík.
- Jónsson, J., 1978, Geological map of the Reykjanes Peninsula [in Icelandic]: *Orkustofnun, Report and map, OS JHD 783*, pp. 303.

- Keeton, J.A., Searle, R.C., Parsons, B., White, R.S., Murton, B.J., Parson, L.M., Peirce, C., and Sinha, M.C., 1997, Bathymetry of the Reykjanes Ridge: Marine Geophysical Research, v. 19, p. 55–64, doi: 10.1023/A:1004266721393.
- Khodayar, M., Björnsson, S., Einarsson, P., and Franzson, H., 2010, Effect of tectonics and earthquakes on geothermal activity near plate boundaries: A case study from South Iceland: *Geothermics*, v. 39, no. 3, p. 207–219, doi: 10.1016/j.geothermics.2010.06.003.
- Khodayar, M., and Einarsson, P., 2002, Strike-slip faulting, normal faulting, and lateral dike injections along a single fault: Field example of the Gljúfurá fault near a Tertiary oblique rift-transform zone , Borgarfjörður, west Iceland: *Journal of Geophysical Research*, v. 107, p. 1–16, doi: 10.1029/2001JB000150.
- Klein, F.W., Einarsson, P., and Wyss, M., 1977, The Reykjanes Peninsula, Iceland, earthquake swarm of September 1972 and its tectonic significance: *Journal of Geophysical Research*, v. 82, p. 865–888, doi: 10.1029/JB082i005p00865.
- Langmuir, C., Humphris, S., Fornari, D., Van Dover, C., Von Damm, K., Tivey, M.K., Colodner, D., Charlou, J.-L., Desonie, D., Wilson, C., Fouquet, Y., Klinkhammer, G., and Bougault, H., 1997, Hydrothermal vents near a mantle hot spot: the Lucky Strike vent field at 37°N on the Mid-Atlantic Ridge: *Earth and Planetary Science Letters*, v. 148, p. 69–91, doi: 10.1016/S0012-821X(97)00027-7.
- Lee, S., 1995, Tectonics of the East Pacific Rise: studies of faulting characteristics and magnetic and gravity anomalies, [PhD Thesis], Woods Hole Oceanographic Institute, pp. 512.
- Leroy, S., D’Acremont, E., Tiberi, C., Basuyau, C., Autin, J., Lucazeau, F., and Sloan, H., 2010, Recent off-axis volcanism in the eastern Gulf of Aden: Implications for plume – ridge interaction: *Earth and Planetary Science Letters*, v. 293, p. 140–153, doi: 10.1016/j.epsl.2010.02.036.
- Lilwall, R.C., Francis, T.J.G., and Porter, I.T., 1980, Some ocean-bottom seismograph observations on the Reykjanes Ridge at 59°N: *Geophysical Journal International*, , no. 62, p. 321–327, doi: 10.1111/j.1365-246X.1980.tb04858.x.
- Litvin, V. M., 1984, The Structure of Sedimentary Series and its Role in the Morphostructure of the Ocean Floor. In: Litvin, V.M. [Ed.], *The Morphostructure of the Atlantic Ocean Floor*, Springer Netherlands, p. 51–76, doi: 10.1007/978-94-009-6245-3
- Macdonald, K.C., Haymon, R.M., Blasius, J., and Benjamin, S., 2002, Off-axis Hydrothermal Activity on the East Pacific Rise near 9°28N: Faulted and Topographic Control of Hydrothermal Discharge? [Abstract]: AGU Fall Meeting, San Francisco, #T11B-1240.
- Magde, L.S., and Smith, D.K., 1995, Seamount volcanism at the Reykjanes Ridge: Relationship to the Iceland hot spot: *Journal of Geophysical Research*, v. 100, p. 8449–8468, doi: 10.1029/95JB00048.
- Maochang, H., 2001, Possible environmental impacts of drilling exploratory wells for geothermal development in the Brennisteinsfjöll area, SW Iceland: Geothermal training programme, Report 5/2001: The United Nations University, pp. 32.



- Markússon, S.H., and Stefánsson, A., 2011, Geothermal surface alteration of basalts, Krýsuvík Iceland - Alteration mineralogy, water chemistry and the effects of acid supply on the alteration process: *Journal of Volcanology and Geothermal Research*, v. 206, p. 46–59, doi: 10.1016/j.jvolgeores.2011.05.007.
- Mawejje, P., 2007, Geothermal exploration and geological mapping at Seltun in Krýsuvík Geothermal Field, Reykjanes Peninsula, Sw Iceland:, 257–276 p.
- Mochizuki, M., Brandsdóttir, B., Shiobara, H., Gudmundsson, G., Stefansson, R., and Shimamura, H., 2000, Detailed distribution of microearthquakes along the northern Reykjanes Ridge, off SW-Iceland: *Geophysical Research Letters*, v. 27, p. 1945–1948, doi: 10.1029/1999GL011264.
- Murton, B.J., and Parson, L.M., 1993, Segmentation, volcanism and deformation of oblique spreading centres: a quantitative study of the Reykjanes Ridge: *Tectonophysics*, v. 222, p. 237–257, doi: 10.1016/0040-1951(93)90051-K.
- Pałgan, D., Devey, C.W., and Yeo, I.A., 2016, Dike control of hydrothermal circulation in the Tertiary Icelandic crust and implications for cooling of the seafloor: *Journal of Volcanology and Geothermal Research*, v. 316, p. 22–33, doi: 10.1016/j.jvolgeores.2016.02.021.
- Parnell-Turner, R.E., White, N.J., Maclennan, J., Henstock, T.J., Murton, B.J., and Jones, S.M., 2013, Crustal manifestations of a hot transient pulse at 60°N beneath the Mid-Atlantic Ridge: *Earth and Planetary Science Letters*, v. 363, p. 109–120, doi: 10.1016/j.epsl.2012.12.030.
- Parson, L.M., Murton, B.J., Searle, R.C., Booth, D., Evans, J., Field, P., Keeton, J., Laughton, A., McAllister, E., Millard, N., Redbourne, L., Rouse, I., Shor, A., Smith, D., et al., 1993, En echelon axial volcanic ridges at the Reykjanes Ridge: a life cycle of volcanism and tectonics: *Earth and Planetary Science Letters*, v. 117, p. 73–87, doi: 10.1016/0012-821X(93)90118-S.
- Pedersen, G.B.M., and Grosse, P., 2014, Morphometry of subaerial shield volcanoes and glaciovolcanoes from Reykjanes Peninsula, Iceland: Effects of eruption environment: *Journal of Volcanology and Geothermal Research*, v. 282, p. 115–133, doi: 10.1016/j.jvolgeores.2014.06.008.
- Peirce, C., Gardiner, A., and Sinha, M., 2005, Temporal and spatial cyclicity of accretion at slow-spreading ridges-evidence from the Reykjanes Ridge: *Geophysical Journal International*, v. 163, p. 56–78, doi: 10.1111/j.1365-246X.2005.02738.x.
- Peirce, C., and Sinha, M.C., 2008, Life and death of axial volcanic ridges: Segmentation and crustal accretion at the Reykjanes Ridge: *Earth and Planetary Science Letters*, v. 274, p. 112–120, doi: 10.1016/j.epsl.2008.07.011.
- Perfit, M.R., and Chadwick, Jr., W.W., 1998, Magmatism at mid-ocean-ridges: constraints from volcanological and geochemical investigations, In: Buck, W.R., Delaney, P.T., Karson, J.A., and Lagabriele, Y. [Eds.], *Faulting and Magmatism at Mid-Ocean Ridges*, American Geophysical Union, Washington D.C., p. 59–116, doi: 10.1029/GM106p0059.

- Poore, H., White, N., and Maclennan, J., 2011, Ocean circulation and mantle melting controlled by radial flow of hot pulses in the Iceland plume: *Nature Geosci.*, v. 4, p. 558–561, doi: 10.1038/ngeo1161.
- Rossi, M.J., 1996, Morphology and mechanism of eruption of postglacial shield volcanoes in Iceland: *Bulletin of Volcanology*, v. 57, p. 530–540, doi: 10.1007/BF00304437.
- Ruddiman, W., 1972, Sediment Redistribution on the Reykjanes Ridge: Seismic Evidence: *Geological Society of America Bulletin*, v. 83, p. 2039–2062, doi: 10.1130/0016-7606(1972)83[2039:SROTRR]2.0.CO;2.
- Russell, J.K., Edwards, B.R., Porritt, L., and Ryane, C., 2014, Tuya: a descriptive genetic classification: *Quaternary Science Reviews*, v. 87, p. 70–81, doi: 10.1016/j.quascirev.2014.01.001.
- Sæmundsson, K., 1992, Geology of the Thingvallavatn Area: *Oikos*, v. 64, p. 40–68, doi: 10.2307/3545042.
- Sæmundsson, K., 1979, Outline of the geology of Iceland: *Jökull*, v. 29, p. 7–28.
- Sæmundsson, K., Johannesson, H., Hjartarson, Á., Kristinsson, S.G., and Sigurgeirsson, M.A., 2010, Geological Map of the Southwest Iceland, [Map], 1:100 000, Iceland GeoSurvey, Reykjavik.
- Sauter, D.L.M., and Cannat, M., 2010, The ultraslow spreading Southwest Indian Ridge, *in* Diversity of Hydrothermal Systems on Slow Spreading Ocean Ridges, Volume Diversity of Hydrothermal Systems on Slow Spreading Ocean Ridges, *Geophys. Monogr. Ser.*, AGU, Washington D.C., p. 153–173.
- Schopka, H.H., Gudmundsson, M.T., and Tuffen, H., 2006, The formation of Helgafell, southwest Iceland, a monogenetic subglacial hyaloclastite ridge: Sedimentology, hydrology and volcano–ice interaction: *Journal of Volcanology and Geothermal Research*, v. 152, p. 359–377, doi: 10.1016/j.jvolgeores.2005.11.010.
- Searle, R.C., Field, P.R., and Owens, R.B., 1994, Segmentation and nontransform ridge offset on the Reykjanes Ridge near 58°N: *Journal of Geophysical Research*, v. 99, p. 159–172, doi: 10.1029/94JB01549.
- Searle, R.C., Keeton, J.A., Owens, R.B., White, R.S., Mecklenburgh, R., and Parsons, B., 1998, The Reykjanes Ridge: structure and tectonics of a hot-spot-influenced, slow-spreading ridge, from multibeam bathymetry, gravity and magnetic investigations: *Earth and Planetary Science Letters*, v. 160, p. 463–478, doi: 10.1016/S0012-821X(98)00104-6.
- Sigmundsson, F., Hooper, A., Hreinsdóttir, S., Vogfjörd, K.S., Ófeigsson, B.G., Heimisson, E.R., Dumont, S., Parks, M., Spaans, K., Gudmundsson, G.B., Drouin, V., Árnadóttir, T., Jónsdóttir, K., Gudmundsson, M.T., et al., 2015, Segmented lateral dyke growth in a rifting event at Bárðarbunga volcanic system, Iceland: *Nature*, v. 517, p. 191–195, doi: 10.1038/nature14111.

- Sinha, M.C., Constable, S.C., Peirce, C., White, A., Heinson, G., Macgregor, L.M., and Navin, D.A., 1998, Magmatic processes at slow spreading ridges: implications of the RAMESSES experiment at 57°45'N on the Mid-Atlantic Ridge: *Geophysical Journal International*, v. 135, p. 731–745, doi: 10.1046/j.1365-246X.1998.00704.x.
- Skilling, I.P., 2009, Subglacial to emergent basaltic volcanism at Hlōðufell, south-west Iceland: A history of ice-confinement: *Journal of Volcanology and Geothermal Research*, v. 185, p. 276–289, doi: 10.1016/j.jvolgeores.2009.05.023.
- Smellie, J.L., 2007, Quaternary volcanism, subglacial landforms, *in* Elias, S.A. ed., *Encyclopedia of Quaternary Science*, Elsevier, Amsterdam, p. 784–798.
- Smith, D.K., and Cann, J., 1993, Building the crust at the Mid-Atlantic Ridge: *Nature*, v. 365, p. 707–715, doi: 10.1038/365707a0.
- Standish, J.J., and Sims, K.W.W., 2010, Young off-axis volcanism along the ultraslow spreading Southwest Indian Ridge: *Nature Geoscience*, v. 3, p. 286–292, doi: 10.1038/ngeo824.
- Stefánsson, R., Böðvarsson, R., Slunga, R., Einarsson, P., Jakobsdóttir, S., Bungum, H., Gregersen, S., Havskov, J., Hjelme, J., and Korhonen, H., 1993, Earthquake prediction research in the South Iceland Seismic Zone and the SIL project: *Seismol. Soc. Am. Bull.*, v. 83, no. 3, p. 696–716.
- Talwani, M., Windisch, C.C., and Langseth, M.G., 1971, Reykjanes Ridge crest: A detailed geophysical study: *Journal of Geophysical Research*, v. 76, p. 473–577, doi: 10.1029/JB076i002p00473.
- Thorarinsson, S., 1969, The Lakagigar Eruption of 1783: *Bulletin of Volcanology*, v. 33, p. 910–929, doi: 10.1007/BF02596756.
- Titarenko, S.S., and McCaig, A.M., 2015, Modelling the Lost City hydrothermal field: influence of topography and permeability structure: *Geofluids*, v. 16, p. 314–328, doi: 10.1111/gfl.12151.
- Torfason, H., 2003, Geothermal Map of Iceland [Map], 1: 500 000, Náttúruminjasafn Íslands og Orkustofnun, Reykjavík.
- Tryggvason, E., 1980, Subsidence events in the Krafla area, North Iceland, 1975–1979: *J. Geophys.*, v. 47, p. 141–153.
- Tuckwell, G.W., Bull, J.M., and Sanderson, D.J., 1998, Numerical models of faulting at oblique spreading centers: *Journal of Geophysical Research Solid Earth*, v. 103, no. 5473–15482, doi: 10.1029/97JB03673.
- Valdimarsson, H., and Malmberg, S., 1999, Near-surface circulation in Icelandic waters derived from satellite tracked drifters: *Rit Fiskideildar*, v. 16, p. 23–39.
- Vogt, P.R., 1971, Asthenosphere motion recorded by the ocean floor south of Iceland: *Earth and Planetary Science Letters*, v. 13, p. 153–160, doi: 10.1016/0012-821X(71)90118-X.

- Was, E., Edwards, B.R., Pollock, M., Hauksdottir, S., Gudmundsson, M.T., Hiatt, A.R., Perpalaj, A., Plascencia, E., Reinthall, M., and Silverstein, A., 2013, Along-axis variations in volcanology and geochemistry of a pillow-dominated tindar: Comparison of exposures in Undirhlithar and Vatnsskarth quarries, Reykjanes Peninsula, Iceland [Abstract]: AGU Fall Meeting, #V41D-2839.
- Weir, N.R., White, R.S., Brandsdottir, B., Einarsson, P., Shimamura, H., Shiobara, H., and the RISE FieldworkTeam, 2001, Crustal structure of the northern Reykjanes Ridge and Reykjanes Peninsula, southwest Iceland: *Journal of Geophysical Research*, v. 106, p. 6347–6368, doi: 10.1029/2000JB900358.
- Yeo, I.A., 2012, Detailed studies of mid-ocean ridge volcanism at the Mid-Atlantic Ridge (45°N) and elsewhere [PhD Thesis], Durham University, United Kingdom, pp. 299.
- Yeo, I.A., Clague, D.A., Martin, J.F., Paduan, J.B., and Caress, D.W., 2013, Preeruptive flow focussing in dikes feeding historical pillow ridges on the Juan de Fuca and Gorda Ridges: *Geochemistry, Geophysics, Geosystems*, v. 14, p. 3586–3599, doi: 10.1002/ggge.20210.
- Yeo, I.A., and Searle, R.C., 2013, High-resolution Remotely Operated Vehicle (ROV) mapping of a slow-spreading ridge: Mid-Atlantic Ridge 45°N: *Geochemistry, Geophysics, Geosystems*, v. 14, p. 1693–1702, doi: 10.1002/ggge.20082.



# Chapter 6

## Conclusions



## 6 Conclusions

This dissertation focused on investigation of volcano-tectonic controls of low-temperature hydrothermal venting in off-axis region of Iceland (Westfjords) but high-temperature venting in on-axis setting (Reykjanes Peninsula) has also been studied. The unique setting of Iceland was used as a proxy for the adjacent shallow, hot spot-influenced Reykjanes Ridge. This northern segment of the Mid-Atlantic Ridge generally lacks hydrothermalism, with only one high-temperature hydrothermal vent field, the Steinahóll, being confirmed. The results of this work have been used for hydrothermal prospection along the Reykjanes Ridge, and may be applied to other hot spot-influenced ridges and possibly ridges of different spreading rates. The main conclusions of this study are as follows:

1. The Tertiary crust of Iceland in Westfjords (>7 Ma), located >100 km away from the active neovolcanic zone, is still hydrothermally active with abundant low-temperature ( $\leq 100^{\circ}\text{C}$ ) hydrothermal systems. These systems are exclusively controlled by dike intrusions dissecting the local lava pile. This observation is in contrast to fault-controlled hydrothermal activity that occurs at the on-axis settings. This is most likely linked to change in permeability in fault vs dike margins as plate migrates from on-axis to off-axis position with time. It appears that in on-axis settings, active faults maintain high crustal permeability and become preferable pathways for high-temperature hydrothermal circulation above the axial magma chambers and reservoirs. In off-axis setting (i.e., outside the seismically-defined neovolcanic zone extending ~25 km on each side of the ridge axis), the permeability of now-inactive faults drops significantly. This is due to quick sealing and clogging of the fault zone as the fine-grained fault gouge reacts with hydrothermal fluid forming secondary minerals. Dike margins and jointed dike rims are inherently less permeable but also less reactive; therefore, in the off-axis setting the dike margins (damage zones associated with dikes) become the preferable pathways for hydrothermal circulation. With lower temperatures, flow rates and dissolved species load, fluids in such convection cells have much lower impact on the rocks and lead to negligible sealing of the permeable zone even for millions of years.
2. Dikes hosting low-temperature hydrothermal systems in Westfjords display relatively high alteration overall. Phenocrysts of primal phases (plagioclase, clinopyroxene and olivine) show a range of alteration intensity from pristine (no observed alteration) to complete replacement (i.e., olivine and clinopyroxene). The groundmass, consisting of

fine-grained plagioclase, clinopyroxene and opaques shows higher level of alteration, ranging from weak to very intense. Volcanic glass in the groundmass of all studied dikes is either absent or has been completely replaced by secondary mineralization. The alteration is dominated by clay minerals from the smectite group, suggesting that dikes were subjected to intermediate argillic alteration with low water/rock ratio environment, slightly reduced conditions and temperature of hydrothermal fluids not exceeding 250°C. The plagioclase phenocrysts in the studied dikes are mostly bytownite and labradorite in composition, with minor anorthite and andesine. They show low wt. % K<sub>2</sub>O, with concentrations ranging from 0.061% to 0.120%. The plagioclase phenocrysts show little precipitation of secondary minerals in fractures and cracks, but no potassium leaching has been observed over grain boundaries. Due to high levels of preservation, the plagioclase phenocrysts are suitable for <sup>40</sup>Ar/<sup>39</sup>Ar dating of dikes from Westfjords that host hydrothermal vent sites.

3. The majority of the obtained <sup>40</sup>Ar/<sup>39</sup>Ar ages of the dikes overlap within 2σ errors with previous K-Ar whole rock ages of the dike-hosting lavas of Westfjords determined by McDougall et al. (1984). This suggests that the dikes erupted synchronously with the surrounding lava flows, which probably occurred along active between 15–7 Ma and currently inactive Snæfellsnes-Skagi Rift Zone (SSRZ) before the rift jump relocated it to its current position along the Western Rift Zone (WRZ). Additionally, all the <sup>40</sup>Ar/<sup>39</sup>Ar dike ages overlap with each other within 2σ errors, suggesting that they all intruded roughly coeval, most likely within the neovolcanic zone of the SSRZ. The above results indicate that these dike emplacements are not younger, off-axis volcanic episodes, and no volcanic rejuvenation occurred in the Westfjords over the past 7 Ma. Interestingly, despite the lack of young volcanic and/or tectonic activity in Westfjords, low-temperature hydrothermal circulation is still abundant. This indicates that old rift-related dikes (and dike margins) remain open and penetrable for the lower temperature hydrothermal circulation up to 15 Ma after they left the neovolcanic zone.
4. The <sup>40</sup>Ar/<sup>39</sup>Ar plagioclase ages determined in this study yielded high errors on individual step and plateau ages. This has been attributed mainly to the overall very low potassium concentrations in the plagioclases (from 0.061% to 0.120%) and low quantities of the material for the dating. The observed in fractures and cracks of plagioclase secondary mineralization had minor influence on the <sup>40</sup>Ar/<sup>39</sup>Ar ages. This is due to acid treatment of the plagioclase separates (with 3% hydrochloric and 5% hydrofluoric acid), which was used to remove this alteration. The acid treatment

proved to be fairly successful as no visible alteration has been observed in the plagioclase minerals under the binocular microscope after the acid treatment. Nevertheless, some degassing from the alteration has been observed during the step-heating experiments. The final  $^{40}\text{Ar}/^{39}\text{Ar}$  ages have been corrected for this degassing and geologically meaningful ages have been produced.

5. The on-axis hydrothermal activity in Iceland along the Reykjanes Peninsula is confined to active en echelon arranged volcanic systems intersected by trending roughly NE-SW fissure swarms, which consist of tensional fractures, normal and/or strike-slip faults, and volcanic or tectonic fissures. These on-land volcanic systems are the equivalent to off-shore Axial Volcanic Ridges (AVRs). Seven AVRs have been mapped along the Reykjanes Ridge between  $62^{\circ}30'\text{N}$  and  $63^{\circ}30'\text{N}$ . The interpretation of their volcano-tectonic status suggests that the formation of AVRs is more complex than in the 4-stage model proposed by Murton and Parson (1993) and Parson et al. (1993). It has been shown that the magma is not evenly supplied along the entire length of a given AVR, and in some cases volcanism seems to be migrating along the AVR. On some AVRs, the youngest volcanism appears to be associated with elongated eruptive fissures up to 7 km in length, suggesting a strong tectonic control and low effusion-rate eruption mechanisms. On other AVRs, the most recent volcanic activity has a point-source origin, characteristic of longer-lived magma supply and higher effusion rates. Interestingly, the two above mentioned eruption mechanisms can co-exist on one AVR, which further contrasts with the 4-stage formation model of Murton and Parson (1993) and Parson et al. (1993).
6. The one known high-temperature hydrothermal vent on the Reykjanes Ridge (Steinahóll) is located on top of a young eruptive fissure, reaching ~250 mbsl, located between two east-facing minor faults. This distinctive morphology strongly resembles elongated tindars and hyaloclastite ridges observed on the Reykjanes Peninsula, which are known to host high-temperature geothermal activity (e.g., Krýsuvík or Brennisteinsfjöll geothermal areas). Bathymetric features similar to those observed at Steinahóll have also been mapped elsewhere on shallow regions of all the AVRs, where they are sometimes the highest topographic features (preferable targets for hydrothermal prospection).
7. The similarities between the Reykjanes Peninsula and Reykjanes Ridge suggest that all of the AVRs along the Reykjanes Ridge may also be hydrothermally active, but activity has only been confirmed on one AVR. The fact that more hydrothermal

systems have not been detected, despite previous prospecting, is probably due to the sensitivity of the instruments used to search for them. Topographic highs on the axial ridges of the Reykjanes Ridge are the regions where strongest currents occur, probably causing plumes to be swept away from their source and dispersed rapidly. Therefore, an instrumentation that can be deployed closer to the seafloor than the traditionally lowered from the ship CTDs or Miniature Autonomous Plume Recorders (MAPRs) is needed, ideally autonomous and remote vehicles and direct seafloor observations.

8. Based on the observations from Iceland (in particular in the far off-axis Westfjords), it appears that the hydrothermal activity along hot spot-influenced ridges, such as the Reykjanes Ridge, may be dominated by widespread off-axis low-temperature ( $\leq 100^{\circ}\text{C}$ ) venting in  $>2$  Ma crust, controlled by old rift-related (but also possibly off-axis/intraplate in origin) dikes. These dikes can be recognized in the off-axis regions of the Reykjanes Ridge as volcanoes sitting on top of faults, or where they are exposed on unsedimented seafloor, e.g., steep slopes of volcanic edifices or fault scarps. Based on the observations from Westfjords it is predicted that at least one low-temperature vent should be present for each  $13 \text{ km}^2$  of the oceanic crust  $>2$  Ma on the Reykjanes Ridge.
9. The results from this dissertation emphasize that low-temperature ( $\leq 100^{\circ}\text{C}$ ) venting may meaningfully contribute to the planetary cooling as they might be more abundant on the seafloor than currently is known. Additionally, low-temperature, off-axis systems might be remnants of former on-axis high-temperature systems, as the activity slowly wanes after they move away from the spreading axis, and which are known to form seafloor massive sulfide (SMS) deposits. Interestingly, some of the largest SMS deposits have been discovered along the slow-spreading mid-ocean ridges. Therefore, locating low-temperature systems in the off-axis settings of northern Mid-Atlantic Ridge may be of high interest for prospecting for SMS deposits. This is especially important for countries where hydrothermal activity occurs and/or which plan to extend their Exclusive Economic Zones (EEZs) to areas where such deposits may be present, for example, Iceland. Therefore, future work will focus on prospecting for the off-axis low-temperature hydrothermal activity along the flanks of the Reykjanes Ridge. Additionally, according to one of the hypothesis resulting from this dissertation, if the current AVRs situated on the spreading axis are hydrothermally active it is very likely that in the past older AVRs have also been active. If this is the

case, work will also focus in mapping older AVRs on the ridge flanks as they might be of high relevance for locating old SMS deposits in off-axis settings.

**Appendix A**



Appendix A

**Table 14 Major elements data measured in plagioclase and clinopyroxene in sample 1-2.**

No.	Na <sub>2</sub> O	K <sub>2</sub> O	FeO	SiO <sub>2</sub>	MnO	CaO	MgO	Al <sub>2</sub> O <sub>3</sub>	TiO <sub>2</sub>	Total	Comment
<i>Plagioclase</i>											
1	1.950	0.069	0.579	47.420	-	16.610	0.152	32.850	0.041	99.7	1-2_Plg_1_rim1
2	2.000	0.078	0.670	47.540	-	16.610	0.142	32.860	0.028	99.9	1-2_Plg_1_rim2
3	1.920	0.068	0.674	47.560	-	16.770	0.138	33.080	0.039	100.2	1-2_Plg_1_rim3
4	1.650	0.060	0.547	46.630	-	17.130	0.111	33.570	0.030	99.7	1-2_Plg_1_core1
5	1.610	0.067	0.570	46.740	-	17.430	0.138	33.560	0.038	100.2	1-2_Plg_1_core2
6	1.700	0.059	0.653	46.980	-	17.100	0.156	33.530	0.027	100.2	1-2_Plg_1_core3
7	1.940	0.069	0.570	47.150	-	16.810	0.145	32.880	0.044	99.6	1-2_Plg_2_rim1
8	1.890	0.072	0.720	45.760	-	16.730	0.144	32.860	0.036	98.2	1-2_Plg_2_rim2
9	1.950	0.072	0.626	47.210	-	16.620	0.158	32.820	0.044	99.5	1-2_Plg_2_rim3
10	1.950	0.065	0.608	47.200	-	16.580	0.144	32.800	0.032	99.4	1-2_Plg_2_core1
11	1.880	0.071	0.651	47.470	-	16.730	0.153	33.210	0.047	100.2	1-2_Plg_2_core2
12	1.920	0.067	0.641	47.420	-	16.770	0.144	32.880	0.030	99.9	1-2_Plg_2_core3
13	2.450	0.109	0.622	49.320	-	15.590	0.169	31.970	0.047	100.3	1-2_Plg_3_rim1
14	1.870	0.082	0.607	47.650	-	16.630	0.143	33.100	0.047	100.1	1-2_Plg_3_rim2
15	2.380	0.094	0.670	48.800	-	15.750	0.168	32.090	0.054	100.0	1-2_Plg_3_rim3
16	1.910	0.063	0.660	47.570	-	16.720	0.148	32.980	0.031	100.1	1-2_Plg_3_core1
17	1.950	0.058	0.692	47.490	-	16.640	0.150	33.070	0.050	100.1	1-2_Plg_3_core2
18	1.900	0.062	0.618	47.480	-	16.740	0.135	33.020	0.031	100.0	1-2_Plg_3_core3
19	1.770	0.060	0.654	47.340	-	16.840	0.140	33.420	0.035	100.3	1-2_Plg_4_rim1
20	1.800	0.066	1.254	47.350	-	16.440	0.472	32.260	0.026	99.7	1-2_Plg_4_rim2
21	2.160	0.062	0.724	48.390	-	16.120	0.170	32.410	0.048	100.1	1-2_Plg_4_rim3
22	1.400	0.040	0.619	46.400	-	17.560	0.129	34.040	0.039	100.2	1-2_Plg_4_core1
23	1.860	0.082	0.588	47.620	-	16.660	0.159	33.050	0.059	100.1	1-2_Plg_4_core2
24	1.730	0.049	0.647	47.020	-	17.020	0.158	33.510	0.037	100.2	1-2_Plg_4_core3
25	3.540	0.125	0.724	51.600	-	13.480	0.156	30.130	0.068	99.8	1-2_Plg_5_rim1
26	3.390	0.124	0.688	51.270	-	13.830	0.188	30.420	0.070	100.0	1-2_Plg_5_rim2
27	2.370	0.128	1.380	49.450	-	14.760	0.689	30.830	0.054	99.7	1-2_Plg_5_rim3
28	1.630	0.042	0.528	46.790	-	17.180	0.145	33.810	0.019	100.1	1-2_Plg_5_core1
29	1.640	0.115	0.715	47.240	-	16.840	0.243	33.240	0.041	100.1	1-2_Plg_5_core2
30	1.770	0.045	0.618	47.090	-	16.840	0.154	33.430	0.042	100.0	1-2_Plg_5_core3
31	1.540	0.041	0.683	46.610	-	17.350	0.132	33.890	0.025	100.3	1-2_Plg_6_rim1
32	1.570	0.039	0.612	46.310	-	17.320	0.121	34.060	0.022	100.1	1-2_Plg_6_rim2
33	2.350	0.087	0.629	48.880	-	15.720	0.152	32.620	0.049	100.5	1-2_Plg_6_rim3
34	1.530	0.055	0.570	46.350	-	17.350	0.154	33.950	0.034	100.0	1-2_Plg_6_core1
35	1.580	0.051	0.601	46.610	-	17.310	0.116	33.900	0.013	100.2	1-2_Plg_6_core2
36	1.530	0.049	0.659	46.530	-	17.220	0.115	33.760	0.029	99.9	1-2_Plg_6_core3
<b>Average</b>	<b>1.972</b>	<b>0.071</b>	<b>0.686</b>	<b>47.646</b>	<b>-</b>	<b>16.472</b>	<b>0.180</b>	<b>32.880</b>	<b>0.040</b>		
<i>Clinopyroxene</i>											
37	0.338	0.011	9.180	50.200	0.138	17.920	16.250	4.700	0.975	99.7	1-2_Cpx_1
38	0.332	0.003	8.420	50.550	0.183	18.930	15.690	4.780	1.090	100.0	1-2_Cpx_2
39	0.225	0.007	9.130	53.620	0.254	16.550	18.520	1.804	0.443	100.6	1-2_Cpx_3

Appendix A

No.	Na <sub>2</sub> O	K <sub>2</sub> O	FeO	SiO <sub>2</sub>	MnO	CaO	MgO	Al <sub>2</sub> O <sub>3</sub>	TiO <sub>2</sub>	Total	Comment
40	0.303	0.007	9.020	51.610	0.225	17.870	16.450	3.900	0.829	100.2	1-2_Cpx_4
41	0.254	0.008	8.390	52.070	0.192	18.520	16.760	3.360	0.704	100.3	1-2_Cpx_5
42	0.229	0.018	9.280	52.890	0.180	17.320	16.400	2.680	0.562	99.6	1-2_Cpx_6
43	0.338	0.005	9.460	51.070	0.154	17.890	15.900	4.190	0.946	100.0	1-2_Cpx_7
44	0.277	0.008	7.790	51.370	0.179	19.420	16.150	3.680	0.784	99.7	1-2_Cpx_8
45	0.339	0.008	9.630	49.690	0.179	18.490	15.130	5.290	1.395	100.2	1-2_Cpx_9
46	0.340	0.002	8.150	51.000	0.120	19.010	15.630	4.560	0.855	99.7	1-2_Cpx_10
47	0.262	0.006	7.620	52.080	0.193	19.530	16.480	2.870	0.616	99.7	1-2_Cpx_11
48	0.268	0.003	7.520	50.960	0.172	20.150	15.440	4.110	0.924	99.5	1-2_Cpx_12
<b>Average</b>	<b>0.292</b>	<b>0.007</b>	<b>8.633</b>	<b>51.426</b>	<b>0.181</b>	<b>18.467</b>	<b>16.233</b>	<b>3.827</b>	<b>0.844</b>		
<b>Average Full Sample</b>	<b>1.503</b>	<b>0.053</b>	<b>2.904</b>	<b>48.701</b>	<b>0.181</b>	<b>17.028</b>	<b>4.660</b>	<b>24.772</b>	<b>0.264</b>		

Table 15 Major elements data measured in plagioclase and clinopyroxene in sample 10-1.

No.	Na <sub>2</sub> O	K <sub>2</sub> O	FeO	SiO <sub>2</sub>	MnO	CaO	MgO	Al <sub>2</sub> O <sub>3</sub>	TiO <sub>2</sub>	Total	Comment
<i>Plagioclase</i>											
1	1.416	0.032	0.670	46.730	-	17.800	0.142	34.590	0.023	101.4	10-1_plg_1_rim1
2	1.487	0.035	0.547	46.920	-	17.510	0.157	34.220	0.032	100.9	10-1_plg_1_rim2
3	1.458	0.038	0.595	46.560	-	17.780	0.153	34.450	0.037	101.1	10-1_plg_1_rim3
4	1.713	0.047	0.573	47.400	-	17.110	0.181	33.950	0.027	101.0	10-1_plg_1_core1
5	1.775	0.040	0.540	47.510	-	17.140	0.176	33.810	0.030	101.0	10-1_plg_1_core2
6	1.592	0.028	0.539	47.190	-	17.370	0.181	34.010	0.046	101.0	10-1_plg_1_core3
7	3.298	0.114	0.694	51.060	-	14.110	0.193	30.950	0.060	100.5	10-1_plg_2_rim1
8	4.801	0.223	0.958	54.620	-	11.390	0.108	28.740	0.113	101.0	10-1_plg_2_rim2
9	3.853	0.146	0.836	52.630	-	13.070	0.157	29.900	0.056	100.6	10-1_plg_2_rim3
10	1.697	0.047	0.634	47.340	-	17.240	0.176	34.030	0.044	101.2	10-1_plg_2_core1
11	1.770	0.037	0.576	47.590	-	17.010	0.192	33.340	0.020	100.5	10-1_plg_2_core2
12	1.658	0.035	0.552	47.300	-	17.300	0.194	33.960	0.043	101.0	10-1_plg_2_core3
13	3.337	0.123	0.753	51.410	-	13.990	0.228	30.620	0.062	100.5	10-1_plg_3_rim1
14	3.329	0.108	0.783	51.380	-	14.050	0.219	30.630	0.059	100.6	10-1_plg_3_rim2
15	1.578	0.040	0.540	47.010	-	17.250	0.159	33.960	0.044	100.6	10-1_plg_3_rim3
16	1.589	0.033	0.535	47.010	-	17.270	0.180	34.160	0.034	100.8	10-1_plg_3_core1
17	1.672	0.038	0.653	47.530	-	17.220	0.183	33.740	0.033	101.1	10-1_plg_3_core2
18	1.857	0.053	0.518	47.540	-	16.870	0.175	33.490	0.036	100.5	10-1_plg_3_core3
19	3.088	0.121	0.761	50.830	-	14.510	0.195	31.170	0.054	100.7	10-1_plg_4_rim1
20	4.587	0.203	0.951	54.010	-	11.680	0.129	28.780	0.081	100.4	10-1_plg_4_rim2
21	4.002	0.145	0.993	52.980	-	12.830	0.166	29.650	0.100	100.9	10-1_plg_4_rim3
22	1.321	0.039	0.489	46.120	-	17.670	0.145	34.190	0.032	100.0	10-1_plg_4_core1
23	1.416	0.040	0.515	46.220	-	17.720	0.162	34.340	0.016	100.4	10-1_plg_4_core2
24	1.714	0.044	0.593	47.230	-	17.190	0.141	33.820	0.043	100.8	10-1_plg_4_core1
25	3.171	0.107	0.584	51.130	-	14.470	0.218	31.130	0.045	100.9	10-1_plg_5_rim1
26	3.797	0.141	0.700	52.240	-	13.330	0.137	30.170	0.067	100.6	10-1_plg_5_rim2
27	4.413	0.195	0.821	53.700	-	12.180	0.137	29.160	0.071	100.7	10-1_plg_5_rim3

Appendix A

No.	Na <sub>2</sub> O	K <sub>2</sub> O	FeO	SiO <sub>2</sub>	MnO	CaO	MgO	Al <sub>2</sub> O <sub>3</sub>	TiO <sub>2</sub>	Total	Comment
28	1.796	0.046	0.497	47.520	-	17.030	0.178	33.820	0.031	100.9	10-1_plg_5_core1
29	1.909	0.048	0.580	47.910	-	16.840	0.164	33.360	0.031	100.8	10-1_plg_5_core2
30	1.509	0.037	0.518	46.840	-	17.560	0.162	34.210	0.042	100.9	10-1_plg_5_core3
31	3.347	0.111	0.638	51.290	-	13.990	0.228	30.560	0.076	100.2	10-1_plg_6_rim1
32	4.476	0.194	0.866	54.140	-	11.960	0.107	28.980	0.080	100.8	10-1_plg_6_rim2
33	2.813	0.074	0.679	50.260	-	14.990	0.213	31.510	0.054	100.6	10-1_plg_6_rim3
34	1.499	0.030	0.565	46.640	-	17.600	0.158	34.090	0.003	100.6	10-1_plg_6_core1
35	1.468	0.025	0.514	46.870	-	17.460	0.147	33.820	0.032	100.3	10-1_plg_6_core2
36	1.448	0.033	0.483	46.840	-	17.610	0.159	34.210	0.021	100.8	10-1_plg_6_core1
<b>Average</b>	<b>2.435</b>	<b>0.079</b>	<b>0.646</b>	<b>49.097</b>	<b>-</b>	<b>15.781</b>	<b>0.169</b>	<b>32.487</b>	<b>0.047</b>		
<i>Clinopyroxene</i>											
37	0.311	0.000	14.760	50.570	0.400	18.510	12.040	2.450	1.149	100.2	10-1_cpx_1
38	0.174	0.001	8.180	53.380	0.194	17.960	17.700	1.882	0.513	100.0	10-1_cpx_2
39	0.183	0.000	8.230	53.180	0.171	18.990	17.100	1.856	0.548	100.3	10-1_cpx_3
40	0.216	0.000	6.740	52.850	0.170	20.020	17.000	2.770	0.531	100.3	10-1_cpx_4
41	0.339	0.000	14.690	50.100	0.264	18.750	11.960	2.670	1.336	100.1	10-1_cpx_5
42	0.296	0.000	10.960	50.590	0.181	19.450	14.190	3.800	1.029	100.5	10-1_cpx_6
43	0.368	0.002	13.520	49.530	0.362	18.940	12.660	3.390	1.409	100.2	10-1_cpx_7
44	0.238	0.008	10.980	52.650	0.367	17.280	16.640	1.811	0.557	100.5	10-1_cpx_8
45	0.227	0.000	7.520	52.660	0.159	18.840	17.120	2.440	0.491	99.5	10-1_cpx_9
46	0.205	0.000	10.040	52.960	0.241	17.880	16.650	1.777	0.574	100.3	10-1_cpx_10
47	0.232	0.000	6.780	52.670	0.089	20.540	16.370	2.520	0.488	99.7	10-1_cpx_11
48	0.288	0.001	7.260	51.390	0.187	19.330	16.230	4.560	0.656	99.9	10-1_cpx_12
49	0.237	0.000	7.840	51.670	0.228	19.440	16.220	3.950	0.806	100.4	10-1_cpx_13
50	0.320	0.025	12.520	49.570	0.208	16.490	14.050	3.900	0.793	97.9	10-1_cpx_14
51	-	-	14.910	49.750	0.421	18.120	12.330	2.140	-	97.7	10-1_cpx_15
52	-	-	14.370	49.030	0.403	17.930	12.650	2.800	-	97.2	10-1_cpx_16
53	-	-	11.290	49.490	0.284	19.540	13.760	3.190	-	97.6	10-1_cpx_17
<b>Average</b>	<b>0.260</b>	<b>0.003</b>	<b>10.623</b>	<b>51.296</b>	<b>0.254</b>	<b>18.706</b>	<b>14.981</b>	<b>2.818</b>	<b>0.777</b>		
<b>Average Full Sample</b>	<b>1.8378</b>	<b>0.0581</b>	<b>3.7866</b>	<b>49.7896</b>	<b>0.2544</b>	<b>16.7017</b>	<b>4.8322</b>	<b>23.1465</b>	<b>0.2471</b>		

Table 16 Major elements data measured in plagioclase, clinopyroxene and olivine in sample 2-1.

No.	Na <sub>2</sub> O	K <sub>2</sub> O	FeO	SiO <sub>2</sub>	MnO	CaO	MgO	Al <sub>2</sub> O <sub>3</sub>	TiO <sub>2</sub>	Total	Comment
<i>Plagioclase</i>											
1	1.640	0.056	0.565	46.920	-	17.200	0.163	33.690	0.019	100.3	2-1_Plg_1_rim1
2	1.920	0.064	0.535	47.140	-	16.810	0.180	33.080	0.035	99.8	2-1_Plg_1_rim2
3	1.860	0.048	0.589	47.550	-	16.730	0.181	33.310	0.043	100.3	2-1_Plg_1_rim3
4	1.980	0.054	0.600	47.730	-	16.530	0.189	32.930	0.048	100.1	2-1_Plg_1_core1
5	1.810	0.050	0.614	47.330	-	16.900	0.173	33.380	0.040	100.3	2-1_Plg_1_core2
6	1.780	0.056	0.608	47.060	-	16.880	0.183	33.320	0.041	99.9	2-1_Plg_1_core3
7	1.740	0.044	0.558	47.220	-	16.800	0.175	33.520	0.041	100.1	2-1_Plg_2_rim1
8	1.730	0.048	0.603	47.270	-	16.840	0.186	33.320	0.047	100.0	2-1_Plg_2_rim2

Appendix A

No.	Na <sub>2</sub> O	K <sub>2</sub> O	FeO	SiO <sub>2</sub>	MnO	CaO	MgO	Al <sub>2</sub> O <sub>3</sub>	TiO <sub>2</sub>	Total	Comment
9	1.730	0.046	0.559	47.320	-	16.870	0.169	33.410	0.045	100.1	2-1_Plg_2_rim3
10	1.940	0.045	0.554	47.910	-	16.610	0.172	33.380	0.040	100.7	2-1_Plg_2_core1
11	2.020	0.056	0.521	47.810	-	16.390	0.168	32.900	0.025	99.9	2-1_Plg_2_core2
12	1.960	0.061	0.569	47.590	-	16.580	0.208	32.980	0.030	100.0	2-1_Plg_2_core3
13	3.520	0.146	0.575	51.400	-	13.590	0.154	30.430	0.077	99.9	2-1_Plg_3_rim1
14	3.960	0.199	0.767	52.500	-	12.540	0.174	29.580	0.103	99.8	2-1_Plg_3_rim2
15	1.820	0.057	0.637	47.010	-	16.580	0.194	32.980	0.051	99.3	2-1_Plg_3_rim3
16	1.630	0.041	0.622	46.990	-	17.020	0.149	33.670	0.038	100.2	2-1_Plg_3_core1
17	1.720	0.056	0.579	47.040	-	17.000	0.194	33.660	0.020	100.3	2-1_Plg_3_core2
18	1.770	0.047	0.489	47.230	-	16.870	0.152	33.460	0.039	100.1	2-1_Plg_3_core3
19	1.821	0.071	0.643	47.480	-	16.760	0.193	33.780	0.033	100.8	2-1_Plg_4_rim1
20	1.942	0.066	0.599	47.490	-	16.780	0.189	33.410	0.036	100.5	2-1_Plg_4_rim2
21	1.973	0.070	0.627	47.610	-	16.660	0.178	33.120	0.038	100.3	2-1_Plg_4_rim3
22	1.902	0.068	0.520	47.800	-	16.580	0.174	33.300	0.007	100.4	2-1_Plg_4_core1
23	1.517	0.054	0.518	46.470	-	17.410	0.153	34.120	0.022	100.3	2-1_Plg_4_core2
24	1.881	0.078	0.550	47.760	-	16.760	0.174	33.440	0.035	100.7	2-1_Plg_4_core3
25	1.830	0.075	0.608	47.370	-	16.720	0.159	33.390	0.038	100.2	2-1_Plg_5_rim1
26	1.911	0.059	0.670	47.470	-	16.610	0.177	33.460	0.074	100.4	2-1_Plg_5_rim2
27	3.700	0.167	0.533	51.890	-	13.280	0.223	30.620	0.081	100.5	2-1_Plg_5_rim3
28	2.072	0.059	0.636	47.840	-	16.550	0.197	33.080	0.038	100.4	2-1_Plg_5_core1
29	1.940	0.057	0.579	47.710	-	16.610	0.172	33.300	0.048	100.1	2-1_Plg_5_core2
30	2.041	0.063	0.538	47.760	-	16.340	0.206	33.130	0.046	100.5	2-1_Plg_5_core3
31	1.546	0.049	0.593	46.780	-	17.310	0.161	34.050	0.030	100.2	2-1_Plg_6_rim1
32	1.556	0.044	0.533	46.630	-	17.410	0.161	33.880	0.027	100.0	2-1_Plg_6_rim2
33	1.525	0.050	0.566	46.250	-	17.330	0.168	34.080	0.044	100.2	2-1_Plg_6_rim3
34	1.858	0.055	0.537	47.350	-	16.700	0.169	33.530	0.025	100.1	2-1_Plg_6_core1
35	1.585	0.052	0.577	46.520	-	17.270	0.162	33.950	0.029	100.4	2-1_Plg_6_core2
36	1.686	0.060	0.508	46.810	-	17.090	0.165	34.020	0.019	100.3	2-1_Plg_6_core3
<b>Average</b>	<b>1.967</b>	<b>0.066</b>	<b>0.580</b>	<b>47.667</b>	-	<b>16.525</b>	<b>0.176</b>	<b>33.185</b>	<b>0.040</b>		
<i>Clinopyroxene</i>											
37	0.283	0.014	5.820	52.380	0.130	20.490	16.680	3.200	0.512	99.5	2-1_Cpx_1
38	0.270	0.018	5.970	52.540	0.158	20.530	16.810	3.030	0.514	99.8	2-1_Cpx_2
39	0.242	0.004	6.000	52.670	0.158	20.600	16.580	3.070	0.539	99.9	2-1_Cpx_3
40	0.251	0.000	5.740	52.700	0.123	20.770	16.730	2.870	0.509	99.7	2-1_Cpx_4
41	0.243	0.003	6.090	52.290	0.138	20.460	16.840	3.220	0.526	99.8	2-1_Cpx_5
42	0.266	0.000	5.850	52.450	0.076	20.520	16.680	3.020	0.504	99.4	2-1_Cpx_6
<b>Average</b>	<b>0.259</b>	<b>0.006</b>	<b>5.912</b>	<b>52.505</b>	<b>0.130</b>	<b>20.562</b>	<b>16.720</b>	<b>3.068</b>	<b>0.517</b>		
<i>Olivine</i>											
43	-	-	17.860	40.230	0.292	0.352	42.710	0.035	-	101.5	2-1_Ol_1
44	-	-	17.700	40.120	0.290	0.352	42.620	0.032	-	101.1	2-1_Ol_2
45	-	-	17.980	39.850	0.304	0.352	42.600	0.038	-	101.1	2-1_Ol_3
46	-	-	18.030	39.950	0.289	0.354	42.660	0.036	-	101.3	2-1_Ol_4
47	-	-	24.080	39.070	0.353	0.340	37.840	0.031	-	101.7	2-1_Ol_5
48	-	-	17.940	40.240	0.297	0.349	42.860	0.036	-	101.7	2-1_Ol_6
49	-	-	17.960	39.860	0.297	0.349	42.880	0.034	-	101.4	2-1_Ol_7
50	-	-	18.000	40.300	0.290	0.357	42.840	0.036	-	101.8	2-1_Ol_8

Appendix A

<b>Average</b>	-	-	<b>18.694</b>	<b>39.953</b>	<b>0.301</b>	<b>0.351</b>	<b>42.126</b>	<b>0.035</b>	-
<b>Average Full Sample</b>	<b>1.723</b>	<b>0.057</b>	<b>4.118</b>	<b>47.013</b>	<b>0.228</b>	<b>14.422</b>	<b>8.873</b>	<b>24.267</b>	<b>0.108</b>

**Table 17 Major elements data measured in plagioclase and olivine in sample 4-1.**

<b>No.</b>	<b>Na<sub>2</sub>O</b>	<b>K<sub>2</sub>O</b>	<b>FeO</b>	<b>SiO<sub>2</sub></b>	<b>CaO</b>	<b>MgO</b>	<b>Al<sub>2</sub>O<sub>3</sub></b>	<b>TiO<sub>2</sub></b>	<b>Total</b>	<b>Comment</b>
<i>Plagioclase</i>										
1	3.948	0.152	0.787	52.230	12.870	0.165	29.920	0.096	100.2	4-1_Plg_1_rim1
2	3.109	0.093	0.583	50.380	14.310	0.221	31.140	0.071	99.9	4-1_Plg_1_rim2
3	3.129	0.108	0.828	50.350	14.350	0.111	31.310	0.068	100.3	4-1_Plg_1_rim3
4	1.463	0.026	0.485	46.690	17.600	0.205	34.500	0.029	101.0	4-1_Plg_1_core1
5	1.433	0.043	0.532	46.450	17.570	0.186	34.270	0.036	100.5	4-1_Plg_1_core2
6	1.443	0.047	0.453	46.540	17.540	0.157	34.520	0.032	100.7	4-1_Plg_1_core3
7	1.600	0.037	0.573	47.030	17.140	0.206	33.900	0.039	100.5	4-1_Plg_2_rim1
8	1.480	0.032	0.611	46.560	17.290	0.155	34.240	0.043	100.4	4-1_Plg_2_rim2
9	1.460	0.028	0.526	46.540	17.380	0.187	34.320	0.040	100.5	4-1_Plg_2_rim3
10	1.610	0.051	0.529	47.120	16.930	0.205	34.180	0.037	100.7	4-1_Plg_2_core1
11	1.360	0.041	0.457	46.290	17.470	0.207	34.510	0.034	100.4	4-1_Plg_2_core2
12	1.680	0.040	0.513	47.170	16.930	0.200	34.060	0.024	100.6	4-1_Plg_2_core3
13	1.380	0.074	2.490	46.800	15.940	1.250	31.940	0.049	99.9	4-1_Plg_3_rim1
14	1.560	0.024	0.520	46.930	17.290	0.163	34.340	0.036	100.9	4-1_Plg_3_rim2
15	1.670	0.039	0.626	46.940	17.040	0.227	33.970	0.027	100.5	4-1_Plg_3_rim3
16	1.620	0.038	0.473	47.220	17.200	0.198	33.800	0.038	100.6	4-1_Plg_3_core1
17	1.600	0.024	0.451	46.720	17.150	0.213	33.970	0.035	100.2	4-1_Plg_3_core2
18	1.550	0.043	0.619	46.580	17.090	0.246	33.920	0.025	100.1	4-1_Plg_3_core3
19	3.880	0.139	0.896	52.380	12.970	0.163	30.220	0.113	100.8	4-1_Plg_4_rim1
20	2.990	0.092	0.733	50.270	14.430	0.174	31.650	0.057	100.4	4-1_Plg_4_rim2
21	1.700	0.051	0.516	47.140	16.940	0.223	33.820	0.041	100.4	4-1_Plg_4_rim3
22	1.620	0.053	0.400	46.810	17.020	0.174	34.130	0.023	100.2	4-1_Plg_4_core1
23	1.600	0.032	0.425	47.100	17.240	0.170	34.040	0.020	100.6	4-1_Plg_4_core2
24	1.550	0.056	0.464	46.820	17.280	0.179	34.400	0.027	100.8	4-1_Plg_4_core3
25	3.050	0.088	0.627	50.580	14.410	0.170	31.640	0.076	100.6	4-1_Plg_5_rim1
26	3.190	0.107	0.798	50.910	14.100	0.275	31.000	0.062	100.4	4-1_Plg_5_rim2
27	2.990	0.088	0.755	50.560	14.570	0.227	31.720	0.074	101.0	4-1_Plg_5_rim3
28	1.440	0.042	0.435	46.530	17.540	0.192	34.140	0.033	100.4	4-1_Plg_5_core1
29	1.450	0.042	0.499	46.530	17.320	0.197	34.210	0.040	100.3	4-1_Plg_5_core2
30	3.040	0.098	0.582	50.640	14.410	0.210	31.350	0.056	100.4	4-1_Plg_6_rim1
31	1.590	0.044	0.581	46.810	17.180	0.123	34.080	0.042	100.4	4-1_Plg_6_rim2
32	2.170	0.132	2.000	48.480	14.890	0.905	31.280	0.053	99.9	4-1_Plg_6_rim3
33	1.177	0.039	0.472	45.720	17.930	0.142	35.040	0.032	100.6	4-1_Plg_6_core1
34	1.088	0.051	0.399	45.810	18.000	0.143	35.230	0.025	100.7	4-1_Plg_6_core2
35	1.033	0.040	0.416	45.740	18.250	0.122	35.170	0.034	100.8	4-1_Plg_6_core3
<b>Average</b>	<b>1.962</b>	<b>0.061</b>	<b>0.659</b>	<b>47.811</b>	<b>16.388</b>	<b>0.237</b>	<b>33.312</b>	<b>0.045</b>		
<i>Olivine</i>										
36	-	-	17.460	40.250	0.345	43.390	0.038	-	101.5	4-1_Ol_1

Appendix A

No.	Na <sub>2</sub> O	K <sub>2</sub> O	FeO	SiO <sub>2</sub>	CaO	MgO	Al <sub>2</sub> O <sub>3</sub>	TiO <sub>2</sub>	Total	Comment
37	-	-	16.410	40.450	0.350	44.070	0.033	-	101.3	4-1_OI_2
38	-	-	15.640	40.570	0.348	44.620	0.032	-	101.2	4-1_OI_3
39	-	-	14.870	40.650	0.350	45.150	0.036	-	101.1	4-1_OI_4
40	-	-	15.500	40.590	0.353	44.860	0.038	-	101.3	4-1_OI_5
41	-	-	15.660	39.840	0.354	44.770	0.039	-	100.7	4-1_OI_6
42	-	-	15.780	39.870	0.347	44.790	0.035	-	100.8	4-1_OI_7
43	-	-	15.810	39.910	0.351	44.710	0.043	-	100.8	4-1_OI_8
44	-	-	15.800	40.000	0.350	44.750	0.036	-	100.9	4-1_OI_9
45	-	-	17.050	39.620	0.350	43.410	0.030	-	100.5	4-1_OI_10
46	-	-	16.010	40.030	0.348	44.450	0.025	-	100.9	4-1_OI_11
47	-	-	15.380	39.860	0.350	45.070	0.032	-	100.7	4-1_OI_12
48	-	-	15.060	40.500	0.350	45.100	0.043	-	101.1	4-1_OI_13
<b>Average</b>			<b>15.879</b>	<b>40.165</b>	<b>0.349</b>	<b>44.549</b>	<b>0.035</b>			
<b>Average Full Sample</b>	<b>1.962</b>	<b>0.061</b>	<b>4.781</b>	<b>45.740</b>	<b>12.044</b>	<b>12.238</b>	<b>24.300</b>	<b>0.045</b>		

**Table 18 Major elements data measured in plagioclase and clinopyroxene in sample 16-2**

No.	Na <sub>2</sub> O	K <sub>2</sub> O	FeO	SiO <sub>2</sub>	MnO	CaO	MgO	Al <sub>2</sub> O <sub>3</sub>	TiO <sub>2</sub>	Total	Comment
<i>Plagioclase</i>											
1	3.584	0.149	0.619	51.650	-	13.670	0.161	30.580	0.080	100.5	16-2_plg_1_rim1
2	3.317	0.137	0.619	51.080	-	14.160	0.190	30.660	0.070	100.2	16-2_plg_1_rim2
3	2.742	0.126	1.370	49.730	-	14.220	1.025	30.340	0.058	99.6	16-2_plg_1_rim3
4	1.951	0.055	0.571	47.820	-	16.640	0.180	33.050	0.043	100.3	16-2_plg_1_core1
5	1.766	0.050	0.588	47.460	-	16.910	0.181	33.270	0.038	100.3	16-2_plg_1_core2
6	1.664	0.054	1.099	47.020	-	16.460	0.910	32.270	0.041	99.5	16-2_plg_1_core3
7	3.738	0.163	0.764	51.900	-	13.380	0.159	30.070	0.078	100.3	16-2_plg_2_rim1
8	2.711	0.089	0.621	49.610	-	15.390	0.197	32.060	0.045	100.7	16-2_plg_2_rim2
9	3.254	0.132	0.713	51.070	-	14.200	0.185	30.900	0.071	100.5	16-2_plg_2_rim3
10	1.632	0.045	0.613	47.030	-	17.270	0.155	34.060	0.027	100.8	16-2_plg_2_core1
11	1.354	0.036	0.495	46.620	-	17.800	0.141	34.250	0.026	100.7	16-2_plg_2_core2
12	1.329	0.035	0.639	46.630	-	17.690	0.176	33.920	0.040	100.5	16-2_plg_2_core3
13	3.160	0.120	0.659	50.720	-	14.210	0.155	30.850	0.057	99.9	16-2_plg_3_rim1
14	1.373	0.036	0.588	45.770	-	17.750	0.121	34.190	0.015	99.8	16-2_plg_3_rim2
15	1.467	0.037	0.425	46.720	-	17.490	0.176	34.170	0.007	100.5	16-2_plg_3_core1
16	1.415	0.038	0.501	46.470	-	17.600	0.157	34.150	0.025	100.4	16-2_plg_3_core2
17	1.590	0.039	0.575	47.080	-	17.310	0.160	33.890	0.025	100.7	16-2_plg_3_core3
18	2.697	0.095	1.710	49.660	-	13.850	1.390	29.690	0.068	99.2	16-2_plg_4_rim1
19	1.887	0.067	0.685	47.980	-	16.560	0.148	32.990	0.030	100.3	16-2_plg_4_rim2
20	1.456	0.028	0.557	46.830	-	17.510	0.181	33.800	0.031	100.4	16-2_plg_4_rim3
21	1.307	0.026	0.529	46.540	-	17.800	0.160	34.420	0.013	100.8	16-2_plg_4_core1
22	1.328	0.033	0.450	46.670	-	17.760	0.161	34.420	0.039	100.9	16-2_plg_4_core2
23	1.379	0.038	0.450	46.440	-	17.720	0.185	34.080	0.015	100.3	16-2_plg_4_core3
24	1.292	0.035	0.676	46.230	-	17.810	0.152	34.260	0.021	100.5	16-2_plg_5_rim1
25	2.961	0.110	0.607	50.490	-	14.690	0.215	31.550	0.067	100.7	16-2_plg_5_rim2



Appendix A

No.	Na <sub>2</sub> O	K <sub>2</sub> O	FeO	SiO <sub>2</sub>	MnO	CaO	MgO	Al <sub>2</sub> O <sub>3</sub>	TiO <sub>2</sub>	Total	Comment
26	1.326	0.038	0.573	46.330	-	17.680	0.170	34.140	0.037	100.3	16-2_plg_5_rim3
27	1.639	0.051	0.549	47.520	-	17.250	0.204	33.540	0.031	100.8	16-2_plg_5_core1
28	1.772	0.043	0.507	47.500	-	16.910	0.219	33.530	0.057	100.5	16-2_plg_5_core2
29	1.853	0.043	0.471	47.770	-	16.730	0.227	33.420	0.046	100.6	16-2_plg_5_core3
30	4.496	0.248	0.710	54.050	-	11.710	0.103	28.750	0.075	100.1	16-2_plg_6_rim1
31	6.780	0.501	0.518	60.140	-	7.110	0.042	25.500	0.050	100.6	16-2_plg_6_rim2
32	4.783	0.251	0.844	54.760	-	11.200	0.113	28.620	0.094	100.7	16-2_plg_6_rim3
33	1.772	0.064	0.557	47.520	-	16.970	0.147	33.550	0.038	100.6	16-2_plg_6_core1
34	1.741	0.078	0.643	47.490	-	16.940	0.194	33.670	0.033	100.8	16-2_plg_6_core2
35	1.752	0.071	0.579	47.550	-	16.930	0.182	33.420	0.038	100.5	16-2_plg_6_core3
<b>Average</b>	<b>2.293</b>	<b>0.090</b>	<b>0.659</b>	<b>48.739</b>	<b>-</b>	<b>15.865</b>	<b>0.246</b>	<b>32.458</b>	<b>0.044</b>		
<i>Clinopyroxene</i>											
36	0.256	0.000	5.680	51.460	0.186	21.070	16.700	3.090	0.513	99.0	16-2_cpx_1
37	0.241	0.006	6.460	53.190	0.186	20.690	16.870	2.200	0.483	100.3	16-2_cpx_2
38	0.331	0.013	9.210	51.170	0.236	19.880	14.990	3.030	0.821	99.7	16-2_cpx_3
39	0.321	0.000	9.260	51.120	0.198	20.150	15.120	3.080	0.859	100.1	16-2_cpx_4
40	0.247	0.009	5.830	51.860	0.139	21.210	16.270	3.510	0.610	99.7	16-2_cpx_5
41	0.244	0.005	5.620	52.230	0.092	21.220	16.360	3.280	0.532	99.6	16-2_cpx_6
42	0.235	0.007	5.580	52.110	0.149	21.360	16.420	3.070	0.563	99.5	16-2_cpx_7
43	0.241	0.004	5.750	52.370	0.179	21.180	16.680	2.740	0.500	99.6	16-2_cpx_8
44	0.241	0.003	6.410	52.130	0.112	21.080	16.080	3.080	0.503	99.6	16-2_cpx_9
45	0.241	0.001	5.590	52.160	0.155	21.490	16.500	3.140	0.487	99.8	16-2_cpx_10
46	0.245	0.000	5.830	52.170	0.099	21.190	16.410	3.440	0.540	99.9	16-2_cpx_11
47	0.310	0.004	8.100	50.690	0.254	20.460	15.170	3.580	0.898	99.5	16-2_cpx_12
48	0.241	0.000	8.490	52.830	0.137	19.630	16.150	1.910	0.588	100.0	16-2_cpx_13
49	0.230	0.006	7.040	52.420	0.177	20.160	16.660	1.960	0.519	99.2	16-2_cpx_14
50	-	-	12.250	50.370	0.316	18.790	13.700	2.730	-	98.2	16-2_cpx_15
51	-	-	7.280	51.020	0.182	20.380	16.120	3.460	-	98.4	16-2_cpx_16
52	-	-	9.160	50.790	0.223	20.360	14.830	3.140	-	98.5	16-2_cpx_17
<b>Average</b>	<b>0.259</b>	<b>0.004</b>	<b>7.267</b>	<b>51.770</b>	<b>0.178</b>	<b>20.606</b>	<b>15.943</b>	<b>2.967</b>	<b>0.601</b>		
<b>Average Full Sample</b>	<b>1.712</b>	<b>0.066</b>	<b>2.819</b>	<b>49.730</b>	<b>0.178</b>	<b>17.415</b>	<b>5.378</b>	<b>22.817</b>	<b>0.203</b>		

Table 19 Major elements data measured in plagioclase and clinopyroxene in sample 14-1

No.	Na <sub>2</sub> O	K <sub>2</sub> O	FeO	SiO <sub>2</sub>	MnO	CaO	MgO	Al <sub>2</sub> O <sub>3</sub>	TiO <sub>2</sub>	Total	Comment
<i>Plagioclase</i>											
1	3.125	0.104	0.740	50.740	-	14.400	0.231	30.820	0.067	100.2	14-1_plg_1_rim
2	3.309	0.122	0.598	51.580	-	14.040	0.190	30.930	0.071	100.8	14-1_plg_1_rim
3	1.895	0.058	1.390	47.590	-	16.120	0.411	32.540	0.048	100.1	14-1_plg_1_rim
4	2.305	0.072	0.647	48.800	-	15.830	0.165	32.570	0.053	100.4	14-1_plg_1_core1
5	2.470	0.073	0.674	48.770	-	15.660	0.203	32.550	0.056	100.5	14-1_plg_1_core2
6	2.255	0.070	0.587	48.740	-	16.030	0.173	32.970	0.046	100.9	14-1_plg_1_core3
7	2.132	0.063	0.625	48.370	-	16.280	0.157	32.750	0.031	100.4	14-1_plg_2_rim1
8	3.321	0.123	0.656	51.260	-	14.060	0.178	31.200	0.050	100.8	14-1_plg_2_rim2

Appendix A

No.	Na <sub>2</sub> O	K <sub>2</sub> O	FeO	SiO <sub>2</sub>	MnO	CaO	MgO	Al <sub>2</sub> O <sub>3</sub>	TiO <sub>2</sub>	Total	Comment
9	3.526	0.135	1.223	52.160	-	13.000	0.529	29.360	0.066	100.0	14-1_plg_2_rim3
10	2.224	0.057	0.624	48.690	-	16.040	0.174	32.480	0.033	100.3	14-1_plg_2_core1
11	2.071	0.054	0.753	48.490	-	16.380	0.163	32.790	0.043	100.7	14-1_plg_2_core2
12	2.225	0.068	0.635	49.000	-	16.040	0.148	32.820	0.040	101.0	14-1_plg_2_core3
13	3.670	0.138	0.717	52.170	-	13.330	0.179	30.320	0.062	100.6	14-1_plg_3_rim1
14	4.173	0.176	0.833	53.210	-	12.350	0.138	29.160	0.084	100.1	14-1_plg_3_rim2
15	1.917	0.045	0.679	48.180	-	16.710	0.129	33.400	0.040	101.1	14-1_plg_3_rim3
16	2.184	0.069	0.700	48.880	-	16.040	0.154	32.660	0.044	100.7	14-1_plg_3_core1
17	2.564	0.073	0.672	49.740	-	15.480	0.152	32.180	0.028	100.9	14-1_plg_3_core2
18	2.441	0.306	6.210	48.160	-	12.340	2.380	24.410	0.436	96.7	14-1_plg_3_core3
19	3.046	0.105	0.723	50.670	-	14.500	0.190	31.070	0.063	100.4	14-1_plg_4_rim1
20	3.272	0.123	0.627	51.530	-	14.060	0.185	30.940	0.057	100.8	14-1_plg_4_rim2
21	3.601	0.137	0.607	51.990	-	13.510	0.167	30.310	0.060	100.4	14-1_plg_4_rim3
22	0.987	0.037	0.396	45.760	-	18.550	0.156	35.240	0.002	101.1	14-1_plg_4_core1
23	0.882	0.037	0.349	45.210	-	18.690	0.155	35.390	0.021	100.7	14-1_plg_4_core2
24	1.204	0.091	2.750	46.450	-	16.660	3.210	27.610	0.178	98.2	14-1_plg_4_core3
<b>Average</b>	<b>2.533</b>	<b>0.097</b>	<b>1.017</b>	<b>49.423</b>		<b>15.254</b>	<b>0.413</b>	<b>31.520</b>	<b>0.070</b>		
<i>Clinopyroxene</i>											
25	0.239	0.005	7.780	52.320	0.217	19.830	16.450	2.880	0.599	100.3	14-1_cpx_1
26	0.264	0.000	7.590	51.490	0.105	19.930	15.800	3.610	0.764	99.6	14-1_cpx_2
27	0.350	0.007	13.740	49.900	0.355	18.220	12.750	3.020	1.306	99.6	14-1_cpx_3
28	0.290	0.005	9.460	50.970	0.159	20.070	14.370	3.320	0.943	99.6	14-1_cpx_4
29	0.316	0.007	10.710	51.280	0.283	18.370	14.870	3.000	0.901	99.7	14-1_cpx_5
30	0.269	0.001	7.650	52.670	0.187	20.300	16.120	2.570	0.551	100.3	14-1_cpx_6
31	0.300	0.004	9.730	51.320	0.189	19.250	15.070	3.230	0.886	100.0	14-1_cpx_7
32	0.166	0.004	8.660	52.470	0.255	17.790	17.450	2.160	0.523	99.5	14-1_cpx_8
33	0.371	0.000	12.660	49.910	0.285	19.160	12.790	3.190	1.157	99.5	14-1_cpx_9
34	0.257	0.000	13.800	51.600	0.357	17.300	13.930	1.613	0.743	99.6	14-1_cpx_10
35	0.300	0.001	10.170	50.940	0.259	19.330	14.490	3.230	0.993	99.7	14-1_cpx_11
36	0.193	0.000	9.610	53.250	0.215	18.110	16.730	1.669	0.532	100.3	14-1_cpx_12
37	0.228	0.000	8.900	53.140	0.218	18.710	16.550	1.848	0.523	100.1	14-1_cpx_13
38	0.290	0.004	8.000	51.830	0.204	19.820	16.130	2.550	0.501	99.3	14-1_cpx_14
39	-	-	12.250	50.370	0.316	18.790	13.700	2.730	-	98.2	14-1_cpx_15
40	-	-	7.280	51.020	0.182	20.380	16.120	3.460	-	98.4	14-1_cpx_16
41	-	-	9.160	50.790	0.223	20.360	14.830	3.140	-	98.5	14-1_cpx_17
<b>Average</b>	<b>0.274</b>	<b>0.003</b>	<b>9.832</b>	<b>51.486</b>	<b>0.236</b>	<b>19.160</b>	<b>15.185</b>	<b>2.778</b>	<b>0.780</b>		
<b>Average Full Sample</b>	<b>1.6643</b>	<b>0.0609</b>	<b>4.7951</b>	<b>50.3071</b>	<b>0.2358</b>	<b>16.9281</b>	<b>6.7441</b>	<b>19.2016</b>	<b>0.3315</b>		

**Table 20 Major elements data measured in plagioclase and clinopyroxene in sample 17-1**

No.	Na <sub>2</sub> O	K <sub>2</sub> O	FeO	SiO <sub>2</sub>	MnO	CaO	MgO	Al <sub>2</sub> O <sub>3</sub>	TiO <sub>2</sub>	Total	Comment
<i>Plagioclase</i>											
1	3.873	0.197	0.720	52.280	-	12.820	0.167	30.030	0.083	100.2	17-1_plag_rim1
2	4.175	0.235	0.712	53.140	-	12.430	0.157	29.790	0.073	100.7	17-1_plag_rim2

Appendix A

No.	Na <sub>2</sub> O	K <sub>2</sub> O	FeO	SiO <sub>2</sub>	MnO	CaO	MgO	Al <sub>2</sub> O <sub>3</sub>	TiO <sub>2</sub>	Total	Comment
3	4.111	0.223	0.802	52.800	-	12.360	0.165	29.750	0.081	100.3	17-1_plag_rim3
4	1.987	0.070	0.664	48.290	-	16.490	0.125	33.510	0.047	101.2	17-1_plag_1_core1
5	1.945	0.070	0.619	47.940	-	16.480	0.141	33.590	0.066	100.9	17-1_plag_1_core2
6	1.955	0.066	0.636	47.700	-	16.350	0.141	33.240	0.058	100.1	17-1_plag_1_core3
7	4.388	0.267	0.953	53.670	-	11.940	0.197	29.400	0.085	100.9	17-1_plag_2_rim1
8	3.971	0.212	0.794	52.620	-	12.660	0.149	30.130	0.094	100.6	17-1_plag_2_rim2
9	2.110	0.076	0.770	48.830	-	16.060	0.117	33.340	0.042	101.3	17-1_plag_2_rim3
10	2.130	0.059	0.697	48.440	-	15.990	0.160	33.320	0.037	100.8	17-1_plag_2_core1
11	2.265	0.087	0.712	49.380	-	15.740	0.121	32.970	0.040	101.3	17-1_plag_2_core2
12	2.171	0.069	0.623	48.990	-	15.970	0.138	33.090	0.060	101.1	17-1_plag_2_core3
13	4.902	0.331	0.914	55.080	-	10.780	0.105	28.350	0.123	100.6	17-1_plag_3_rim1
14	4.381	0.263	0.793	54.560	-	11.740	0.131	29.170	0.099	101.1	17-1_plag_3_rim2
15	2.045	0.072	0.685	48.840	-	16.150	0.127	32.960	0.036	100.9	17-1_plag_3_rim3
16	1.712	0.040	0.544	47.330	-	16.850	0.150	33.970	0.029	100.6	17-1_plag_3_core1
17	1.753	0.065	0.671	48.180	-	16.810	0.109	33.840	0.044	101.5	17-1_plag_3_core2
18	1.701	0.071	0.639	47.970	-	16.870	0.130	33.920	0.028	101.3	17-1_plag_3_core3
19	3.858	0.215	0.699	53.340	-	12.850	0.137	30.040	0.077	101.2	17-1_plag_4_rim1
20	3.857	0.228	0.689	53.500	-	12.800	0.171	30.060	0.106	101.4	17-1_plag_4_rim2
21	2.053	0.072	0.597	49.200	-	16.260	0.126	33.070	0.061	101.4	17-1_plag_4_rim3
22	1.356	0.035	0.587	47.430	-	17.600	0.103	34.660	0.023	101.8	17-1_plag_4_core1
23	1.492	0.052	0.589	47.640	-	17.310	0.132	34.010	0.035	101.3	17-1_plag_4_core2
24	1.575	0.062	0.610	47.760	-	17.090	0.111	33.950	0.037	101.2	17-1_plag_4_core3
25	3.832	0.204	0.701	53.370	-	12.910	0.153	30.030	0.087	101.3	17-1_plag_5_rim1
26	3.831	0.205	0.734	53.340	-	12.790	0.140	29.980	0.077	101.1	17-1_plag_5_rim2
27	2.174	0.085	0.820	49.090	-	15.990	0.185	32.870	0.044	101.3	17-1_plag_5_rim3
28	1.470	0.061	0.570	47.360	-	17.300	0.100	34.210	0.040	101.1	17-1_plag_5_core1
29	1.645	0.056	0.667	47.530	-	17.070	0.118	34.010	0.030	101.1	17-1_plag_5_core2
30	1.521	0.056	0.502	47.500	-	17.300	0.111	34.240	0.037	101.3	17-1_plag_5_core3
31	2.172	0.093	0.759	49.300	-	15.960	0.146	33.130	0.061	101.6	17-1_plag_6_rim1
32	3.102	0.129	0.730	51.860	-	14.210	0.186	31.580	0.073	101.9	17-1_plag_6_rim2
33	2.223	0.080	0.628	49.250	-	16.000	0.136	32.920	0.043	101.3	17-1_plag_6_rim3
34	1.995	0.067	0.644	48.680	-	16.510	0.157	33.320	0.057	101.4	17-1_plag_6_core1
35	2.304	0.081	0.635	49.520	-	15.820	0.144	32.820	0.034	101.4	17-1_plag_6_core2
36	1.973	0.061	0.630	48.840	-	16.480	0.132	33.390	0.039	101.5	17-1_plag_6_core3
Average	2.611	0.120	0.687	50.015	-	15.187	0.139	32.296	0.058		
<i>Clinopyroxene</i>											
37	0.310	0.004	8.960	51.240	0.200	19.560	15.500	4.350	1.274	101.4	17-1_cpx_1
38	0.247	0.000	7.320	53.550	0.198	20.060	16.580	2.430	0.672	101.1	17-1_cpx_2
39	0.301	0.005	8.580	52.660	0.201	20.030	15.680	2.850	0.820	101.1	17-1_cpx_3
40	0.268	0.002	7.650	53.090	0.159	19.980	16.270	2.720	0.692	100.8	17-1_cpx_4
41	0.282	0.004	7.780	52.050	0.175	20.280	15.770	3.660	0.866	100.9	17-1_cpx_5
42	0.288	0.000	8.710	53.050	0.184	19.590	15.990	2.750	0.799	101.4	17-1_cpx_6
43	0.275	0.002	6.870	52.990	0.149	20.870	16.270	2.850	0.657	100.9	17-1_cpx_7
44	0.291	0.003	8.120	52.870	0.095	20.290	15.870	2.970	0.840	101.3	17-1_cpx_8
45	0.258	0.006	6.900	52.230	0.194	20.770	16.160	3.200	0.712	100.4	17-1_cpx_9
46	0.285	0.008	9.310	52.850	0.182	19.670	15.530	2.790	0.851	101.5	17-1_cpx_10

Appendix A

No.	Na <sub>2</sub> O	K <sub>2</sub> O	FeO	SiO <sub>2</sub>	MnO	CaO	MgO	Al <sub>2</sub> O <sub>3</sub>	TiO <sub>2</sub>	Total	Comment
47	0.333	0.004	9.140	49.950	0.193	20.570	14.500	4.570	1.294	100.6	17-1_cpx_11
48	0.294	0.008	8.700	50.750	0.108	20.220	14.670	4.740	1.362	100.9	17-1_cpx_12
49	0.318	0.003	11.220	50.840	0.207	18.460	15.190	2.880	0.981	100.1	17-1_cpx_13
50	0.302	0.004	10.010	50.300	0.167	20.340	14.190	4.920	1.251	101.5	17-1_cpx_14
51	0.328	0.012	9.990	52.260	0.169	19.530	15.190	3.200	0.857	101.5	17-1_cpx_15
52	0.325	0.000	8.460	51.220	0.100	19.550	15.390	4.610	1.151	100.8	17-1_cpx_16
53	0.290	0.000	9.140	53.130	0.209	19.530	15.790	2.500	0.759	101.3	17-1_cpx_17
54	0.335	0.008	9.360	51.230	0.164	19.730	14.940	4.540	1.259	101.6	17-1_cpx_18
55	-	-	8.800	51.370	0.225	19.650	15.900	2.240	-	98.2	17-1_cpx_19
56	-	-	5.740	51.750	0.133	21.460	16.470	2.880	-	98.4	17-1_cpx_20
57	-	-	6.010	51.600	0.145	21.340	16.440	2.830	-	98.4	17-1_cpx_21
58	-	-	5.870	51.570	0.138	21.290	16.440	2.820	-	98.1	17-1_cpx_22
59	-	-	5.880	52.260	0.134	21.400	16.440	2.890	-	99.0	17-1_cpx_23
60	-	-	5.430	52.410	0.124	21.630	16.680	2.880	-	99.2	17-1_cpx_24
<b>Average</b>	<b>0.296</b>	<b>0.004</b>	<b>8.081</b>	<b>51.968</b>	<b>0.165</b>	<b>20.242</b>	<b>15.744</b>	<b>3.295</b>	<b>0.950</b>		
<b>Average Full Sample</b>	<b>1.869</b>	<b>0.083</b>	<b>3.555</b>	<b>50.789</b>	<b>0.163</b>	<b>17.169</b>	<b>6.227</b>	<b>20.973</b>	<b>0.338</b>		



**Appendix B**



Appendix B

Table 21 Detailed results of the  $^{40}\text{Ar}/^{39}\text{Ar}$  step-heating experiments, inverse isochrones and Alteration Index calculations from the dike sample 1-2 aliquot 1.

Step	$^{40}\text{Ar}/^{39}\text{Ar}$	$^{37}\text{Ar}/^{39}\text{Ar}$	$^{36}\text{Ar}/^{39}\text{Ar}$	$^{39}\text{Ar}_K$ (moles)	% $^{40}\text{Ar}_{\text{atmos.}}$	Cum. $^{39}\text{Ar}$	Age (Ma)	$\pm 2\sigma$ (Ma)	Alteration Index, cut-off $<0.00006^a$	Inverse isochron				
										$^{39}\text{Ar}/^{40}\text{Ar}$	$1\sigma$ error	$^{36}\text{Ar}/^{40}\text{Ar}$	$1\sigma$ error	
1	12268.60	182.41	41.26	2.36E-17	99.26	0.03	181.68	416.84	0.0229329	7.11E-05	3.82E-05	3.36E-03	2.70E-05	
2	3370.04	128.39	11.41	5.28E-17	99.77	0.09	15.69	79.11	0.0089585	2.70E-04	3.83E-05	3.38E-03	1.98E-05	
3	2141.86	174.42	7.33	4.06E-17	100.52	0.13	-23.44	31.48	0.0041909	4.10E-04	1.31E-05	3.40E-03	1.17E-05	
4	1166.27	156.23	4.00	6.39E-17	100.20	0.20	-4.84	25.46	0.0025156	7.63E-04	2.63E-05	3.39E-03	1.79E-05	
5	447.92	188.26	1.57	8.57E-17	100.01	0.30	-0.08	11.61	0.0007590	1.94E-03	2.90E-05	3.38E-03	2.07E-05	
6	239.13	195.21	0.84	1.11E-16	97.65	0.42	11.94	6.73	0.0003514	3.61E-03	8.11E-05	3.30E-03	2.23E-05	
7	71.20	216.54	0.27	1.15E-16	89.55	0.55	16.04	4.43	0.0000409	1.19E-02	1.60E-04	3.03E-03	4.88E-05	
8	26.32	223.44	0.12	1.45E-16	72.34	0.71	15.79	2.76	-0.0000312	3.20E-02	6.17E-04	2.45E-03	8.33E-05	
9	18.39	228.54	0.09	7.72E-17	50.34	0.80	19.86	5.24	-0.0000466	4.57E-02	2.21E-03	1.70E-03	2.36E-04	
10	19.23	243.33	0.10	4.58E-17	54.92	0.85	19.10	9.94	-0.0000456	4.31E-02	3.34E-03	1.86E-03	4.14E-04	
11	19.07	222.79	0.09	3.49E-17	51.80	0.89	19.90	10.71	-0.0000453	4.42E-02	4.53E-03	1.75E-03	4.71E-04	
12	21.92	230.77	0.11	3.61E-17	66.42	0.93	16.05	11.90	-0.0000388	3.82E-02	3.28E-03	2.25E-03	4.33E-04	
13	26.51	224.68	0.11	3.00E-17	60.53	0.96	22.67	11.22	-0.0000359	3.18E-02	2.75E-03	2.05E-03	3.50E-04	
14	35.98	228.17	0.13	2.59E-17	53.02	0.99	36.58	14.55	-0.0000317	2.33E-02	1.76E-03	1.79E-03	3.38E-04	
15	269.18	249.43	0.92	1.08E-17	93.63	1.00	37.79	30.35	0.0002875	3.06E-03	1.19E-04	3.17E-03	8.74E-05	
<b>Mass (mg)</b>	<b>J value</b>	<b>2<math>\sigma</math> % error</b>								<b>J value</b>	<b>2<math>\sigma</math> % error</b>			
9.756	0.001018	0.237								0.001018	0.237			

<sup>a</sup> after Baksi (2007)

## Appendix B

Table 22 Detailed results of the  $^{40}\text{Ar}/^{39}\text{Ar}$  step-heating experiments, inverse isochrones and Alteration Index calculations from the dike sample 1-2 aliquot 2.

Step	$^{40}\text{Ar}/^{39}\text{Ar}$	$^{37}\text{Ar}/^{39}\text{Ar}$	$^{36}\text{Ar}/^{39}\text{Ar}$	$^{39}\text{Ar}_K$ (moles)	% $^{40}\text{Ar}_{\text{atmos.}}$	Cum. $^{39}\text{Ar}$	Age (Ma)	$\pm 2\sigma$ (Ma)	Alteration Index cut-off <0.00006 <sup>a</sup>	Inverse isochron				
										$^{39}\text{Ar}/^{40}\text{Ar}$	1 $\sigma$ error	$^{36}\text{Ar}/^{40}\text{Ar}$	1 $\sigma$ error	
1	2211.87	147.35	7.50	4.76E-17	99.71	0.10	12.93	57.15	0.0050946	0.0004053	0.00003443	0.003374	2.15E-05	
2	675.12	189.23	2.33	4.71E-17	99.84	0.19	2.27	22.54	0.00116625	0.001284	0.00003704	0.003379	2.67E-05	
3	170.60	216.44	0.66	2.91E-17	104.02	0.25	-14.90	10.51	0.00022185	0.004971	0.0000607	0.00352	4.78E-05	
4	40.42	225.16	0.17	1.18E-16	81.42	0.49	16.30	4.16	-0.0000102	0.02083	0.0002147	0.002755	8.04E-05	
5	50.83	227.48	0.21	1.04E-16	85.32	0.69	16.23	4.52	0.0000051	0.01653	0.000127	0.002887	6.94E-05	
6	13.83	227.98	0.08	7.78E-17	50.83	0.85	14.81	2.62	-0.0000499	0.06073	0.001854	0.00172	0.000154	
7	20.53	238.37	0.12	4.52E-17	81.88	0.94	8.18	3.05	-0.0000362	0.04055	0.001423	0.002771	0.000116	
8	104.47	247.35	0.39	2.98E-17	90.79	1.00	21.25	8.49	0.0000715	0.00791	0.0001194	0.003072	6.26E-05	
<b>Mass (mg)</b>	<b>J value</b>	<b>2<math>\sigma</math> % error</b>								<b>J value</b>	<b>2<math>\sigma</math> % error</b>			
5.763	0.001018	0.237								0.001018	0.237			

<sup>a</sup> after Baksi (2007)

## Appendix B

Table 23 Detailed results of the  $^{40}\text{Ar}/^{39}\text{Ar}$  step-heating experiments, inverse isochrones and Alteration Index calculations from the dike sample 10-1 aliquot 1.

Step #	$^{40}\text{Ar}/^{39}\text{Ar}$	$^{37}\text{Ar}/^{39}\text{Ar}$	$^{36}\text{Ar}/^{39}\text{Ar}$	$^{39}\text{Ar}_K$ (moles)	% $^{40}\text{Ar}_{\text{atmos.}}$	Cum. $^{39}\text{Ar}$	Age (Ma)	$\pm 2\sigma$ (Ma)	Alteration Index, cut-off <0.00006 <sup>a</sup>	Inverse isochron			
										$^{39}\text{Ar}/^{40}\text{Ar}$	1 $\sigma$ error	$^{36}\text{Ar}/^{40}\text{Ar}$	1 $\sigma$ error
1	140.71	287.59	0.56	2.44E-18	102.09	0.01	-6.79	167.38	0.0001115	0.005672	0.000951	0.003455	0.000872
2	124.20	321.95	0.46	8.18E-18	88.04	0.03	34.90	36.74	0.0000564	0.006232	0.0003893	0.002979	0.000215
3	27.57	343.92	0.16	3.14E-17	70.45	0.09	19.62	10.90	-0.0000411	0.02751	0.001562	0.002384	0.000284
4	15.77	332.96	0.12	4.55E-17	64.96	0.18	13.19	5.06	-0.0000499	0.04858	0.003294	0.002198	0.000241
5	13.87	339.92	0.12	6.89E-17	67.59	0.31	10.81	5.01	-0.0000510	0.05488	0.002826	0.002287	0.00026
6	14.12	332.56	0.11	1.54E-16	54.43	0.61	15.35	3.61	-0.0000526	0.05428	0.001239	0.001842	0.000185
7	19.17	331.11	0.12	8.86E-17	42.04	0.79	26.39	4.00	-0.0000521	0.04003	0.001153	0.001423	0.000159
8	11.09	330.14	0.11	3.87E-17	47.94	0.86	13.74	8.31	-0.0000550	0.06929	0.007815	0.001622	0.000569
9	12.28	352.92	0.13	3.01E-17	84.95	0.92	4.51	12.85	-0.0000503	0.06126	0.007839	0.002875	0.00073
10	11.07	338.88	0.14	5.77E-18	127.54	0.93	-7.36	53.47	-0.0000462	0.06883	0.05131	0.004316	0.003448
11	12.10	339.22	0.14	7.48E-18	112.31	0.95	-3.59	47.06	-0.0000467	0.06296	0.03317	0.003801	0.002734
12	13.93	351.47	0.12	1.53E-17	59.40	0.98	13.73	21.31	-0.0000524	0.05409	0.01201	0.00201	0.001112
13	13.77	345.43	0.11	1.19E-17	35.54	1.00	21.39	26.27	-0.0000556	0.05501	0.01596	0.001203	0.001483
<b>Mass (mg)</b>	<b>J value</b>	<b>2<math>\sigma</math> % error</b>								<b>J value</b>	<b>2<math>\sigma</math> % error</b>		
9.579	0.001018	0.237								0.001018	0.237		

<sup>a</sup> after Baksi (2007)

Appendix B

Table 24 Detailed results of the  $^{40}\text{Ar}/^{39}\text{Ar}$  step-heating experiments, inverse isochrones and Alteration Index calculations from the dike sample 10-1 aliquot 2.

Step #	$^{40}\text{Ar}/^{39}\text{Ar}$	$^{37}\text{Ar}/^{39}\text{Ar}$	$^{36}\text{Ar}/^{39}\text{Ar}$	$^{39}\text{Ar}_K$ (moles)	% $^{40}\text{Ar}_{\text{atmos.}}$	Cum. $^{39}\text{Ar}$	Age (Ma)	$\pm 2\sigma$ (Ma)	Alteration Index, cut-off <0.00006 <sup>a</sup>	Inverse isochron				
										$^{39}\text{Ar}/^{40}\text{Ar}$	1 $\sigma$ error	$^{36}\text{Ar}/^{40}\text{Ar}$	1 $\sigma$ error	
1	618.44	288.75	1.81	1.32E-18	82.99	0.0030	227.33	196.92	0.0005516	0.001289	0.00023	0.002808	0.000249	
2	213.58	380.61	0.68	1.99E-18	79.69	0.01	105.53	106.02	0.0000935	0.003431	0.000608	0.002697	0.000347	
3	57.73	319.10	0.26	1.04E-17	89.55	0.03	14.22	28.38	-0.0000047	0.01344	0.001133	0.00303	0.000355	
4	30.95	318.94	0.16	3.48E-17	71.90	0.10	20.46	8.89	-0.0000365	0.02507	0.001059	0.002433	0.000211	
5	21.61	330.41	0.13	5.47E-17	64.35	0.21	18.32	3.90	-0.0000460	0.03554	0.001372	0.002178	0.000136	
6	16.31	330.62	0.12	9.47E-17	59.93	0.39	15.56	5.22	-0.0000503	0.04707	0.001362	0.002028	0.000231	
7	15.20	324.23	0.11	6.63E-17	44.53	0.53	19.93	4.44	-0.0000533	0.05082	0.002313	0.001507	0.000225	
8	15.49	334.16	0.11	9.09E-17	49.75	0.71	18.58	5.13	-0.0000526	0.04941	0.0016	0.001683	0.000242	
9	18.06	329.41	0.12	5.75E-17	51.47	0.82	20.81	7.15	-0.0000508	0.04258	0.001894	0.001742	0.000291	
10	17.14	341.32	0.13	3.94E-17	72.47	0.90	11.35	7.36	-0.0000480	0.04437	0.00292	0.002453	0.000308	
11	14.33	349.66	0.12	2.44E-17	54.30	0.95	15.86	17.16	-0.0000529	0.05268	0.0066	0.001837	0.000861	
12	13.99	337.06	0.14	9.27E-18	98.27	0.97	0.58	32.66	-0.0000465	0.05458	0.01853	0.003326	0.001643	
13	14.40	338.85	0.11	9.74E-18	46.57	0.99	18.45	27.76	-0.0000537	0.05291	0.0166	0.001576	0.001478	
14	16.96	347.01	0.12	3.92E-18	48.58	0.99	21.05	77.06	-0.0000524	0.04459	0.02932	0.001644	0.003398	
<b>Mass (mg)</b>	<b>J value</b>	<b>2<math>\sigma</math> % error</b>								<b>J value</b>	<b>2<math>\sigma</math> % error</b>			
9.070	0.001018	0.237								0.001018	0.237			

<sup>a</sup> after Baksi (2007)

Appendix B

Table 25 Detailed results of the  $^{40}\text{Ar}/^{39}\text{Ar}$  step-heating experiments, inverse isochrones and Alteration Index calculations from the dike sample 2-1 aliquot 1.

Step #	$^{40}\text{Ar}/^{39}\text{Ar}$	$^{37}\text{Ar}/^{39}\text{Ar}$	$^{36}\text{Ar}/^{39}\text{Ar}$	$^{39}\text{Ar}_K$ (moles)	% $^{40}\text{Ar}_{\text{atmos.}}$	Cum. $^{39}\text{Ar}$	Age (Ma)	$\pm 2\sigma$ (Ma)	Alteration Index, cut-off <0.00006 <sup>a</sup>	Inverse isochron				
										$^{39}\text{Ar}/^{40}\text{Ar}$	1 $\sigma$ error	$^{36}\text{Ar}/^{40}\text{Ar}$	1 $\sigma$ error	
1	401.13	168.66	1.24	2.24E-18	88.12	0.006	96.62	118.72	0.0006613	0.002198	0.0002567	0.002982	0.000253	
2	595.06	172.00	2.15	1.60E-18	104.42	0.008	-55.71	242.12	0.0011836	0.001478	0.0002259	0.003534	0.000319	
3	323.14	174.46	1.24	3.01E-18	109.37	0.012	-64.47	122.09	0.0006371	0.002716	0.000331	0.003701	0.000294	
4	197.92	238.75	0.74	6.14E-18	101.44	0.020	-6.28	52.09	0.0002291	0.004206	0.000262	0.003433	0.000201	
5	101.61	254.74	0.39	2.24E-17	94.37	0.051	12.76	13.08	0.0000691	0.008082	0.0002643	0.003193	9.82E-05	
6	47.64	258.44	0.21	4.72E-17	88.91	0.12	11.81	8.86	-0.0000041	0.01718	0.000548	0.003009	0.000141	
7	47.30	253.57	0.21	1.09E-16	87.08	0.26	13.60	6.17	-0.0000046	0.01738	0.0002381	0.002947	9.97E-05	
8	53.03	257.27	0.23	2.08E-16	88.21	0.55	13.96	3.37	0.0000021	0.01545	0.0001095	0.002985	4.84E-05	
9	30.36	252.47	0.15	1.37E-16	77.72	0.73	15.04	5.38	-0.0000283	0.0271	0.0004329	0.00263	0.000136	
10	16.12	252.51	0.11	3.81E-17	75.83	0.79	8.67	9.88	-0.0000439	0.05103	0.005133	0.002566	0.000474	
11	72.30	272.22	0.30	2.58E-17	92.02	0.82	13.05	13.26	0.0000236	0.01119	0.000432	0.003114	0.000138	
12	35.80	273.40	0.17	2.82E-17	80.84	0.86	15.52	10.14	-0.0000241	0.02257	0.001378	0.002736	0.000216	
13	24.74	255.48	0.13	4.47E-17	74.31	0.92	14.17	12.16	-0.0000357	0.03317	0.001874	0.002515	0.000378	
14	56.52	258.94	0.24	3.44E-17	91.28	0.97	11.02	9.63	0.0000081	0.01448	0.0005113	0.003089	0.00013	
15	17.24	246.95	0.10	2.31E-17	53.15	1.00	17.85	13.84	-0.0000478	0.04796	0.007532	0.001799	0.000664	
<b>Mass (mg)</b>	<b>J value</b>	<b>2<math>\sigma</math> % error</b>								<b>J value</b>	<b>2<math>\sigma</math> % error</b>			
10.278	0.001018	0.237								0.001018	0.237			

<sup>a</sup> after Baksi (2007)

Appendix B

Table 26 Detailed results of the  $^{40}\text{Ar}/^{39}\text{Ar}$  step-heating experiments, inverse isochrones and Alteration Index calculations from the dike sample 2-1 aliquot 2.

Step #	$^{40}\text{Ar}/^{39}\text{Ar}$	$^{37}\text{Ar}/^{39}\text{Ar}$	$^{36}\text{Ar}/^{39}\text{Ar}$	$^{39}\text{Ar}_K$ (moles)	% $^{40}\text{Ar}_{\text{atmos.}}$	Cum. $^{39}\text{Ar}$	Age (Ma)	$\pm 2\sigma$ (Ma)	Alteration Index, cut-off <0.00006 <sup>a</sup>	Inverse isochron			
										$^{39}\text{Ar}/^{40}\text{Ar}$	1 $\sigma$ error	$^{36}\text{Ar}/^{40}\text{Ar}$	1 $\sigma$ error
1	47.61	293.47	0.23	4.10E-18	95.15	0.03	5.33	66.08	-0.0000074	0.01668	0.004186	0.00322	0.001019
2	25.16	263.50	0.14	1.40E-17	79.47	0.11	11.60	24.43	-0.0000344	0.03239	0.004499	0.002689	0.00074
3	41.82	244.77	0.19	2.76E-17	88.18	0.27	10.93	12.72	-0.0000086	0.0198	0.000878	0.002984	0.000234
4	34.68	250.05	0.16	4.94E-17	79.84	0.56	15.51	6.06	-0.0000224	0.02377	0.000731	0.002702	0.000135
5	19.09	261.72	0.10	4.90E-17	52.07	0.84	20.47	6.22	-0.0000474	0.04275	0.002253	0.001762	0.00026
6	17.16	266.85	0.11	2.08E-17	60.39	0.96	15.29	10.43	-0.0000472	0.04736	0.006431	0.002044	0.000491
7	42.46	274.02	0.17	6.24E-18	66.29	1.00	32.25	34.84	-0.0000252	0.01902	0.003602	0.002243	0.000651
<b>Mass (mg)</b>	<b>J value</b>	<b>2<math>\sigma</math> % error</b>								<b>J value</b>	<b>2<math>\sigma</math> % error</b>		
5.763	0.001018	0.237								0.001018	0.237		

<sup>a</sup> after Baksi (2007)

## Appendix B

Table 27 Detailed results of the  $^{40}\text{Ar}/^{39}\text{Ar}$  step-heating experiments, inverse isochrones and Alteration Index calculations from the dike sample 4-1 aliquot 1.

Step #	$^{40}\text{Ar}/^{39}\text{Ar}$	$^{37}\text{Ar}/^{39}\text{Ar}$	$^{36}\text{Ar}/^{39}\text{Ar}$	$^{39}\text{Ar}_K$ (moles)	% $^{40}\text{Ar}_{\text{atmos.}}$	Cum. $^{39}\text{Ar}$	Age (Ma)	$\pm 2\sigma$ (Ma)	Alteration Index, cut-off <0.00006 <sup>a</sup>	Inverse isochron			
										$^{39}\text{Ar}/^{40}\text{Ar}$	1 $\sigma$ error	$^{36}\text{Ar}/^{40}\text{Ar}$	1 $\sigma$ error
1	13387.40	1376.86	45.32	1.18E-19	99.24	0.01	2543.67	7976.08	0.0032628	0.0000025	0.0000071	0.0033580	0.0000177
2	3808.61	673.98	13.12	4.79E-18	100.45	0.02	-60.32	130.75	0.0018944	0.0001383	0.0000087	0.0033990	0.0000161
3	1929.85	529.77	6.63	1.21E-17	99.41	0.06	33.07	42.85	0.0011867	0.0003255	0.0000138	0.0033640	0.0000131
4	899.25	453.18	3.11	2.39E-17	98.41	0.14	38.13	35.86	0.0006120	0.0007583	0.0000164	0.0033300	0.0000256
5	694.95	436.89	2.48	1.91E-17	100.40	0.20	-7.38	40.00	0.0004895	0.0009976	0.0000251	0.0033980	0.0000366
6	276.49	410.42	1.03	2.93E-17	98.59	0.30	10.04	18.43	0.0001682	0.0025750	0.0000388	0.0033360	0.0000440
7	37.41	389.40	0.21	7.74E-17	84.40	0.55	14.69	5.50	-0.0000326	0.0194200	0.0002768	0.0028560	0.0000994
8	31.22	390.30	0.18	4.03E-17	77.16	0.68	17.94	10.36	-0.0000393	0.0232600	0.0008687	0.0026110	0.0002249
9	39.00	404.92	0.22	2.69E-17	87.62	0.77	12.34	17.30	-0.0000315	0.0183500	0.0007311	0.0029650	0.0002949
10	59.42	387.15	0.28	3.51E-17	86.80	0.88	19.66	10.79	-0.0000146	0.0122500	0.0002759	0.0029380	0.0001233
11	145.94	399.80	0.57	9.29E-18	94.08	0.91	21.91	21.77	0.0000578	0.0049290	0.0002491	0.0031840	0.0000999
12	56.48	402.71	0.27	1.84E-17	84.30	0.97	22.56	13.98	-0.0000198	0.0127000	0.0005871	0.0028530	0.0001663
13	67.63	401.83	0.29	6.82E-18	78.93	0.99	36.08	37.47	-0.0000148	0.0106200	0.0010130	0.0026710	0.0003775
14	265.44	484.22	0.86	2.27E-18	80.95	1.00	135.47	147.38	0.0000923	0.0024870	0.0004244	0.0027390	0.0003513
<b>Mass (mg)</b>	<b>J value</b>	<b>2<math>\sigma</math> % error</b>								<b>J value</b>	<b>2<math>\sigma</math> % error</b>		
8.350	0.001018	0.237								0.001018	0.237		

<sup>a</sup> after Baksi (2007)



Appendix B

Table 28 Detailed results of the  $^{40}\text{Ar}/^{39}\text{Ar}$  step-heating experiments, inverse isochrones and Alteration Index calculations from the dike sample 16-2 aliquot 1.

Step	$^{40}\text{Ar}/^{39}\text{Ar}$	$^{37}\text{Ar}/^{39}\text{Ar}$	$^{36}\text{Ar}/^{39}\text{Ar}$	$^{39}\text{Ar}_K$ (moles)	% $^{40}\text{Ar}_{\text{atmos.}}$	Cum. $^{39}\text{Ar}$	Age (Ma)	$\pm 2\sigma$ (Ma)	Alteration Index, cut-off <0.00006 <sup>a</sup>	Inverse isochron				
										$^{39}\text{Ar}/^{40}\text{Ar}$	1 $\sigma$ error	$^{36}\text{Ar}/^{40}\text{Ar}$	1 $\sigma$ error	
1	2082.09	315.66	7.07	2.38E-17	99.19	0.03	39.50	38.64	0.0022056	0.000374	0.000012	0.003357	0.000014	
2	570.46	244.09	1.98	3.57E-17	99.19	0.08	10.31	21.59	0.0007424	0.001453	0.000020	0.003357	0.000029	
3	306.51	229.06	0.96	4.85E-17	87.07	0.14	85.14	15.68	0.0003430	0.002738	0.000035	0.002947	0.000041	
4	123.88	220.25	0.46	7.15E-17	95.37	0.23	12.48	7.89	0.0001253	0.006824	0.000076	0.003227	0.000050	
5	108.76	217.06	0.39	7.83E-17	89.44	0.32	24.84	5.72	0.0000947	0.007793	0.000082	0.003027	0.000041	
6	22.30	211.65	0.11	1.41E-16	71.42	0.50	13.77	3.42	-0.0000345	0.038180	0.000714	0.002417	0.000122	
7	16.42	214.66	0.09	1.42E-16	58.30	0.68	14.83	2.59	-0.0000451	0.051720	0.001253	0.001973	0.000128	
8	14.15	217.73	0.08	6.31E-17	48.75	0.76	15.74	4.62	-0.0000496	0.059880	0.003784	0.001650	0.000277	
9	11.59	221.02	0.06	5.57E-17	13.92	0.83	21.67	5.82	-0.0000580	0.072900	0.006366	0.000471	0.000466	
10	15.57	211.22	0.09	4.32E-17	61.08	0.88	13.09	6.91	-0.0000449	0.054710	0.004607	0.002067	0.000366	
11	19.81	209.65	0.10	2.67E-17	66.80	0.92	14.18	9.19	-0.0000387	0.043060	0.004656	0.002261	0.000384	
12	24.69	211.12	0.14	2.34E-17	102.06	0.95	-1.10	14.31	-0.0000192	0.034500	0.003411	0.003454	0.000452	
13	36.03	216.41	0.16	3.60E-17	81.96	0.99	14.09	8.28	-0.0000133	0.023540	0.001081	0.002774	0.000182	
14	1077.47	245.48	3.80	7.12E-18	102.35	1.00	-57.35	82.53	0.0014955	0.000768	0.000036	0.003464	0.000056	
<b>Mass (mg)</b>	<b>J value</b>	<b>2<math>\sigma</math> % error</b>								<b>J value</b>	<b>2<math>\sigma</math> % error</b>			
9.296	0.001024	0.163								0.001024	0.163			

<sup>a</sup> after Baksi (2007)

Appendix B

Table 29 Detailed results of the  $^{40}\text{Ar}/^{39}\text{Ar}$  step-heating experiments, inverse isochrones and Alteration Index calculations from the dike sample 14-1 aliquot 1.

Step #	$^{40}\text{Ar}/^{39}\text{Ar}$	$^{37}\text{Ar}/^{39}\text{Ar}$	$^{36}\text{Ar}/^{39}\text{Ar}$	$^{39}\text{Ar}_K$ (moles)	% $^{40}\text{Ar}_{\text{atmos.}}$	Cum. $^{39}\text{Ar}$	Age (Ma)	$\pm 2\sigma$ (Ma)	Alteration Index, cut-off <0.00006 <sup>a</sup>	Inverse isochron				
										$^{39}\text{Ar}/^{40}\text{Ar}$	1 $\sigma$ error	$^{36}\text{Ar}/^{40}\text{Ar}$	1 $\sigma$ error	
1	6583.77	800.28	22.39	4.82E-18	99.56	0.02	118.12	86.52	0.0027603	0.000067	0.000012	0.003369	0.000005	
2	2601.09	522.68	8.97	1.06E-17	100.35	0.06	-26.65	108.54	0.0016594	0.000243	0.000015	0.003396	0.000024	
3	1346.07	436.04	4.61	1.06E-17	98.71	0.10	45.27	42.48	0.0009890	0.000516	0.000026	0.003341	0.000021	
4	1368.59	438.73	4.73	9.00E-18	99.69	0.13	11.11	70.46	0.0010105	0.000506	0.000025	0.003374	0.000033	
5	901.58	416.80	3.16	1.11E-17	100.02	0.17	-0.47	55.38	0.0006846	0.000785	0.000033	0.003385	0.000040	
6	603.78	369.90	2.14	1.62E-17	99.87	0.23	1.93	33.35	0.0005009	0.001226	0.000030	0.003380	0.000038	
7	310.38	334.50	1.11	2.70E-17	97.30	0.33	19.98	15.61	0.0002504	0.002465	0.000053	0.003293	0.000036	
8	190.72	332.26	0.70	3.74E-17	95.03	0.47	22.56	11.52	0.0001273	0.004020	0.000084	0.003216	0.000043	
9	50.02	332.11	0.23	4.34E-17	83.00	0.64	20.25	12.05	-0.0000175	0.015330	0.000405	0.002809	0.000173	
10	257.91	351.87	0.93	9.00E-18	96.00	0.67	24.96	39.64	0.0001818	0.002920	0.000119	0.003249	0.000108	
11	38.44	339.36	0.20	2.53E-17	84.39	0.77	14.40	18.08	-0.0000276	0.019820	0.001122	0.002856	0.000334	
12	30.49	313.25	0.17	2.39E-17	86.96	0.85	9.33	16.56	-0.0000314	0.025590	0.001931	0.002943	0.000394	
13	28.93	325.95	0.16	1.72E-17	75.17	0.92	17.02	22.90	-0.0000375	0.026650	0.002892	0.002544	0.000575	
14	60.04	348.14	0.27	9.94E-18	85.82	0.96	20.57	47.14	-0.0000096	0.012590	0.001189	0.002904	0.000554	
15	62.93	295.30	0.33	1.17E-17	117.59	1.00	-25.82	35.05	0.0000258	0.012600	0.000981	0.003979	0.000403	
<b>Mass (mg)</b>	<b>J value</b>	<b>2<math>\sigma</math> % error</b>								<b>J value</b>	<b>2<math>\sigma</math> % error</b>			
5.954	0.001018	0.237								0.001018	0.237			

<sup>a</sup> after Baksi (2007)

Appendix B

**Table 30** Detailed results of the  $^{40}\text{Ar}/^{39}\text{Ar}$  step-heating experiments, inverse isochrones and Alteration Index calculations from the dike sample 17-1 aliquot 1.

Step #	$^{40}\text{Ar}/^{39}\text{Ar}$	$^{37}\text{Ar}/^{39}\text{Ar}$	$^{36}\text{Ar}/^{39}\text{Ar}$	$^{39}\text{Ar}_K$ (moles)	% $^{40}\text{Ar}_{\text{atmos.}}$	Cum. $^{39}\text{Ar}$	Age (Ma)	$\pm 2\sigma$ (Ma)	Alteration Index, cut-off <0.00006 <sup>a</sup>	Inverse isochron				
										$^{39}\text{Ar}/^{40}\text{Ar}$	1 $\sigma$ error	$^{36}\text{Ar}/^{40}\text{Ar}$	1 $\sigma$ error	
1	2416.61	283.22	8.34	9.09E-18	101.08	0.01	-60.57	98.16	0.0029097	0.000332	0.000009	0.003420	0.000029	
2	1097.14	242.70	3.82	1.79E-17	101.03	0.03	-25.11	40.99	0.0015124	0.000756	0.000012	0.003419	0.000028	
3	398.46	214.95	1.40	4.07E-17	99.33	0.08	5.75	13.52	0.0005736	0.002131	0.000022	0.003361	0.000027	
4	102.56	198.18	0.38	1.07E-16	94.59	0.20	11.78	5.77	0.0001081	0.008394	0.000100	0.003201	0.000045	
5	67.27	197.19	0.26	1.78E-16	89.88	0.40	14.44	4.44	0.0000451	0.012810	0.000120	0.003042	0.000053	
6	20.83	196.85	0.10	1.47E-16	69.78	0.56	13.36	3.45	-0.0000351	0.041370	0.000904	0.002361	0.000134	
7	14.27	195.79	0.08	1.59E-16	50.84	0.74	14.87	2.29	-0.0000478	0.060460	0.001748	0.001721	0.000137	
8	13.07	195.70	0.07	6.49E-17	45.89	0.82	14.99	4.37	-0.0000500	0.065990	0.005073	0.001553	0.000302	
9	13.42	200.53	0.08	5.23E-17	59.39	0.87	11.60	5.31	-0.0000468	0.064050	0.005927	0.002010	0.000339	
10	12.64	196.58	0.07	4.27E-17	46.08	0.92	14.46	10.24	-0.0000503	0.068190	0.008213	0.001559	0.000684	
11	13.49	194.23	0.08	3.23E-17	70.81	0.96	8.35	13.04	-0.0000436	0.064010	0.009580	0.002396	0.000787	
12	15.63	199.00	0.09	2.85E-17	70.66	0.99	9.76	15.38	-0.0000414	0.055050	0.008071	0.002391	0.000797	
13	28.84	196.27	0.16	8.23E-18	111.03	1.00	-6.79	53.24	-0.0000043	0.029890	0.008301	0.003757	0.001465	
<b>Mass (mg)</b>	<b>J value</b>	<b>2<math>\sigma</math> % error</b>								<b>J value</b>	<b>2<math>\sigma</math> % error</b>			
9.213	0.001018	0.237								0.001018	0.237			

<sup>a</sup> after Baksi (2007)

Appendix B

Table 31 Detailed results of the  $^{40}\text{Ar}/^{39}\text{Ar}$  step-heating experiments, inverse isochrones and Alteration Index calculations from the dike sample 17-1 aliquot 2.

Step #	$^{40}\text{Ar}/^{39}\text{Ar}$	$^{37}\text{Ar}/^{39}\text{Ar}$	$^{36}\text{Ar}/^{39}\text{Ar}$	$^{39}\text{Ar}_K$ (moles)	% $^{40}\text{Ar}_{\text{atmos.}}$	Cum. $^{39}\text{Ar}$	Age (Ma)	$\pm 2\sigma$ (Ma)	Alteration Index, cut-off $<0.00006^a$	Inverse isochron			
										$^{39}\text{Ar}/^{40}\text{Ar}$	1 $\sigma$ error	$^{36}\text{Ar}/^{40}\text{Ar}$	1 $\sigma$ error
1	14332.60	624.40	48.45	1.93E-18	99.55	0.00	199.58	530.54	0.0078094	0.000039	0.000010	0.003369	0.000021
2	1508.35	228.98	5.10	1.48E-17	98.77	0.02	40.18	41.45	0.0021802	0.000556	0.000014	0.003342	0.000022
3	357.59	221.25	1.25	3.68E-17	98.14	0.05	14.40	14.11	0.0004858	0.002362	0.000022	0.003321	0.000031
4	54.19	204.62	0.22	1.09E-16	88.28	0.16	13.56	3.58	0.0000200	0.015800	0.000198	0.002988	0.000053
5	23.95	204.61	0.11	1.42E-16	70.41	0.30	15.13	1.98	-0.0000321	0.035750	0.000663	0.002383	0.000067
6	13.67	200.02	0.08	2.38E-16	54.20	0.54	13.32	2.52	-0.0000478	0.062880	0.001176	0.001834	0.000150
7	11.30	203.18	0.07	1.58E-16	47.75	0.69	12.60	2.20	-0.0000514	0.075870	0.002502	0.001616	0.000165
8	10.44	200.34	0.07	8.42E-17	42.65	0.77	12.75	3.66	-0.0000529	0.082290	0.005501	0.001443	0.000307
9	10.03	196.80	0.06	6.28E-17	36.25	0.84	13.57	5.15	-0.0000542	0.085940	0.008021	0.001227	0.000456
10	10.83	202.15	0.07	3.01E-17	34.54	0.87	15.10	9.61	-0.0000542	0.079260	0.014190	0.001169	0.000810
11	11.51	195.90	0.07	5.77E-17	47.05	0.92	12.93	5.04	-0.0000510	0.074930	0.006675	0.001592	0.000383
12	13.43	199.57	0.07	3.09E-17	36.64	0.95	18.08	9.96	-0.0000520	0.064030	0.009083	0.001240	0.000663
13	16.69	200.54	0.09	2.41E-17	64.94	0.98	12.46	11.09	-0.0000419	0.051480	0.007521	0.002197	0.000557
14	13.72	212.24	0.08	1.04E-17	43.52	0.99	16.64	24.03	-0.0000508	0.062040	0.025190	0.001473	0.001586
15	16.49	195.91	0.05	9.22E-18	-8.88	1.00	37.81	36.01	-0.0000631	0.052320	0.020250	-0.000300	0.002264
16	39.92	220.15	0.10	3.10E-18	30.71	1.00	59.09	83.73	-0.0000414	0.021180	0.009991	0.001039	0.001998
<b>Mass (mg)</b>	<b>J value</b>	<b>2<math>\sigma</math> % error</b>								<b>J value</b>	<b>2<math>\sigma</math> % error</b>		
10.679	0.001018	0.237								0.001018	0.237000		

<sup>a</sup> after Baksi (2007)

## Curriculum Vitae

### Dominik Pałgan

Date of birth: 30.09.1988

Place of birth: Gdynia

Nationality: Polish

#### Academic Education:

2012-2017	PhD Candidate at GEOMAR Helmholtz Centre for Ocean Research Kiel, Germany
2010-2012	M.Sc. Marine Geology, University of Gdańsk, Poland
2007-2010	B.Sc. Oceanography, University of Gdańsk, Poland

#### Publications related to this thesis:

Pałgan, D., Devey, C.W., and Wartho, J.-A., 2017,  $^{40}\text{Ar}/^{39}\text{Ar}$  dating of the dikes from Westfjords, Iceland: applicability for of the method and insights into hydrothermal activity in the off-axis oceanic crust, to be submitted at Journal of Geophysical Research: Solid Earth.

Pałgan, D., Devey, C., W., and Yeo, I.A., 2017, Volcanism and hydrothermalism on a hot spot-influenced ridge: Comparing Reykjanes Peninsula and Reykjanes Ridge, Iceland, under review at Journal of Volcanology and Geothermal Research.

Pałgan, D., Devey, C., W., and Yeo, I.A., 2016, Dike control of hydrothermal circulation in the Tertiary Icelandic crust and implications for cooling of the seafloor: Journal of Volcanology and Geothermal Research, v. 316, p. 22–33, doi: 10.1016/j.jvolgeores.2016.02.021.

#### Conferences:

Pałgan D., Devey C.W., and Yeo I.A., (2015) Hydrothermal activity in Tertiary Icelandic crust: Implications for cooling processes along slow-spreading mid-ocean ridges [Poster], In: AGU Fall Meeting 2016, 14-18.12.2015, San Francisco, USA, (OS43A-2010).

Pałgan D., Jamieson J.W., Breusing C. and Devey C.W., 2015, Role of Hydrothermal systems in Development of the Oceans. Where to find them on the seafloor? [Poster], In: Sustainable Ocean Development Symposium, 28-30.09.2015, New York, USA.

Pałgan D., and Devey C.W., (2015) Dike controlled low-temperature hydrothermal activity in far off-axis regions of NW Iceland [PICO], In: EGU General Assembly 2015, 12-17.04.2015, Vienna, Austria, (EGU2015-1374).

Pałgan D., Devey C.W. and Loudon K., (2015) Iceland – on shore reflection of the Mid-Atlantic Ridge. Can Iceland help us locate new hydrothermal fields? [Invited talk], In: PhD Student Conference 2015 at Institut de Physique du Globe de Paris, 23–27.03.2015, Paris, France.

Devey, C.W., Jamieson, J.W., Petersen, S., Yeo, I.A., Walter, M., Buss, A., Collins, J., Koehler, J., Pałgan, D., Vishiti, A., 2013, Predicting the location of extinct massive sulfide deposits on the Atlantic Seafloor [Poster], In: AGU Fall Meeting 2013, 9-13.12.2013, San Francisco, USA, (OS43A-2010).